FACULTY OF ENGINEERING
AND ARCHITECTURE

Mechanical Properties and Durability of 3D Printed Cementitious Materials

Jolien Van Der Putten

Doctoral dissertation submitted to obtain the academic degree of
Doctor of Civil Engineering

Supervisors

Prof. Kim Van Tittelboom, PhD - Prof. Geert De Schutter, PhD

Department of Structural Engineering and Building Materials
Faculty of Engineering and Architecture, Ghent University

June 2021

GHENT
UNIVERSITY

FACULTY OF ENGINEERING AND ARCHITECTURE

Mechanical Properties and Durability of 3D Printed Cementitious Materials

Jolien Van Der Putten

Doctoral dissertation submitted to obtain the academic degree of
Doctor of Civil Engineering

Supervisors
Prof. Kim Van Tittelboom, PhD - Prof. Geert De Schutter, PhD

Department of Structural Engineering and Building Materials
Faculty of Engineering and Architecture, Ghent University

June 2021

GHENT UNIVERSITY

ISBN 978-94-6355-495-4
NUR 971
Wettelijk depot: D/2021/10.500/43

Members of the Examination Board

Chair

Prof. Em. Luc Taerwe, PhD, Ghent University

Other members entitled to vote

Prof. Nele De Belie, PhD, Ghent University
Prof. Steffen Grünewald, PhD, Ghent University
Prof. Viktor Mechtcherine, PhD, Technische Universität Dresden, Germany
Bjorn Van Belleghem, PhD, Ghent University
Timothy Wangler, PhD, Eidgenössische Technische Hochschule Zürich, Switzerland

Supervisors

Prof. Kim Van Tittelboom, PhD, Ghent University
Prof. Geert De Schutter, PhD, Ghent University

Acknowledgments

6 jaar onderzoek, 6 jaar onderwijs, 6 jaar lang ondergedompeld worden in een wereld vol beton… het lijkt in eerste instantie een enorm lange periode maar het gaat ontzettend snel voorbij. Tot op de dag van vandaag heb ik er nog geen seconde spijt van. Zou ik het opnieuw doen? Zeker! Op één voorwaarde. Dat ik omringd mag worden door dezelfde personen als weleer.

"If you cannot do great things, do small things in a great way"

Een klein gebaar met een grote impact is het verwoorden van een welgemeende dank je wel. Daarom wil ik in eerste instantie mijn beide promoteren prof. dr. ing. Kim Van Tittelboom en prof. dr. ir. Geert De Schutter bedanken voor de mogelijkheden die jullie mij boden, voor de nieuwe inzichten die jullie mij gaven en vooral voor het vertrouwen dat jullie in mij hadden om deze uitdaging aan te gaan. Jullie gaven mij de kans om niet alleen een nieuwe constructietechniek, maar ook mezelf verder te ontwikkelen. In het bijzonder Kim, nog eens een extra dank je wel. Jouw deur stond altijd open op eender welk moment en jouw motiverende (en geruststellende) woorden hebben me meermaals geholpen om de vooropgestelde deadlines te kunnen behalen. Verder wil ik ook prof. dr. ir. Nele De Belie, hoofd van de onderzoeksgroep, bedanken om mij de mogelijkheid te bieden om in haar laboratorium onderzoek te mogen verrichten.

Mede door de leden van de examencommissie is dit manuscript nu het eindresultaat. Hun suggesties en vragen hebben de kwaliteit van het werk enkel maar verbeterd. Prof. dr. ing. Kim Van Tittelboom, prof. dr. ir. Geert De Schutter, prof. dr. ir. Nele De Belie, prof. dr. ir. Steffen Grünewald, prof. dr. Victor Mechtcherine, dr. ir. Timothy Wangler en dr. ir. Bjorn Van Belleghem, bedankt voor jullie tijd en oog voor detail.

Naast de universiteit wens ik ook de partners van het C3PO project te bedanken. Jullie technische visie, gedrevenheid en doorzettingsvermogen heeft ervoor gezorgd dat het eerste geprinte huis in België werd gerealiseerd binnen dit project en ook zichtbaar werd binnen de constructie industrie. Ook al stonden jullie misschien in eerste instantie sceptisch ten opzichte van de nieuwe constructietechniek, het eindresultaat heeft jullie toch (gedeeltelijk) kunnen overtuigen.

De veelvuldigheid aan proeven die beschreven staan in dit doctoraat zouden nooit mogelijk geweest zijn zonder een goede planning en zonder de vele hulp en inzichten van alle techniekers. Tommy, bedankt om mijn proeven te blijven inplannen, ook al had ik mijn pijlen reeds verschoten tijdens de eerste werkdag. Jouw amusante verhalen en anekdotes tijdens de koffie- en middagpauzes zorgden bijkomend ook steeds voor een aangename werkonderbreking en voor een glimlach op mijn gezicht. Bart, Tom, Stefan, Dennis, Eric, Peter L., Peter VdB en Marc, zonder jullie zouden veel testen niet uitgevoerd zijn. Jullie waren telkens bereid om *last-minute* om het even welk probleem op te lossen. Sandra, bedankt om me op te leiden als SEM-operator en de vele aangename gesprekken tijdens het uitvoeren van de metingen. Dieter, manusje van alles, bedankt voor het ontwerpen van mijn printtoestel, de vele hulp tijdens de ontwikkeling van om het eender welke opstelling en bij het 3D printen van grotere structurele elementen. Nathan, ook voor jou in het bijzonder een grote dank je wel. Al sinds mijn masterthesisjaar stond je altijd klaar om te helpen, op om het even welk moment en voor om het even welk probleem, in en buiten het labo.

Christel, Marijke en Jens, bedankt voor de vele hulp bij alle administratieve rompslomp, het regelen van alle buitenlandse verblijven in functie van congressen of buitenlandse cursussen en ervoor te zorgen dat zowel de bestellingen als de dienstverleningsprojecten correct werden afgerond.

Onder het motto “lachende collega’s werken harder”, wil ik in eerste instantie de leden van de 3D printing groep bedanken, ook al zijn we als groep in principe nog onbestaande binnen de vakgroep. Karel, Yaxin, Manu, Rahul en Michiel, bedankt om steeds met (geveinsde?!) interesse naar mijn presentaties te luisteren tijdens de vele groepsvergaderingen. Jullie bedenkingen en inzichten hebben enkel maar een positieve bijdrage geleverd aan dit manuscript. En om volledig te zijn, breid ik de groep natuurlijk uit met de mensen van Schoonmeersen: Wouter, Gieljan en Ticho, jullie positieve *vibe* zorgde er voor dat ook de niet werk gerelateerde evenementen, zoals de afsluiter van de printdagen en het printen van kerstboom, samen in een aangename sfeer verliepen.

Verder wil ik ook nog alle collega’s bedanken, jullie zorgden ervoor dat ik met plezier kwam werken. In het bijzonder Didier, het was een genoegen om met jouw hulp polymeren te introduceren in geprinte elementen. Ook bedankt voor de sociale evenementen die je telkens organiseerde. Philip, jouw blijvend enthousiasme bij het kaarten onder de middag en jouw gedrevenheid is me telkens blijven inspireren. Tim, de motiverende woorden tijdens het schrijven zorgden ervoor dat de laatste loodjes draaglijk werden.

Ook jullie hulp en de aangename sfeer tijdens de vierdaagse metingen in Zwitserland zorgden voor voldoende verstrooiing tijdens de nachtelijke metingen in PSI. Michiel, het was een genoegen om jou als petekind en bureaugenoot te hebben. Pitchai en Hanne, bedankt voor de toffe week in Delft tijdens de microscopiecursus. En Brenda, ook jij verdient meer dan één speciaal woordje van dank. Je was altijd bereid om te helpen bij het printen en de kleine attenties vol motiverende woorden waren een echte steun tijdens de laatste maanden. Bedankt ook om telkens mee te gaan in het kerstgebeuren (al dan niet voor Sinterklaas...) en om gewoon jezelf te zijn. #nofilter.

Verder wil ik ook graag mijn bureaugenoten bedanken: Karel, Allesandro, Weixi, Bjorn, Mert, Mahzad, Davide en Michiel; De *small talks*, verdreven de *monday blues* keer op keer en brachten telkens een aangename verstrooiing.

Raphaël, Robby, Kim, Eline, Thomas, Pieterjan, bedankt om mijn in eerste instantie beperkt enthousiasme om les te geven toch aan te wakkeren en samen de vele uren aan projectverdedigingen te trotseren. Verder wil ik ook nog alle 17 masterstudenten bedanken die ik tijdens de voorbije 6 jaar heb mogen begeleiden. Jullie hebben niet alleen enorm veel werk verricht, maar jullie zorgden ook voor nieuwe inzichten en brachten me vaak op nieuwe ideeën. Uit de grond van mijn hart, het was een plezier om jullie begeleider te zijn.

Verder wil ik ook nog mijn vrienden en vriendinnen bedanken. Jullie waren een echte steun en toeverlaat. Tijdens de vele uitstapjes, etentjes, sportieve ontspanningen en weekendactiviteiten zorgden jullie ervoor dat ik het beton even achter mij kon laten… ook al wisten jullie vaak niet waar ik elke dag mee bezig was, toch bedankt.

En *last but not least*, zijn er in het bijzonder nog twee mensen die ik nooit met woorden alleen voldoende ga kunnen bedanken. Mama en papa, bedankt om er zo voor mij te zijn, zonder jullie had ik dit nooit gekund. En ondanks de moeilijke periodes, de vele paniekaanvallen en stressmomenten, tijdens het tijdens het studeren maar ook tijdens het doctoreren, op professioneel en persoonlijk vlak, jullie stonden altijd klaar. Met raad en daad. Met open armen en een luisterend oor. Bedankt. 1000 keer bedankt.

Lieve pepe en meme's, ook al zijn jullie er niet meer bij, ik weet dat jullie trots zouden zijn.

Jolien Van Der Putten, Sint-Lievens-Houtem, Juni 2021

Research funding

The majority of this research was supported by the C3PO-project (B/15100/01), funded by EFRO. Furthermore, as a research assistant, I would like to thank Ghent University for the financial support.

Table of contents

Notation index

Abbreviations

3DCP	3D Concrete Printing	
ALM	Automatic Laser Measurements	
AM	Additive manufacturing	
CAST	Traditionally cast specimens composed out of the reference composition	
CC	Contour Crafting	
CF	Cement filtrate	
CH	Calcium hydroxide	
CP	Cement paste	
CSA	Calcium silicate aluminate	
CT	Computed Tomography	
CSH	Calcium silicate hydrates	
DOF	Degrees of freedom	
DST	Direct shear test	
DW	Demineralized water	
MIP	Mercury Intrusion Porosimetry	
(O)PC	(Ordinary) Portland cement	
REF	Printed specimens composed out of the reference mixture	
RH	Relative humidity	[%]
rpm	Rotation per minute	
SAP	Superabsorbent polymer (plural SAPs)	
SDC	Smart Dynamic Casting	
SEM	Scanning Electron Microscopy	
SP	Superplasticizer	
Stdev	Standard deviation	
UH	Unhydrated cement	
UUCT	Uniaxial unconfined compression test	
W/B	Water/binder ratio	[-]
W/C	Water/cement ratio	[-]
W/C_{entr}	Water/cement ratio with entrained water	[-]
UUCT	Uniaxial unconfined compression test	

Chemical formula

$AgNO_3$	Silver nitrate
$BaSO_4$	Barium sulphate
C_2S	Dicalcium silicate (Belite)
C_3A	Tricalcium aluminate (Aluminate)
C_3S	Tricalcium silicate (Alite)
C_4AF	Tetracalcium alumino ferrite (Ferrite)
$CaCO_3$	Calcium carbonate
$Ca(OH)_2$	Calcium hydroxide (portlandite)
CO_2	Carbon dioxide
H_2O	Water
NaCl	Natrium chloride

Roman symbols

A017	Reference composition with the addition of SAP type A	
A_{thix}	Structuration rate	[Pa/s]
C_s	Chloride surface concentration	[m%binder]
D_{NSS}	Non-steady state diffusion coefficient	$[.10^{-12}\ m^2/s]$
d_{50}	Mean particle size	[µm]
E(t)	Young's modulus at time t	[kPa]
f_c	Compressive strength	$[N/mm^2]$
f_f	Flexural strength	$[N/mm^2]$
G025	Reference composition with the addition of SAP type G	
G(t)	Storage modulus at time t	
g	Gravitational acceleration	$[m^2/s]$
h	Height	[mm]
h_0	Initial height	[mm]
i	Cumulative absorbed volume of water	$[kg/m^2]$
k	Surface moisture content	[-]
M3	Reference composition with the addition of fibers	
M022	Reference composition with the addition of SAP type M	
m_d	Dry weight	[g]
m_{sat}	Saturated weight	[g]
R_a	Centre-line roughness	[-]

S1	Low printing speed	[m/s]
S2	High printing speed	[m/s]
TX	Interlayer time interval of x minutes	[min]
t_{knee}	Knee-point	[s]
t_{max}	Maximum time of a printed layer to be produced	[s]
V	Printing speed	[m/s]

Greek symbols

α	Coefficient depending on the cement type	[-]
α_{ds1}	Coefficient depending on the cement type	[-]
α_{ds2}	Coefficient depending on the cement type	[-]
β_{bs}	Time dependent parameter (fib ModelCode90)	[-]
β_{ds}	Time dependent parameter depending on the drying surface exposed to environmental conditions	[-]
β_{RH}	Time dependent parameter, depending on the relative humidity	[-]
ε_{auto}	Autogenous shrinkage, measured with corrugated tubes	[µm/m]
$\varepsilon_{auto,cast}$	Autogenous shrinkage, measured on cast specimens	[µm/m]
ε_{cam}	Total shrinkage, measured on printed specimens	[µm/m]
ε_{cbs}	Autogenous shrinkage (fib ModelCode90)	[µm/m]
$\varepsilon_{cbs,0}$	Basic autogenous shrinkage (fib ModelCode90)	[µm/m]
$\varepsilon_{dry,cast}$	Drying shrinkage, measured on cast specimens	[µm/m]
ε_{cds}	Drying shrinkage (fib ModelCode90)	[µm/m]
$\varepsilon_{cds,0}$	Basic drying shrinkage (fib ModelCode90)	[µm/m]
Ø	Diameter	[mm]
ρ	Density	[kg/m^3]
$\tau_{c,0}$	Initial yield stress	[Pa]
$\tau_c(t)$	Yield stress as a function of time	[Pa]
$\tau_g(t)$	Gravity induced stress	[Pa]
μ_p	Plastic viscosity	[Pa.s]
ν	Poisson's ratio	[-]

Samenvatting

Beton is vandaag de dag één van de meest gebruikte bouwmaterialen wereldwijd. Ook al is het materiaal bros en kan er scheurvorming ontstaan wanneer het onderhevig is aan trek, toch zijn de toepassingsmogelijkheden oneindig. Op materiaaltechnisch vlak heeft beton reeds een enorme evolutie doorgemaakt. De traditionele betonsamenstelling werd bijvoorbeeld vervangen door een samenstelling met zelfverdichtende eigenschappen, of de normale druksterkte werd verdrievoudigd door de ontwikkeling van ultrahogesterktebeton. En dan hebben we het nog niet eens gehad over zelfhelend beton, waarbij optredende scheuren door de inmenging van superabsorberende polymeren zichzelf kunnen helen. De technologie staat niet stil.

Ondanks de sterke evolutie op materiaalniveau is het productieproces vandaag de dag nog quasi onveranderd. Ongeacht het type beton, ongeacht de toepassing waarvoor het gebruikt wordt, de vervaardiging is nog steeds even arbeidsintensief, het maken van een bekisting vraagt veel tijd, zeker wanneer de complexiteit van het ontwerp toeneemt, en het betonstorten op zich vergt nog steeds de nodige hoeveelheid mankracht. Dit alles vergroot niet alleen de constructietijd, maar zorgt bijkomend ook voor een niet economisch materiaalverbruik en beperkt de architecturale vrijheid van de ontwerper.

De droom van een architect = de droom van een ingenieur?

Op internationaal vlak is er de laatste tien jaar intensief gezocht naar een manier om dit productieproces te automatiseren. Veel onderzoekers vonden hiervoor inspiratie in andere takken van de industrie zoals in de geneeskunde of de astronomie. Op basis van die expertise werd de nieuwsgierigheid ook aangewakkerd in de constructie-industrie. Wat als het mogelijk was om structurele elementen, met vaak complexe geometrieën, te construeren door op een automatische manier een cementgebonden materiaal te printen zonder menselijke tussenkomst? Wat als een architect niet meer gelimiteerd werd door het menselijk handelen en kunnen? Ook al leek het in eerste instantie een 'ver van mijn bed show', de voordelen konden niet worden genegeerd; men zou de constructietijd, net zoals het materiaalverbruik, kunnen limiteren, de werkzaamheden zouden veiliger kunnen verlopen en de architecturale vrijheid van de ontwerper zou kunnen zegevieren.

De keerzijde van de medaille

Naast de vele voordelen is er ook een keerzijde aan de medaille. Het traditionele beton leek immers niet geschikt voor deze innovatieve technologie. Uit onderzoek bleek dat, om een cementgebonden materiaal als printbaar te kunnen klasseren, het moest voldoen aan tegenstrijdige eigenschappen. Enerzijds moet het beton voldoende vloeibaar zijn om te kunnen verpompen, terwijl het tegelijkertijd ook voldoende snel moet uitharden om niet te bezwijken onder zijn eigengewicht en het gewicht van de bovenliggende lagen. Anderzijds is ook de tijd tussen het extruderen van twee opeenvolgende lagen (de zogenaamde *time gap*) van groot belang: een te grote tijdspanne zorgt voor een slechte hechting, een te kleine tijdspanne zorgt voor onvoldoende structuuropbouw met bezwijken als gevolg.

Het productieproces op zich verandert niet alleen het materiaalgedrag in verse toestand, ook in verharde toestand heeft de medaille een keerzijde. Door een element laagsgewijs op te bouwen wordt de kans op ingesloten luchtbellen groter. Verder is er ook een grotere kans op scheurvorming door krimp aangezien er geen bekisting gebruikt wordt en het materiaal onmiddellijk na extrusie wordt blootgesteld aan de omgeving, wat zorgt een toename aan invalswegen voor schadelijke stoffen.

Van internationaal naar nationaal onderzoek

Het doel van dit doctoraatsonderzoek is om de invloed van het printproces te begroten, zowel op de mechanische aspecten als op het vlak van duurzaamheid en om een vergelijking te maken met de traditionele manier van bouwen. Om de invloed van de samenstelling zoveel mogelijk te elimineren en enkel te focussen op een variatie in printparameters, werd gekozen om doorheen het volledige doctoraatsonderzoek dezelfde standaardsamenstelling te gebruiken bestaande uit cement, zand, water en superplastificeerder. Naast het karakteriseren van bovenvermelde eigenschappen was het ook de bedoeling om beide aspecten te gaan verbeteren. Hiervoor was het echter wel noodzakelijk om de basissamenstelling uit te breiden en werden vezels of verschillende types superabsorberende polymeren (SAPs) toegevoegd. De water/cement-factor (W/C-factor) werd voor alle samenstellingen constant gehouden (0.365). Het printen van de cementgebonden materialen gebeurde met behulp van een zelfontworpen 2D-print toestel, bestaande uit een verticaal gemonteerd en in hoogte verstelbaar mortelpistool, een horizontaal bewegend platform waarop de lagen konden geprint worden en een ellipsvormige spuitmond. Na het extruderen werden de printbaarheidseisen van elke samenstelling

afgetoetst op vlak van extrudeerbaarheid en opbouwbaarheid. Ook al voldeed het referentiemateriaal op vlak van verprintbaarheid, de verpompbaarheid daarentegen was onvoldoende. Dit was te wijten aan de verhouding zand/cement die, in vergelijking met andere printbare mengsels uit de literatuur, te hoog was en resulteerde in een materiaal met een te hoge vloeigrens en plastische viscositeit om de uitbreiding naar 3D geprinte elementen te realiseren. De verpompbaarheid werd daarom verbeterd door de verhouding zand/cement te verlagen van 2 naar 1,5 en door gebruik te maken van een andere type zand (zeezand in plaats van normzand). De W/C-factor bleef, in vergelijking met de andere samenstellingen, onveranderd.

Isotroop? Anisotroop?

Het laag per laag opbouwen van een structureel element zorgt ervoor dat het element zich niet langer isotroop maar eerder anistroop zal gedragen, wat inhoudt dat de eigenschappen afhankelijk van de richting kunnen verschillen. De mechanische eigenschappen (druk-, trek- en buigsterkte) worden voornamelijk beïnvloed door de kwaliteit van de *interlayer,* de zone tussen twee opeenvolgende lagen. Om de invloed van zowel de printsnelheid als de *time gap* te kunnen evalueren, werd in het eerste deel van dit doctoraatsonderzoek een parameterstudie uitgevoerd, waarbij twee verschillende printsnelheden (1.7 cm/s en 3.0 cm/s) en vier verschillende *time gaps* (0, 10, 30 en 60 minuten) in beschouwing werden genomen. Aangezien er momenteel nog geen standaardmethoden beschikbaar zijn om de mechanische eigenschappen van geprinte elementen te testen, werd een toevlucht gezocht in de 'ouderwetse' methoden: de druksterkte werd getest op basis van een uni-axiale drukproef, de hechting tussen de lagen werd opgemeten via een *pull-off* test en de buisterkte werd bepaald door middel van een driepuntsbuigproef. De druk- en treksterkte werden bepaald in één enkele richting (parallel aan de printrichting). De buigsterkte daarentegen werd zowel parallel als loodrecht op de printrichting bepaald.

Uit de eerste resultaten bleek dat noch de printsnelheid, noch de *time gap* een grote invloed hebben op de druksterkte en dat er slechts een lichte daling is ten opzichte van traditioneel vervaardigd beton. Dit in tegenstelling tot de hechtsterkte, waar zowel een hogere printsnelheid als een grotere *time gap* nefast zijn voor de hechting. Door de grotere tijdspanne tussen het extruderen van twee opeenvolgende lagen, kon er meer water verdampen; hoe droger de onderste laag, hoe meer luchtbellen er werden ingesloten en hoe zwakker de hechting. Dit fenomeen werd bij een hogere printsnelheid nog versterkt door de verminderde oppervlakteruwheid. De grotere druk die noodzakelijk was om de lagen te kunnen extruderen, zorgde voor meer

kinetische energie op de aanwezige zanddeeltjes waardoor deze dieper in het materiaal werden geduwd, met een kleinere oppervlakteruwheid tot gevolg.

Een goede hechting tussen twee opeenvolgende lagen wordt voornamelijk bepaald door het vochtgehalte en de oppervlakteruwheid van de onderste laag. Om deze eigenschappen te verbeteren werden een aantal modificatietechnieken toegepast. De eerste techniek had als doel het vergroten van de oppervlakteruwheid. Hiervoor werden in eerste instantie verschillende zandgradaties (0-1 mm, 1-2 mm en 0-2 mm) verdeeld over de onderste laag. In tweede instantie werd de geometrie van de spuitmond aangepast (de cilindrische vorm werd vervangen door een rechthoekige vorm) en deze werd later ook uitgebreid met groeven. Oppervlakteruwheidsmetingen toonden aan dat beide opties een ruwer oppervlak creëerden (verhoging van 50% en 300%, respectievelijk). Bij de tweede techniek werd getracht om een chemische hechting tussen de lagen tot stand te brengen door een kleine hoeveelheid cement (0.5 g, 1.0 g of 1.5 g) te verdelen over de onderste laag. De laatste modificatietechniek was bedoeld om het vochtgehalte te verhogen door enerzijds het oppervlak te bevochtigen en anderzijds door de toevoeging van superabsorberende polymeren. Het voordelige effect van beide technieken werd aangetoond op basis van vochtmetingen. Uitgaande van de mechanische karakterisatie werd vastgesteld dat voornamelijk het gebruik van een rechthoekige spuitmond voordelen biedt. Het voordelige effect van een hoger vochtgehalte werd niet geobserveerd. De lokale verhoging van de W/C-factor door het vernevelen van water zorgde lokaal voor een verminderde sterkte van de *interlayer* en een verhoging van de porositeit.

En wat op lange termijn?

Om het gedrag op lange termijn te kunnen evalueren moeten we starten met het begin: de microstructuur. Deze werd opgemeten voor samenstellingen met en zonder SAP's en hierbij werd er een onderscheid gemaakt tussen de micro- (voornamelijk de capillaire poriën met afmetingen tussen de 10 µm – 10 nm) en de macroporositeit. Algemeen gezien, ongeacht de grootte van de poriën die we in beschouwing namen, kon een verhoging van de porositeit waargenomen worden wanneer geprint beton werd vergeleken met traditioneel gestort beton. Op vlak van microporositeit speelde voornamelijk de *time gap* een grote rol. Een grotere tijdspanne tussen het printen van twee opeenvolgende lagen veroorzaakte een verschuiving in de poriëndistributie en een groter volume aan kleinere poriën kon worden waargenomen in zowel de onderste laag van een geprint proefstuk als in de *interlayer*. Dit effect werd toegeschreven aan de kleinere hoeveelheid water die beschikbaar was voor

de hydratatie van het cement, wat resulteerde in kleinere poriën. De bovenste laag van een geprint proefstuk was, ongeacht de *time gap,* blootgesteld aan gelijkaardige omstandigheden, wat resulteerde in vergelijkbare poriëndiameters en poriënvolumes. Wanneer de printsnelheid varieerde konden gelijkaardige fenomenen opgemerkt worden. De poriën waren echter wel kleiner door de grotere druk die werd uitgeoefend tijdens het printen. In vergelijking met traditioneel gestort beton zorgde de toevoeging van SAP's voor gelijkaardige resultaten: het aantal poriën tussen de 100 nm en 500 nm verminderde terwijl de hoeveelheid poriën groter dan 700 nm steeg. Dit laatste kon toeschreven worden aan een lokaal verhoogde W/C-factor en een verbeterde weerstand tegen autogene krimp waardoor er minder microscheuren gevormd werden.

De verdeling van de macroporiën werd gevisualiseerd met behulp van µCT-scans. Een verhoogde porositeit ter hoogte van de *interlayer* kon waargenomen worden ongeacht de toegepaste *time gap* of printsnelheid. Dit effect was het meest uitgesproken bij een time gap van 10 en 30 minuten; de porositeit verhoogde van gemiddeld 5% in het bulkmateriaal naar respectievelijk 13% en 21% in de zone van de *interlayer*. De µCT-scans toonden ook een morfologische verandering van de poriën aan. Waar de poriën in traditioneel vervaardigde elementen meer cirkelvormig waren, veroorzaakte het printproces meer ellipsvormige poriën, die zich vooral manifesteerden in de printrichting.

De indringing van schadelijke stoffen (water, chloriden of $C0_2$) wordt voornamelijk bepaald door de microstructuur van het geprinte materiaal. De verhoogde porositeit aan de *interlayer*, gecombineerd met een grotere hoeveelheid microscheuren die gevormd worden tijdens het uitdrogen van geprinte elementen zorgt er in het algemeen voor dat schadelijke stoffen veel makkelijker kunnen binnendringen en dat de duurzaamheid van de elementen daalt. Hoe groter de *time gap*, hoe meer uitgesproken dit fenomeen zich manifesteert. De duurzaamheid van een element kan verder ook geëvalueerd worden op basis van de weerstand tegen vries-dooi. Hiervoor werden de materialen onderworpen aan 14 vries-dooi cycli, in analogie met de Belgische norm NBN B15-231. Ongeacht de proefmethode (opmeten van het massaverlies, de druksterkte of de dynamische elasticiteitsmodulus), was het niet mogelijk om een eenduidige conclusie te trekken. In sommige gevallen bleek het printproces de weerstand tegen vries-dooi te verhogen. De grotere poriën ondervonden minder druk waardoor de inwendige structuur minder beschadigd werd.

Het bleek echter dat de toepassing van de huidige norm onvoldoende was om relevante conclusies te trekken en dat er meer vries-dooi cycli nodig zijn om intern schade te berokkenen.

Naast de indringing van schadelijke stoffen is ook de gevoeligheid aan krimp een niet te onderschatten fenomeen in 3D geprinte elementen. Door de directe blootstelling aan omgevingsfactoren zullen voornamelijk plastische krimp en uitdrogingskrimp een groter aandeel leveren in de algemene vervorming en kunnen er zich reeds in een vroeg stadium scheuren vormen. Om dit effect tegen te gaan worden er twee verschillende methodes getest: de toevoeging van superabsorberende polymeren en de toevoeging van vezels. Algemeen kan gesteld worden dat voornamelijk de superabsorberende polymeren krimp verhinderen, en in sommige gevallen zelfs zwelling veroorzaken. De reeds beschikbare berekeningsmodellen in de Eurocode of de ModelCode90 zijn niet in staat om dit gedrag te modelleren en gaan, voornamelijk op korte termijn, het krimpgedrag onderschatten.

Dit laatste benadrukt nog maar eens de nood om de huidige standaards en normen van een upgrade te voorzien rekening houdende met de invloed van het printproces, niet alleen op vlak van mechanische karakterisatie maar ook op vlak van duurzaamheid. Wanneer we dit kunnen realiseren gecombineerd met een duurzamer materiaal en de complete integratie van wapeningsstaal, dan pas kan de constructie industrie 4.0 echt van start gaan. Dan pas worden de mogelijkheden eindeloos.

Abstract

Concrete is nowadays one of the most widely used building materials worldwide. Even though the material is brittle and prone to cracking when it is subjected to tension, the application possibilities are endless. During the last 50 years, the material has evolved tremendously; traditional cast concrete is for example replaced by compositions with self-compacting properties and the standard compressive strength was tripled by the development of ultra-high-performance concrete. In addition, there was also the development of special concrete types, like for example self-healing concrete, where the addition of superabsorbent polymers (SAPs) allows the material to heal cracks that occur during service life. Technology never sleeps.

Though concrete material science has been progressing rapidly, the improvement of manufacturing processes to place concrete and produce elements or structures was limited. Compared to other rapidly innovating and technologically advanced industries, such as automotive and aerospace, the concrete construction industry has remained a traditional industry. Regardless of the concrete type or its application, a typical concreting process still includes operations such as batching, mixing, and pouring into a formwork with the help of human workforce. The construction process is still labor intensive, the fabrication of the molds is time consuming and requires a lot of man power, especially when the complexity of the design increases. It causes in addition an uneconomical use of materials and limits the architectural freedom of the designer.

An architect's dream = an engineer's dream?

Over the past ten years, a lot of research has been performed on an international level, trying to find a way to automate this old-school construction process. Many researchers got inspired by other branches of the industry, such as medicine or astronomy. Based on this expertise, curiosity was awakened. What if it would become possible to create structural elements, with complex geometries, by automatically printing a cement-based material without human intervention? What if an architect were no longer limited by the actions and ability of humans? Although this sound unrealistic in first instance, the beneficial consequences could not be ignored; construction time could be shortened, the safety level would increase and the geometrical freedom of the designer would prevail.

The downside

In addition to the many advantages, there is also a downside of the digital manufacturing process and traditional cementitious materials did not seem suitable for this innovative technology as there is great interdependency between material, process and final product. Through the years, many researchers investigated different mix compositions in order to obtain a printable material, having the advantages of self-compacting concrete and sprayed concrete at the same time. However, most researchers were faced at a certain point the conflicting requirements the material has to fulfill. First of all, the concrete must be sufficiently fluid. More specifically, the printed material may not set too fast in the reservoir, to prevent blocking or segregation in the tubes while directly after extrusion, an adequate stability of the printed layer is required to sustain its own weight and the weight of the successive layers without relevant deformations. Secondly, the time gap (i.e. the time between the deposition of two successive layers) is also of great importance. When the time gap is too long, the bonding between the layers will be insufficient, when the time gap is too short, this will result in an insufficient structural-buildup and cause structural failure.

The manufacturing process does not only change the material behavior in fresh state, there are also consequences in hardened state. By building up a structure layer by layer, the amount of entrapped air increases. Furthermore, due to the lack of molding, after extrusion the material is directly exposed to environmental conditions, making the material more prone to shrinkage cracking. Due to the higher porosity and crack formation, there are more preferential ingress paths for harmful substances.

From international research to national investigations

The aim of this doctoral thesis is to investigate the effect of the digital manufacturing technique on the mechanical and durable behavior, and to make a comparison with conventional cast concrete. To eliminate the effect of the mix composition as much as possible and focus mainly on the variation in print process parameters, a basic reference material was used throughout this thesis. This reference mixture was composed of cement, sand, water and superplasticizer. In addition to the evaluation of the mechanical performance and durability aspects, the author also aimed to improve both characteristics and for this it was required to expand the base composition with fibers or superabsorbent polymers (SAPs). The water/cement-ratio (W/C) was kept constant (0.37), regardless of the mix composition.

In order to print the cementitious material, an in house developed 2D-printer was used for most experiments, consisting out of a mortar gun vertically mounted on a fixed steel frame, mounted on a horizontal moving platform on which the layers could be printed with an elliptical nozzle. The printability requirements of each composition (i.e. extrudability and buildability) were tested for each composition. Although the previously mentioned printability requirements were fulfilled, the pumpability of the reference composition was insufficient for upscaled 3D print experiment due to the relatively high sand to binder ratio (S/B-ratio). This parameter equaled 2, which is high compared to other printable materials listed in literature and resulted in a material with a high yield stress and plastic viscosity. Therefore, to improve the pumpability, the S/B-ratio was lowered (1.5 instead of 2) and the type of sand was changed (sea sand instead of normsand). As for other mix compositions, the W/C-ratio of this optimized 3D-mixture equaled 0.37.

Isotropic? Anisotropic?

A disadvantage of the layered extrusion process is the anisotropic behavior of the printed element, indicating that the material properties can differ depending on the test direction. The mechanical properties (compressive, tensile and flexural strength) mainly depend on the quality of the interlayer zone (i.e. the zone between two successive layers). In order to evaluate the influence of both the print speed and the applied time gap, a parameter study was executed within the first part of this doctoral thesis. Therefore, two different printing speeds (1.7 cm/s and 3.0 cm/s) and four different time gaps (0, 10, 30 and 60 minutes) between the successive layers were considered. As there are currently no standard test methods available to test the mechanical properties of printed specimens, the 'old-fashioned' methods, applicable for conventional cast concrete, were resorted: the compressive strength was measured by a uniaxial compression test, pull-of tests were applied to evaluate the interlayer bonding and the flexural strength was determined by a three-point bending test. The compressive and interlayer bonding strength were determined in a single direction (parallel to the print direction). The flexural strength on the other hand was evaluated both parallel and perpendicular to the print direction.

Preliminary results showed that nor the print speed, nor the time gap have a major effect on the compressive strength and only a small reduction could be observed compared with traditionally cast specimens. This is in contrast with the interlayer bonding strength, where a higher print speed or time gap were both detrimental for the bond strength. The longer the time gap between the deposition of two layers, the more the water could evaporate; the drier the

substrate layer was, the more air bubbles were entrapped and the weaker the interlayer was. Increasing the printing speed enhanced this effect due to the lower surface roughness. The higher pressure exerted on the particles, increased the kinetic energy working on the bigger sized sand particles, pushing them deeper into the material and resulting in a lower surface roughness.

An adequate bonding between two successive layers is mainly determined by the moisture content and the roughness of the surface. In the second part of this thesis, various modification techniques were applied to improve the properties of the latter. The first technique aimed to increase the surface roughness. Therefore, three different sand gradations (0-1 mm, 1-2 mm and 0-2 mm) were distributed on the substrate layer. Another option within the same category was a redesign of the nozzle; the elliptical nozzle shape was replaced by a rectangular one and in a later stage expanded with grooves and trowels. Surface roughness measurements showed the efficiency of both modification techniques. They increased the roughness with 50% and 300%, respectively. The second modification technique attempted to create a chemical bond between the layers by spreading a small amount of cement (0.5 g, 1.0 g of 1.5 g) on the substrate layer. The last modification intended a higher moisture content by wetting the substrate before the extrusion of the second layer, or by the addition of SAPs. Their beneficial effect was demonstrated by surface moisture measurements. Although these modifications seemed promising, the benefits in terms of mechanical performance were only noticed after redesigning the nozzle (rectangular). The higher W/C-ratio, induced by spraying water, increased the porosity and created a weaker interlayer zone.

And the long-term behavior?

First things first, an evaluation of the long-term behavior starts at the origin: the microstructure. The latter was assessed with mixtures with and without the addition of SAPs. Within these microstructural investigations, a distinction was made between the microporosity (capillary pores ranging from 10 µm – 10 nm) and the macroporosity. In general, regardless of the pore size that was considered, an increased porosity could be observed in printed specimens, compared with conventionally cast elements. In terms of microporosity, the time gap between two successive layers played a major role. A longer time gap caused a shift in the pore size distribution and a higher volume of smaller sized pores could be observed, both in the substrate layer and in the interlayer zone. Due to the enlarged amount of evaporated water, the amount of water available for cement hydration was lower, resulting in

smaller pores. Irrespective of the time gap, the top layer was exposed to similar environmental conditions, causing comparable pore diameters and volumes within the material. Due to the higher pressure in case of a higher printing speed, the overall pore size was smaller. However, in general, similar trends could be observed. Compared with conventionally cast concrete, the addition of SAPs resulted in similar observations; the number of pores between 100 nm and 500 nm decreased, while the amount of bigger sized pores (> 700 nm) increased. The latter could be attributed to a local increase of the W/C-ratio and an improved resistance against autogenous shrinkage, making the material less prone to cracking.

The distribution of the macropores was quantified and visualized based on μCT-scans. An increased porosity at the interlayer zone could be observed, regardless of the applied time gap or print velocity. The effect was most pronounced in case of a 10- or 30-minutes interval; the porosity increased from approximately 5% in the bulk material to 13% and 21%, respectively, in the interlayer zone. μCT-scanning revealed in addition also a morphological change. Where the pores in traditionally cast specimens were more circular, the printing process produced more elliptical pores, mainly manifested in the print direction.

The combination of an increased porosity at the interlayer and a higher amount of (micro)cracks, formed during the hardening process of the printed specimen, enables the intrusion of harmful substances (water, chlorides and CO_2), which can deteriorate the fabricated element. The longer the time gap, the more these interlayers become preferential ingress paths. The durability can also be evaluated based on the resistance against freeze/thaw. Therefore, according to the Belgian standard NBN B15-231, materials were subjected to 14 freeze/thaw cycles. Irrespective of the test method (calculating the weight loss, loss in compressive strength or loss in dynamic elastic modulus), it was not possible to draw unambiguous conclusions as some of the test series showed an improved resistance against freeze/thaw. The larger pores experienced less pressure, resulting in less microstructural damage. However, it appeared that the application of the current standard was insufficient and more freezing cycles are required to cause internal damage.

In addition to the penetration of harmful substances, the sensitivity to shrinkage is another phenomenon that cannot be underestimated in 3D printed elements. Due to the direct exposure to environmental conditions, plastic and drying shrinkage will in general contribute in a higher extend to the overall deformations and as a consequence, more cracks will be formed over the entire specimen's surface. A possible manner to counteract the

latter, is the addition of SAPs or fibers. Although both solutions are beneficial in terms of shrinkage reduction, SAPs showed the biggest effect. The calculation models currently available to predict shrinkage of conventionally cast concrete, e.g. fib ModelCode90 and Eurocode 2, seemed not suitable for printed specimens. Especially shrinkage within the first hours after extrusion was underestimated. The latter once again emphasizes the need to upgrade the current standards and design codes, considering the heterogeneous nature of the printed specimens and the weak interlayer zones. If we can realize this, in combination with a more ecofriendly printable material and the integration of reinforcement, the possibilities will become endless and construction industry 4.0 is ready to take off completely.

Chapter 1

Introduction

Additive manufacturing or rapid prototyping is a technique to fabricate complex geometrical elements directly from a three-dimensional computer model layer by layer. Due to several advantages such as increased geometrical freedom, reduced human labor, cost and time, etc., additive manufacturing has gained huge momentum, recently also in the construction industry. However, despite the many advantages, printing in daily practice still seems far away. This can be attributed to the fact that the construction industry is risk adverse and conservative in its practice. The lack of appropriate design codes and performance testing protocols will also hinder the breakthrough of digital manufacturing in the concrete industry on a short term.

Nowadays, various approaches for 3D printing of concrete exist (e.g. Contour Crafting, D-shape) but the most applied and promising techniques consider extrusion-based processes. To ensure a proper extrusion of the cement-based composition, the material needs to be fluid in a first stage, in order to be easily pumped towards the printing unit and in order to fully fill the print volume during the time the cementitious material is still supported by the print head. However, as soon as the print head does not longer support the material, the concrete should be stiff enough. More specifically, the combination of a significant yield stress and an adequate thixotropic behavior are required. From the moment the concrete is extruded, the yield stress temporarily provides enough stiffness to ensure the shape stability of one layer, while the

thixotropic character of the material should ensure the shape stability of the subsequent layers. However, the more layers are printed, the faster the stiffness and strength of the material has to increase to ensure the shape and buckling stability of the growing structural element. Therefore, the hydration process also should proceed fast enough to provide a load-bearing internal skeleton of solid hydration products. As the reader can expect, these contradicting requirements that the material has to fulfill in fresh state will consequently affect the behavior in hardened state. A fundamental scientific knowledge of the cementitious material in view of well understanding the consequences of the different production conditions compared with conventional cast concrete will become more important in the future.

In digital manufacturing, the role of the interlayers will become increasingly important. Between successive layers, an interlayer zone is present, with qualities depending on the time gap between the deposition of two subsequent layers. These interlayers will influence the mechanical performance, and most prominently the tensile strength, as well as the transport properties and the long-term behavior. Additionally, as there is no formwork available to protect the freshly deposited layer against desiccation, also the effect of shrinkage (in particular plastic and drying shrinkage) will become increasingly important.

Current structural and durability design codes consider concrete as a homogenous material. However, this is no longer the case for printed elements. Due to the layered end result, which in general introduces more pores and weaker interlayers, the material behaves in an anisotropic way and the available design codes and methodologies have to be reconsidered. Furthermore, as the deformation of a new layer is also (partly) restrained by the previous layer, and since traditional curing methods do not fit the new manufacturing method well, shrinkage stresses and cracking as well as their mitigation become increasingly important. New developments will have to be provided, possibly going beyond the current practices.

Objectives

Based on the current research gaps in related literature, the author defined the following objectives and research questions for this doctoral thesis, aimed to understand the effect of the interlayers on the mechanical properties and durability of printed specimens.

- Which print process parameter affects the mechanical performance the most? How can we improve the interlayer quality to minimize the loss in mechanical performance?
- What are the microstructural changes induced by digital manufacturing?
- What is the effect of the layered manufacturing technique on the long-term behavior and is it possible to make an evaluation based on the currently available test methods and standards?
- How can we counteract early-age shrinkage?

Outline of the thesis

Chapter 2 provides a general overview of the digital manufacturing techniques currently available and discusses their pro's and contra's. Furthermore, the challenges and pitfalls of this innovative technique are listed together with the requirements the fresh material has to fulfill.

Chapter 3 describes the different materials, used within this doctoral thesis, and the extrusion techniques applied to fabricate multi-layered specimens.

Chapter 4 discusses the mechanical performance of printed elements, considering different print velocities and time gaps between the deposition of two successive layers. Additionally, a comparison between molded and printed specimens is foreseen to quantify the adverse effect of this layered manufacturing process.

Chapter 5 provides an overview of different surface modification techniques, applied to improve the quality of the interlayer. In general, three different modifications are considered; the first technique causes a different surface roughness, the second technique changes the moisture content of the substrate layer and the last technique tries to create a chemical bond between two successive layers. The effectiveness of those modifications is evaluated based on compressive strength and tensile strength measurements.

Chapter 6 evaluates the microstructure of printed elements on a macro- and microscopic level by the application of different characterization techniques. Mercury intrusion porosimetry (MIP) measurements are applied to characterize the capillary porosity, while µCT-scans allow the author to quantify the bigger sized pores and visualize the morphological changes induced by the different manufacturing processes.

Chapter 7 quantifies the water ingress of printed elements, with special attention for the behavior at the interlayer. This evaluation was made based on standard capillary absorption tests and neutron radiography, considering the effect of different printing speeds, a varying time gap and a variation in the number of layers. Mix compositions with and without the addition of superabsorbent polymers were considered.

Chapter 8 compares the ingress of harmful substances (chlorides and CO_2) and the resistance against freeze/thaw of traditionally cast and printed specimens. The efficiency to use current design codes and standards for printed elements was evaluated.

Chapter 9 investigates the addition of fibers and the addition of superabsorbent polymers as a way to counteract early-age shrinkage (plastic and drying shrinkage) of printed elements. In addition, the efficiency of current design codes and standards to evaluate shrinkage in printed elements was evaluated.

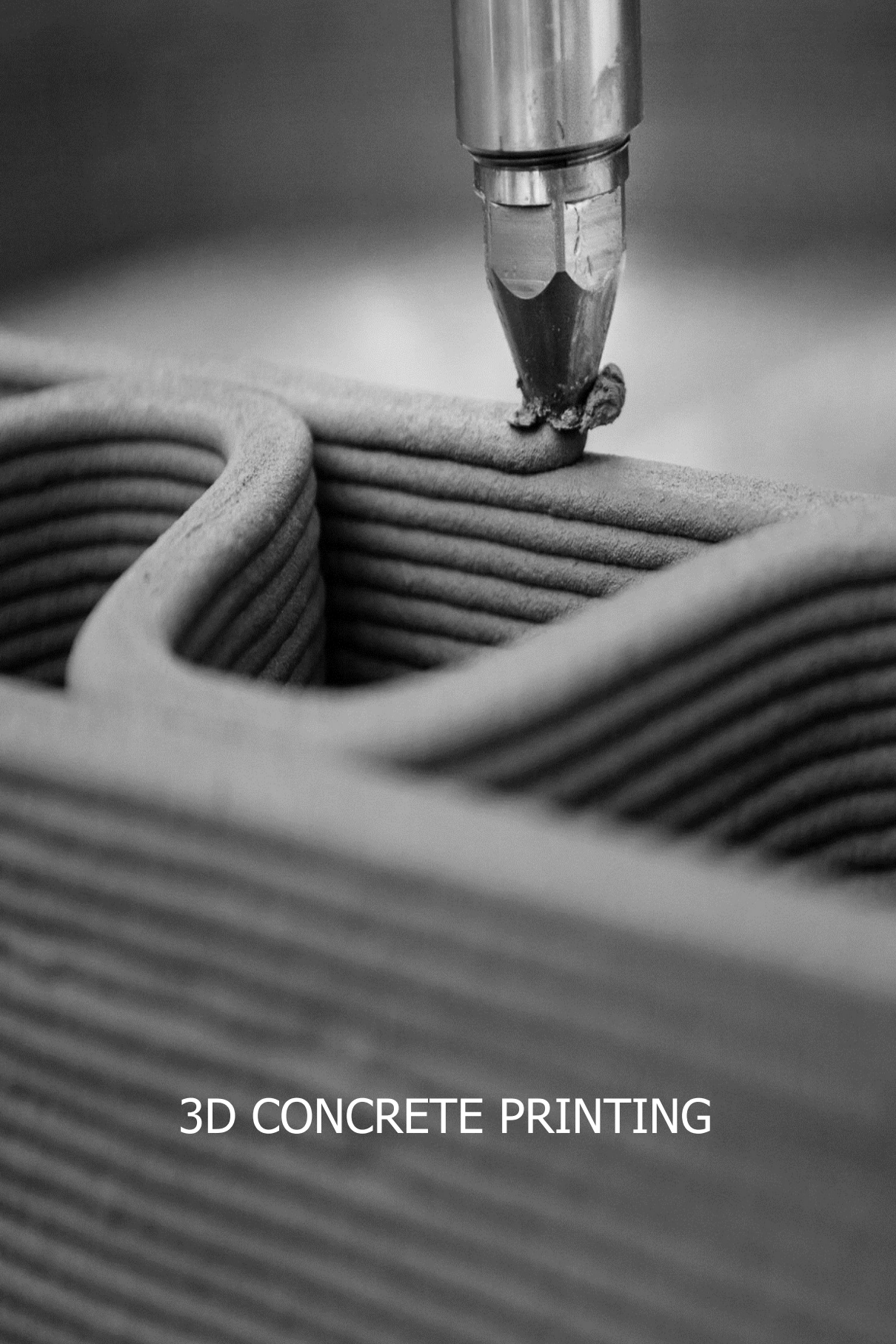
3D CONCRETE PRINTING

Chapter 2

3D Concrete Printing

2.1. Additive manufacturing: a promising technique

2.1.1. Historical background

Concrete is an ubiquitous substance and is, after water, most widely used on earth. The enormous production of approximately 10 bilion tons per year can be attributed to the inherently useful characteristics: the raw materials are easily and globally available, there is a relative ease of processing and concrete has the ability to transform from a liquid state, where it is able to fill a mold, to a solid state, where it is able to bear loads [1]. Over the years, the material science of concrete has evolved tremendously. Special types of concrete such as self-compacting concrete, fiber-reinforced concrete, lightweight concrete, etc. were developed and there was a considerable leap from low strength concrete in the 1960s to ultra-high performance concrete nowadays in order to meet the structural demands of contemporary constructions [2, 3].

Though concrete material science has been progressing, and more and more tools became available to design material efficient shapes, there was still a restriction on the geometrical freedom of engineers due to the 'old-school' construction process. The traditional way of placing concrete still required a lot of human intervention and the necessity of formwork results in a higher cost, a considerable time delay and an increasingly amount of waste, especially in case of complex structures [2, 4].

To counteract the statement '*An architect's dream is an engineer's nightmare*", researchers tried to improve the traditional construction process. Finding their inspiration in technologcially advanced industries like automotive or aerospace, they turned out to additive manufacturing (AM), which is described as 'the process of joining materials to make objects from 3D model data, usually layer upon layer' [5]. The first attempt in the construction industry was made by Pegna [6], who introduced the concept of 'binder jetting', an additive manufacturing method where a reactive powder layer, composed out of sand and cement, was locally injected and activated by water vapour to bond the materials in layers or solid parts. Unfortunately, this method was never conceptualized.

The rapid growth of research in AM with concrete happened mainly in the last decades. Khoshnevis [7], from the University of South Carolina, was the first to automize the concrete construction process by extrusion. He obtained a patent for the combination of his gantry system and material process under the name Contour Crafting (CC). At first, the process appeared as a hybrid method that combined an extrusion proces for shaping the object surfaces, and a filling process (pouring or injection) that build the elements core (Figure 2.1) [8]. The exceptionally smooth and accurate exterior surfaces were obtained by constraining the extruded flow in the vertical and horizontal directions using trowels mounted on the deposition nozzle. The unprecedented surface quality, the increased fabriction rate, the vast choice of materials and the efficient use of materials contribute to the fact that Khoshnevis realizations served as a starting point for many initiatives that followed.

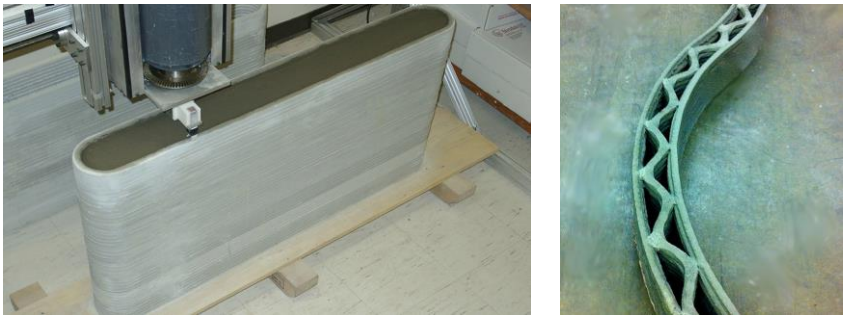

A **B**

Figure 2.1: 3D Concrete printed wall structures with conventionally cast (A) and printed (B) concrete infill, constructed by the Contour Crafting technique [9, 10]

Particle bed fusion (or binder jetting) is another additive manufacturing method in which a layer of particles is spread and a print head moves and selectively injects a binder into the particles. Afterwards, another layer is spread and the process repeats in order to build elements layer upon layer. The high resolution and the ability of creating cantilevers, as the particle bed can serve as temporary support, are denoted as the main advantages of this technique. However, this method requires post processing to remove the unbound particles [1]. In construction, this method has been pioneered by Enrico Dini of D-shape and since the founding, Dini has printed numerous large-scale objects. The Radiolaria (Figure 2.2), an architectural masterpiece, illustrates the enormous possibilities of this technique in terms of geometrical freedom.

Although the above-mentioned techniques provide a lot of advantages, the most popular additive manufacturing method nowadays in construction technology is extrusion-based 3D concrete printing (3DCP). This technique is characterized by a cementitious material that is deposited as a continuous filament in a layer-wise manner by a digitally controlled nozzle [11]. Although this technique has a smaller resolution of deposition and limited deposition rate, it shows great potential from an economical point of view as only the required volume of material is deposited for the build (Figure 2.3) [5]. The first study on 3DCP was performed at the university of Loughborough [5, 12, 13], focusing mainly on the mix design of printable concrete and the assessment of the mechanical properties.

Figure 2.2: Radiolaria [14], manufactured by D-Shape

Figure 2.3: Digital manufacturing of a free-shaped wall-like concrete bench [5]

Unlike the layered extrusion process in 3D printing, Smart Dynamic Casting (SDC), developed at ETH Zürich, scales down the well-known construction technique of vertical slipforming to produce non-standard concrete elements

robotically [15, 16]. In this method, concrete enters a vertically moving formwork as a fluid and exits it in a hardened state. As a consequence of this procedure, hydration control is essential, and this is performed by the use of chemical admixtures. Major advantages of slipforming compared to other techniques include the ability to slipform around conventional steel reinforcement, the relative absence of layer interface problems and the high surface quality.

Since the development of additive manufacturing, numerous academic institutions and industries carried out research on the various aspects of 3DCP and new projects are presented on a regular basis. Though the construction industry is about to embrace this new technology with ambitious large-scale projects, several facets of the material characteristics and the interdependency with the process itself are yet to be understood.

2.1.2. Challenges and pitfalls

When compared to conventional construction processes, the application of 3D printing techniques in concrete construction may offer excellent advantages including [3, 17]:

- Reduction of construction costs by eliminating formwork;
- Reduction of on-site construction time by operating at a constant rate and by eliminating the preparation and disassembling of formwork;
- Reduction of injury rates by eliminating dangerous jobs (e.g. working on heights), resulting in a safer construction site;
- Introduction of a new field in construction profession: high-end-technology-based jobs;
- Minimizing the chance of errors by precise material deposition;
- Increased sustainability as material waste and spillage are minimized;
- Higher quality control;
- Increased architectural freedom which would enable more sophisticated design for structural and aesthetical purposes;
- Enabling the potential of multifunctionality for structural and architectural elements by taking advantage of the complex geometry.

Besides the many advantages, there are also some limitations and challenges concerning the material properties and the print process that have to be faced. Regardless the application of this technique, there will always be an interdependency between material, process and product. Compared to other

industries, this effect is even more pronounced in case of concrete because of two reasons. First, due to the slow setting reaction in the printed concrete, a strong interaction between material and print parameters such as print speed and pump pressure occurs. Secondly, concrete itself is not a fixed material and can have a wide range of compositions, chosen as a function of the print process and the required end product. Consequently, the print strategy cannot be chosen independently from the design, material or final product, as illustrated in Figure 2.4.

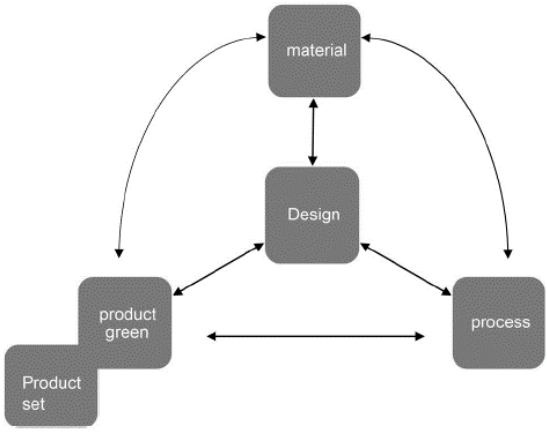

Figure 2.4: Interdependency of design, material, process and product [18]

In the following paragraphs, specific challenges and pitfalls compared with conventional concrete are highlighted, not taking into account a specific mix composition nor printing technique.

Anisotropy

Conventional concrete is commonly placed in one continuous pour into the formwork, and subsequently vibrated to obtain a homogenous and isotropic element with similar properties in all directions. Contrary, 3D printed concrete is reported to be anisotropic and the anisotropic nature of printed elements is correlated with the heterogeneity caused by the interface between the deposited layers. There are currently no studies indicating that anisotropy also exist in the bulk material as the latter is more densified due to the high compaction from the extrusion-process. It should be noted that a significant anisotropy primarily exists with regard to strength. However, as the interfaces are weak links with a higher porosity [19-21], they will also affect the material in terms of durability.

The directional dependency of 3D printed elements has already been investigated thoroughly by many researchers, determining the mechanical properties in three different directions (Figure 2.5). In general, most studies found that both the compressive and flexural-tensile strength were directionally dependent, and resulted in comparable findings: perpendicular to an interface, the tensile strength is lower than in other directions, whereas the results with regard to the directional dependency of the compressive strength are inconsistent [13, 22]. On the other hand, the flexural strength will depend on the region subjected to the peak stress. More specifically, when the maximum stress is inducted at the interface, the flexural strength can be significantly lower. If the loading direction introduces the maximum bending stress in the bulk material, the flexural strength can exceed the strength obtained in case of conventional concrete [13, 23, 24].

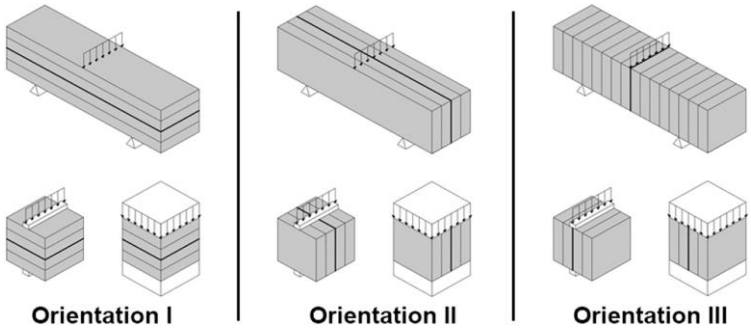

Figure 2.5: Mechanical testing of 3D printed concrete elements in different directions respective to the layer orientation [24]

As mentioned earlier in this section, the anisotropic nature of printed elements is mainly attributed to the layered object structure. The extent to which this affects the structural behavior mainly depends on the quality of the interlayer. In fact, interfaces are not an uncommon phenomenon in concrete construction, however they mostly occur between a hardened material and a freshly deposited material. Extensive research in the field of repair mortars [25-27] already revealed that surface moisture content, surface roughness, surface preparation, curing conditions, air entrapment, etc. play a crucial role in the bonding behavior. Unlike traditional concrete, an adequate bonding has to be created between two freshly deposited layers. In addition to material-related parameters, also process-related parameters such as interlayer time interval, contour length, printing speed, nozzle geometry, nozzle standoff distance etc. will play a crucial role on the interlayer bond. This will be further discussed in Chapter 4.

Reinforcement

The fundamental mechanical behavior of digitally fabricated elements will not differ from conventionally build concrete: they are inherently brittle and their failure behavior is characterized by a low ratio of tensile to compressive strength. Current design methods based on consistent mechanical models are therefore applicable to additively manufactured elements as well – considering that an enhancement of these models is required to account for the effects related to the fabrication method (i.e. anisotropy, shape-related mechanical effects, weak interlayers and a reduced bonding strength). However, many current design provisions are semi-empirical models, based on experimental testing. These models have to be revised and adapted to fit the mechanical performance of digitally fabricated elements, or even abandoned for some technologies since empirical models will never be able to cover the entire range of all complex geometries achievable by digital fabrication [28].

Reinforcement is not only required to improve the tensile strength of the material. Rather a substantial portion of the reinforcement in realistic constructions is so-called "minimum reinforcement", fulfilling one or more of the following functions: *(i)* avoid brittle failure at cracking, *(ii)* ensure a sufficiently ductile behavior to enable stress redistribution and *(iii)* limit deformations (shrinkage) and crack widths [28]. To obtain an adequate safe structural behavior, existing approaches from conventional concrete construction are adapted and new innovative strategies are under development [28]. However, the integration of vertical reinforcement in 3D printed concrete elements is a critical challenge to which no satisfactory solutions are available yet. In general, six major opportunities can be listed:

1. 3DCP formworks: Printed elements do not serve as primary structural material but rather as formwork into which reinforcement bars are positioned. These bars will be enveloped by 'infill' concrete, following the conventional casting process. Although this approach is easy and cost-effective, it also raises concerns about the interface between cast and printed concrete, a sufficient concrete cover and the flexibility in terms of shapes.

2. Free-form reinforcement: As an alternative of the previous one, it is also possible to place the reinforcement first, and subsequently deposit the concrete around it. Smart Dynamic Casting [15], which is already mentioned in previous sections, can serve as one example for this reinforcement technique. In addition, Mesh Molding (ETH

Zürich), where a free-form reinforcement is robot-welded and subsequently used as an open formwork for the application of concrete can be classified within this category [29, 30].

3. 3DCP with entrained reinforcement cable: Multi-arm printing of both concrete and reinforcement, at best, in parallel. In this concept, which is currently under development at the TU/Eindhoven, the reinforcement cable should be sufficiently strong and ductile, but also have enough flexibility to allow the cable to follow all 3D freeform lines. To ensure a uniform bonding between the cables and the printed concrete, an effective control of some process-related aspects (e.g. contour length and concrete matrix compaction) is required to ensure an effective integration of this technique and a scaling-up towards structural elements [31, 32].

4. Fiber reinforced concrete: Extruding concrete with dispersed short fibers (basalt, steel or polymer fibers) in which fibers not only work as a dispersed reinforcement in hardened state but also as shrinkage reducers and early-strength enhancers. In general, a strong fiber alignment in the flow direction is noticed. However, the compatibility of the applied fibers with the system (whether they can pass through the nozzle or not) is a crucial point of attention [1, 23, 33, 34].

5. Active reinforcement: The application of a prestress after hardening in order to introduce compression stresses able to counteract the tensile stresses occurring during use of the element [5, 35].

6. Reinforcing by design: Designing structures as fully compression-loaded by gravity. However, this approach limits the possibilities in terms of geometrical freedom [36].

Some of the above presented approaches have currently a limited applicability in 3DCP (e.g. 1 and 3) or do not address the critical vertical reinforcement (e.g. 4). A process, or a combination of processes, where both reinforcement and material are placed in parallel is regarded as final goal. A trial of the latter is already tested at TU Dresden, were it was investigated by Mechtcherine et al. [37] to print parallel with the concrete steel reinforcement by a special gas-metal arc welding technique. However, the heat development while applying this technique results in some disadvantages.

Another approach is developed at China Building Materials Academy and the university of Catalonia and uses staples as reinforcement (Figure 2.6). As the printer head includes both a print nozzle and a stapler, both processes can occur simultaneously [38-40]. These investigations are still preliminary and the integration in concrete printing is still under development.

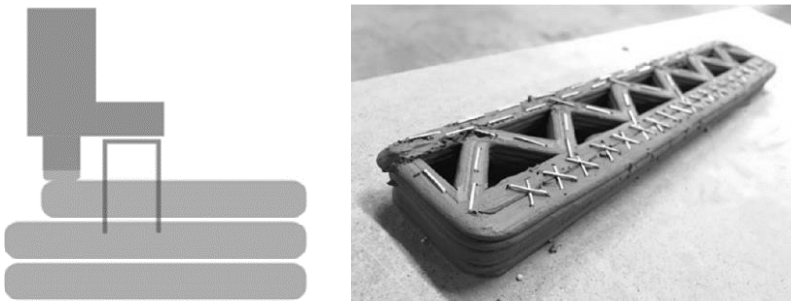

A B

Figure 2.6: Simultaneous reinforcement by using staplers (A) and a printed element reinforced by staplers (B) [40]

Shrinkage

Shrinkage is one of the major obstacles for concrete elements. It will lead to unwanted deformations that affect the geometry as well as the mechanical properties. Especially, when the deformations are restrained, shrinkage may lead to (tensile) stresses and cracking that degrade the quality of the printed element. These cracks increase the amount of preferential ingress paths for chemical substances, with decreased durability as a consequence.

In general, different types of shrinkage can be distinguished: *(i)* plastic shrinkage when the concrete is still in its plastic state, *(ii)* chemical shrinkage due to the volume difference between the formed hydration products and their reactants, *(iii)* autogenous shrinkage due to self-desiccation, *(iv)* drying shrinkage caused by the evaporation of internal water, *(v)* carbonation shrinkage due to the intrusion of CO_2 and *(vi)* thermal shrinkage caused by the cooling action after heat formation during cement hydration. All these types can be distinguished for both conventional and printed concrete, but in a different extent. The lack of formwork and the higher surface area exposed to environmental conditions will make printed elements more prone to drying and plastic shrinkage compared to molded concrete.

Another aspect that has to be considered are differential deformations between the printed layers. As the 3D printed layers get deposited within different time intervals, the subsequent, non-uniform moisture distribution

causes differential length changes as a result of shrinkage, creep and strain relaxation. Such effect could lead to a decrease in bond strength between the different layers [41, 42].

Current durability codes consider concrete as a homogenous material. However, for printed structures this is no longer the case. Durability indicator tests, such as air permeability tests or drying shrinkage measurements, will need to be reassessed before their application on the surface of a 3D printed element. The lack of appropriate design codes and performance testing protocols will hinder the breakthrough of digital manufacturing in concrete industry [4].

Sustainability

The construction industry contributes to about 40% of the solid waste generation, 40% of the energy consumption, 12% of the water depletion, 8% of the CO_2-emission and 38% of the greenhouse gas emissions. However, before the sustainability of 3DCP can be evaluated, a distinction between process and material is required. Based on recent studies [43, 44] one can conclude that digital fabrication provides environmental benefits, especially in terms of complex geometries, and that the 3DCP technique enables a reduction of 86% on CO_2 emission and 87% on energy consumption compared to a precast counterpart.

Unfortunately, these studies also revealed that the environmental impact of the fabrication process was negligible compared to the environmental impact of the production of the concrete constituent materials. Especially the binder system is the most energy-intensive part of the composition. Unlike conventional concrete, the binder content is 40% higher in printable mortars [2]. Therefore, from a material utilization point, 3DCP is not yet an environmentally friendly technology because of its demand for a high amount of energy-intensive constituents in the composition. The sustainability on material level can be improved by using alternative binders instead of Portland cement and in this regard, several studies focused already on developing 3D printable mixtures with alkali-activated binder systems [45-48], calcium-sulfoaluminate (CSA) cements [49], limestone calcined clay cements [49, 50] or magnesium potassium phosphate cements [51]. However, as these alternatives sometimes induce additional challenges in the mix design (e.g. compatibility issues with chemical admixtures), further research is required before one can use the potential of these binders.

In case of large-scale structures, there is no direct relationship between the process and the economic benefits. The enhanced geometric freedom associated with this technology provides several advantages and reduces the required materials. In addition, as there is no formwork required, a reduction of about 25% of the overall construction cost can be obtained compared with the prefab industry. On the other hand, the machine and material costs will be higher. A detailed life cycle analysis and estimation of the life cycle costs could give further understanding.

2.2. Additive manufacturing: material consequences

Digital fabrication of concrete is an innovative way of building with traditional concrete; it is the old dog with new tricks in the world of construction. However, since it features both new technology as well as established theories, old and new obstacles arise, also in terms of the material. As there are no standard methods available yet, the present section will go through most of the current methods used in order to predict to what extend a cementitious material can be extruded or not. In addition, an overview of the requirements a printable material has to fulfil in fresh state is also provided.

2.2.1. Printability assessment

Digital fabrication with concrete is, in a way, a simpler process, as there is no need to build a form before shaping an element. However, this involves many contradicting features the printable material has to fulfill. As there are currently no standards available, most researchers tried to develop their own material evaluation techniques. In general, the printability of a cementitious material can be assessed based on four different requirements: *(i)* pumpability, *(ii)* extrudability, *(iii)* buildability or structural build-up and *(iv)* workability and open time.

Pumpability

Concrete pumping is a mandatory processing step in most digital fabrication techniques as it allows proper feeding of the printing system no matter the considered print technology. Pumpability, or deliverability, can be described as the capacity of concrete under pressure to be mobilized while maintaining its initial properties [52]. Various models and test approaches exist to predict the pumping behavior of concrete. The most old-school prediction is based on empirical design charts. However, these empirical methods have many

limitations and are unreliable for modern concretes such as self-compacting concrete and high-performance concrete [53, 54].

In order to develop analytical approaches to predict the required pumping pressure, many researchers stated that the flow behavior of concrete is complex and differs from the flow of typical viscous fluids such as water or oil. The primary reason for this difference can be attributed to the fact that fresh-cementitious materials are yield-stress fluids. This means that, with regards to shear stress (τ), there is a threshold value (i.e. yield stress τ_0) that needs to be overcome before flow is initiated. As a consequence, there exists at the center of the pipe a zone where the material is not sheared. This yield stress and unsheared zone have been taken into account by assuming that the cementitious materials behave as a Bingham or Herschel Buckley fluid. A prediction of the pump pressure was made based on the Buckingham-Reiner equation. However, this could result in an overestimation of the pumping pressure up to 5 times its original value.

The reason for the systematical failure of these approaches is that they ignore the formation of a lubrication layer. Under the action of shear, a redistribution of particles occurs within the pipe and particles will migrate from high shear rate zones (outer region) to low shear rate zones (bulk material) [55, 56]. The yield stress and the plastic viscosity of this lubrication layer are generally about one fifth to one fifteenth of the corresponding values of the bulk material.

Due to shear induced particle migration, concrete flow during pumping is inhomogeneous, consisting of a lubrication layer, shearing concrete and non-shearing concrete. Kaplan et al. [57] introduced two analytical approaches to predict the required pumping pressure, taking into account the rheological parameters of both the lubrication layer and the bulk material. The first condition, where there is shearing in both the bulk concrete and the lubrication layer, occurs when the yield stress is lower than the pipe wall shear stress. The second condition, where only the lubrication layer is sheared, appears in case of a stiff concrete with a yield stress exceeding the pipe wall shear stress. However, recent studies, performed by Mohan et al. [58] have shown that even for the high yield stress materials, shearing was found to occur both in the lubrication layer and the bulk. It must be noted that the pumping behavior of concrete also depends on the discharge rate, the pipe geometry, etc. Therefore, more studies are needed to gain more in-depth understanding in this regard. As a general overview, the shear stress, shear rate and velocity profiles of concrete during pumping are represented in Figure 2.7.

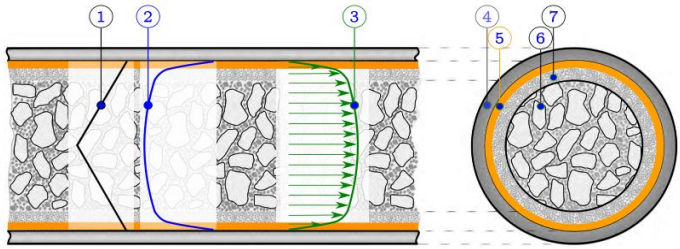

Figure 2.7: (1) Shear stress, (2) shear rate and (3) velocity profiles of a concrete flow inside a pumping pipeline [59]. (4) – (7) indicate pipe, slip layer, plug zone and bulk-shear zone, adapted from [56]

Extrudability

Pumpability refers to transporting concrete/binder fluid from a reservoir to the printhead (nozzle). Extrusion on the other hand, refers to the process of extruding concrete in the printhead, from a reservoir to the nozzle outlet. In literature, the extrudability of a cementitious material can be described as the capacity of the material to continuously pass through the small pipes at the printing head without segregation or blocking.

In general, two asymptotic extrusion regimes can be distinguished. If the yield stress of the material exceeds the gravity induced stress, the layer of the cementitious material will not be deformed after deposition, indicating that the filament section corresponds with the nozzle dimensions. This is referred to as the so-called infinite brick regime (Figure 2.8A). If the gravitational force overcomes the material elongational strength at the bottom, the material will deform until an equilibrium between yield stress and gravity-induced stress is reached. As a result, the deposited layer will deform and spread on the previous one. The limiting case of this behavior tends to the case of shear flow on a horizontal plate and is referred to as free flow regime (Figure 2.8C). The latter normally occurs for low yield stress materials. However, in many 3D print applications, the actual filament deformation behavior ranges somewhere in between the no-flow and pure shear flow, with a small geometrical reduction after deposition as a result (Figure 2.8B).

The final shape of the material will depend on its material yield stress, on the nozzle geometry and on the gap between the nozzle and printed layers. Most common methods to assess extrudability are therefore based on printing a filament layer and visually examining for signs of blockages, tears, deformations or discontinuities. A shortcoming with this approach is that such methods are empirical and do not provide any fundamental material parameter [2].

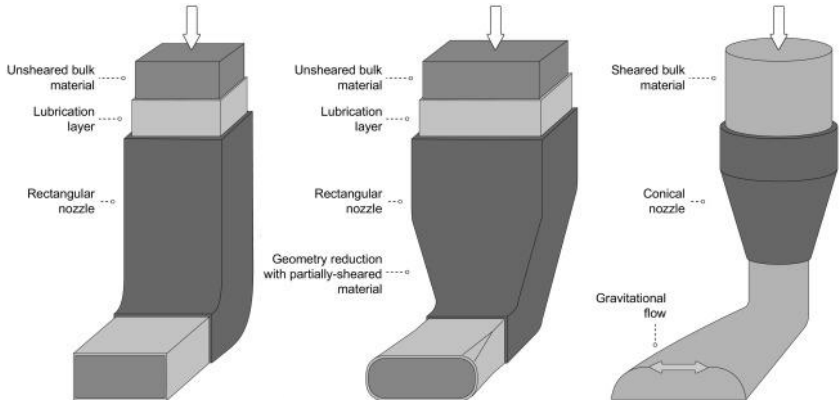

Figure 2.8: The two asymptotical extrusion regimes. The 'infinite brick regime' where the filament section is the one of the nozzle and is not affected by flow or gravity (A) and the so called 'free-flow regime' where the filament section results from a competition between gravity and yield stress (C). (B) shows a more realistic case [60].

Buildability

Buildability is another critical parameter to evaluate the printability of cementitious materials. It refers to the ability of a material to retain its extruded shape under its self-weight and the pressure from upper layers and is considered as the early-stage stiffness [61].

In experimental research, buildability is often obtained empirically, either by measuring the number of layers until failure occurs, or based on the deformation measured for a printed element after the deposition of a given number of layers [62, 63]. However, in recent research, experimental test methods like uniaxial unconfined compression tests (UUCT) [64-66], triaxial compression tests [67], direct shear tests (DST) [67] and non-destructive techniques as ultrasound velocimetry [66] have also gained interest to obtain the evolution of fundamental rheological parameters (i.e. compressive strength, elastic modulus, Poisson ratio, etc.). However, unlike conventional concrete, there is again a lack of uniformity between these test methods and they depend on various factors such as loading rate, preparation method, specimen size, etc.

Workability and open time

Workability encompasses all three above definitions and for this parameter, time serves as a major stakeholder. The period wherein the above-mentioned properties are consistent within acceptable tolerances is called 'open time'. However, due to structural build-up of the material and the corresponding slump loss in time, the open time of most mix compositions is limited. As there are no standard methods available yet, researchers turn back to standard methods compared with the ones used for conventional concrete (i.e. mini-slump flow, flow table test, V-funnel, etc.)

2.2.2. Material behavior in fresh state

In order to meet all the assessments mentioned above, one can conclude that the material has to fulfil some conflicting requirements. From a pumping first-order perspective, the fluidity of the material should be above a certain threshold value, which depends on the pumping system geometry. In terms of material properties, this means that the yield stress and viscosity should be as low as possible. In addition, the pumping rate should also be limited to prevent blocking or segregation within the pumping system or at the nozzle.

This flowing phase is for most print processes rather short. Directly after material deposition through the nozzle, a sufficient layer stability is required to ensure the buildability assessment. This means that the material has to build up an internal structure to sustain its own weight and the weight of the superposed layers without relevant deformations. The structural build-up inside a cementitious material can be divided into different phases (Figure 2.9):

- Dispersion (t = 0s): directly after mixing, all cement particles are dispersed over the entire volume. However, as cement dispersion is only achieved at SP saturation dosage, which is not common as this will make the material too flowable, local cement clusters can still occur;

- Flocculation (t < 20s): colloidal attractive forces on the cement grains make them move together (i.e. flocculate), while they push out the interstitial water in between them. These flocculated (but not yet bonded) grains already show an initial yield stress $\tau_{c,0}$, and shear modulus G_0. Flocculation keeps on going until all particles are bonded or can no longer move. It is important to emphasize that no calcium silicate hydrate (CSH) bridges are formed during flocculation in the first period after mixing.

Initial strength and rigidity solely come from a balance in colloidal forces (i.e. van der Waals forces and electrostatic forces);

- Nucleation (t > 20s): at the same time as flocculation manifests, some hydration bonds begin to form between the particles. These hydration bridges, with mainly CSH connections, are considerably stronger than the colloidal attraction that exists from flocculation. In time, more CSH bridges are formed and the yield strength, shear modulus G and elastic modulus E increase;

  Percolation: with more CSH bridges formed, also more and more cement particles get strongly connected and form longer chains. At this point in time, the cementitious mixture could still be mixed without much effort;

- Structuration (t > 100s): the chain length of percolated particles as well as the number of strong hydrate bonds keep increasing and so do τ_c (t), G(t) and E(t). At microscopic level, irreversible chemical reaction creates hydrate bonds between the particles. These bonds may however be weak enough to be broken by shear and/or remixing whereas new bonds may spontaneously appear again at rest as long as sufficient unhydrated components are available. The formation of these bonds is hence not incompatible with a macroscopic reversible evolution as expected from the thixotropic behavior.

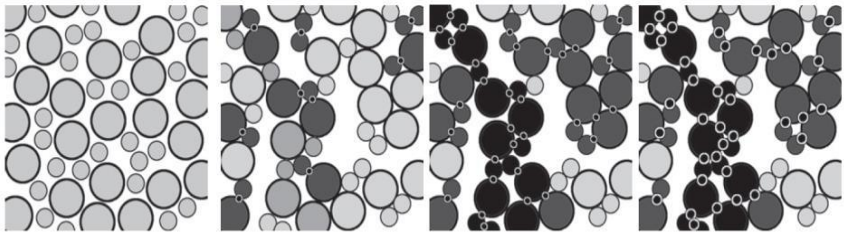

A **B** **C** **D**

Figure 2.9: Structuration phases in cementitious mixtures: dispersion (A), flocculation (B), nucleation (C) and structuration (D) [68]

The rate at which the yield stress increases is defined as the structuration rate A_{thix} [Pa/s]. Roussel [68] concluded after an extensive comparison of other investigations, that the structuration rate is more or less constant during the first hour of resting time, giving rise to the following relationship (Eq. [2.1]):

$$\tau_c(t) = \tau_{c,0} + A_{thix}t \quad [2.1]$$

When the material is at rest (i.e. after extrusion/pumping), gravity acts on the material. The gravity induced stress (τ_g [Pa]), acting on a single layer, can be described based on Eq. [2.2], with ρ [kg/m^3] being the density of the material, g [m/s^2] the gravitational acceleration and h [m] the layer height.

$$\tau_g = \rho g h \quad [2.2]$$

By successively depositing more and more layers, gravity-induced stresses increase progressively. In order to prevent collapse, the structuration kinetics of the printed material must be located in a process-dependent and object-length scale-dependent time window (Figure 2.10). Within this window, the strength (i.e. yield stress) and rigidity (i.e. elastic modulus) of the material increase [1, 60]. After reaching the final height of the printed structure, gravity-induced stress reaches its maximum value in the bottom layer which, as a consequence, could be at the origin of yielding and printing failure when the stress reaches the local yield stress [16, 68, 69]. The difficulty with this approach is that the rising speed is not an input parameter but a parameter resulting from the nozzle velocity, contour length, scale and layer thickness, resulting in full process dependency of the structuration rate [16]. It should be noted that, as the gravity-induced stress on one layer increases, small deformations are likely to occur. Although stress in the layer may stay below the yield stress and flow (or failure) shall not occur, the cumulative amount of strain in all layers could threaten the control of the final geometry [11].

The above-mentioned considerations are in literature translated into different approaches, all trying to quantify the buildability numerically and predict the exact moment of construction failure. Although there is no consistency between the current approaches, two major failure mechanisms could be distinguished: *(i)* material failure, where the material strength is exceeded and *(ii)* stability failure due to loss of equilibrium of forces and moments. However, due to the inconsistency between the approaches, no uniform prediction model is available yet.

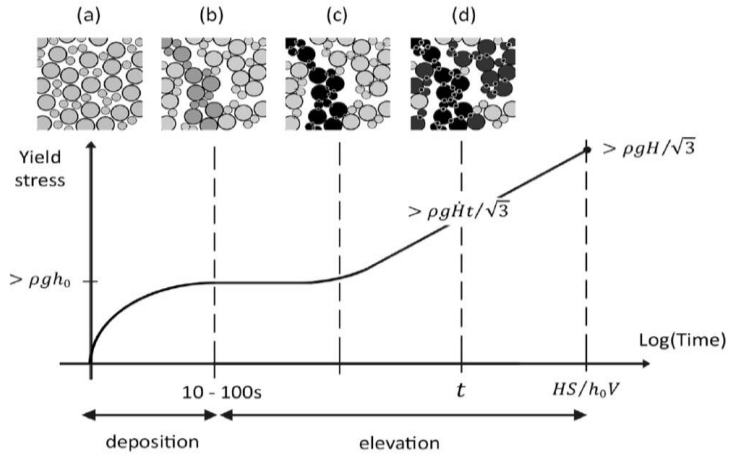

Figure 2.10: Network of interacting cement particles along with yield stress evolution and target requirements with h_0 [mm] the layer height, H [mm] the final height of the specimen, S the contour length [mm], V [m/s] the printing speed and ρ [kg/m^3] the density of the cementitious material [68]

In order to provide a sufficient buildability, one can conclude that a (very) fast structuration rate is beneficial. Controlling the structuration rate after onset can be achieved by modifying the hydration rate, typically in the acceleration phase of cement hydration. Although each layer has to follow the same kinetics, we must consider the fact that successive layers are placed at different times. As a consequence, the same batch of material will deposit layers with different structuration rates. To overcome this, the use of "set on demand" systems should be considered [70]. These are characterized by the use of a non-reacting chemically retarded base mix that is activated with set accelerator which can be added shortly before material delivery by using an inline mixing reactor. However, the main goal is to actively control the rheology and the stiffening of the material [71].

However, in order to ensure also a proper bonding between the layers, there also seems, from a rheological point of view, that an upper limit for this structuration rate exists. Previous research [72], performed on self-compacting concrete showed that the formation of a cold joint is likely to occur in case of an increased thixotropic behavior and in case of longer time intervals. These assumptions result in the definition of t_{max} [s], the maximum time for a layer to be produced.

2.3. Concluding remarks

Digital fabrication of concrete offers immense opportunities for a broad spectrum of stakeholders in the construction sector. Although the technique shows a lot of advantages (i.e. cost and time reduction), there are also some challenges that have to be tackled.

- Potential weak interfaces between the layers, the integration of reinforcement and the higher shrinkage risk are considered as bottlenecks of this technique. They not only affect the structural behavior, but also the durability of the printed element as they increase the amount of preferential ingress paths for chemical substances;

- The conflicting requirements of the material before and after material deposition ask an in-depth investigation before starting a new print project, taking into account the interdependency between material, process, design and product;

- Although digital fabrication demands a more energy-intensive binder phase, due to the inherent advantages, it has the potential to be more sustainable compared to traditional casting techniques;

- The lack of uniform structural and durable design codes hinders the integration of this technique in the construction industry.

Chapter 3

Materials and manufacturing methods

3.1. Materials

The main focus of this research is to investigate the consequences of the manufacturing technique on the mechanical and durable properties of a cementitious material. Therefore, a standard mix composition (REF), adopted from the research of Khalil et al. [73], was used throughout the entire experimental program. To purely focus on the effect of the print process, the reference material for both 2D and 3D print applications, consists out of cement, sand, water and superplasticizer. No alternative binders or chemical additives were applied. Only when the author aimed to counteract shrinkage, additional components like superabsorbent polymers or fibers were added. The different mix compositions, used throughout this doctoral thesis, will be explicitly mentioned when describing the various experiments.

3.1.1. Cement

Portland cement CEM I 52.5 N (OPC, Holcim Belgium, d_{50} = 10.8 µm) was used as binder in the reference material. The quantity of the clinker in this cement amounts to a minimum value of 95%. This type of cement provides a normal strength development (indicated by 'N' in the denomination). The chemical and mineralogical compositions are represented in Table 3.1. The mineralogical composition is calculated based on Bogue equations.

Table 3.1: Chemical and mineralogical composition of CEM I 52.5 N [mass%]

CaO	SiO_2	Al_2O_3	Fe_2O_3	MgO	Na_2O	K_2O	SO_3
64.30	18.30	5.20	4.00	1.40	0.32	0.43	3.50

C_3S	C_2S	C_3A	C_4AF	Blaine [m^2/kg]	Density [kg/m^3]
71.98	1.75	7.02	12.16	408	3160

3.1.2. Sand

Standardized sand (Normsand Germany, ρ = 2650 kg/m^3) with grain sizes ranging from 0.08 mm to 2 mm is used, conform to the requirements of the Comité Européen de Normalisation (CEN). The upscaling towards a 3D printable material was made by using sea sand (Belgium, ρ = 2650 kg/m^3) instead of the normsand with grain sizes ranging from 0 mm to 2 mm. The water absorption of both sand types is guaranteed to be below 0.2%.

3.1.3. Superplasticizer

Due to the low water/cement-ratio (W/C), a superplasticizer (SP) was required to improve the workability of the mixture. Within this research, MasterGlenium 51 (conc. 35%, BASF, Germany, ρ = 1,075 kg/m^3) was applied. This is a high-range water-reducing admixture based on polycarboxylic ethers.

3.1.4. Superabsorbent polymers

Three different bulk-polymerized monovalent salt polyacrylates with an irregular shape and different sizes (SAP A, SAP G and SAP M, for denomination in [74]) are used within the scope of this research. Specific production details, as defined by Snoeck [74], are listed Table 3.2. The size of the polymers refers to the mean particle diameter, under the assumption of SAPs having a spherical shape. The indicated swelling times were measured in demineralized water by means of the Vortex method [75] and indicate the time needed for a certain SAP to reach maximal saturation. The absorption capacity of the SAP was measured in two different solutions (i.e. demineralized water (DW) and cement filtrate (CF)) through the filtration method [76]. The latter was obtained by mixing 10 g CEM I 52.5 N in 100 g of demineralized water and subsequent filtration. The moisture uptakes (MU), determined by vapor sorption testing, are given for a RH of respectively 60%, 90% and 98%, indicated in the last column of Table 3.2.

Table 3.2: Specifications of the superabsorbent polymers [74]

SAP	Type	Production	Company	Morphology
A	Copolymer of acrylamide and sodium acrylate	Bulk	BASF	
G	Cross-linked acrylate polymer	Bulk	SNF Floerger	
M	Cross-linked potassium salt polyacrylate	Bulk	Evonik Industries	

SAP	Size [µm]	Swelling time [s]	Absorption capacity [g/g]		MU [%]
			DW	CF	
A	100 ± 22	10	305 ± 22	61 ± 1	26|83|394
G	157 ± 82	22	332 ± 82	47 ± 2	25|79|392
M	486 ± 141	65	285 ± 2	59 ± 1	26|75|186

3.1.5. Fibers

Synthetic polypropylene micro fibers (Crackstop M195-03, Adfil) are used and denoted as M3 in the following chapters. The micro fibers are extremely fine (d = 22 µm), single filament and cut to a length of 3 mm. The fibers are coated with a surfactant to improve the initial dispersion in the cementitious-bound materials.

3.2. Mix compositions

The mix composition of the reference mixture (REF) is represented in Table 3.3. The W/C ratio equals 0.37. For the development of mixtures including superabsorbent polymers, this equals the effective water-cement ratio as no additional water was used in absence of the SAPs.

From an eco-friendly point of view, the author notes that the binder content is rather high, especially as the only binder component is Portland cement. In order to improve the sustainability, one could (partly) replace cement by an alternative binder (i.e. calcium sulfo-aluminate (CSA) cement, silica fume, fly ash, etc.). However, as the influence of process-related parameters is the main focus within this doctoral thesis, the latter was not considered within the scope of this research.

The REF composition (Table 3.3) was adopted from the research of Khalil et al. [73] in order fulfil the printability requirements in accordance with the print equipment. Unfortunately, the pumpability of the latter was insufficient for upscaled 3D print experiments. This could be attributed to the high sand/binder-ratio (S/B), resulting in a stiff and viscous material. Based on literature [2], the S/B-ratio of a printable material stays below 1.5, while for the reference composition this parameter equals 2.

The pumpability was assessed based on rheological measurements, performed using an Anton-Paar MCR-52 dynamic shear rheometer, equipped with a six-blade vane (radius R_b = 11 mm, h = 16 mm) and building material cell (radius R_c = 36 mm). The rheological experiments were carried out with a relatively low rotational speed (maximum 10 rpm) and with a short test duration; each step took only 20 s to reduce the effect of particle migration and drying of the cementitious material. The protocol for the flow curve is represented in Figure 3.1A. Before the start of every experiment, a pre-shear of 10 rpm for 20 s was applied. The steady-state shear stress from the ramp-down portion of the sweep test was then plotted against the corresponding strain rate to obtain the flow curve. The author assumed a Bingham fluid: the yield stress and plastic viscosity were determined as the y-intercept and slope of a linear regression line. These parameters equaled respectively 900 Pa and 53 Pa.s (Figure 3.1B), which are both approximately 30% higher compared with literature [58].

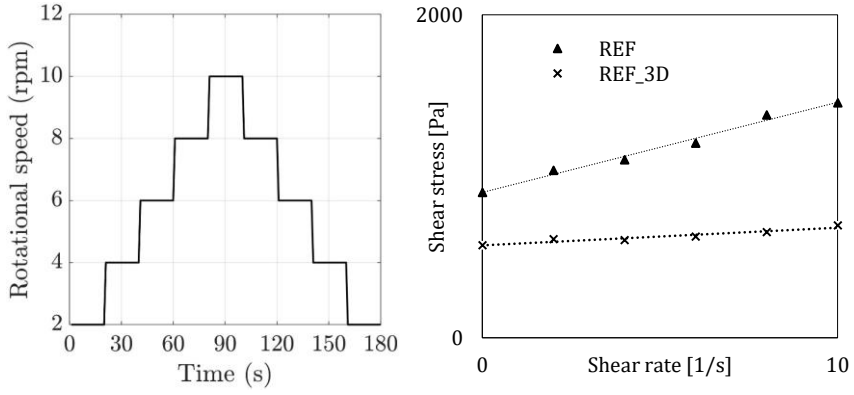

A B

Figure 3.1: Ramp-up and ramp-down for a specific rotational speed (A) and the flow curve of the different mixtures (B). Each point in the graph represents individual data points from rheological measurements and the line represents the regression line for the Bingham model.

To improve the pumpability of the reference composition, two modifications were applied; the S/B-ratio was lowered to 1.5 and the standardized sand was replaced by sea sand. The shift towards sea sand was made based on the lower fines modulus of the latter (2.3 instead of 3.1 in case of normsand) and the smoother particle size distribution, resulting in a mix composition with a lower yield stress and viscosity. Based on flow table measurements (NBN EN 12350-5 [77]), the optimal amount of SP was obtained without changing the W/C-ratio. The flow table test was performed in triplicate for each mix composition as a function of time (i.e. every 5 minutes) during 30 minutes after finalizing the mixing procedure. A deviation of $\pm$ 5 mm on the flow table diameter of the REF mix was allowed for the optimized composition. The reference material for 3D print applications will be denoted in the following as REF_3D. The flow table results are visualized in Figure 3.2; an overview of the exact mix compositions is represented in Table 3.3. The beneficial effects of the mix modifications are represented in Figure 3.1B; the yield stress and plastic viscosity are lowered with 63% and 80%, respectively.

According to Jensen & Hansen [78] and following Powers' model [79] the optimal amount of additional water in case of SAP addition, required to improve internal curing, complete the hydration process and mitigate autogenous shrinkage could be derived. As one gram of cement binds chemically with 0.23 g of water and adheres to 0.19 g of gel water, an effective water-cement ratio of 0.42 is required for complete hydration of the cementitious material. This additional amount of water is either available in the mixture itself or as water entrained in the SAPs ($(W/C)_{entr}$) and 'free' to be used for hydration. In case of the reference material, initially produced without water entrainment and given an original W/C of 0.37, Jensen & Hansen [78] formulated Eq. [3.1], valid for a W/C ranging from 0.36 to 0.42:

$$W/C_{entr} = 0.42 - W/C \qquad [3.1]$$

The optimal amount of water absorbed by the SAPs is added as additional mixing water above the effective W/C of 0.37, in accordance with the REF mixture. The optimal mass percentage of the SAPs was obtained based on trial and error with various amounts of SAPs added on top of the REF composition, after checking the workability of the cementitious materials based on the flow table test, performed in triplicate for each optimized mix composition. The flow table results are visualized in Figure 3.2; an overview of the exact mix compositions is represented in Table 3.3.

Based on material specifications, a fiber addition of 0.1 vol% was recommended. The author chose to maintain the W/C-ratio similar as for the

REF mixture and the required workability was obtained by varying the superplasticizer dosage.

The development of a proper fiber mix composition is performed in accordance with the above-mentioned test procedure, considering similar flow diameter deviations. An evolution of the flow table diameters in time and an overview of the mix composition can be found in Figure 3.2 and Table 3.3, respectively.

Table 3.3: Overview of the mix compositions

Mix (*)	Cement	Sand	Water	SP	SAP	Fiber
	[g]	[g/g_{cement}]	[g/g_{cement}]	[g/g_{cement}]	[g/g_{cement}]	[g/g_{cement}]
REF	1	2	0.37	0.0015	-	-
REF_3D	1	1.5	0.37	0.0063	-	-
A017	1	2	0.42	0.0015	0.0017	-
G025	1	2	0.42	0.0015	0.0025	-
M022	1	2	0.42	0.0015	0.0022	-
M3	1	2	0.37	0.0020	-	0.007

(*) The denominator with the SAP mixtures states the amounts added expressed as mass percentage over cement weight.

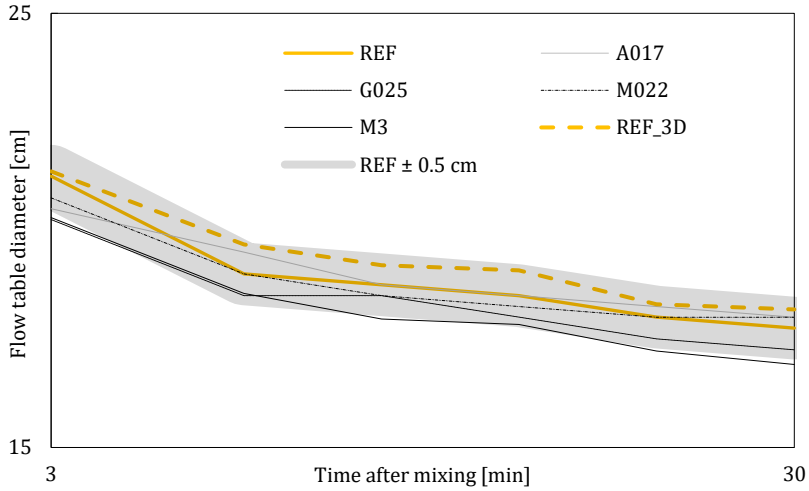

Figure 3.2: Flow table diameter as a function of time for mixtures with and without SAP or fiber addition (n=3). The graphs represent the mean value, error bars are left out)

3.3. Fresh state characterization

3.3.1. Extrudability

As a result of the applied print process and nozzle shape, printed layers will deform due to gravitational forces acting on the material after deposition. To limit the deformation of a single-layer filament, the extrudability was evaluated based on visual observations. The requirements were adopted from Kazemian et al. [63] and could be listed as follows:

- Printed layer is free of surface defects, including any discontinuity due to excessive stiffness and inadequate cohesion;
- Layer edges are visible and well-defined;
- Layer dimensions are consistent with limited deformations. More specifically, deformations of the cross-sectional width within a range of 10% were accepted.

Figure 3.3 visualizes single-layer filaments with insufficient (Figure 3.3 A-C) and adequate (Figure 3.3D) extrudability.

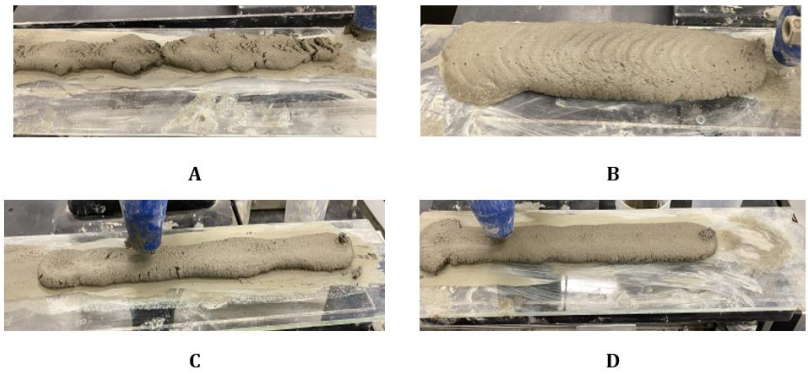

Figure 3.3: Single-layered filaments with insufficient extrudability due to discontinuities resulting from excessive material stiffness (A), unacceptable deformations (B) and inconsistent layer dimension (C). (D) represent an element with an adequate extrudability.

3.3.2. Buildability

As no standards are available, adequate buildability was according to literature obtained when at least 5 layers could be printed upon each other without failure [5, 12, 80]. However, buildability also depends on the mix proportions and the workability, in particular workability variation over time

(also called open time). Within this doctoral research, the open time is quantitatively assessed by measuring the initial and final setting time according to NBN EN 196-3, using an automated Vicat apparatus [81]. For this test method, the mortar is placed in a 40 mm high Vicat mold with an internal diameter equal to 75 mm. A needle with a 1 mm^2 cross section penetrates the mortar sample every 15 minutes, measuring the penetration depth and correlated resistance. The initial and final setting times are specified based on the measured penetration depth, more specifically as the time at which the distance between the needle and the base plate of the mold is respectively equal to (6 ± 3) mm and 0.5 mm. The initial and final setting time of REF equal 210 and 420 minutes, respectively. In case of REF_3D, these values are 330 and 420 minutes, respectively, indicating the longer workability of the latter composition.

3.4. Mixing procedure

Before mixing, all constituents were carefully weighted by using a Kern Electronic balance (0.01 g accuracy), whereas the SP amount was determined by the use of a syringe. Before the start of every mixing procedure, a surface-wet condition of the stainless-steel bowl and stirrer of the planetary mortar mixer (Macben, Belgium) was ensured. The mixing procedure, carried out in standardized conditions (20 ± 2°C, 60 ± 5% RH), maintained throughout the experimental research is the following:

- 30 s premixing of dry components at low speed (140 rpm);
- Water and SP addition;
- 30 s mixing at low speed (140 rpm);
- 30 s mixing at an increased speed (285 rpm);
- 30 s scraping off material from the sides of the bowl;
- 60 s resting time;
- 60 s mixing at a high mixing speed (285 rpm).

In case of SAP addition, the polymers were added in a dry state and mixed together with the dry materials (cement and sand). To ensure a proper dispersion of the micro fibers, the last step in the general mixing procedure was replaced by the following steps:

- Fiber addition (half of the amount);
- 30 s mixing at high mixing speed (285 rpm);
- Fiber addition + 30 s mixing at high mixing speed (285 rpm).

3.5. Print equipment

A Quick-point mortar gun was used to simulate a screw extrusion-based 3D print process. The mortar gun consisted mainly out of a container to insert the cementitious material, a Black&Decker 5.2 Amp drill built-in and an Archimedes screw to move the cementitious material towards the nozzle (Figure 3.4A). The extrusion nozzle was elliptical shaped (28 x 18 mm^2, Figure 3.4B). The mortar gun was mounted vertically on a fixed steel frame. The latter was in turn fixed to a rigid printable table, provided with a sliding steel carrier. The translational motion of the latter was controlled by a complementary software program, regulated by a rotational frequency. During extrusion, a glass plate was positioned under the steel carrier on which the cementitious material could be deposited.

The mortar gun could manually be altered in height to ensure a proper clearance between the nozzle and the building platform. The rotational speed of the augur could be influenced by changing the voltage input of the drill. The complete printing system is visualized in Figure 3.5.

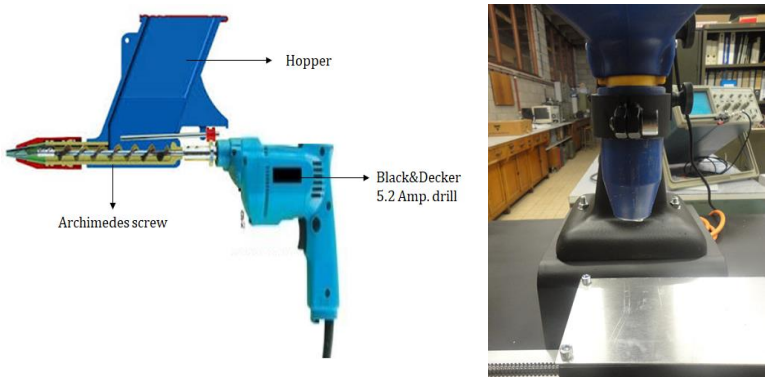

Figure 3.4: Quick-point mortar gun (A) and elliptical extrusion nozzle (B)

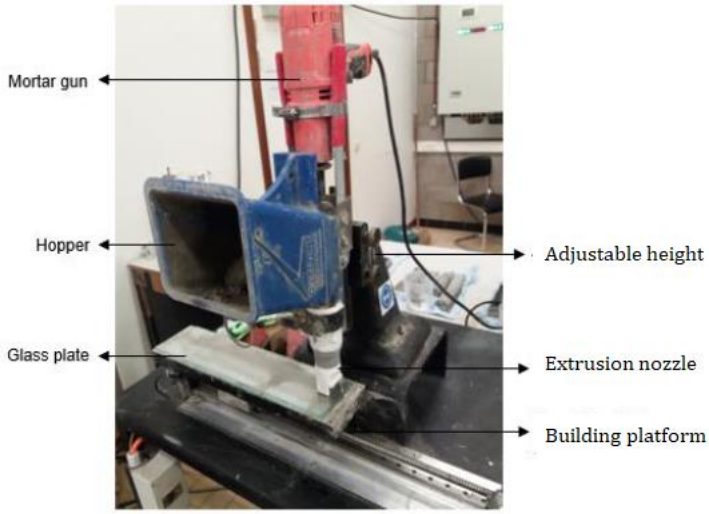

Figure 3.5: In-house developed printing system

The in-house developed system is able to print up to 300 mm long cementitious layers, with different printing speeds and different flow rates. Within the scope of this research, two different velocities will be considered: 1.7 cm/s and 3.0 cm/s and will be denoted as S1 and S2, respectively. The printing speeds correspond with a different rotational speed of the auger as the printed specimens for both velocities have to fulfil the printability requirements. Regardless of the printing speed, the height of a single layer equals 10 mm. The velocities and corresponding settings are listed in Table 3.4.

Table 3.4: Flow properties

Nomination	Printing speed [cm/s]	Voltage [V]	Frequency [Hz]	Flow rate [cm^3/s]
S1	1.7	45	750	5.6
S2	3.0	55	1000	9.9

Within this doctoral thesis, the upscaled 3D experiments were carried out with a six-axis industrial robot. The fresh cementitious material was transported to the print head with a progressive screw-based pump, connected to a 5 m long rubber hose. The layers were printed with an elliptical nozzle (33 x 20 mm^2) and a horizontal printing speed of 15 cm/s. The height of the layers equaled 10 mm.

Figure 3.6: Six-axis robot used for 3D print experiments

3.6. Sample preparation

3.6.1. Printed specimens

Every print process starts by moisturizing the hopper's internal surface and auger with a predefined amount of water. Thereafter, the hopper was filled with the cementitious material and extruded through the elliptical nozzle at a predefined speed. Extrusion of this substrate layer, with a total length of 300 mm, was the first step for every printed sample.

After a predefined time gap, the next layer was deposited on top of the previous one. In total, four different interlayer time intervals (i.e. 0, 10, 30 and 60 minutes) were considered and will be denoted as T0, T10, T30 and T60, respectively. However, it is important to note that not all of them are investigated for every experiment and the applied time gap will be mentioned explicitly in the description of the specific experiment. Another import remark is that T0 implicates the superpositioning of two layers 'as soon as possible', resulting in a time gap which equals approximately 15 s (i.e. the time required for the building platform to move back to its original X-position).

In case of T0, layers were printed from the same batch of material while for increased time gaps, a new batch of material was mixed for every superpositioned layer to ensure similar rheological parameters.

The author acknowledges that the latter is only an assumption and small deviations could occur due to fluctuations in room temperature, relative humidity, water temperature and content, etc. However, as every print experiment was manufactured in a standardized environment (20 ± 2°C, 60 ± 5% RH) and a water temperature of 20°C was maintained, these fluctuations were kept as small as possible.

After changing the vertical position (Z-direction) of the nozzle, extrusion of the next layer started at the same horizontal position (X-direction) to ensure a similar time gap between deposition. According to the experiment, samples consisting of two to four layers were manufactured and stored in standard conditions (20 ± 2°C, 60 ± 5% RH) until the day of testing. Real-life print conditions were mimicked by not covering the specimens with foil.

3.6.2. Conventional cast specimens

In order to draw relevant conclusions with regards to the manufacturing technique, cast specimens were made as a comparison. Therefore, prismatic molds (160 x 40 x 40 mm^3) were filled in two steps and compacted by jolting 60 times. The molds were covered with foil during 24 h and demolded after 24 h. Thereafter, the prisms were stored under the same conditions as mentioned before (20 ± 2°C, 60 ± 5% RH) until the day of testing. The conventional cast specimens were produced with the same mix compositions and the same mixing procedure as mentioned in section 3.4 was followed.

3.7. Statistical analysis

Due to the high variability of the test results, a statistical comparison of the test results and an establishment whether they differ in a significant way is required. Therefore, the software program SPSS Statistics 25 was used to perform the following analyses:

- An independent t-test analysis was executed for the comparison of two means. It was reasonable to assume in this research that the tested specimens of different series were indeed independent from each other;
- Multiple means were compared by doing a (one-way) analysis of variance (ANOVA) as t-tests suffer more type-I errors due to multiplicity. ANOVA only concludes whether there is a significant difference between at least one set of two means, but it does not reveal which means mutually differ;

- In case of homogeneity of variances (verified by means of a Levene's test), the Student-Newman-Keuls (SNK), Bonferroni and Tukey multiple comparison tests were performed;
- In case of inhomogeneity of variances, a Dunnett's T3 test was also carried out.

Whenever deemed important in the next chapters, the exact statistical method as well as its outcome are explained in detail. In general (and if not stated otherwise), a significance level α of 5% was implemented. In all statistics, a sample size n of at least 3 was available.

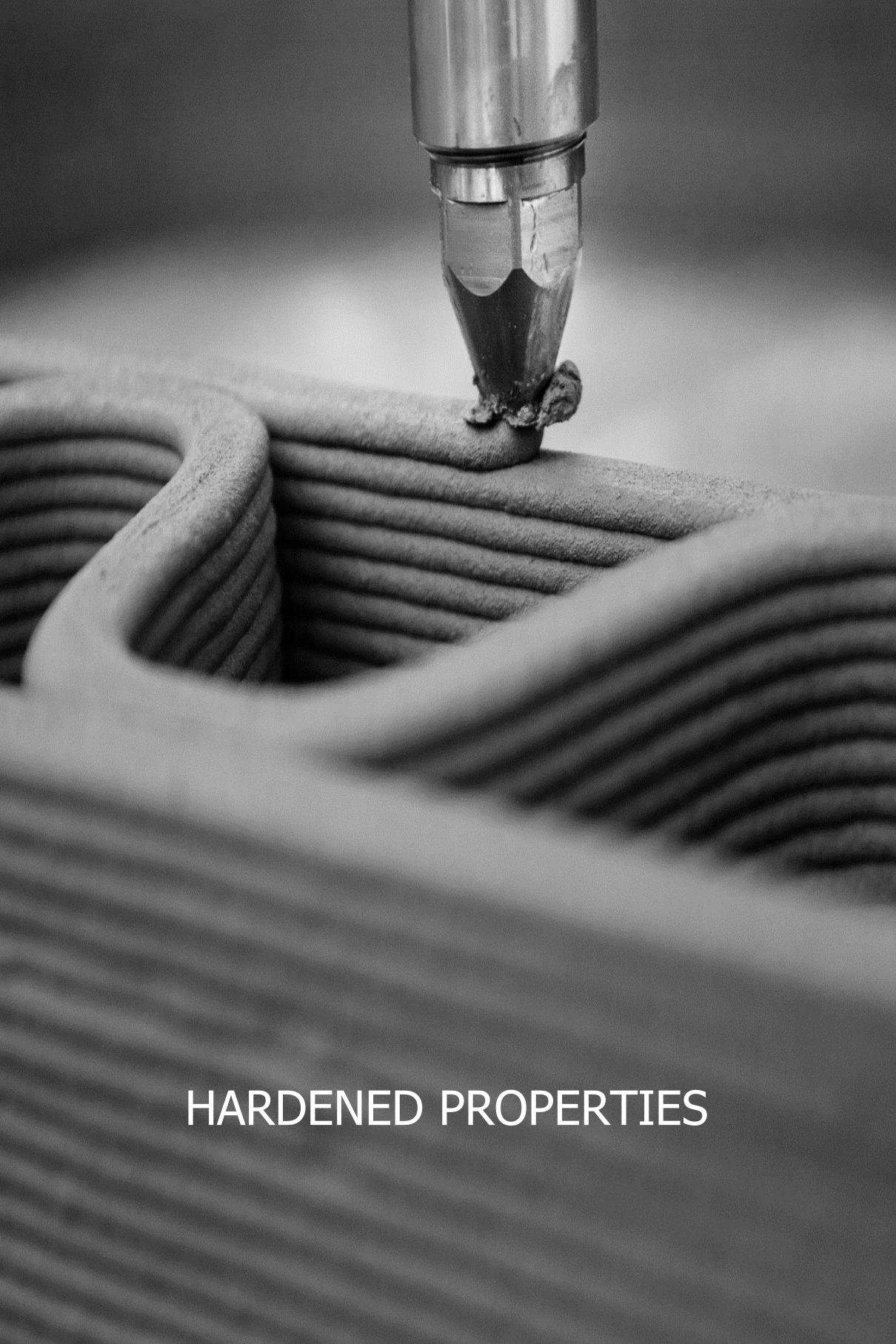

HARDENED PROPERTIES

Chapter 4

Mechanical properties

4.1. Mechanical properties

3D concrete printing has progressed rapidly over the last decades and the viability of this manufacturing method for actual structures in the domain of infrastructure and residential buildings is now being explored. With this expansion of projects, there is also a growing need for reliable mechanical properties that can serve as input for structural calculations. Unlike traditional cast concrete, where the material is placed in one continuous pour in a formwork and vibrated afterwards to obtain a homogenous material, printed elements are build-up layer by layer and the existing design codes may be insufficiently compatible with the specific properties of the printed materials and elements.

Due to the existence of different extrusion techniques, the high variability of printable materials and the high dependency between material, design, and process parameters, there are no standards or requirements available yet, nor for the characterization in fresh state, nor for testing the mechanical performance in hardened state. The classical concept of compression testing on cubes or cylinders, as the basic for compliance testing, might not be applicable for printed elements. Researchers start therefore adapting the conventional methods or developing their own test methods. As a consequence, a high discrepancy between the results listed in literature can be observed and an accurate comparison between the results is therefore difficult to make.

Kruger and van Zijl [82] listed, based on their findings in literature, numerous mechanical investigations of extrusion-based cementitious materials, considering three different loading directions (Figure 4.1); Orientation I and II, where layers were aligned horizontally or vertically, and Orientation III were layers were aligned in transvers direction.

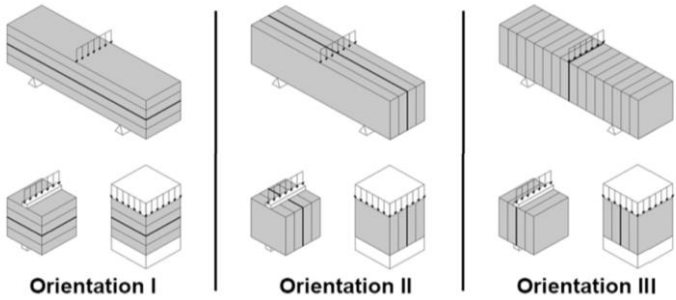

Figure 4.1: Directionally dependent mechanical testing respective to layer orientation of digital manufactured elements [24]

A general observation from all experimental studies is the orthotropic mechanical behavior of printed materials, irrespective of the type of material. This is mainly attributed to the weak interlayer bonding, whereas the internal stress state induced by the external loading further dictates the extent of the strength reduction depending on the layer orientation. As a consequence of this weak interlayer bonding, cracks initiate and propagate along the interlayer and extruded layers start to separate, resulting in a global failure of the element. The extent of the latter increases as a function of the time interval between the deposited layers. Furthermore, in most studies, a large reduction in mechanical strength (approximately 46%) is observed in digitally fabricated elements compared to mold-cast specimens, with coefficients of variations of 54%. Whether the results differ in a significant way cannot be confirmed without further details, however, these coefficients of variations portray the high variation in reduced mechanical performance obtained across various laboratories, which could pose design and quality assurance challenges for the 3D concrete printing industry due to reproducibility issues.

4.2. Test methods

4.2.1. Compressive strength

Similar as in conventionally cast concrete, the compressive strength of printed elements is mostly determined by means of a uniaxial compression test on cubic or cylindrical specimens, saw-cut or drilled from multi-layered printed elements. The effect of the layered structure and the anisotropic behavior is examined by considering different test directions.

4.2.2. Interlayer bonding strength (tensile strength)

Interlayer bonding test methods, currently available to evaluate the bond between concrete and repair mortars, are schematically represented in Figure 4.2. They can be subdivided in three main categories; interlayer bonding tests under tensile stress (Category I, Figure 4.2A, B, and C), under shear stress (Category II, Figure 4.2E and F), or under the combination of shear and compression (Category III, Figure 4.2D).

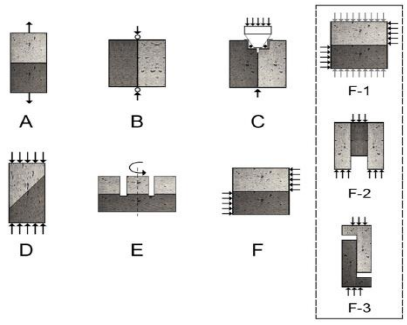

Figure 4.2: Interlayer bonding test methods, applied to determine the bonding between concrete and repair mortars [26]

Although the pull-off test (A) encounters several problems, it is the most common test method within the first category. The test results may be strongly influenced by the eccentricity during loading and damage caused by coring. Pull-off measurements often show a large scatter, which makes it difficult to interpret the measurements. Additionally, the interlayer pull-off strength is hard to quantify on properly placed overlays with a high bonding, yet easy to quantify in cases where the tensile interlayer strength is lower than the material tensile strength. Another test method within the same category is the splitting tensile test (B). Within this test setup, a longitudinal compression load is applied on the cross section in the middle of the sample.

This causes compression at the interface and tension in the remaining cross-section which splits the sample into two parts. The splitting tensile test has a higher efficiency compared to pull-off tests. An extension of the latter is the wedge splitting test (C), where the interlayer strength is assessed with fracture mechanics parameters such as crack opening, specific fracture energy, and tensile interlayer strength in bending. In the second test category the interlayer bonding strength is determined under shear and is called direct shear test. Common shear bond tests apply only a force parallel to the interlayer (F), or a combination of a shear stress and a small bending moment (E). The smaller stress concentration causes a smaller scatter on the results. An example within the third category is the slant shear test (D), were a prism or a cylindrical sample, made out of two identical halves bonded under 30° or 45° are tested under axial compression.

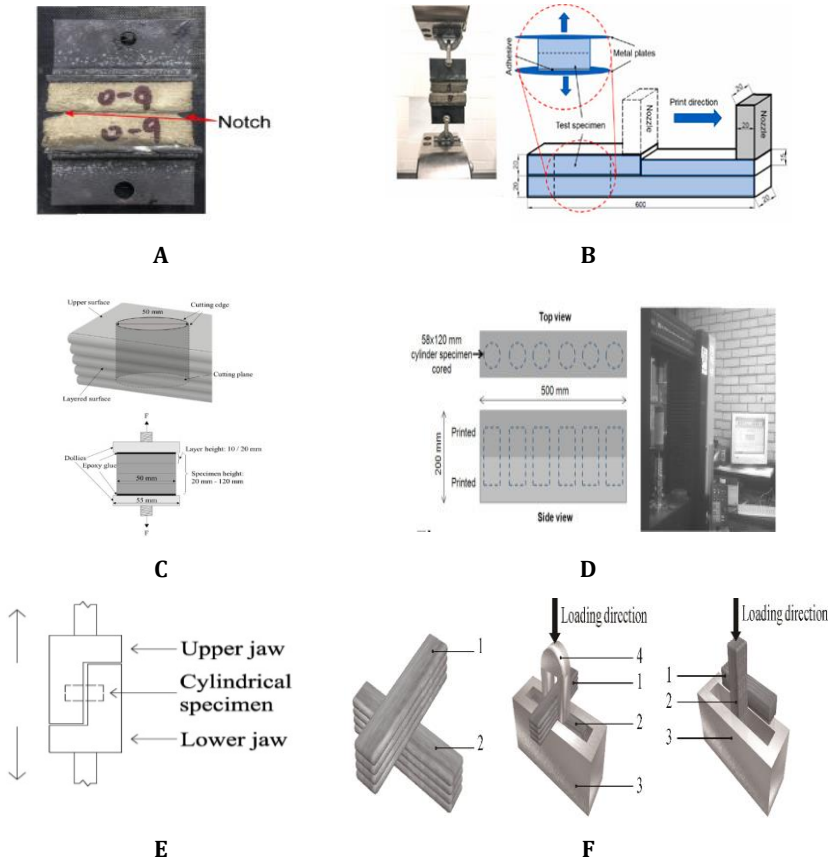

Figure 4.3: Interlayer bond test setups employed for interlayer bond determination of 3D printed concrete by Sanjayan et al. (A), Panda et al. (B), Lee et al. (C) and Le et al. (D), Rahul et Al. (E) and Liu et al. (F) [13, 23, 83-86]

Based on literature, pull-off tests are commonly applied for the mechanical characterization of 3D printed concrete, as depicted in Figure 4.3A-D. To overcome eccentricity issues, Rahul et al. [23] updated these original pull-off tests (Figure 4.3E) and placed the interlayer of a printed specimen horizontally in the grooves of upper and lower jaws of fixture. Liu et al. [86] on the other hand developed the cross-bonding method (Figure 4.3F), which enables the evaluation of both tensile strength and shear strength. As already stated before, the choice of a proper bond strength test is crucial, and different test methods cause distinct interface stress conditions within the specimens. Consequently, test results will differ when comparing different test methods. Literature shows that the measured bond strength decreases with the test method in the following order: slant shear, direct shear, splitting test and pull-off tests. The appropriate test for a particular case is the one for which the nature of loading is most similar to the stress condition of the actual structure.

It should be noted that sample preparation is extremely important, especially in terms of 3D printed specimens which have originally an irregular shape. Saw-cutting for example should preferably be avoided as much as possible since it may influence the weaker interlayers microstructure. In addition, sharp notches will lead to stress concentrations in the section, whereby the uniform tensile stress distribution in the interlayer is disturbed, and errors are introduced to the peak tensile stress by dividing the peak force with the net cross-sectional area [82]. Preliminary studies indicate in addition that significant plastic shrinkage occurs when only two layers are printed upon each other, due to the relatively large exposed surface area to volume ratio; hence, a visual inspection of possible crack occurrence before testing the interlayer bonding strength is required.

Depending on the test method, the failure mode of a specimen can differ. In general, two failure modes can be distinguished: adhesive failure and cohesive failure. Adhesive failure, or interlayer debonding, occurs at the interlayer whenever the bond strength is reached; cohesive or monolithic failure on the other hand occurs in the bulk material [87]. The failure mode of a specific element can be influenced by the surface roughness; increasing the surface roughness will increase the number of cohesive failures. Secondly, the failure mode also depends on the compressive strength of the material. Two layers, elaborated on different times, will have different Young's modulus, causing a differential stiffness of the composite concrete member, which will change the stress distribution at the interlayer. Literature revealed an increasing number of cohesive failures with an increased difference in the Young's modulus of each layer.

4.2.3. Flexural strength

The flexural strength depends mainly on the region subjected to the peak bending stress. More specifically, if the loading direction is such that the maximum bending stress is induced at the interface, the flexural strength can be significantly lower. On the other hand, high flexural strength values, even higher than those obtained for mold cast specimens, can be achieved when the direction of loading is such that the maximum bending stress occurs only in the bulk concrete [2].

Similar to traditional cast concrete, three- and four-point bending tests are employed as a pragmatic approach to evaluate the mechanical performance of printed specimens. In general, 3D printed structures will be subjected to more general loading than uniaxial tension. Therefore, three- or four-point bending test can also be applied to characterize the bonding between the layers. For this purpose, four-point bending tests are recommended due to the imposed constant bending moment and zero internal shear force in the central region of the specimen. This in contrast with three-point bending tests, where the maximum bending moment is concentrated in the middle of the specimen. Additionally, geometrical imperfections such as the undulating surface finish pattern may further cause stress concentrations and premature failure of the specimen, unless these imperfections are carefully removed by saw-cutting or grinding without introducing new imperfections [82].

4.3. Influencing parameters

The mechanical performance of a printed specimen is mainly influenced by the quality of the interlayer and the correlated bonding between two super positioned layers. Factors affecting this bonding are already investigated thoroughly in the field of repair mortars [25]. However, there the connection between a layer of fresh and hardened concrete should be provided, while in terms of 3D printing, the bonding between two freshly deposited layers should be foreseen. Therefore, the most important parameters, affecting the latter, are listed below.

4.3.1. Surface moisture

The loss of surface moisture after extrusion is the most prominent mechanism for interlayer debonding encountered in 3D concrete printing [24, 41, 84, 88]. Water evaporates from the free surface, of which the rate depends on environmental conditions such as temperature, relative humidity, wind, etc. This evaporation process dries out the printed surface

and makes it more rigid than the following layer, limiting the ability to form a strong bond. As a consequence of this difference in surface moisture state, the bottom layer will absorb water from the freshly deposited layer and this will force more air out of the bottom layer into the inter and top layer. Some of this entrapped air moves into the interlayer region, where it increases the porosity and permeability and causes a poor physical bonding between the layers. Further on, due to the water migration between two layers, cement hydration is negatively influenced over the interlayer region, yielding increased amounts of unhydrated cement. The longer the interlayer time gap between the layers, the more water evaporates from the surface, and the more water will migrate between two super positioned layers [82]. A schematic overview of the surface moisture mechanism in terms of 3D printing is represented in Figure 4.4.

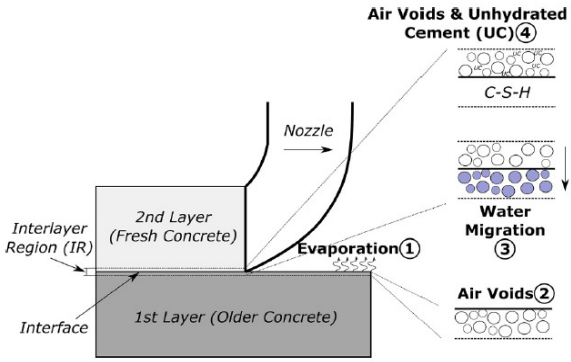

Figure 4.4: Surface moisture reduction due the evaporation, resulting in air voids, which will fill up with water after placement of the consecutive layer due to capillary absorption, ultimately yielding in an increased porosity and permeability as well as unhydrated cement in the interlayers [82]

It seems evident that, with an increasing time gap between two printed layers, the moisture content of the surface will decrease over time, however, these results are not generally accepted. An experimental study by Sanjayan et al. [84] revealed a linear decrease in surface moisture for interval times ranging between 0 and 20 min, followed by an increase in moisture content up to 30 min, caused by the rise of bleeding water. Although this study also validates the surface moisture mechanism, it is important to consider and account for other material properties such as bleeding and the effects thereof on the interlayer bonding strength.

A general trend, stated by different researchers [24, 41, 88, 89], is that the interlayer bond strength decreases with a lower surface moisture content.

The latter is also represented in Figure 4.5. When the first layer is protected from drying, the reduction in bond strength is minimal for resting periods up to 2 hours. This in contrast with specimens who are exposed to environmental conditions, where even after 10 minutes a reduction in bonding strength could be observed. The difference in bonding strength between sealed and exposed specimens increases as the interlayer time interval increases, presenting a strong evidence of the surface moisture mechanisms that induce lack of bonding between different concrete layers.

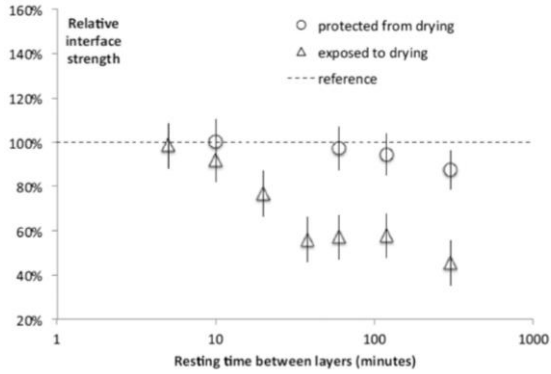

Figure 4.5: Relative interlayer bonding strength as a function of the interlayer time interval for a sealed and exposed first layer in a wind tunnel. The dashed line indicates the reference bonding strength in case of a zero minute time gap [88]

4.3.2. Surface roughness

The surface roughness of printed filaments is another important mechanism that is related to the mechanical interaction between the substrate and overlay filaments. He et al. [90] investigated the bond strength of repair systems for conventional cast concrete and concluded that increased surface roughness increases the mechanical interlock effects between old and new concrete. The concept of mechanical interlocking (i.e. holding elements together by geometrical constraints) is also investigated by Zareiyan and Khoshnevis [91] for printed specimens and will be further discussed in Chapter 5.

4.3.3. Thixotropy

Filament layers can also bond to one another due to intermolecular attractive van der Waals forces via thixotropy, given that the interlayer time interval is relatively short. This is especially relevant for 3DCP materials which are typically designed to demonstrate thixotropic behavior to assist with

pumping, extrudability and buildability. Kruger et al. [92] developed a bi-linear thixotropy model, that specifically pertains to the 3D printing process. In the first stage, a de-flocculated microstructure is prevalent when the material exits the nozzle for placement due to shearing induced by pumping of the material. Since no energy is imparted on the deposited concrete, the material re-flocculates, trying to restore the original microstructure before agitation. This re-flocculation period can last up to 5 minutes on average for high thixotropic material [92-94]; however, this is material dependent. Once the original microstructure has been restored, structuration of the material commences (stage II). During this phase, early hydration products such as ettringite needles form and bond particles together that present pseudo-thixotropy behavior.

Roussel and Cussigh [72] found that thixotropy of self-compacting concrete (SCC) may induce distinct layer casting (debonding between the layers) and they reported a specific distinct-layer prevention methodology that may be relevant to the digital fabrication of concrete in fresh state: (i) the interface between two layers of fresh concrete must be rough; the roughness at the interface creates a (frictional) bond between two layers even if they do not mix and (ii) A_{thix} of the first layer has to be low enough to allow the stresses generated at the interface between the two layers to re-initiate flow in the first layer. If the first pour of concrete structurates too much and/or too fast after placement, and the apparent yield stress increases above a critical value, then the following pour of concrete will not entirely mix with the previous one, yielding a weak interlayer.

In addition, high thixotropic materials also lead to an increased amount of entrapped air. To prevent distinct layer casting, the authors suggest not to exceed the critical time gap t_c [s] between the deposition of two layers (Eq. [4.1]). The latter depends on the density of the material ρ [kg/m^3], the gravitational acceleration g [m/s^2], the layer height h [m], the structuration rate A_{thix} [Pa/s], the plastic viscosity μ_p [Pa.s] and the print velocity V [m/s].

$$t_c = \frac{\sqrt{\frac{(\rho g h)^2}{12} + \left(\frac{2\mu_p V}{h}\right)^2}}{A_{thix}} \qquad [4.1]$$

4.3.4. Air entrapment

Large elliptical or longitudinal cavities at the interlayer region are frequently reported in literature [41, 47, 95, 96]. Nerella et al. [41] ascribe the formation of these voids to air "enclosure" that occurs when the upper layer is deposited onto the substrate layer with significant surface unevenness. This surface unevenness may be a result of natural surface roughness via exposed aggregates or due to long time gaps where water evaporates from the surface. In addition, also a poorly executed printing process, such as a slightly oscillating nozzle, an inadequate print velocity or an inappropriate functioning of the pump can induce voids. These voids are in general bigger (1.6 – 4.0 mm) compared to mold-cast concrete (0.2 – 1.6 mm) [13]. The consequence of macro pores presence in the interlayer bonding region is less chemical or physical bonding between the layers.

4.3.5. Print process parameters

Individual process parameters cannot be considered independently of the applied material and other process parameters and general conclusions are hard to make. However, some general trends could be observed. As stated by Bos et al. [18] and Paul et al. [97], the nozzle shape would have a significant influence. As the printed layers are more difficult to stack, circular nozzles introduce more voids in the printed object which might lower the strength, while the latter phenomenon is not significant in case of rectangular or squared nozzles.

Panda et al. [83] examined on the other hand the variation in nozzle standoff distance (i.e. the position of the nozzle above the printed surface) as this parameter not only affects the bond strength but also the specimen surface quality. The default standoff distance is considered equal to the nozzle section width, as this allows smooth deposition of the cementitious material and avoids interaction between the print head and the deposited layer. However, reducing the standoff distance improved the bonding, which could be attributed to the higher force exerted on the substrate layer and the corresponding higher amount of air that could escape at the interlayer. It is important to note that there are also limitations; when the standoff distance is too small, the substrate layer will deform and this may affect the dimensional integrity and accuracy of the printed geometry.

Additionally, also the printing speed is considered as an influencing parameter. Although research is limited, it can be assumed that higher printing speeds possibly generate micro voids in the deposited later which sometimes affect the hardened properties of the printed part. However, further investigations are required to prove the above-mentioned assumptions.

4.4. Materials and methods

4.4.1. Materials

This part of the doctoral thesis aims to investigate the influence of the print parameters on the mechanical properties of the printed elements. Therefore, only the reference material was considered without the addition of fibers or superabsorbent polymers. The elements were printed with different time gaps (T0, T10, T30 and T60) and different printing speeds (S1 and S2). In addition, a comparison with conventional cast elements was made.

4.4.2. Surface roughness

After hardening for 28 days, the surface roughness of a single layered element was quantified by measuring the height of the surface peaks and valleys with a high precision laser beam (5 µm resolution), mounted on an in-house developed Automatic Laser Measurement (ALM) table [98]. The ALM device was equipped with two stepping motors, controlling the motion in both X- and Y-direction. The profile measurements were used to calculate the center-line roughness R_a [-] of the printed layers with an accuracy of 7 µm. This value is determined with an average line, drawn through the measured profile. R_a is then calculated as the sum of the surface areas a_i [-] between the profile and the center-line over a selected reference length Eq. [4.2].

$$R_a[-] = \frac{1}{n}\sum_{i=1}^{n}|a_i| \qquad [4.2]$$

For the purpose of this research, the reference length equals 200 mm in the X-direction and 15 mm in the Y-direction. The latter was selected to include important roughness features but exclude errors of form. As depicted in Figure 4.6, roughness measurements were performed in triplicate every 50 mm and 5 mm in the X- and Y-direction, respectively.

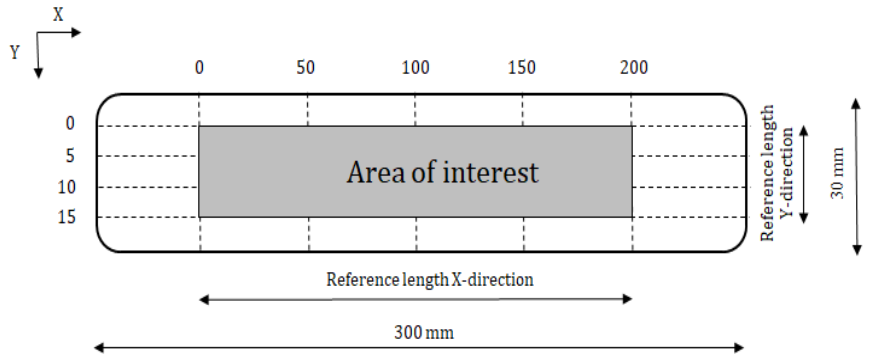

Figure 4.6: Schematic representation of the automated laser measurement (ALM) technique (dimensions in mm)

4.4.3. Surface moisture

The moisture content of a single layered sample (l = 300 mm) was registered in triplicate for one hour by gently pressing blotting paper (Aurora ref.10 blotting paper) strips (75 mm x 25 mm) on top of the printed surface. The uniform pressure (77.5 ± 0.1 Pa) on the blotting strips was executed by means of a plastic weight with a mass of 34.3 g and a surface area of 66 x 66 mm^2 for a duration of 60 s. The mass change was measured at predefined time steps (i.e. 0, 10, 30 and 60 min after printing). The mass of the absorbed fluid per unit area k [g/cm^2] is obtained by using Eq. [4.3]:

$$k[g/cm^2] = \frac{m_{sat} - m_{dry}}{A_{strip}} \qquad [4.3]$$

Within this equation, m_{sat} [g] is the weight of the paper strip after water absorption on the printed surface, m_{dry} [g] is the weight of the paper strip in dry conditions (i.e. before positioning on the freshly printed layer) and A_{strip} [cm^2] is the area of the strip placed on the printed surface. To avoid the influence of particles sticking on the filter paper after performing a measurement, every strip was additionally weighed after drying for 24 hours in order to obtain a correct value for m_{sat}. A_{strip} is obtained by a calculation in reverse, knowing the areal paper density (125 g/m^2) and the initial dry weight of the paper strip (m_{dry}).

4.4.4. Optical microscopy

Correlations between the surface roughness and the applied printing speed were based on optical microscopy. Therefore, thin sections (40 mm x 25 mm x 30 µm, Figure 4.7) were prepared in order to study the sand particle distribution through a printed sample.

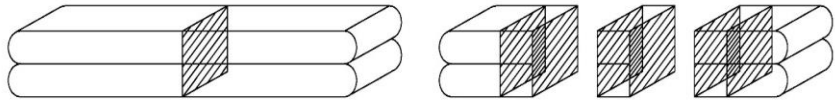

Figure 4.7: Thin section sample preparation

Thin sections were impregnated with fluorescent epoxy (Stuers NV.), scanned afterwards using a Leica DMPL microscope with DFC 295 camera and analyzed with ImageJ. Different regions with a cumulative height of 0.5 µm, starting from the top surface were selected and the amount of sand particles was calculated within the different areas. For both printing speeds, two thin section were analyzed. Within each sample, eight areas were defined in total to calculate the changing sand volume.

4.4.5. Compressive strength

Uniaxial unconfined compression test in fresh state

The characterization of the compressive strength in fresh state allows the author to evaluate the structural build-up of the cementitious material and to quantify the evolution of the elastic parameters (Young's modulus E and static Poisson ratio v) as a function of time. The uniaxial unconfined compression test (UUCT) in fresh state was performed on cylindrical samples. The dimensions of the latter were designed according to ASTM D2166. The diameter Ø = 25 mm is large enough to eliminate size effects due to particle size and distribution. The height equals 50 mm, such that h/ Ø = 2 to allow a diagonal shear failure plane to form. After mixing, the material was poured into a plastic mold, which was removed just before testing. The samples were loaded in a Walter+Bai DB 250/15 test rig, equipped with a 3 kN load cell. The displacement rate was set equal to 30 mm/min, similar to the rate used by Wolfs et al. [64] and with a maximal vertical displacement of 25 mm, which equals the limits of the testing device. To avoid additional deformations before testing, a teflon plate was directly attached to the upper part of the compression device (Figure 4.8). Teflon is used to avoid water absorption and will create a lower friction with the fresh concrete, resulting in a larger unconfined region.

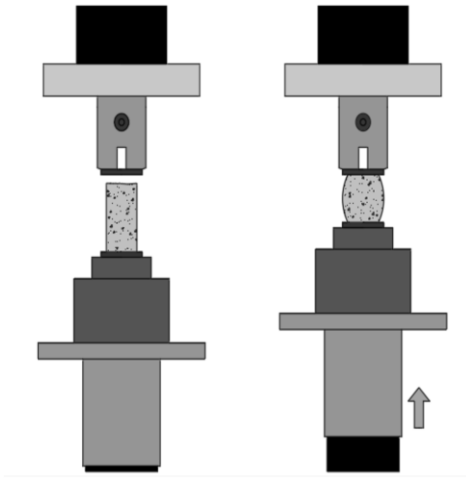

Figure 4.8: Schematic overview of the UUCT test-setup in unloaded initial situation (A) and loaded situation (B)

Initially, UUCT tests were executed every 5 minutes, starting at the earliest time after sample preparation (i.e. 5 min after the addition of water). Specimens older than 60 min were not characterized. For each concrete age, the test was performed in triplicate.

During testing, the displacement and applied load were continuously measured and recorded, while the deformations of the samples were filmed with a Nikon D3200 camera. These recordings were afterwards processed in ImageJ and/or Tracker to measure the initial sample diameter, the initial sample height and the lateral deformations caused by UUCT. In order to track automatically the lateral deformation of the cylindrical sample, two red drawing pins, which define a clear pattern of pixels, were inserted at both sides of the fresh concrete sample. To enhance the contrast in pictures (which improves the measuring accuracy) a blanc paper was taped at the back of the UUCT device and a LED video light was positioned behind the camera set-up.

The force-displacement data was processed for each sample in order to obtain the stress-strain diagrams. As the samples largely deform during compression, an updated cross-section A(t) [mm^2] was used to calculate the stress. This updated cross-section is calculated according to ASTM D2166 (Eq. [4.4]) and assuming a conservation of volume. It is important to note that this is only an assumption as the material can be compacted during the experiments.

$$A(t) = \frac{A_0}{1 - \varepsilon(t)} = \frac{A_0 \cdot h_0}{h(t)} = \frac{A_0 \cdot h_0}{h_0 - \Delta h(t)} \quad [4.4]$$

Within this equation, A_0 [mm^2] is the initial cross-section, based on the initial sample diameter d_0 [mm], $\varepsilon(t)$ [-] is the vertical strain as a function of time, h_0 [mm] the initial sample height and h(t) [mm] the sample height over time. The initial dimensions d_0 and h_0 were measured twice with a caliper before the start of the test. The sample height h(t) is calculated based on the measured displacements Δh, the stress $\sigma(t)$ and strain $\varepsilon(t)$ can be found based on Eq. [4.5] and Eq. [4.6], respectively.

$$\sigma(t) = \frac{F(t)}{A(t)} \quad [4.5]$$

$$\varepsilon(t) = \frac{h_0 - h(t)}{h(t)} \quad [4.6]$$

Within this equation, F(t) [N] is the vertical force measured by the test equipment. This force does not include the self-weight of the sample above the failure plane. According to Wolfs [67], a correction for the self-weight hampers the comparison between different test series as the position of the failure plane occurs each time at different heights and only the self-weight of the failure plane should be included. By not implementing the latter in the stress calculation, a safe approximation of the strength is made. Similar to Wolfs et al. [64], the data is cut-off when the vertical strain equals 25%, as severe deformations and cracks were occurring after this threshold value (resulting in unrealistic values).

Uniaxial unconfined compression test in hardened state

The compressive strength f_c [N/mm^2], measured perpendicular to the printing direction, is determined by a Walter+Bai DB 250/15 testing device according to NBN EN 12390-3 [99]. The test procedure was executed under load control with an incremental rate of 100 N/s. After a hardening period of 28 days in standardized environmental conditions, at least three cylindrical samples (Ø = 25 mm, h = 20 mm), drilled from an original two-layered printed specimen (l = 300 mm) were tested per print parameter.

To obtain representative results, the top and bottom surfaces of the samples were smoothened before testing and all surfaces were found to be parallel (accuracy equals 0.05 mm). Additionally, 3 mm thick high-density fiberboard plates were put in between the bases and the hydraulic pressure system. The same procedure was followed in case of conventional cast concrete, where

cylinders (Ø = 38 mm, h = 40 mm) were drilled from molded specimens. The h/d-ratio was kept the same in order to induce a similar failure mode.

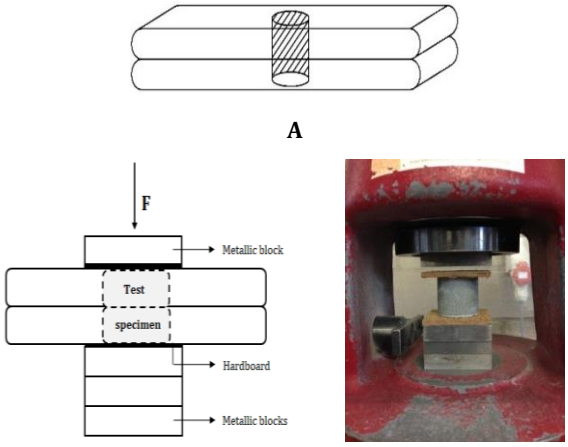

Figure 4.9: Compressive strength test setup: cylindrical test sample (A), schematic representation (B) and complete test setup (C)

4.4.6. Flexural strength

Three-point bending tests were performed on two-layered specimens, according to NEN EN 196-1 [100]. Original two-layered samples were saw-cut into specimens with a total length of 90 mm and loaded in a Walter+Bai DB 250/15 test rig with a rate of 50 N/s until failure. For this test method, two different loading directions were considered, i.e. Orientation I and II (Figure 4.1). The free span l [mm] between the supports equaled 70 mm. At failure, the load F_f [kN] was recorded and used to calculate the flexural strength f_f [N/mm^2] of the specimen.

$$f_f = \frac{3F_f \cdot l}{2b^3} \qquad [4.7]$$

Where l [mm] is the distance between the supports and b [mm] is the width of the specimen. Due to the irregular shape of the printed specimens, the latter is measured at the first and second printed layer and the mean value of both measurements is considered within the calculations. To exclude the effect of geometrical imperfections, a thin layer of plaster covered, depending on the test direction, the top or side surfaces of the printed specimen. The test setup is depicted in Figure 4.10.

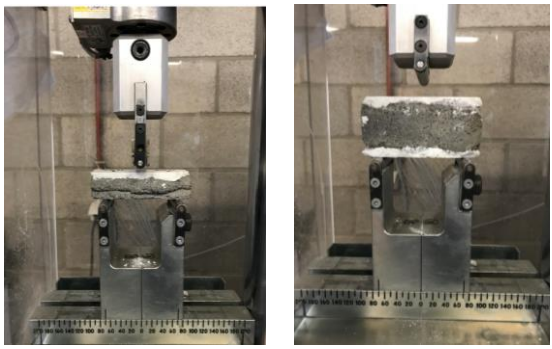

A B

Figure 4.10: Flexural test setup in Orientation I (A) and Orientation II (B)

4.4.7. Interlayer bonding strength

Cylindrical samples (Ø = 25 mm, h = 20 mm), dry-drilled from an original two-layered specimen (l = 300 mm), were sawn to a height of approximately 10 mm, with the interlayer positioned at the center. The top and bottom surfaces were covered with Sikadur 30 two-component epoxy and glued to circular steel dollies (Figure 4.11A, Ø = 25 mm, h = 20 mm). Afterwards, one of the steel mounts was anchored to a rigid table, while the other one was connected to the testing knob of a Proceq DY-2-pull-off device (Figure 4.11B). The tensile test was executed according to the specifications in NBN EN 1542 [101], under displacement control at a rate of 50 N/s. The deformation rate was monitored continuously and limited at 78 µm/s. At least 3 specimens were tested for each mix composition and only the results of clear interlayer failure were considered.

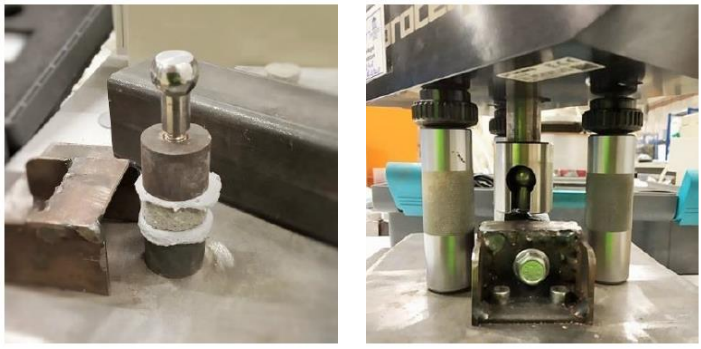

A B

Figure 4.11: Interlayer bonding strength measurements: sample preparation (A) and test equipment (B)

4.5. Surface characterization of printed specimens

4.5.1. Surface roughness

The surface roughness, measured as a function of the printing speed is represented in Table 4.1. One can conclude that the applied printing speed affects the surface roughness of the element in a significant way and more specifically, fabricating elements at a lower speed introduces a higher roughness in both directions. In case of a lower printing speed, the high roughness is most pronounced in the print direction (X-direction), while statistical analysis revealed that in case of higher printing speeds the difference in surface roughness is insignificant for both print directions.

Table 4.1: Average surface roughness R_a of elements printed with different velocities (n=3)

Printing speed	$R_{a,x}$ [mm]	Stdev [mm]	$R_{a,y}$ [mm]	Stdev [mm]
S1	0.95	0.05	0.68	0.15
S2	0.39	0.07	0.46	0.08

The higher surface roughness for lower printing speeds can be explained based on two different phenomena: shear stress and kinetic energy. In case of a cementitious material, the material can be described as a Bingham fluid. Based on Eq. [4.7], this type of fluid shows a linear relationship between the shear stress τ_{xy} and shear rate Υ there will be no flow until a critical stress level (i.e. yield stress τ_{xy}) is reached.

$$\tau_{xy} = \tau_0 + \dot{\gamma} \cdot \mu_p = \tau_0 + \frac{dv_{xy}}{dx} \cdot \mu_p \qquad [4.7]$$

With τ_{xy} [Pa] the shear stress, τ_0 [Pa] the yield stress, $\dot{\gamma}$ [m/s] the shear rate, μ_p [-] the plastic viscosity and v_{xy} [m/s] the velocity. The yield stress and plastic viscosity are characteristics, describing the material's behavior, and can be derived based on rheological measurements. For the aim of this research, the mix composition is kept the same and the author assumes that a similar yield stress and plastic viscosity are generated during printing. Based on Eq. [4.7], one can conclude that if a higher print speed is applied during extrusion, a higher shear stress will be exerted on the particles of the cementitious composition, resulting in a smoother surface.

Another phenomenon that can explain the higher surface roughness for lower printing speeds is the kinetic energy E_{kin}, which is directly proportional to the mass m [kg] of a certain particle and squared proportional to its moving velocity v [m/s]. As a consequence, higher printing speeds will increase the kinetic energy of the particles and the higher the mass of the particles, the more pronounced this effect will be. The higher energy will force the sand particles deeper into the bulk material, creating a top layer with a lower amount of sand particles, which will create a smoother surface.

This explanation is proved by thin section analysis. Purely based on a visual inspection, no clear distinction between the thin sections could be made (Figure 4.12A and Figure 4.12B). However, image analysis showed that the distribution of sand particles differs spatially for both printing speeds. Printing speed S1 shows a larger area of sand particles in the first millimeter compared to the thin section created from a sample printed with higher velocity. However, beneath 2 mm, the volume of sand particles exceeds the one obtained for a low printing speed. Based on Figure 4.13, one can conclude that within the second millimeter below the printed surface, the volume of sand increases with a ratio equal to 1.76, while in case of a low printing speed this is only 1.24. This can be explained by the formation of a so-called lubrication layer during pumping, which has a typical thickness of around 2 mm [53, 55] and where the inner bulk material contains a relatively higher amount of larger particles.

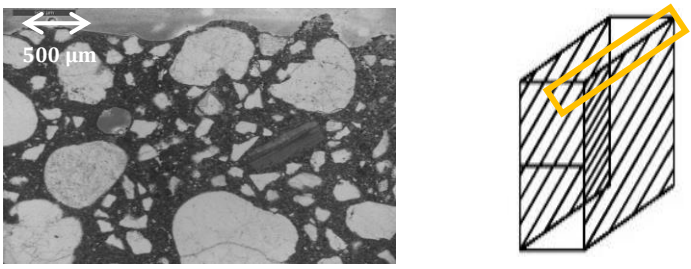

A **B**

Figure 4.12: Thin section photograph (A) and the corresponding height within a printed specimen (yellow rectangle, B)

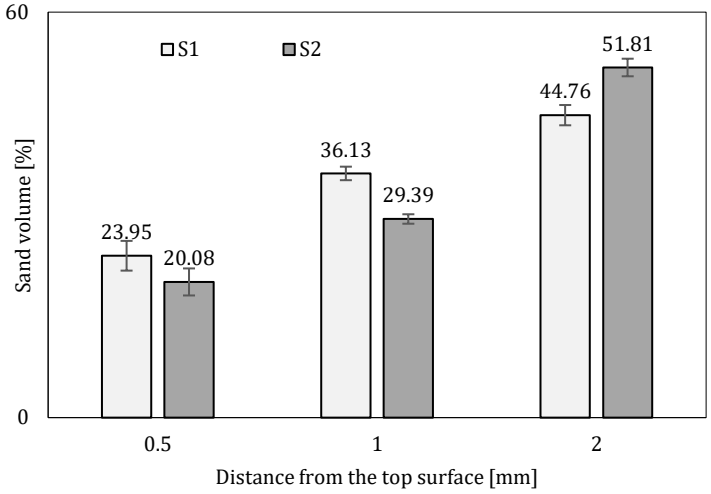

Figure 4.13: Cumulative sand volume [%] within the cement matrix in the first 2 mm of a printed sample in case of different printing speeds (n = 2, error bars represent standard deviation)

4.5.2. Surface moisture content

After extrusion, the entire surface area of the cementitious material is directly exposed to environmental conditions. This means that during the proposed delay time, surface moisture evaporates and the printed layers become drier over time (Figure 4.14). The highest evaporation of water is observed during the first ten minutes after printing ($\Delta = 0.00229$ g/cm^2). Afterwards, a statistical analysis was executed and proved that the difference in moisture content between the following time gaps is not significant anymore.

The reader has to be careful when interpreting these results. The given test method allows the author to determine the moisture content at some specific time steps. This content is the dynamic equilibrium between evaporation on the one hand, and water coming from the inside on the other hand. So, we have to be careful when stating that the difference between two measurements is due to evaporation only. However, in order to make a clear distinction between both phenomena, further investigations are required. In case of 3D printing, the reader should also keep in mind that, due to the lack of molding, water evaporates from the top surface as well as from the sides. The evaporated amount of water of a single-layer element (300 x 28 x 10 mm^3) enlarges with 1.78 if we consider only the top surface or the entire surface exposed to environmental conditions (i.e. 0.192 g water or 0.342 g water, respectively when the time interval equals 10 minutes).

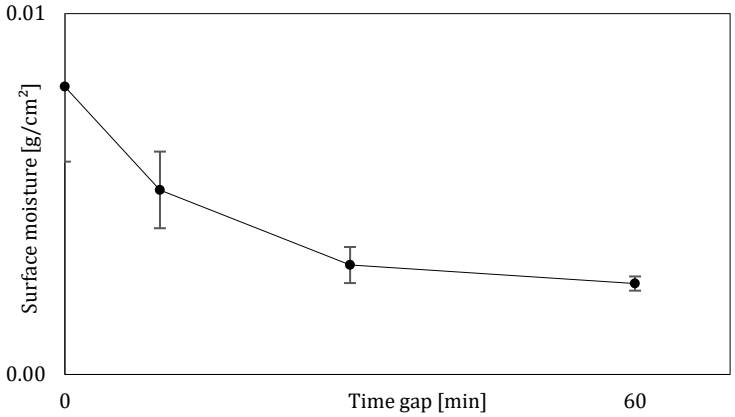

Figure 4.14: Surface moisture content of a printed element measured at different time gaps (n = 3, error bars represent standard deviation)

4.6. Mechanical properties of printed specimens

4.6.1. Compressive strength in fresh state

Table 4.2 represents the early age compressive strength of the reference material, measured at predefined time gaps after the addition of water. The compressive strength is derived based on the stress-strain relationship and equals the maximum stress at every age.

Table 4.2: Compressive strength, derived from the uniaxial unconfined compression test at predefined time steps (n=3, mean values are represented)

Concrete age	σ_u[kPa]	Stdev. [kPa]	Concrete age	σ_u[kPa]	Stdev. [kPa]
5 minutes	4.39	0.53	25 minutes	8.09	3.24
10 minutes	6.85	1.40	30 minutes	9.40	2.25
15 minutes	7.69	1.37	45 minutes	10.24	1.94
20 minutes	7.92	3.84			

Immediately after extrusion, the compressive strength of the specimens equals 4.39 kPa and increases until 10.24 kPa after 45 minutes of extrusion. This indicates that, if one considers a time gap of 10 minutes or 60 minutes, the compressive strength of the substrate layer will be almost doubled. Enlarging the time gap will induce less deformations, but, in combination with the above-mentioned lower surface moisture content, this can also cause a lower bonding between the layers. Although the compressive

strength at early age is higher than the results obtained by Wolfs et al. [64] (i.e. 2.11 kPa and 8.44 kPa, respectively), a similar trend can be observed. The higher values can be attributed to the lower W/C-ratio (0.37 instead of 0.50) applied within this doctoral thesis.

The Young's modulus is a second parameter which can be derived based from the measured stress-strain relationships and equals the slope of the initial part. The average values, accompanied by their standard deviations, are represented in Table 4.3 and shows a linear increase over time (Figure 4.15). The equation of the best fitting curve enables the author to calculate the Young's modulus at different concrete ages.

Table 4.3: Young's modulus up to 45 minutes derived from the UUCT (n=3, mean values are represented)

Concrete age	E [kPa]	Stdev. [kPa]	Concrete age	E [kPa]	Stdev. [kPa]
5 minutes	62.65	2.59	25 minutes	114.24	2.75
10 minutes	78.67	3.78	30 minutes	124.45	8.88
15 minutes	90.53	7.13	45 minutes	160.79	2.85
20 minutes	104.09	2.59			

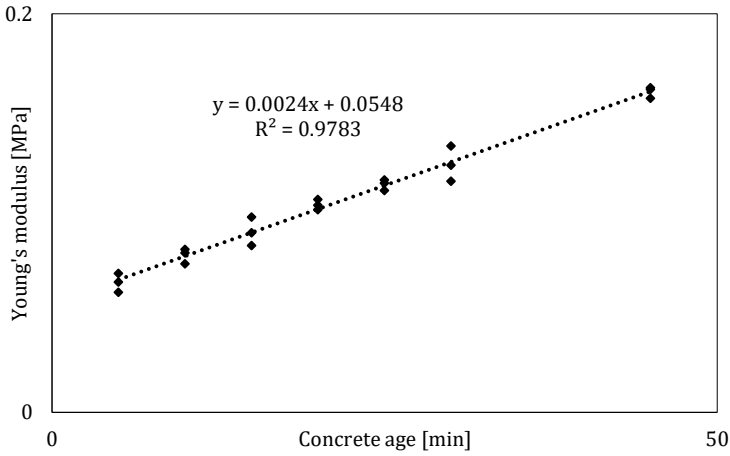

Figure 4.15: Young's modulus as a function of time. The dots represent the individual results, the dotted line represent the best fitting curve

4.6.2. Compressive strength in hardened state

Unlike for conventionally cast specimens, there are no standardized manufacturing techniques nor characterization methods available for 3D printed elements. This results in a large variety in material compositions, extrusion techniques, and specimen geometries that differ from mold-casted elements. Within this doctoral research, the test specimens have also non-standard and varying dimensions. Therefore, to ensure an accurate comparison between the results of the different test series, a correction factor C_c [-] (Eq. [4.8]) was calculated based on the specimen's geometry and according to NBN B15-220 [102]. Within this formula, A [mm^2] and h [mm] represent the specimen's surface area and height, respectively.

$$C_C = 0.65 + \frac{0,7}{\left(1 + \frac{\sqrt{A}}{200}\right) \cdot \left(\frac{h}{\sqrt{A}}\right)^{1.05}} \quad [4.8]$$

Figure 4.16 depicts the compressive strength after a hardening period of 28 days. Compared with conventional cast concrete and regardless of the applied printing speed, digital manufacturing decreases the compressive strength. The latter phenomenon becomes even more pronounced in case of higher printing speeds, with a reduction of 19.4% instead of 9.7%. Further on, an increasing time gap lowers in general the compressive strength, although the differences are not significant (i.e. a reduction of 18.5% and 6.5% after a time interval of 60 minutes for low and high printing speeds, respectively).

On the other hand, the general lower strength in case of S2 can be attributed to the higher number of pores introduced in the cement matrix (Chapter 6). The reduction in strength for an increasing interlayer time interval is in line with findings by other researchers [13, 24, 103]. However, a quantitative comparison of these studies indicates that the interlayer interval time cannot be considered as an independent value, but should be considered in relation to the material and other process parameters adopted in each study.

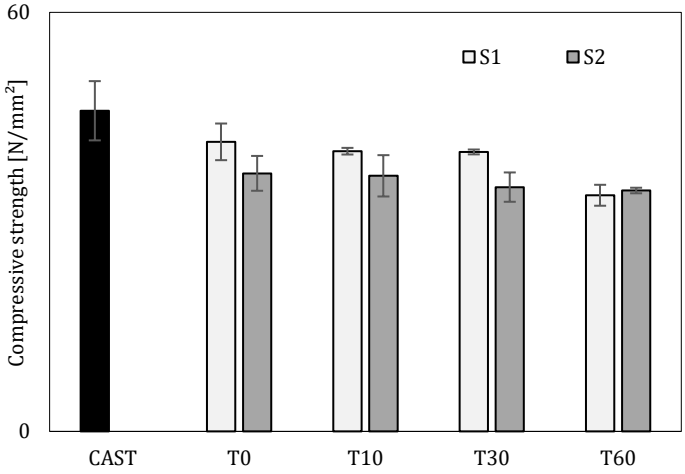

Figure 4.16: Compressive strength in hardened state (n=3, error bars represent standard deviation). The different colors refer to different printing speeds.

Based on the specimen's dimensions, different failure modes can occur (Figure 4.17A). When the ratio between the height and the diameter (h/d-ratio) is lower than one, specimens will fail by crushing while, if the h/d-ratio exceeds one, failure by cracking is the most common failure mode. As stated by Hamad [104] and in different international standards, when the h/d-ratio equals one, the usual fracture of a cylindrical specimens is a cone. The latter is proven in case of conventional cast concrete; however, it could also be observed in case of printed specimens, regardless of the printing speed and regardless of the applied interlayer time interval between the layers (Figure 4.17B).

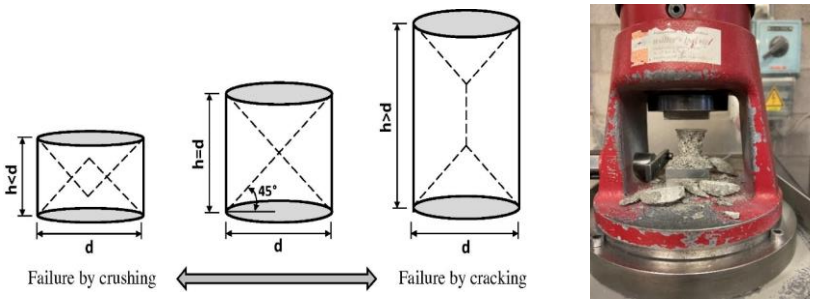

A **B**

Figure 4.17: Failure modes, depending on the specimen's geometry in case of conventional cast concrete (A) and the observed failure mode in case of printed specimens (B) regardless of the applied print parameters.

4.6.3. Interlayer bonding strength

The interlayer bonding strength for specimens printed with different time gaps is depicted in Figure 4.18 and similar to conventionally cast concrete, the tensile strength is about 10% of the compressive strength. Irrespective of the applied print velocity, a general trend can be observed; the higher the time gap in between the deposition of the layers, the lower the interlayer bond strength, which is in accordance with other research [24, 41, 89]. The highest decrease in bond strength (i.e. approximately 48% irrespective of the print velocity) is observed after 10 minutes. The latter can be attributed to the lower moisture content of the surface (Figure 4.14). The longer the time gap, the drier the substrate layer, the more air will be entrapped in the interlayer region which will weaken the interlayer. Specimens printed with a higher velocity have in addition also a lower surface roughness, which explains the lower values compared with print velocity S1. However, the differences are rather small and cannot be considered as significant.

All specimens, depicted in Figure 4.18, showed interlayer failure, or in other words, material failure very close to the interlayer. Actual failure along the interlayer would refer to separation of overlay and substrate without leaving overlay material attached to the substrate or vice versa. Substrate concrete surfaces always have a certain roughness provided by open pores and cavities (micro-roughness), and surface roughness (macro-roughness). Mechanical keys are formed between the two materials when the successive layer flows into the interface texture and fills the open pores and cavities in the substrate layer. Interface failure as such could only occur if these mechanical keys were pulled out of their anchored zone, which is virtually impossible. Therefore, failure mostly occurs inside the materials. In some test specimens, it was clearly visibly with the naked eye that a very thin layer of the second layer remained at the interface. Interlayer failure was sometimes also observed to be substrate failure very close to the interface.

Based on these observations, one can conclude that the weakest part of the bond between two successive layers is not the interlayer itself, but the material very close to the interlayer. As the moisture content of the substrate layer has a crucial influence on the moisture movement and the corresponding strength development in this interlayer region, the effect on the bond strength will be more pronounced. The effect of the surface roughness will be less pronounced, if both phenomena are considered separately. However, elements printed with a higher printing speed and larger time gap are influenced by both, which can explain the lower bonding compared to printing speed S1.

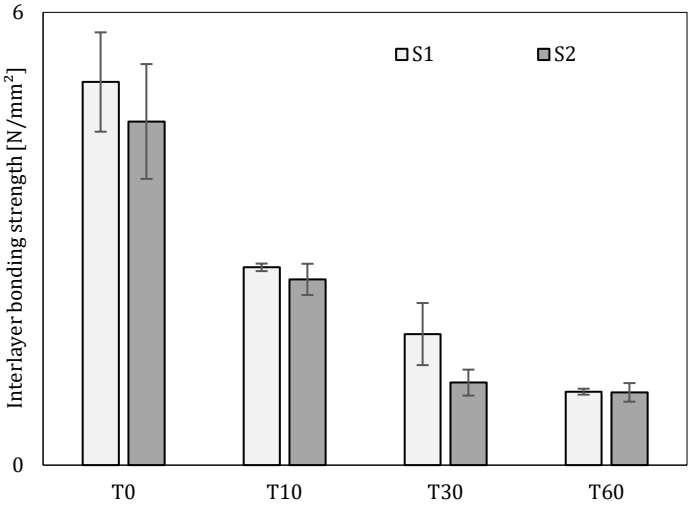

Figure 4.18: Interlayer bonding strength of 3D printed samples, printed with different velocities and time gaps (n=3, error bars represent standard deviation). The different colors refer to different printing speeds.

4.6.4. Flexural strength

The average results of the flexural strength for various interlayer time intervals, measured in Orientation I and II, are plotted in Figure 4.19 and Figure 4.20, respectively. In general, Orientation II is superior and results in flexural strengths which are 63% (S1) or 222% (S2) higher compared with conventional cast specimens. This general trend is similar with the results presented by Wolfs [24], although the strength improvement is in most cases not that pronounced. Due to the high scatter on the results, it is very hard to draw general conclusions on the flexural strength, measured in Orientation II for specimens printed with S2.

When the load is applied in the print direction (Orientation I), an average strength reduction of 45% was found compared with conventional cast specimens. This strength reduction is similar to the results presented by Le et al. [13] and Panda et al. [105], who report flexural strength differences of up to around 50%. For the layer interval times of 10 and 60 minutes, only a minor drop in flexural strength is observed, irrespective of the applied print velocity and test orientation. The impact of the interlayer time interval could not be observed in the failure mode of the specimens. All interlayer time intervals show a distinct vertical crack, positioned at the interface of two layers.

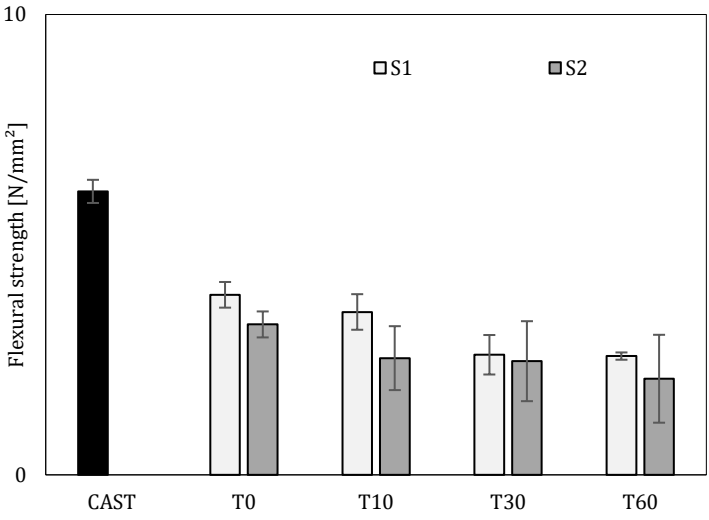

Figure 4.19: Flexural strength measured on cast or printed specimens in Orientation I (n=3, error bars represent standard deviation). The different colors refer to different printing speeds.

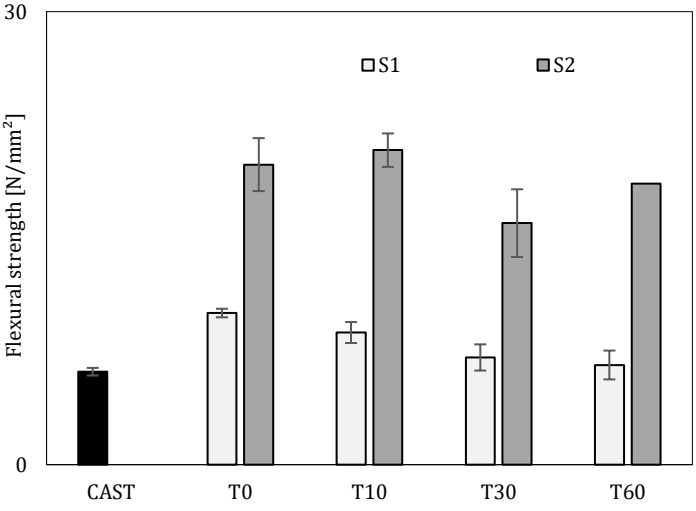

Figure 4.20: Flexural strength measured on cast or printed specimens in Orientation II (n=3, error bars represent standard deviation). The different colors refer to different printing speeds.

Figure 4.21: Failure pattern for printed specimens

4.7. Conclusions

The reduction in strength for increasing time intervals is in accordance with findings by other researchers. However, a quantitative comparison of these studies indicates that the interlayer time interval cannot be considered as an independent value, but should be considered in relation to the material and other process parameters adopted for each study. For instance, reductions up to 72% have been reported for the interlayer time interval of 60 minutes by Kim et al. [106], while the results of Panda et al. [105] indicate a 75% reduction at a time gap of 20 minutes. In comparison, the reductions found in the current study are quite modest and the studied process-material combination seems rather robust in terms of interlayer interval time sensitivity. In general, regardless of the mechanical property, it seems that the lower surface moisture content affects the mechanical performance the most, due to the higher amount of entrapped air.

To counteract the drying phenomena at the interlayer and to obtain the lowest reduction in mechanical performance, a zero-minutes time gap and a low printing speed are recommended regarding the applied 2D-print technique.

Chapter 5

Bond improvement

5.1. Interlayer bonding strength

As stated in Chapter 4, the properties of the interlayer are extremely important and affect the mechanical performance of the structural element. In order to improve the quality of this interlayer, researchers tried to find the ultimate solution in the field of repair mortars. Parameters that could affect the interlayer quality and the correlated bonding are[84, 87, 107, 108]:

- Surface preparation;
- Compressive and tensile strength of the substrate layer;
- Moisture content of the substrate layer
- Curing method or coating;
- Stress state of the interface and the presence of cracks;
- Deformation behavior of the repair mortar;
- Amount of steel reinforcement crossing the interface.

However, the situation is not completely similar for digital manufacturing as in this case, two relatively fresh materials have to bond with each other and the effect of the print process parameters themselves has to be considered. The occurrence of a chemical bonding as well as the effect of restrained shrinkage and a changing stiffness over time are phenomena that, although they are also valid for repair mortars, cannot be neglected and will be more pronounced. The theories behind the bond formation can be classified as either mechanical or chemical. Mechanical bonding relies solely on the

physical attributes of the layers, while chemical bonding refers to the hydration and the bonding of the cement particles at the interlayer. In the following sections, different surface modification techniques are listed as possible improvements of the interlayer quality in 3D printed elements.

5.1.1. Mechanical bonding

Current research on the interlayer bond of printed concrete identifies that localized voids are present in the interlayer region. These voids are a direct result of the surface roughness and the stiffness of the layers being extruded, the successive layer bonds or is anchored with the substrate layer over a reduced surface area. Marchment et al. [109] tried to increase the contact area at the interlayer by the addition of different OPC pastes between two successive layers, denominated as effective bond area amplification. Preliminary results showed that, the higher the workability of the OPC paste, the better the interlayer bonding. The addition of fibers is a second possibility to increase the surface roughness. Peled and Shah [110] detected that, when the cementitious material contains 2 mm long fibers, a large number of long fibers were lying on top of the fracture surface. The latter will increase the roughness of the surface and indicates an aggressive pullout process with high friction between the fiber and the cement matrix, suggesting a strong bond between the layers. In the extruded composite, also a layer of cementitious material is seen on the fiber surface, indicating that the de-bonding process has taken place not only at the fiber-matrix interface, but also in the matrix near the fibers

Although some research institutes focusing on 3D printing concrete use nozzles equipped with side trowels to flatten the substrate layer and to ensure a similar roughness over the entire length of the printed specimen, it is generally accepted from the field of repair mortars that a higher surface roughness will improve the interlayer bond strength. Mechanical interlocking is generally recognized as one of the governing mechanisms of adherence between old and new concrete and this principle is also adopted in 3D printing applications. Zareiyan and Khosnevis [91] for example designed, based on this principle, a topological interlock system with a simple tongue and groove shape (Figure 5.1A). This design principle holds the elements together purely by geometrical constraints without using any binder or connecter. Elements printed with interlocked parts increase the bonding strength due to an increased contact surface between the layers. Nonetheless, similar to the findings in the field of the repair mortars [111], a threshold value of the interlock depth could be observed; exceeding a certain interlock depth will not improve the bond strength any further (Figure 5.1B).

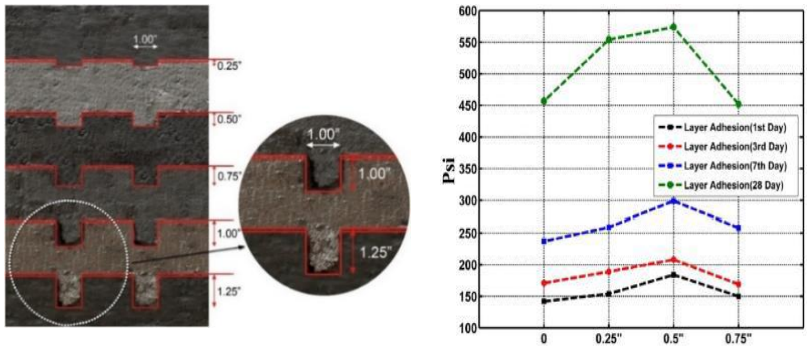

A **B**

Figure 5.1: Topological interlocking [A] and the corresponding interlayer bonding strength as a function of time (B) [91]

5.1.2. Moisture content and curing conditions

Curing prevents the evaporation of water and can improve the bonding between the layers. Storage of the specimens in laboratory moist conditions will lead to a higher interlayer adhesion compared to specimens stored outside due to the changing relative humidity. Also curing immediately after the addition of the top layer, and this for at least 3-7 days, will improve the bonding strength.

Water is one of the critical factors influencing the bond development between concretes with different ages. It may accumulate at the interlayer or migrate through it in either direction, as a result of mechanical (i.e. gravity), chemical (i.e. hydration) or physical (i.e. temperature gradients) driving forces. The moisture condition of the concrete substrate surface at the deposition time of the successive layer directly affects the transport mechanism between the materials. Lukovic and Guang [95] studied this moisture exchange by X-ray absorption. They observed that, when the substrate layer is dry, it will absorb water from the successive layer while the fresh deposited material is losing water (Figure 5.2A). On the other hand, when the repair material was cast on a saturated substrate, the repair material did not lose water as the saturated substrate layer was not able to absorb water (Figure 5.2B). In case of a saturated substrate layer, even a water gain was visible. This phenomenon could be attributed to the hygral equilibrium the material tried to gain between the hydration reaction and the water redistribution in the repair material. In addition, also different moisture transport parameters such as diffusion and permeability, will affect the formation and behavior of the interlayer zone.

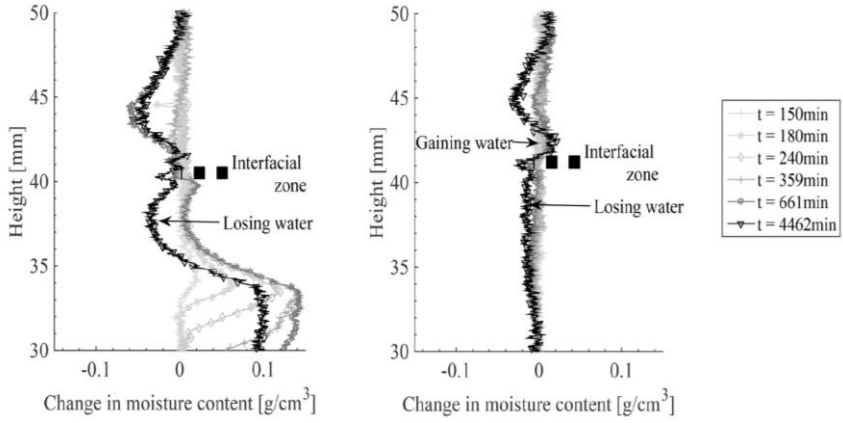

Figure 5.2: Moisture profiles in the repair systems close to the interlayer (dashed lines), quantified by X-ray absorption in case of a dry (A) or wet (B) substrate layer as a function of time [95]

The evaporation of water dries out the substrate layer after extrusion and affects the interlayer bonding in a negative way. However, the moisture content is a very specific issue and literature shows very contradictory results. On the one hand, dry, "thirsty" concrete surfaces tend to suck water from the overlay, which may result in a weak inlayer region and a lower bond strength. On the other hand, an excessive moisture content in the substrate tends to dilute the interlayer material and increased the W/C-ratio locally, resulting in a low material strength, increased shrinkage, and reduced bond strength. Water in open pores further prevents the interlocking effect, while free water at the surface may destroy the bond completely. Being considered by many as the best compromise Is the saturated surface dry (SSD) condition of the substrate layer.

5.1.3. Mix composition

In addition to the time gap, also the mix composition will affect the interlayer bonding strength. Zareiyan and Khoshnevis [112] stated that mixtures with small aggregates improve the cylindrical splitting tensile strength by approximately 80%. On the other hand, Sonebi et al. [113] found a correlation between the interlayer bond strength and the W/B-ratio, where both silica fume and fly ash were used as binders. These preliminary results showed that an increased W/B-ratio reduces the interlayer bonding and adhesion with almost 40%. Further on it was also reported that the combination of silica fume and fly ash exhibits the greatest adhesion in slant-shear tests.

5.2. Materials and methods

Within this part of the research, the reference material is used for the majority of the applied surface modifications. However, as the addition of SAPs also increases the surface moisture content, the effect of the latter on the mechanical properties is also considered. Nonetheless the observed reduction, a similar trend in mechanical performance could be observed, regardless of the applied print velocity. For that reason, only printing speed S1 is selected for this part of the doctoral thesis. The successive layers were printed with three different time intervals: 0, 10 and 30 minutes (denoted as T0, T10 and T30). Based on the mechanical properties discussed in Chapter 4, the highest strength reduction could be observed within the first 30 minutes after printing the second layer. For that reason, an interlayer time interval of 60 minutes was not included within this chapter.

5.2.1. Surface modification techniques

Physical bonding

Effective bond area amplification

To strengthen the bond between two successive layers, an OPC mixture solely composed out of water and cement, was used as bonding interface and tends to act as a 'glue' between two printed layers (Figure 5.3, denominated as GLUE). The W/C-ratio of this paste equaled 0.37, similar as for the reference composition. The mixing procedure is unchanged and described in Chapter 3. The cement paste was extruded by the same print equipment, changing nor the printing speed (S1) nor the layer height (10 mm). The cementitious material was extruded on the substrate layer 'as soon as possible'. However, due to practical issues (time required for mixing of the cement paste and cleaning of the print equipment), this was only performed after 10 minutes. The results of this modification technique will therefore be compared with the results of the reference material printed with a 10-minutes time interval.

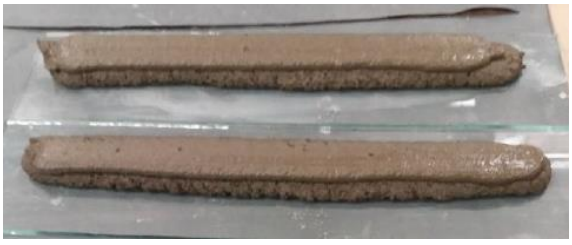

Figure 5.3: Effective bond area amplification

Sand addition

In order to improve the surface roughness, sand particles were added to the freshly deposited substrate layer. For this modification technique, the same standardized sand was employed as used in the reference composition, although in different gradations (0-1 mm, 1-2 mm and 0-2 mm, denoted as Sand 0-1, Sand 1-2 and Sand 0-2) to create variations in the roughness. As a first option to control the sand addition, the principle of an hourglass was investigated. By means of a funnel, which was attached next to the print head, a pre-defined amount of sand could be distributed on the printed specimen. To ensure a consistent flow of all sand gradations due to gravity and prevent clogging, a minimum diameter of the funnel opening was required. However, during practical application of this first option, the sand was not homogenously distributed during extrusion. Therefore, a new system with trapdoor was developed (Figure 5.4). This system allows to spread out in advance a predefined amount of sand on the trapdoor system and to distribute it as uniform as possible. The sand gradations were added immediately after the extrusion of the substrate layer.

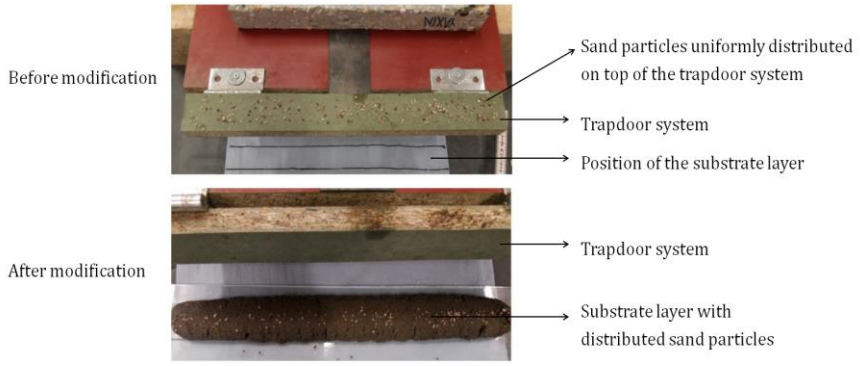

Figure 5.4: Trapdoor system to ensure a uniform distribution of the sand particles

Topological interlocking

A first option to increase the surface area between two successive layers is to change the nozzle geometry and based on literature, the elliptical nozzle was replaced by a rectangular nozzle geometry. This will decrease the amount of entrapped air and will ensure a better bonding between the layers. To limit the deviations from the original nozzle shape, the length and width of the rectangular nozzle equaled 30 mm and 20 mm, respectively.

An automatic way to introduce the principle of topological interlocking is by using a print nozzle with grooves. These grooves will automatically leave a notched pattern during printing, increasing the contact surface area between the printed layers. At the same time, side trowels were added to create a smooth surface and to optimize the material use. Within the scope of this doctoral research, two different nozzle types were used. The first nozzle (Nozzle I, Figure 5.5A) consist of only two large grooves, while the second nozzle (Nozzle II, Figure 5.5B) consists out of different smaller grooves. Both designs were based on the original height and width of the reference layers. In order to meet the extrudability requirements, it was necessary to increase the rotation speed of the auger, which resulted in a flow rate that equaled 0.039 m^3/h (instead of 0.034 m^3/h).

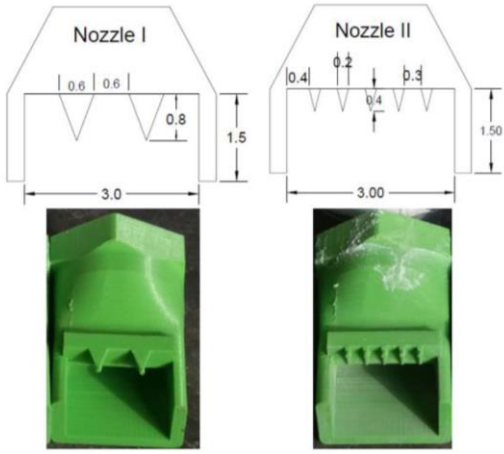

Figure 5.5: Geometry of Nozzle I (A) and Nozzle II (B), equipped with grooves and side trowels

Chemical bonding

As the addition of sand is used to improve the mechanical bonding between the layers, the addition of cement tends to create chemical bonds between the added cement particles and the water that is absorbed from the freshly deposited layer. In order to add a predefined amount of cement (i.e. 0.5, 1.0 or 1.5 g/cm^2, denominated as CEM 0.5, CEM 1.0 or CEM 1.5, respectively) in a controlled way, the same trapdoor system was used as for the addition of sand. However, due to the fineness of the particles, the uniformity of the cement addition over the substrate layer is harder to control and small cement particles sometimes stay attached to the trapdoor which could result

in a higher scatter on the results. Regardless of the applied amount, cement particles were added immediately after printing the substrate layer.

Surface moisturizing

Immediately after extrusion, the substrate layer was moisturized by spraying a predefined amount of water (i.e. 0.001 g/cm^2 or 0.002 g/cm^2, denominated in this chapter as Water I and Water II, respectively). In order to ensure similar conditions, the distance between the sprayer and the substrate layer was kept the same (15 cm). In addition, superabsorbent polymers also tend to increase the moisture content of the surface and are therefore also considered. According to Chapter 3, they will be denominated as A017, G025 and M022.

5.2.2. Characterization techniques

Surface moisture and surface roughness measurements were performed to characterize the surface and evaluate the effectiveness of the applied modification technique. The mechanical performance of the printed layers was evaluated based on the compressive strength and the interlayer bonding strength, measured by compression tests and pull-off tests. However, as the used characterization techniques are similar with the ones explained in Chapter 4, they will not be described within this chapter. Every test was executed in triplicate and the graphs depicted below represent the mean value of multiple test results.

5.3. Surface characterization of printed elements

5.3.1. Surface moisture content

Figure 5.6 depicts the surface moisture content, measured on a single-layered element, after application of different surface modification techniques. Due to the limited contact between the surface and the absorption paper, moisture measurements after the addition of sand were not included as no accurate measurements were possible for this modification technique. However, as the standardized sand does not absorb water in a high extent (water absorption equals 0.2%), the author assumes that the moisture content after sand addition follows the same trend as the reference material, irrespective of the applied sand gradation. The surface moisture content of the effective surface area modification could not be measured over time as it is located in between two successive layers.

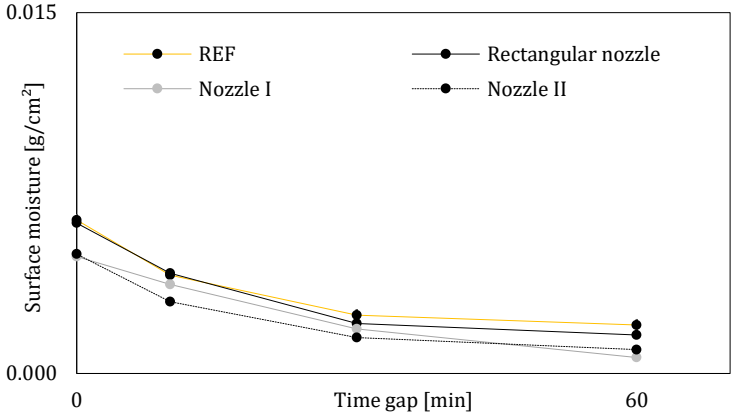
0.015
0.000
Surface moisture [g/cm²]
REF
Rectangular nozzle
Nozzle I
Nozzle II
0
Time gap [min]
60

A

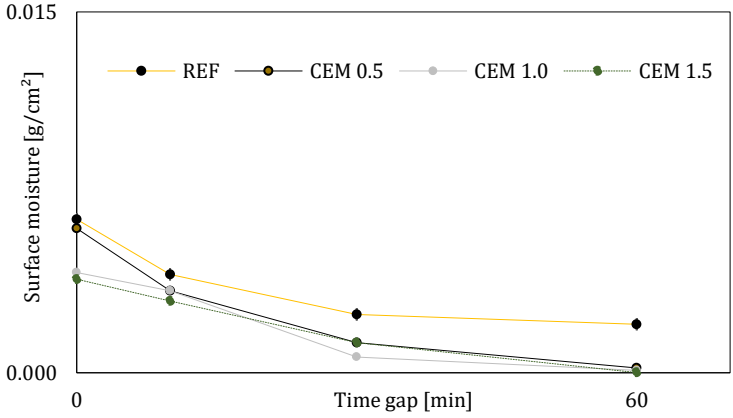
0.015
0.000
Surface moisture [g/cm²]
REF
CEM 0.5
CEM 1.0
CEM 1.5
0
Time gap [min]
60

B

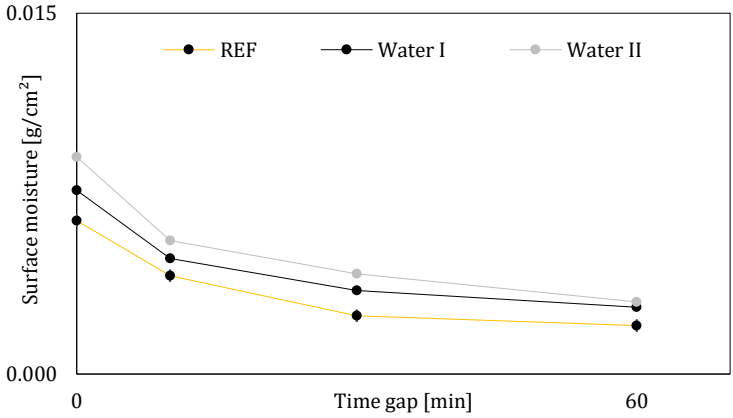
0.015
0.000
Surface moisture [g/cm²]
REF
Water I
Water II
0
Time gap [min]
60

C

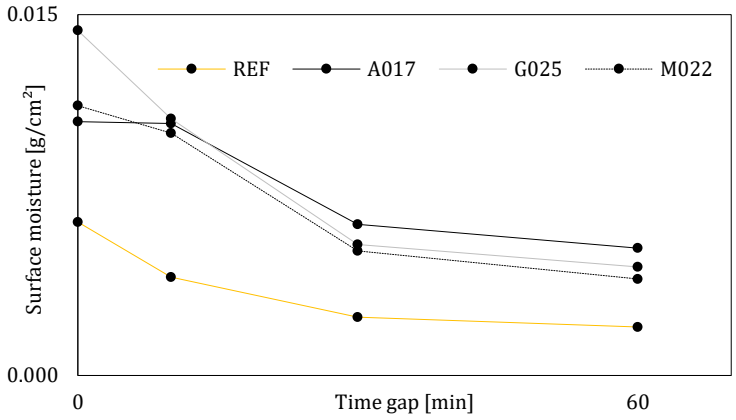

D

Figure 5.6: Surface moisture content of the different surface modification techniques, measured on a single-layer printed element (n=3)

A different nozzle geometry (i.e. rectangular instead of elliptical) does not affect the moisture content in a significant way (Figure 5.6A) and a similar trend can be observed for every time gap. On the other hand, grooved nozzles decrease the moisture content of the surface. To ensure accurate comparison among the other test series, it is important to note the moisture content of grooved nozzles is calculated based on a modified contact area. More specifically, only the surface area of the substrate layer in contact with the blotting paper is considered. Due to the higher surface area exposed to environmental conditions, the evaporated amount of water will be higher, causing a lower moisture content. However, as the differences are rather small, they cannot be considered significant. The reader should keep in mind that the application of grooved nozzles requires a higher pressure during printing to meet the printability requirements. However, as can be noticed, this will not affect the moisture content in a significant way. The latter phenomenon was also observed in Chapter 4, when the moisture content of layers printed with different printing speeds was discussed.

After the addition of cement (Figure 5.6B), the moisture content of the surface is lower than the value measured for the reference material, regardless of the time interval and the more cement is added on top of the surface, the lower the surface moisture content. When the applied cement content is higher, more material will be consumed in the hydration process at the interlayer region, resulting in a lower surface moisture content. Unlike the reference material, the moisture content still decreases significantly after 30 and

60 minutes, which could indicate that more cement is consumed during the hydration process, decreasing the moisture content even more.

The addition of water increases the surface moisture content of the surface (Figure 5.6C), in the same extent as the amount of water added on top of the surface. However, with regard to the variation in interlayer time gap, a similar trend could be observed compared with the reference material, with no significant decrease in moisture content after 30 or 60 minutes. Figure 5.6D on the other hand depicts the evolution of the moisture content for mixtures containing SAPs. It is quite clear that REF results in a lower surface moisture and generally about half of the value of the other mix designs. Again, all mixtures show a decreasing surface moisture content over time, ascribed to the chemical consumption of water and its evaporation to the environment.

5.3.2. Surface roughness

Table 5.1 represents the R_a-values of the roughness measurements, obtained in different directions and after different surface modifications. Roughness measurements were performed after a hardening period of 28 days. Again, no roughness measurements could be obtained for samples with an effective bond area amplification.

In general, one can conclude that the difference in surface roughness is more pronounced than the measured difference in moisture content. Considering the measurements along the print direction, adding sand particles enlarges the surface roughness and the highest increase could be observed after the addition of sand with particles ranging between 1 and 2 mm. Compared with other sand gradations, this result is expected as only the larger grains of the standardized sand are distributed over the substrate layer. The surface roughness of elements printed with Nozzle I or II was not evaluated along the print direction. In y-direction, it shows the highest values due to the groove dimensions.

The addition of cement on the other hand does not affect the roughness in a significant way. The addition of cement can lead to some local roughness increase due to stacking of the cement particles and the effect of the latter will become more pronounced for higher cement amounts. Compared with the reference material, one could also observe a higher standard deviation in the print direction, regardless of the amount of cement.

On the other hand, the addition of water lowers the surface roughness and this effect is more pronounced in x-direction. The higher the amount of water, the lower the surface roughness as it will smoothen the surface. The

roughness along the print direction does not differ significantly from the reference material. A similar trend can be observed for mixtures containing SAPs. Although the differences are small, the higher moisture content of SAP G does lower the roughness in the same way. At the contrary, G025 is slightly rougher which could be explained by the higher stiffness of the mix composition, as discussed in Chapter 3.

Table 5.1: Surface roughness, measured in different directions after the application of different surface modification techniques (n=3)

Surface modification	$R_{a,x}$ [mm]	Stdev [mm]	$R_{a,y}$ [mm]	Stdev [mm]
Reference	0.95	0.05	0.68	0.15
Sand 0-1	1.80	0.11	1.87	0.08
Sand 1-2	3.08	0.11	2.65	0.11
Sand 0-2	2.45	0.10	2.20	0.46
Rectangle	0.50	0.07	0.99	0.02
Nozzle I	-	-	4.47	0.35
Nozzle II	-	-	2.77	0.18
CEM 0.5	0.97	0.13	0.82	0.01
CEM 1.0	1.16	0.09	0.66	0.07
CEM 1.5	1.26	0.24	0.85	0.15
Water I	0.72	0.07	0.63	0.12
Water II	0.43	0.11	0.68	0.05
A017	0.90	0.10	0.70	0.18
G025	1.01	0.10	0.95	0.10
M022	0.87	0.13	0.6	0.08

5.4. Mechanical performance of printed elements after surface modification

5.4.1. Compressive strength

Figure 5.7 depicts the compressive strength of printed elements, measured on cylindrical samples after a hardening period of 28 days and after different surface modification techniques.

One can conclude, that the addition of a paste layer in between two successive layers is not beneficial for the compressive strength. Although the difference is not significant, the compressive strength is slightly lower. After the distribution of sand particles, the author observed only for the lowest sand gradation an improvement in compressive strength. Additionally, the latter phenomenon could only be noticed after a zero-minute time gap; a prolonged time gap causes compressive strengths lower than the reference material. However, as the standard deviation is rather high, concise conclusions are difficult to make. The compressive strength of specimens printed with T30 could not be measured as complete debonding occurred during sample preparation. The application of a rectangular nozzle improves the compressive strength, regardless of the applied interlayer time interval. The latter nozzle geometry will introduce less pores in the printed specimens and densifies the material to a higher extend during extrusion. Similar to the results of the reference material, the difference in compressive strength after various interlayer time intervals is not significant. On the other hand, the fabrication of elements with Nozzle I is not beneficial for the compressive strength, while Nozzle II improves the compressive strength for all time intervals.

The addition of cement, irrespective of the amount, has no significant influence on the results of the compressive strength. In contrary, the addition of water improves the compressive strength for enlarged time gaps. The higher amount of water seems to be beneficial for the hydration process, creating a denser structure with the bulk of the printed layers. The difference in compressive strength between mix compositions with and without SAPs is insignificant after a zero-minute time interval. However, two observations stand out: the reference material has the largest compressive strength, related to the low air content and the denser matrix. Contradictory to this result is the high compressive strength of M022, which has the largest air content. In this case, the result is explained by the fact that SAP M particles are the largest in dry and swollen state, indicating that the larger air volume

is actually divided over a smaller number of voids in the specimen. consequently, the matrix connections between the voids are thicker and stronger to withstand compression and enable some kind of dome action around the SAP particles. Also, by having a larger volume, the irregularly shaped voids create less stress concentrations. Enlarged time gaps result in higher compressive strength. This could be explained by the shrinkage behavior of this mix composition, which is discussed in Chapter 9. The second layer, printed after 10 minutes, is more restricted in its early age shrinkage and results in a denser matrix.

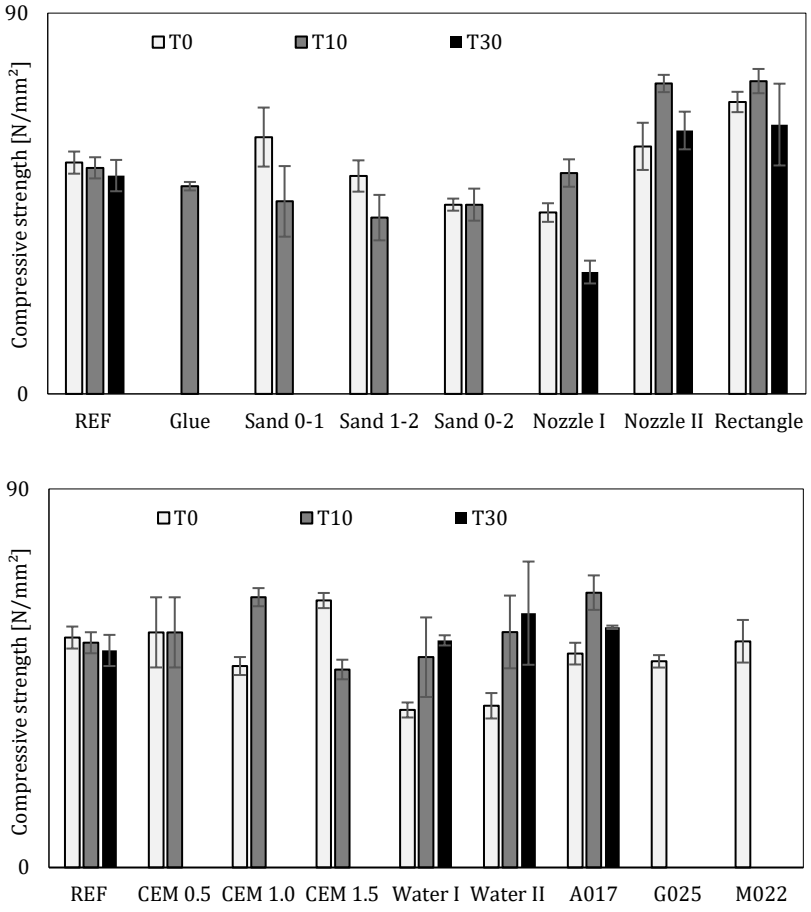

Figure 5.7: Compressive strength of the printed element, measured after a hardening period of 28 days and after surface modification, considering different interlayer time intervals (n=3, error bars represent standard deviation). For some test series, the results of T10 and T30 are missing due to debonding of the layers during sample preparation.

5.4.2. Interlayer bonding strength

Figure 5.8 depicts the interlayer bonding strength of printed elements, measured on cylindrical samples after a hardening period of 28 days and after different surface modification techniques. Similar as for the reference material, a general decrease in interlayer bonding strength can be observed with increasing time gaps, regardless of the surface modification technique.

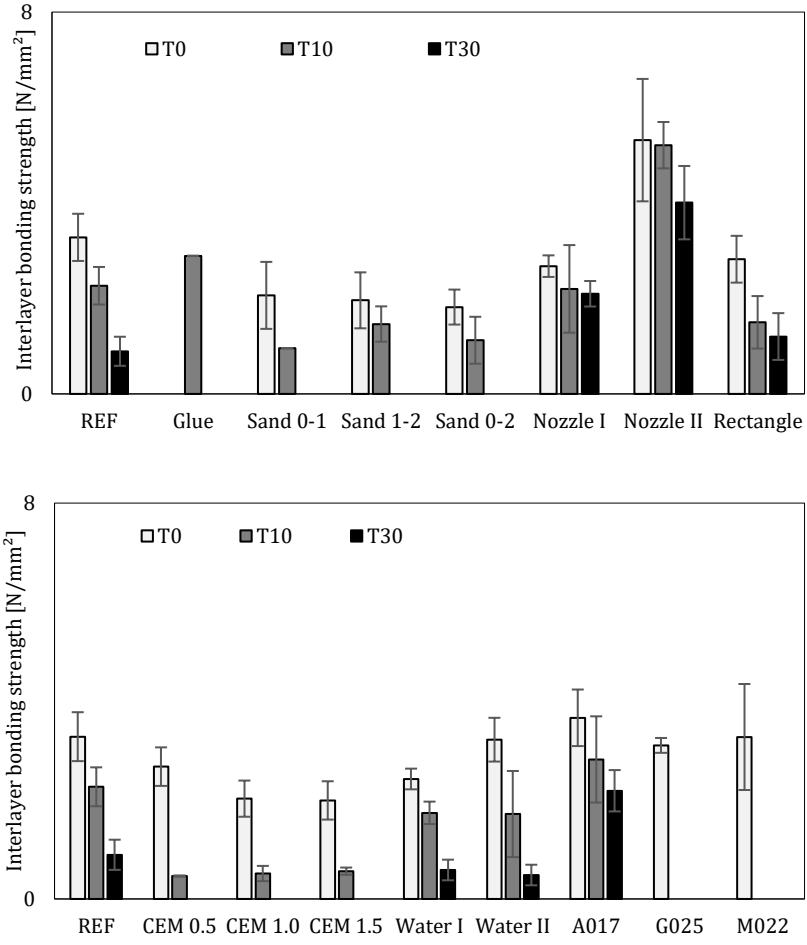

Figure 5.8: Interlayer bonding strength of the printed element, measured after a hardening period of 28 days and after surface modification, considering different interlayer time intervals (n=3, error bars represent standard deviation). For some test series, the results of T10 and T30 are missing due to debonding of the layers during sample preparation.

Similar to the findings of Marchment et al. [109], the addition of a paste layer provides an increase in interlayer strength of 27%. Although the composition of the cement paste is similar, this found value is higher than the results observed in literature. Due to the relatively high surface roughness and possible surface defects of the printed elements within this doctoral thesis, the cement paste would increase the effective bonding area to a higher extend, which could explain this deviation.

Secondly, sand gradations were added in order to increase the surface roughness of the substrate layer, which was successful based on the results shown in Table 5.1. With the addition of bigger grain sizes, a higher surface roughness was obtained. The main reason for the addition of sand was to increase the mechanical interlocking between the successive layers and therefore mainly increase the shear strength. Unfortunately, the addition of sand, irrespective of the sand gradation, affects the tensile strength in a negative way. A reduction up to 40% is noticed for each of the respective sand gradations in case of a zero-minute time gap. At T10, the reduction is more than 50% compared with the reference material. T30 results in complete debonding of the printed specimen. The surfaces of both printed layers after debonding are depicted in Figure 5.9. Although the sand particles were added on the substrate layer, all particles could be observed in the second layer, which could indicate that the bonding between the sand particles and the substrate layer will decrease with an increased time gap and lowered moisture content. On the other hand, as the material has a high viscosity, it does not have the ability to flow sufficiently around the sand particles, which will increase the porosity at the interlayer region and weaken the interlayer even more. The bigger the sand particles, the bigger the air voids introduced in the system and the more pronounced this effect will be.

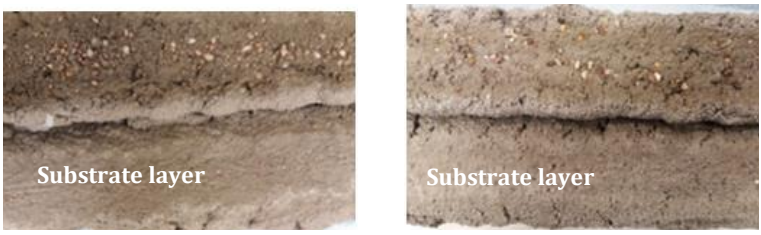

A **B**

Figure 5.9: Complete debonding at T30 after the addition of sand gradations 0-2 (A) and 0-1 (B)

Unlike the compressive strength results, the rectangular nozzle geometry does not seem beneficial for the interlayer bond strength. After a zero-minute time gap, the bonding between the layers is comparable, while an enlarged time gap tends to decrease the interlayer bonding. The latter could be attributed to the material behavior after printing. In case of a rectangular nozzle, gravity will deform the extruded layer less compared with an elliptical nozzle shape. Although this will not affect the moisture content of the surface, it will create less bonding when the second layer is printed and this effect becomes more pronounced with enlarged time gaps.

The above-mentioned findings are in contrast with the application of grooved nozzles where in general a higher interlayer bonding strength is noticed. However, as already stated by He et al. [90], an increase in interfacial roughness can also induce a higher void fraction. If the successive layer cannot penetrate in an accurate way into the roughened profile, longitudinal cavities form along the printed surface, reducing the bond strength. The occurrence of these longitudinal cavities is also depicted in Figure 5.10 for both nozzle types.

However, as the interlocked surface is higher than the induced void fraction, and the voids are distributed in a more uniform way, the interlayer bond strength is still higher compared with the reference material. In addition, both nozzle I and nozzle II facilitate vertical stacking due to their side trowels.

A **B**

Figure 5.10: Cylindrical samples, drilled from an original two-layered specimen, printed with nozzle I (A) and nozzle II (B)

The addition of cement aimed to *(i)* increase the formation of hydration products at the interlayer after the addition of a freshly deposited layer and *(ii)* decrease locally the number of voids within this interlayer region. However, out of the broken samples, it became clear that the cement particles, distributed on the substrate layer, did not receive enough water

from the superpositioned layer to improve the hydration process. Secondly, as cement addition dries out the substrate even further (Figure 5.6A), the latter tends to absorb more water from the freshly deposited layer and less water will remain available for the formation of hydration products. The more cement is added on the substrate layer, the more the surface layer dries out and the weaker the interlayer becomes, which even results in a complete debonding after an interlayer time interval of 30 minutes.

To compensate for the evaporated amount of water, the substrate layer of the printed samples is moisturized with different water volumes. The latter can be seen as an external curing condition, which is also applied thoroughly in case of conventional cast concrete. However, based on Figure 5.8, this curing method is not beneficial in terms of interlayer bonding strength as the bonding strengths do not differ from the reference material in a significant way, which could be explained as follows. Spraying water results in a higher moisture content of the substrate layer. However, if the water addition is too high, this can result in a local increase of the W/C-ratio in the interlayer region. It is generally known that a higher W/C-ratio will decrease the strength of the cementitious material and increase the porosity. The benefits of a higher moisture content will be counteracted by the lower strength due to the higher W/C-factor and an equilibrium between both phenomena will be reached, resulting in an interlayer bonding strength which is comparable with the reference material. These results are contradictory to the results obtained by Sanjayan et al. [84], who observed a higher bond strength with a higher surface moisture content. However, nor the material, nor the applied print procedure is comparable and this shows again the interdependency between the process parameters and the cementitious material.

The interlayer bond strength of mix compositions containing superabsorbent polymers tends to be inversely proportional to the amount of SAPs added. However, more in-depth investigations related to the kinetics of the polymers and their absorption behavior are required in order to prove the latter statement. Crack initiation will generally happen at the interface as air gets entrapped between superposed layers, but the propagation will cross a normally dense matrix, which as such defines the overall tensile strength. The longer the time gap, the drier and more rigid the outer surface of the substrate layer will be, obstructing entrapped air to be squeezed out of the interlayer. Longer time gaps lead to more and bigger air voids at the interface which decrease the tensile strength as the crack propagates, connecting them one by one. A more important influence is accounted to the difference in shrinkage rates between the two layers. The restriction of the sublayer to the free shrinkage of the upper layer might however lead to (micro-)cracking in

the connections between the layers and this reduces the resistance to tensile loading.

The fact that A017 loses less of its initial strength as the time gap increases, is due to the better water management, as discussed before in Chapter 3. The lack of such a capacity in the reference mixture leads to the lower values in comparison. This was also stated by Buswell et al. [11] as the temporary lifetime of cold joint in SAP mixtures: cold joints may disappear when hydration between the layers commences.

5.5. Conclusions

Based on the above-mentioned observations, the author can conclude that increasing the surface roughness by changing the nozzle geometry is the most beneficial way to improve the interlayer bonding. Although a higher surface moisture content is reported in literature as one of the most influencing characteristics, wetting the substrate layer can cause a local increase of the W/C-factor and a decrease in strength of the interlayer region. The addition of SAPs on the other hand seems beneficial for the interlayer bonding strength, irrespective of the applied time gap.

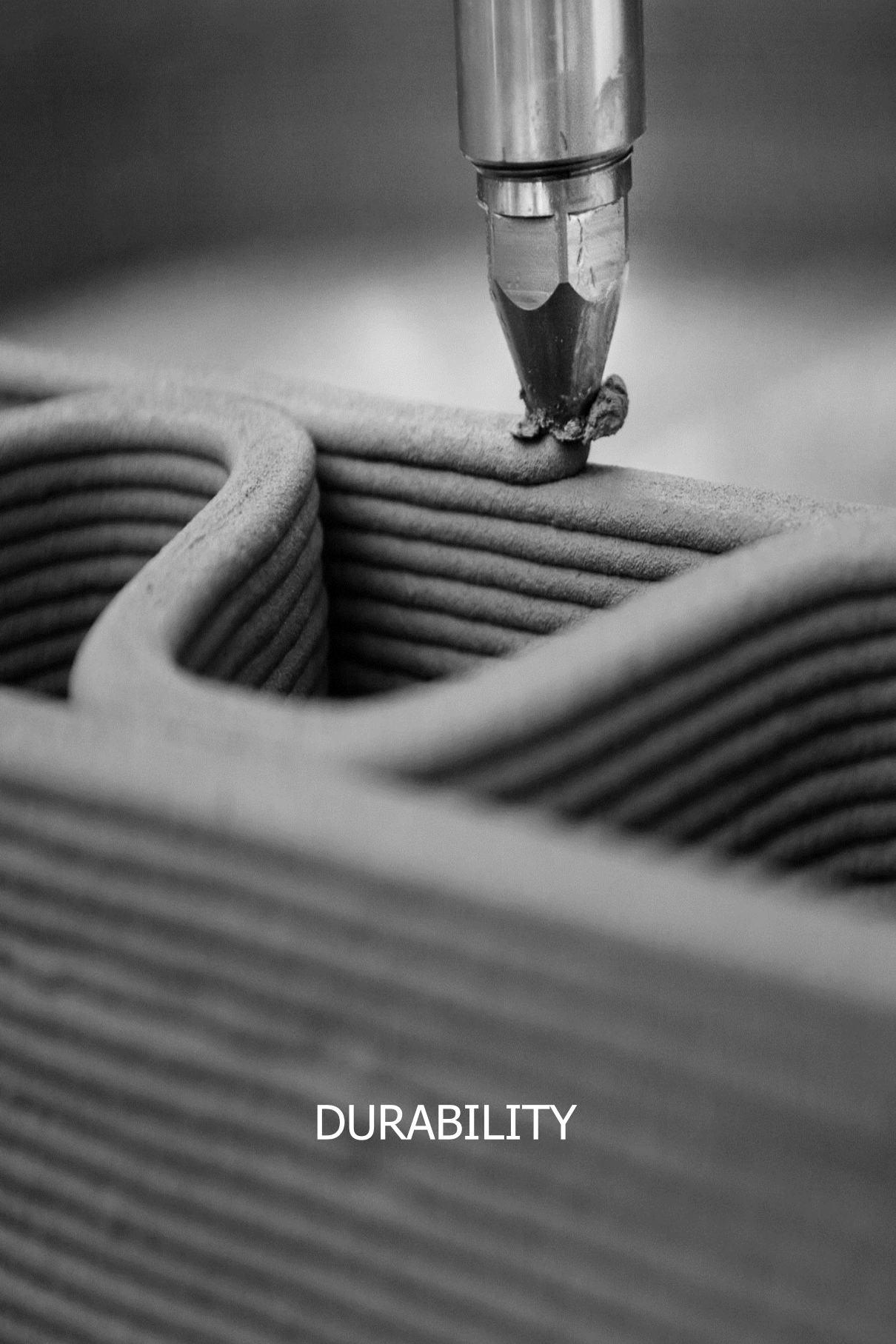
DURABILITY

Chapter 6

Microstructure

6.1 Microstructure

Although concrete is the most widely used construction material, its microstructure is heterogenous and highly complex. The relationship between the microstructure and the correlated properties is not yet fully understood, neither in conventionally cast concrete, nor in digitally fabricated concrete where both the cementitious material and the variation in process parameters will affect the microstructure.

Regardless of the manufacturing method, at macroscopic level, concrete may be considered as a two-phase material, consisting of aggregate particles dispersed in a matrix of cement paste. At microscopic level, the complexity of the microstructure is evident. It becomes obvious that the two phases of the microstructure are neither homogenously distributed with respect to each other, nor are they themselves homogenous. First of all, in some areas, the hydrated cement paste appears to be as dense as the aggregates, while in others it is highly porous. Secondly, the hydrated cement paste contains a heterogenous distribution of different types and amounts of solid phases, pores and microcracks. Third, unlike other engineering materials, the microstructure of concrete is not an intrinsic characteristic of the material as it is subjected to change with time, environmental conditions and temperature. In conventional concrete, these inhomogeneities can lead to serious effects on strength and other related parameters because these properties are controlled by the microstructural extremes and, not by the

average microstructure. This effect becomes even more pronounced in terms of digital fabrication. More inhomogeneities and microcracks are created at the interlayer between two successive layers, causing weak links within the structure and affecting the overall structural performance in a negative way, as discussed in Chapter 4. In addition, due to tearing during the production process and due to shrinkage as a result of drying, also more cracks will occur at other locations (mainly at the outside of the printed layers). In general, the formation of the microstructure (i.e. the hydration process) starts from the moment water is added to the binder material, creating a denser and more stable network as hydration further proceeds. This densification will not only change the amount of hydration products, it will also change the pore characteristics such as total pore volume, pore distribution, tortuosity, connections between the pores, etc. constantly over time. As reported by Mehta and Monteiro [114], the pores can be classified into gel pores, capillary pores and air voids, all with different dimensions, formed during various hydration stages and affecting different properties of the material both in fresh and hardened state [115].

- Gel pores: are part of the CSH structure, with dimensions ranging from 0 till 2.5 nm. Although the dimensions of these pores are too small to affect the strength or permeability of the hardened cement paste, the water inside these pores (gel water) can affect the long-term performance of the material such as shrinkage and creep of the material.

- Capillary pores: are formed as a result of the hydration process, in which the hydration products take up less space compared with the water and the cement from which they originated. The volume and dimensions of these pores, which are irregularly shaped, depend on the cement amount, the W/C-ratio and the degree of hydration. Depending on the particular pore size, they will affect various material properties, as listed in Table 6.1.

Table 6.1: Capillary pore classification and influencing parameters

Pores	Diameter	Description	Influencing parameters
Gelpores Capillary pores	2.5 – 10 nm	Small	Shrinkage between 50% and 80% RH
Capillary pores	10 – 50 nm	Medium	Strength and permeability
	0.05 – 10 µm	Big	Strength and permeability and shrinkage in case of a higher RH

The capillary pore distribution depends on the water distribution over the entire specimen, which can be assumed as homogenous in case of molded elements causing a similar hydration degree throughout the entire element. However, in case of 3D printed materials, water distribution cannot be considered as homogenous. The lack of molding causes a lower surface moisture content at the side surfaces and, in case of prolonged time gaps, at the interlayer of the printed specimen. The latter results in various hydration degrees within the sample due to a changing water amount. This will not only affect the microstructure, but in addition also the formation of hydration products.

- Air voids: depend on the fabrication process and can be embedded due to a lack of compaction or inserted by for example air entraining agents. Whereas capillary voids are irregular in shape, air voids are generally spherical. Entrapped air voids may be as large as 3 mm; entrained air voids usually range from 50 to 200 μm.

Throughout the rest of this doctoral thesis, the pores are labeled according to the IUPAC (International Union of Pure and Applied Chemist) classification: micropores ($d < 2$ nm), mesopores (2 nm $< d < 50$ nm) and macropores ($d > 50$ nm). It is important to note that this classification is purely based on pore dimensions, nor on chemical or physical properties.

Under electron microscopic examination, voids in the hydrated cement paste appear to be empty. This is because the specimen's preparation technique calls for vacuum drying of the specimen. Actually, depending on the environmental humidity and the porosity of the paste, the untreated cement paste is capable of holding a large amount of water, which can exist in the hydrated cement paste in many forms depending on the degree of ease with which water can be removed [114]:

- Capillary water: water present in the voids larger than 50 nm. This water can be pictured as the bulk water that is free from the influence of the attractive forces exerted by the solid surface. It is desirable to divide the capillary water into two categories: the water in large voids (> 50 nm), which may be called free water because its removal does not cause any volume change, and the water held by capillary tension in small capillaries (5 – 50 nm), the removal of which may cause shrinkage of the system.

- Adsorbed water: water that is close to the solid surface. The loss of adsorbed water is responsible for shrinkage of the hydrated cement paste.

- Interlayer water: Water associated with the CSH structure. The interlayer water is lost only after strong drying.

- Chemically combined water: water that is an integral part of the microstructure. This water is not lost due to drying; it evolves when the hydrates decompose during heating.

6.2 Parameters affecting the microstructure

6.2.1. Mix composition

The mix composition affects the hydration process and the correlated microstructure in a significant way. For example, a higher W/C-ratio alters both the amount and size of the capillary pores, while the addition of supplementary cementitious materials such as fly ash or silica fume can cause a densification of the microstructure. However, as this is not the scope of this research, the latter will not be further discussed.

Cementitious mixtures containing superabsorbent polymers (SAPs) will undergo microstructural changes related to the size and amount of the SAPs, the W/C-ratio (original and effective) and the way of addition (i.e. saturated or dry). Due to their internal curing effect, hydration is stimulated locally [116]. A study has shown that, especially at later ages (> 2 weeks), the hydration degree of specimens with SAPs was higher than that of the reference material [117]. Furthermore, SAPs tend to reduce the microporosity due to a prolonged hydration and mitigation of autogenous cracking, resulting in a decreased permeability. The meso- and macroporosity on the other hand are larger since SAPs are in essence water reservoirs, acting as soft aggregates or voids when they are filled or empty, respectively [74].

6.2.2. Print parameters

As a result of the extrusion process, the porosity in 3D printed specimens is not homogenously distributed. The void fractions, pore morphology, interconnectivity and distribution may vary, both within the layer and in-between the layers, which is expected to affect the material properties in a significant way.

First of all, the interlayer time interval will not only affect the mechanical properties (Chapter 4), but will also induce microstructural changes. SEM analysis, focusing on the interlayer of 3D printed specimens, revealed large elliptical or longitudinal-type cavities. The formation of these voids can be ascribed to air "enclosures" that occur when the upper layer is deposited on the substrate with significant surface unevenness. These longitudinal cavities were observed by Nerella et al. [41], even after 1 day of hydration). After a hardening period of 28 days, these cavities were often filled with hydration products (calcite, ettringite and/or portlandite). However, the higher plastic/drying shrinkage rate in case of digital manufacturing causes a delayed growth of these hydration products, making them incapable to fill the voids completely. Additionally, depending on the time interval between the layers, also a change in pore morphology could also observed. Time gaps of 2 minutes caused spherical voids, where enlarged time gaps created more elongated cavities (Figure 6.1).

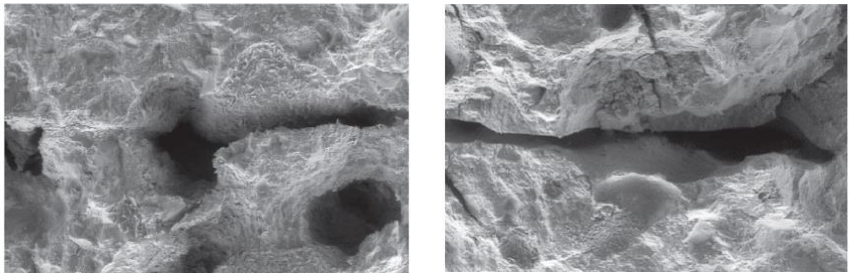

A **B**

Figure 6.1: Pore morphology at the interlayer between layers printed with a 2-minute (A) and 10-minutes interlayer time interval [41]

The changing pore morphology was also confirmed in recent research performed by Kruger [21]. He observed, based on μCT visualization, a shift from spherical voids in case of conventional cast concrete towards more elongated pores when the specimens were printed. The latter phenomenon could be attributed to tearing executed during the print process. Considering the total porosity, a higher value was observed for printed specimens compared to molded ones. In addition to the time gap, also the nozzle standoff distance (i.e. distance between the nozzle and the printed layer) affects the microstructure. Reducing the deposition height, without altering concrete discharge rate and/or printhead velocity, should lead to a better ''compaction" of the deposited material against the substrate, resulting in enhanced interface properties.

6.3 Materials and methods

6.3.1. Microscopy

The sizes of the dry and swollen SAPs as well as the pores in longitudinal sections of hardened double-layered specimens (Figure 6.2) were visually inspected and photographed by means of a Leica DFC295 digital microscope. The acquired images where then analyzed making use of the software ImageJ. A multitude of similar pores, ranging from 9 to 90 depending on the test case, was measured in two perpendicular directions. The average of these measurements in both directions was considered as the diameter of the equivalent spherical object.

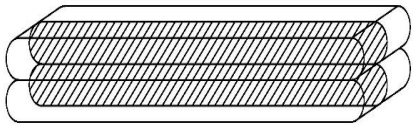

Figure 6.2: Longitudinal section of a double-layered printed element

6.3.2. Air voids analysis

Air void measurements were performed for mix compositions including superabsorbent polymers (REF, A017, G025 and M022 as denominated in Chapter 3). The influence of different printing speeds and interlayer time intervals on macropores and their distribution along the entire specimen was quantified and visualized by means of µCT-scanning. This method allows a more accurate distinction between the different zones of a printed specimen and allows the author to draw specific conclusions about the behavior at the interlayer.

After a hardening period of 28 days, printed samples (l = 110 mm) were sawn at half of the height in longitudinal direction (Figure 6.2), followed by a polishing procedure with variable grading (320 grit, 500 grit, 1200 grit, 2400 grit, 3 µm, 1 µm and ¼ µm). After polishing and prior to the use of black ink, samples were dried for one hour at 35°C in order to remove water/lubricant, oil and isopropanol. Thereafter, the sample surfaces were treated with black ink and barium sulphate ($BaSO_4$) powder to enhance the contrast between the air voids and the cementitious matrix.

The air content of four longitudinal sections were analyzed according to the linear traverse method ascribed in NBN EN 480-11 by means of a fully automated Concrete Experts International Rapid Air 457 device. The range of

void sizes which could be analyzed with the latter method is limited between 8 µm and 10 mm. Smaller pores can be studied by means of mercury intrusion porosimetry, as discussed in the next paragraph. During the analysis, the camera moves stepwise, taking overlapping pictures of about 1 cm^2 of surface at the time. The outermost 10 pixels were not considered in order to reproduce a complete and relevant surface image in two dimensions. The thresholding level [-] equaled 200. Within the pictures, 7 parallel lines (called chords) were drawn in the direction of the measurement. A total chord length of at least 2500 mm was applied, exceeding the minimal length of 2413 mm recommended by NBN EN 480-11 for aggregates smaller than 25 mm, which is valid for all mix compositions [118].

The most important characteristics obtained from the air void analysis include:

- Histograms and (cumulative) distributions;
- Total length of chord segments intersecting voids T_a [m];
- Total chord length T_{tot} [m];
- The air content A [%], calculated as the ratio between T_a and T_{tot}.

6.3.3. Mercury intrusion porosimetry

Capillary pores, ranging from 10 nm to 10 µm, were studied with mercury intrusion porosimetry (MIP) measurements (Pascal 140 and 440 series, Thermo Fisher Scientific Inc.). MIP measurements were executed for mix compositions with and without the addition of SAPs (i.e. REF, A017, G025 and M022 as denominated in Chapter 3). Both printing speeds (S1 and S2) and time gaps (T0, T10, T30 and T60) were selected for the reference composition and a comparison with conventional cast concrete was made. Mixtures containing superabsorbent polymers were printed with the lowest print velocity (S1) and a zero-minute time gap (T0). To minimize microstructural damage during pre-conditioning, samples were freeze-dried for one week at the age of 28 days. During MIP measurements, mercury is forced into a printed specimen of approximately 1.5 g ($\pm$15 mm^3) with a random shape. These small specimens are obtained by sawing a drilled cylindrical specimen (Ø = 14 mm, h = 20 mm) into smaller pieces. These pieces are obtained from the upper, center and lower part of a drilled specimen (denoted as Top, Inter and Bottom, respectively) to characterize the effect of the applied time gap on the capillary pores. During the experiments, the maximum pressure was limited to 200 MPa to avoid crack formation. For each test series, only one specimen was analyzed.

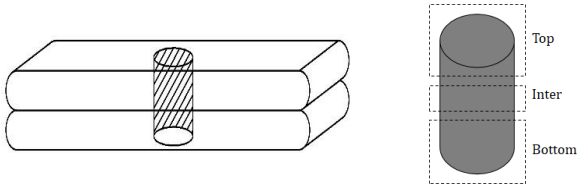

Figure 6.3: Cylindrical test samples (A) and representation of the different zones (B) analyzed of a printed sample during MIP analysis

MIP measurements performed at the center part of a drilled specimen serve as a first estimation of the porosity and the pore size distribution in that region, as these samples also contain bulk material of the upper and bottom layer, although in a smaller extent. The porosity at the interlayer itself will be visualized in a more accurate way by µCT-scanning (section 6.4.4.). However, as the center part samples were carefully extracted, it allows the author to draw relevant conclusion with respect to the different time gaps.

As a specific pressure corresponds to an aperture of a pore, and the amount of mercury intrusion approximates to the pore volume, the amount and pore size could be determined. MIP measurements do not directly quantify the amount of macro pores, but the latter show up in the total porosity of the measured sample. However, as illustrated in Figure 6.4, some pore types do not participate in the intrusion of the mercury. Only continuous pore types do, and even ink bottle pores account for a measurement of only the smallest opening diameters, as they require a larger pressure on the mercury (which gradually increases during the test). The presence of dead-end and isolated pores can lead to an underestimation of the total void volume. Purely based on MIP measurements, they are hard to quantify. On the other hand, the difference between the intrusion and extrusion of mercury can give an idea about the ink-bottle pores.

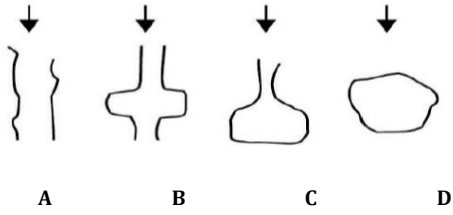

Figure 6.4: Schematic representation of different pore types: continuous pore (A), continuous ink bottle pore (B), dead-end ink bottle pore (C) and isolated pore (D) [118]

6.3.4. BSE-SEM analysis

The pore size distribution can be determined by measuring the pores in a random plane section of a specimen. Although the size distribution in 2D is not the same as in 3D, it is generally accepted that this distribution is similar and comparable. For this analysis, small cylinders (Ø = 25 mm, h = 20 mm), drilled out of an original double-layered printed specimen were sawn in longitudinal direction. In order to see the influence of a prolonged time gap on the hydration products in the vicinity of the interlayer, only specimens composed of the reference material and printed at the lowest velocity (S1) with different time gaps (T0, T10, T30 and T60) were considered. At the age of 28 days, these cylinders were freeze-dried for 7 days to stop the hydration process and to ensure a relevant comparison between the different elements.

After freeze-drying, specimens were prepared for BSE-SEM analysis based on a method proposed by Snellings et al. [119]. As a first step, samples were impregnated with a low-viscosity epoxy resin (100 g Conpox Harpiks BY 158 and 28 g of Hærder HY 2996) under vacuum and subsequently cured for 24 hours at 35 $\pm$ 1°C. The specimens were ground on a rotating wheel using a SiC abrasive paper (No. 320-grit) and water, followed by polishing with SiC abrasive paper (No. 2400-grit) and DP-lubricant brown (Struers). Subsequently, the specimens were polished with diamond paste (3 µm, 1 µm and 0.25 µm) and methanol. At the end, specimens were cleaned with a soft cloth to remove all impurities.

Prior to electron microscopy analysis, samples were coated with a thin carbon layer (approximately 20 nm). Scanning Electron Microscopy (SEM) analysis was performed on a JEOL JSM-5600 instrument, equipped with a BSE detector operating at an acceleration voltage of 20 kV. The BSE mode is an excellent way to visualize the capillary pores as they appear as dark areas when the BSE detector is used in the compositional contrast mode (Figure 6.5A). The applied magnification equaled x300. After sample preparation, different lines were selected on the specimen for the subsequent analysis (Figure 6.5C), one horizontal line at the top part (line 1), one horizontal line at the bottom part (line 2), and three vertical lines covering the entire interlayer zone, which the author assumed to have a total width of 5 mm (line 3-5). On both horizontal lines, 20 images were taken. The mean value of these figures corresponds with the hydration phases of both specimen's part. On the vertical lines, a total of 10 images were analyzed every half millimeter and the mean value of three measurements covered the phased at a specific position.

The calculation of the hydration products was based on grey level histograms obtained with ImageJ. The different phases were determined as the grey level is dependent on the atomic number of the phase. All images were taken with the same brightness and contrast and based on the obtained grey levels (black 0 – 255 white) , three regions could be clearly distinguished [120]: pores from 0 – 80, CSH (Calcium Silicate Hydrate) and CH (Calcium Hydroxide) products from 101-175 and UH (UnHydrated cement) from 176-255. The boundaries were determined as the distinct changes in the grey-level histogram (Figure 6.5B).

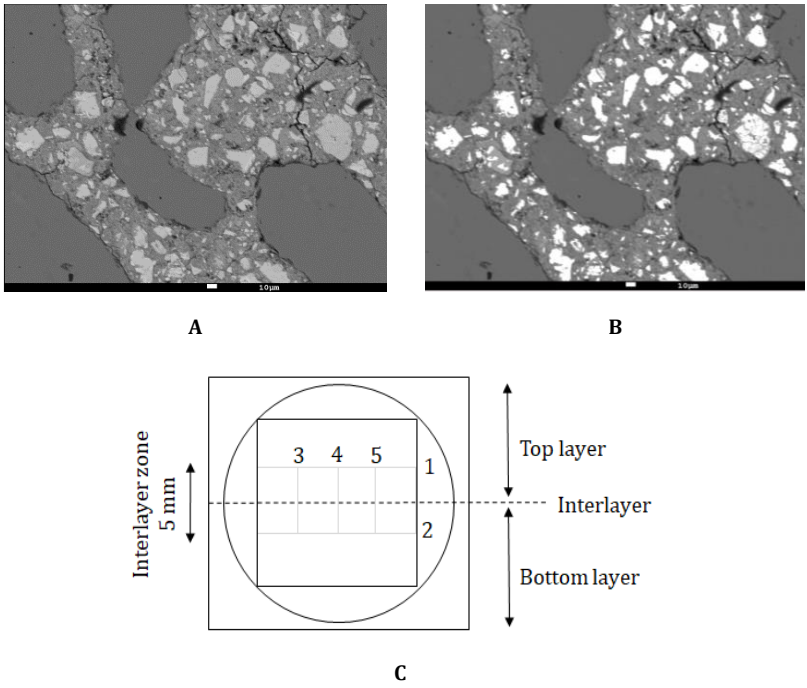

Figure 6.5: Original BSE-SEM image (A), BSE image with selected UnHydrated cement (indicated in white, B) and a schematic representation of a sample used for SEM-BSE measurements and analysis (C). The black and grey lines indicate the sample border and the lines along which measurements were performed, respectively.

6.3.5. µCT-scanning

To visualize the pore distribution through the sample in a three-dimensional way, X-ray micro-computed tomography (µCT) was performed at the Ghent University Centre for Tomography (UGCT) using HECTOR [121], which comprises a micro-focus directional target X-ray source (X-ray WorX XWT 240-SE), a large flat-panel detector (40 x 40 cm^2; PerkinElmer 1620 CN3 CS). An aluminum filter of 1 mm was placed in front of the X-ray source to reduce beam hardening artefacts.

Cylindrical samples (Ø = 14 mm; h = 20 mm), considering both print velocities (S1 and S2) and time gaps (T0, T10, T30 and T60), were drilled out of an original double-layered printed specimen and freeze-dried at the age of 28 days. During image acquisition, HECTOR operated with a tube voltage of 200 keV and a tube power of 10 W. The resulting magnification and the voxel size equaled 24.64 and 8 µm, respectively, and 2401 projections were taken per scan. The cast sample was shaped differently (i.e. squared instead of cylindrical with side lengths of 30 mm), and therefore, an alternation of the applied scan parameters was required. For this sample, the power was increased until 11 W, the amount of projections until 2601 per scan and the magnification and voxel size until 17.92 and 11 µm. To image the total sample volume with the highest possible spatial resolution, the top half and bottom half of each sample were imaged separately.

Reconstruction of the raw CT data was done using Octopus Reconstruction software. Afterwards, Aquila software (Tescan XRE) was used to merge the sets of two reconstructed volumes per sample into one. Image analysis to determine the porosity and pore sizes was done using Avizo software (ThermoFisher Scientific).

6.4 Quantification of the mirco-, meso- and macro-porosity related to the print process parameters

6.4.1. Micro- and mesoporosity

In terms of mechanical behavior, samples printed with a zero-minute time gap showed the lowest influence of the printing process and could be assumed as more or less homogenous. However, when comparing the pore size distribution of molded samples and printed samples with a zero-minute time gap (Figure 6.6), one could observe more and bigger sized capillary pores for 3D printed samples, regardless of the considered zone.

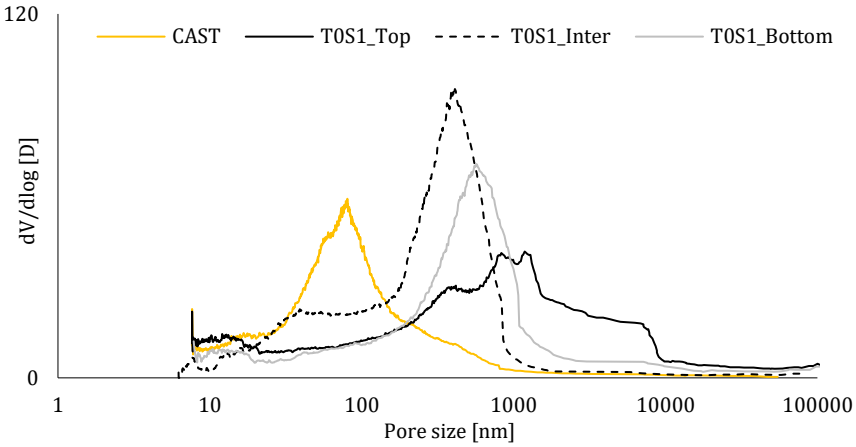

Figure 6.6: Comparison of the pore size distribution between molded and printed specimens (n=1)

Figure 6.7 compares the pore size distributions of samples fabricated with both print velocities (S1 and S2) and a zero-minute time gap. In general, a higher printing speed causes smaller pores as the pressure, executed on the cementitious material during extrusion is higher, resulting in a higher degree of compaction. At the bottom part of the specimens, the capillary pore volume (i.e. the area below the derivative intrusion curve) is slightly smaller for S2 compared to S1, which can be explained based on two phenomena. First of all, regardless of the print velocity, the substrate layer will be compacted after printing the second layer. Especially in case of zero-minute time gap, where the internal structure of the material is still under development when the second layer is extruded. Secondly, the higher kinetic energy working on the sand particles, causes in case of S2 a more densified bulk material. As these MIP measurements are performed on drilled cylinders, obtained from the bulk material, evaporation or shrinkage from the sides cannot have a significant effect. The critical diameter (i.e. the peak value of the derivative intrusion curve) of the capillary pores at the top part becomes smaller, which can be observed by a minor shift to the left in case of S2. Compared with the bottom part, the pore volume and the critical pore diameter are lower at the top part, confirming the higher evaporation rate and the correlated shrinkage (cracking) in this part of the printed element. However, at the interlayer both the pore size and pore volume are comparable, indicating a similar moisture exchange phenomenon between the layers. The latter can be attributed to the same age, hydration degree and moisture content of the top and bottom layer, irrespective of the printing speed.

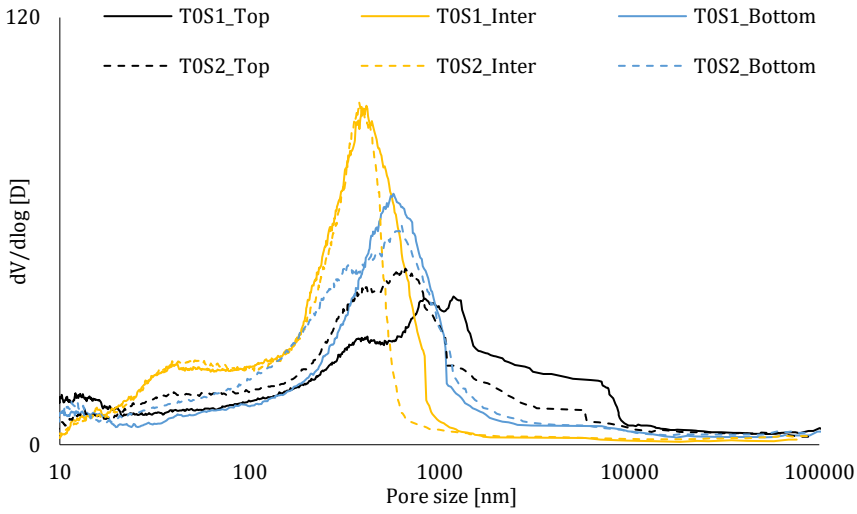

Figure 6.7: Pore size distribution of REF samples, fabricated with a zero-minute time gap and different print speeds (S1 and S2) (n=1)

Regardless of the printing speed, similar trends can be observed. Therefore, only the particle size distributions of one printing speed are considered when discussing the influence of a prolonged time gap on the pore size distributions.

Figure 6.8A – Figure 6.8C compare the pore sizes, measured at different zones throughout the specimen, considering different interlayer time intervals. In general, a prolongation of the time gap causes a volume increase of smaller pores at the center and bottom region of the specimen. The latter phenomenon can be attributed to the moisture exchange between the layers. When the time between the deposition of two layers increases, the substrate layer becomes drier over time and it consequently absorbs more water from the freshly deposited layer. This water absorption reduces the hydration degree of the top layer in the vicinity of the interlayer, while, in the interface region, more water is available to proceed the hydration. This confirms the results stated by [95], measured in case of repair mortars. At the bottom part of the specimen (Figure 6.8C) the capillary porosity is lower. After 0 and 10 minutes of deposition, the substrate layer is more prone to deformations and will be more compressed by the addition of a second layer. This in contrast with a 30- or 60-minute time gap, where the material developed already more strength and is less affected by printing a second layer. The pore size distribution at the top part is comparable for all the interlayer time intervals.

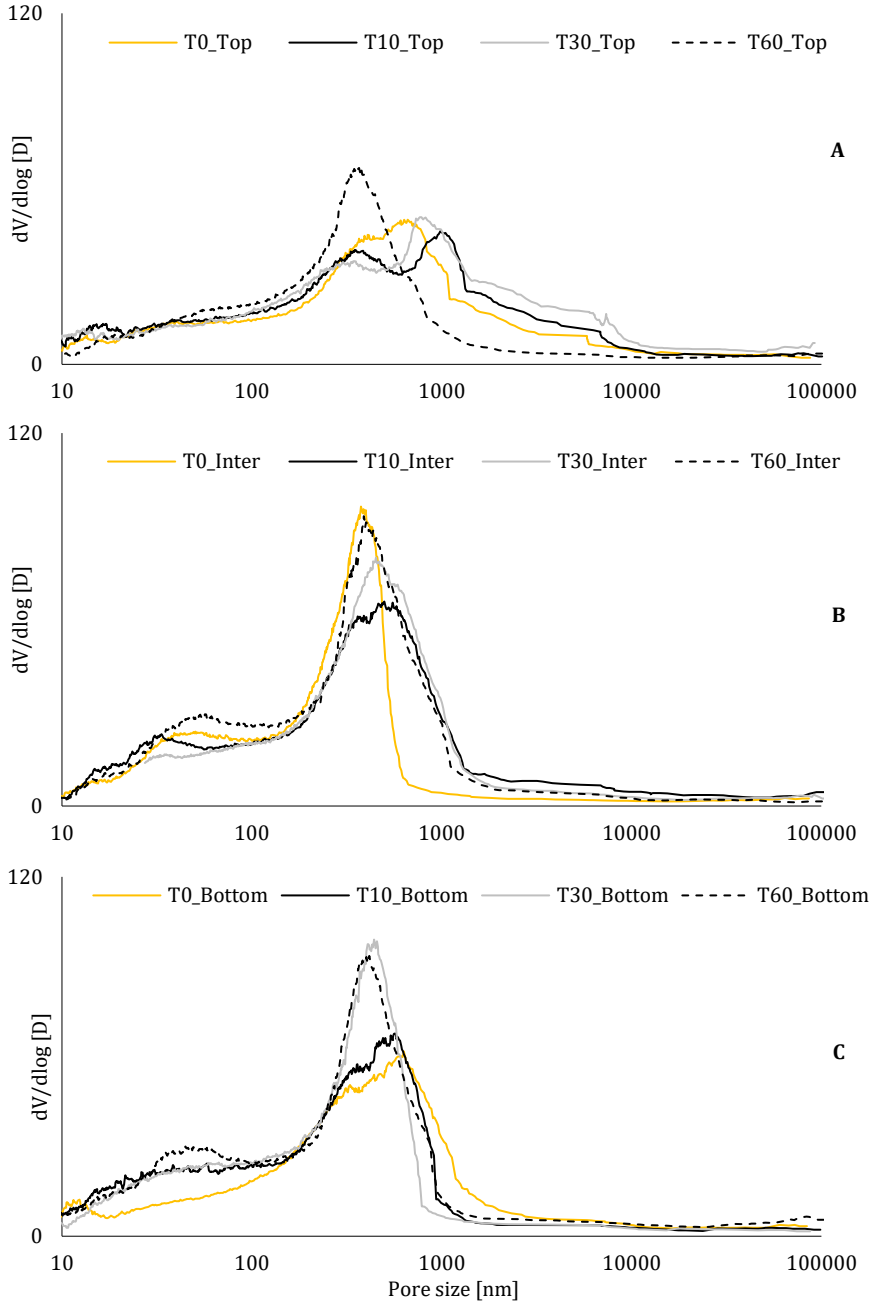

Figure 6.8: Derivative intrusion curves for top (A), inter (B) and bottom (C) zones obtained for printed REF specimens fabricated with different interlayer interval times (n=1)

It is important to note that the results, depicted in Figure 6.8, are measured on small cylindrical specimens, drilled from original printed samples. As a consequence, only the bulk material of the specimens is considered, regardless of the specific zone. The water evaporation and related plastic/drying shrinkage from the sample sides is not considered, which can explain the similar behavior in the upper part of the printed samples.

In addition to the pore sizes and pore size distribution, also the percolation (i.e. the connection between the different hydration phases) is an important aspect of the microstructure as it also affects the transport properties and the mechanical strength. Considering the cement paste, there are in general three important percolation limit values: the setting point, the capillary porosity and the CSH-phase. Setting occurs as soon as the cement particles are connected by hydration products. As hydration proceeds, more hydration products will be formed, reducing the capillary porosity and the connection between the capillary pores. The fraction of connected pores is reflected by the total capillary porosity [115]. When the total porosity is lower than the percolation limit (approximately between 18% and 20%), percolation of the pore structure stops and the number of isolated pores increases. Boel [115] stated that in case of a lower W/C-ratio, isolated pores are more likely to occur. When assuming the lower hydration degree in the vicinity of the interlayer for enlarged time gaps, this indicated that MIP measurements could underestimate the pore sizes and pore size distributions. However, to state this theory, more in dept visualizations of the connectivity between the pores is required.

Table 6.2 represents the critical pore size diameter of the different zones, which in general corresponds with the steepest slope in the cumulative intrusion curve. Different researchers consider this diameter as the maximum diameter of the continuous pore network and this serves often as an indicator for some microstructural changes: *(i)* the lower the critical diameter, the finer the pore structure and *(ii)* the lower the W/C-ratio, the lower the critical diameter. The latter phenomenon can also be observed in Table 6.2: the lower the W/C-ratio for enlarged time gaps, the lower the critical diameter [95]. The environmental conditions of the second layer are similar, irrespective of the applied time gap, which is represented by the critical diameters listed in case of the top part.

Table 6.2: Critical pore size diameter of samples printed with different time gaps (n=1)

Sample	Critical diameter [nm]		
	Top	Inter	Bottom
T0	662.0	376.4	631.9
T10	984.7	499.8	567.1
T30	821.8	450.9	440.1
T60	693.3	389.0	415.1

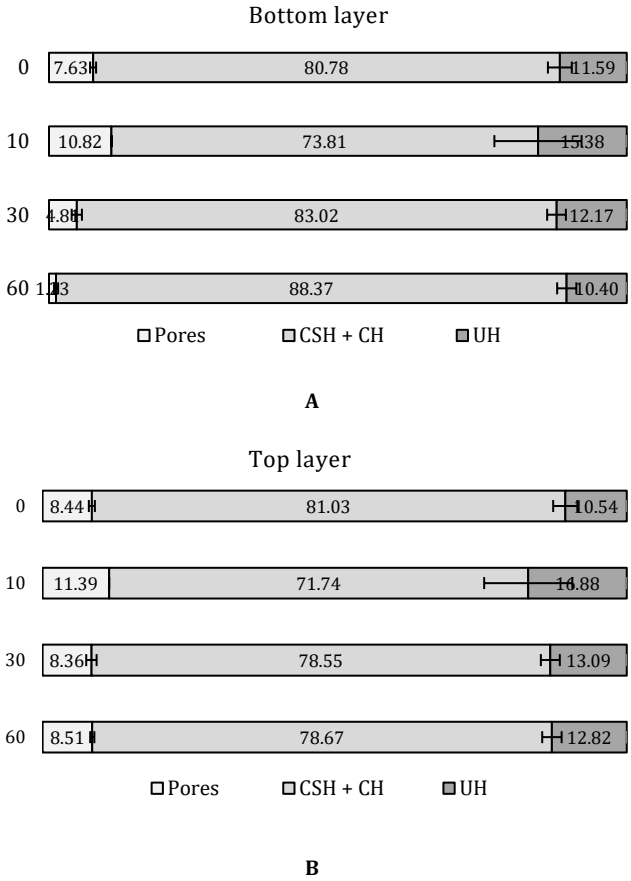

Figure 6.9: Analysis of the BSE-SEM micrographs as a quantification of the inner microstructure and present phases (Capillary pores, CSH + CH and UH) for the bottom (A) and top (B) part of a printed layer (n=20, error bars represent standard deviation)

The results of the microstructural analysis based on BSE-SEM measurements are depicted in Figure 6.9 and show a quantitative comparison of the present phases at the bottom and top layer. In case of a zero-minute time gap, the amount of UH is comparable for both layers. This phenomenon confirms the fact that as two successive layers, with the same age and similar moisture content, are printed on top of each other, the moisture exchange at the interlayer is negligible. A prolonged time gap induces a higher amount of UH in the top layer compared to the bottom layer. The higher amount of UH indicates a lower amount of water available for the hydration of cement and confirms the moisture exchange phenomenon that occurs when the layers become drier over time.

Besides UH cement particles, BSE-SEM analysis also allows the determination of the capillary pores formed during the hydration process (Figure 6.9). The highest volume of capillary pores is observed for a 10-minute time gap. Plotting and comparing these results with the pores measured based on MIP experiments and CT-scanning (see further), the same conclusion can be made. These observations stroke with the assumption that lowering the moisture content of the surface will increase the moisture exchange between the layers, creating a higher capillary pore volume. After a critical time gap of 10 minutes, the capillary porosity of the elements decreases and a comparable amount in case of 30- and 60-minute time gaps can be observed.

The varying amount of UH over the interlayer zone is depicted in Figure 6.10 and the exact position of the interlayer, observed during BSE-SEM analysis, is indicated by means of black rectangles. When two layers are printed directly on top of each other (T0), less cement particles are left unhydrated which can be attributed to the similar moisture content of both layers and the fact that the evaporation of water is blocked by directly printing the second layer. Consequently, a smaller surface area of the substrate layer is exposed to environmental conditions, resulting in a higher amount of water available for hydration. This correlates with the results obtained for T10; the moisture content of these elements (discussed in Chapter 4) shows the largest decrease, resulting in a higher volume of evaporated water and more UH cement particles. The difference in surface moisture content is not significant for T30 and T60, which in also translated in the results of the BSE-SEM analysis.

Focusing on the exact position of the interlayer, the concentration of UH decreases at the bottom layer, irrespective of the time gap, as it will extract more water from the successive one. However, this effect is most pronounced for a time interval of 10 minutes. This phenomenon can be attributed to the

formation of hydration products over time. In the first stage of hydration, mainly CSH and ettringite are formed, creating needles on top of the cement particles to create structuration bridges at a later stage. These bridges become stronger over time and improve the mechanical strength. Immediately after printing, these bridges are very weak and can be partly broken due to the addition of a second layer. The water exchange between the layers at an early age will therefore serve as extra water for rebuilding this structuration bridges, resulting in a higher and more pronounced effect of the hydration degree at the interlayer. Three millimeters above the interlayer zone, another area with less UH particles can be observed. This can be due to the shear action of applying a second layer on top of the base layer, resulting in a small amount of extra water which can be used for hydration. Again, as the standard deviation is noteworthy, only a qualitative trend can be seen. To state the above-mentioned assumptions in a quantitative way, more specific calculations and analysis of the formed hydration products based on XRD measurements would be required.

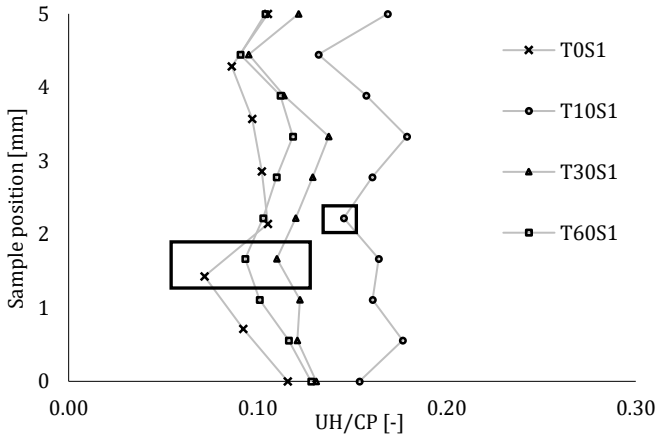

Figure 6.10: Amount of UH cement particles over the total cross-section (CP) within an interlayer zone of 5 mm. The exact position of the interlayer, observed during BSE-SEM analysis, is indicated with rectangular areas (n=3, error bars are left out).

6.4.2. Macroporosity

The overall porosity, obtained by µCT-scanning, is represented in Table 6.3. In general, a lower overall porosity can be observed for conventional cast concrete (1.7% vs. 5% in case of printed specimens) which could be related to the compaction process during fabrication. Although the porosity seems to

increase with increasing time gap and print velocity, statistical analysis revealed no significant difference. Kloft et al. [122] measured a mean air void content of 3.4% for their extruded material using μCT-scanning at 36 μm voxel size. Noting that a higher scanning resolution was used in this research, higher porosity values are expected compared to that of the studies presented from literature.

Table 6.3: Overall porosity as a function of interlayer time interval and printing speed (n=1)

Sample	**CAST**	**T0S1**	**T10S1**	**T30S1**	**T60S1**
Air void volume	1.68%	5.12%	4.58%	5.16%	5.34%
Sample		**T0S2**	**T10S2**	**T30S2**	**T60S2**
Air void volume		5.35%	4.40%	5.46%	5.57%

By applying a labelling algorithm on this 3D air void data, different orientation and shape parameters per object (single air void) can be determined on the obtained dataset. Flatness is a shape parameter between 0 and 1, and is defined by the ratio between the middle and the shortest axis of the air void. Pores are considered flat when the flatness is close to 0. Flat objects can typically be found on the boundary between the two printed layers. For this reason, objects with a flatness between 0.10 and 0.45 were filtered from the dataset containing all air voids.

The objects with an equivalent diameter larger than 100 μm and a flatness between 0.10 and 0.45 are shown in Figure 6.11. By further inspection, it can be observed that mold-cast concrete voids seem more spherical than those of 3D printed concrete, possessing many small and irregularly shaped voids. These voids, on average, also seem larger in volume then the mold-cast concrete's voids. It is theorized that, especially in the case of longer voids, smearing of the voids occurs due to the imparted pressure from printing. The larger voids tend to elongate and smear, perhaps also reducing in size to form a few extra smaller and irregularly shaped voids in the process. The latter phenomenon will mainly occur in the print direction. This may have a significant influence on especially the mechanical strength of the printed concrete, since stress concentrations may occur at sharp edges of the voids.

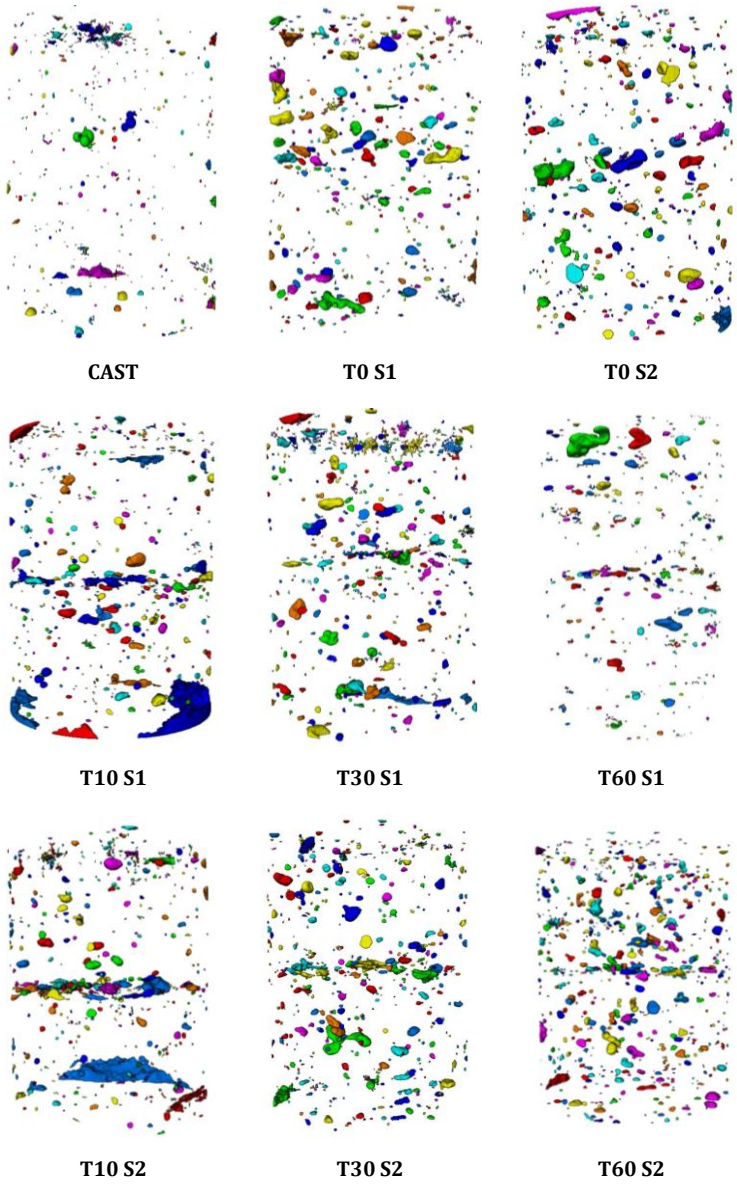

Figure 6.11: 3D rendering of air voids with a flatness between 0.10 and 0.45 obtained with Octopus reconstruction software in case of molded specimens (CAST) and specimens printed different time gaps (T0, T10, T30 and T60) and varying print velocity (S1 and S2)

The porosity between successively deposited layers, i.e. in the interlayer regions (IRs), were investigated for interlayer time gaps ranging from 0 to

60 minutes. The results are depicted in Figure 6.12 and 6.13. It is evident that the IR is almost not visible at all for the zero-minute time gap. This is due to the minimal moisture evaporating from the filament surface, thereby preventing water migration between the filaments. The IR does, however, become notably more visible in the CT images as the time gaps increases. These IRs are also evident in the 3D porosity render (Figure 6.12). More specifically, at shorter time gaps, the IR mostly consists out of many small voids. At longer time gaps, the IR seems to consist out of larger voids, or, many interconnected small voids that constitute one large void. The latter confirms the MIP observations.

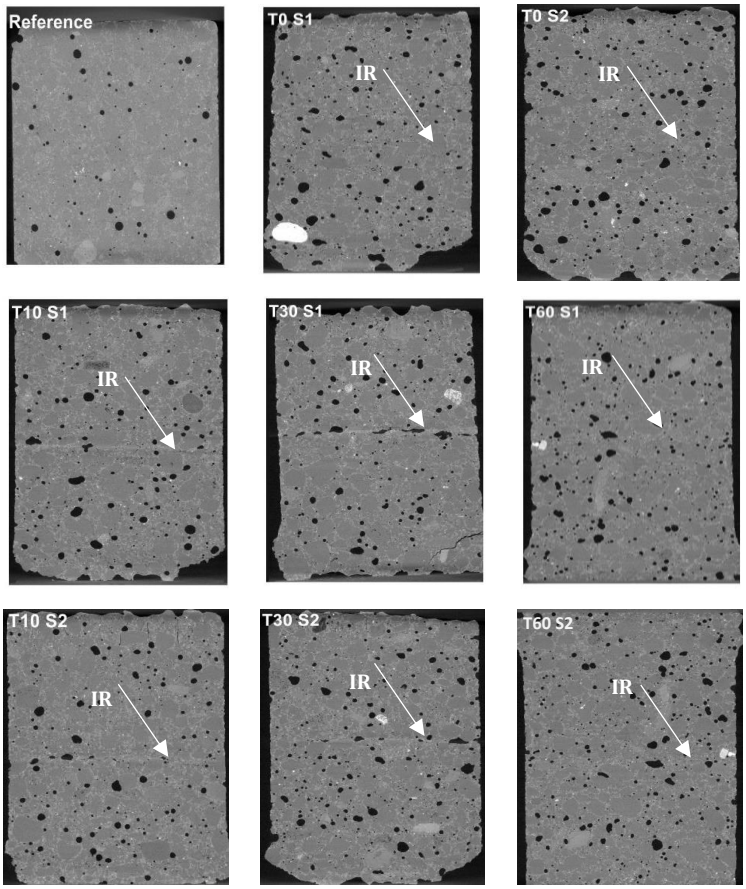

Figure 6.12: CT images of conventionally cast (Reference) and 3D printed specimens printed with time gaps ranging between 0 and 60 minutes (n=1)

The porosity as a function of the specimen height is depicted in Figure 6.13 for all time intervals and both printing speeds. Conventionally cast concrete shows a homogenous distribution of the porosity, with an approximated value of about 1.7%. A stochastic porosity pattern is observed at lower time gaps. In case of a zero-minute time gap, no pertinent deviation in porosity is noted at the IR, likely due to the limited water mass loss. At 10- and 30-minute time interval, the porosity at the IR changes from approximately 5% to 13.2% and 21.4%, respectively in case of low printing speeds and to 11.4% and 17.7%, respectively for higher printing speeds. No clear trend is observed in the 60 minutes time gap specimens due to their increased amount of slightly larger voids throughout the layers.

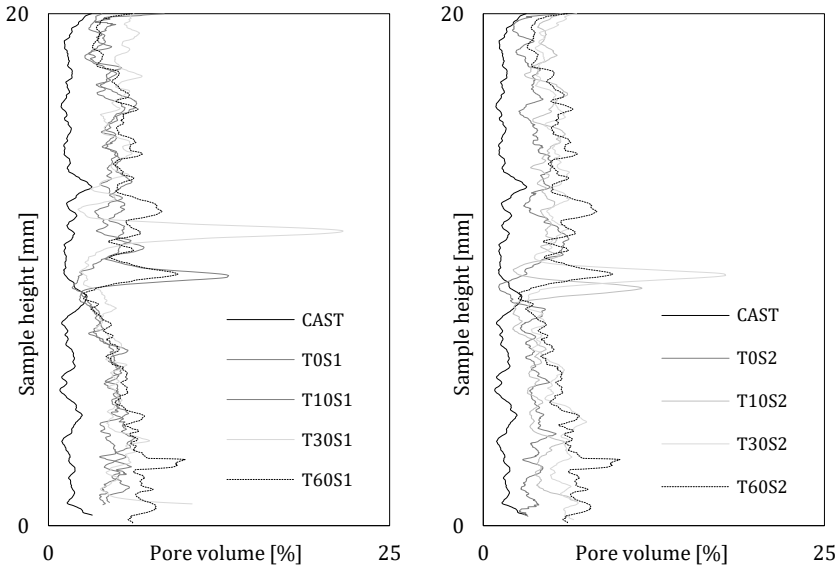

Figure 6.13: Porosity percentage over the specimen height for interlayer time intervals ranging between 0 and 60 minutes (n=1)

It is important to note that the severity of the interlayer porosity presented here may not necessarily be extrapolated to and generalized for all printable mixtures, since various print parameters, material rheology characteristics, and environmental or climatic conditions influencing evaporation and surface roughness of exposed layers collectively contribute towards the interlayer porosity.

6.5 Quantification of the micro-, meso- and macro-porosity after the addition of SAPs

6.5.1. Micro- and meso-porosity

Mercury intrusion porosimetry measurements of mix compositions with the addition of superabsorbent polymers led to the findings represented in Table 6.4 and Figure 6.14. In general, mixtures including SAPs tend to increase the total nanoporosity in both layers of the hardened specimens. However, no conclusive statement can be made about which zone has the largest nanoporosity.

As suggested by the distinct variations in derivative intrusion curves (Figure 6.14), there is a clear difference in continuous pore network. In general, SAPs tend to reduce the amount of nanopores in the range of 100 nm to 500 nm and increase the amount of voids with a diameter above 700 nm; This can be ascribed to the ink-bottle effect and a better hydration rate around the SAPs, closing up all the smaller pores, as well as to their autogenous shrinkage mitigation that reduces the amount of micro-cracking [74].

Table 6.4: Capillary porosity of the printed samples containing SAPs

Sample	Total porosity < 10 μm [%]			Critical diameter [nm]		
	Top	Inter	Bottom	Top	Inter	Bottom
REF	15.2	16.2	15.9	255.6	273.2	246.6
A017	19.1	18.4	18.4	384.4	336.1	327.5
G025	18.0	16.5	17.1	255.3	141.0	183.9
M022	19.0	18.3	16.7	391.8	311.3	227.0

G025 shows a distinct peak in the derivative intrusion curve of each layer, taking into account pore diameters ranging from 10 nm to 100 nm, while a reduction in the number of pores with a diameter above 400 nm can be observed. G025 is even denser than REF, which would suggest a lower effective W/C and may be due to internal curing and further stimulated hydration.

In case of SAP G, water that is released by the swollen particles over time, will migrate away from the polymer and take part in hydration, reducing the diameter of introduced pores. As such, it is believed the water will close off

the porous network by connecting the sides. The water might not be able to penetrate the smallest pore connections as an air pocket is entrapped for example, under cohesion to the matrix, adhesion and/or capillary tension from a larger water mass in its proximity. This would explain the relatively large fraction of small pores (< 100 nm) that get closed off, and small fraction of intermediate nanopores (400 nm to 1100 nm) that keep reducing in pore diameter as type G SAPs provide them with water to maintain hydration.

Accordingly, the other mixtures would seem less efficient in supplying water to their surroundings as they show a greater presence of larger nanopores (500 to 1000 nm) associated with accumulated water that was not able to migrate away and take part in the hydration reaction. M022 shows a tendency similar to G025. However, the behavior of the applied SAPs is believed to be explained in more detail by the swelling kinetics of each respective SAP type.

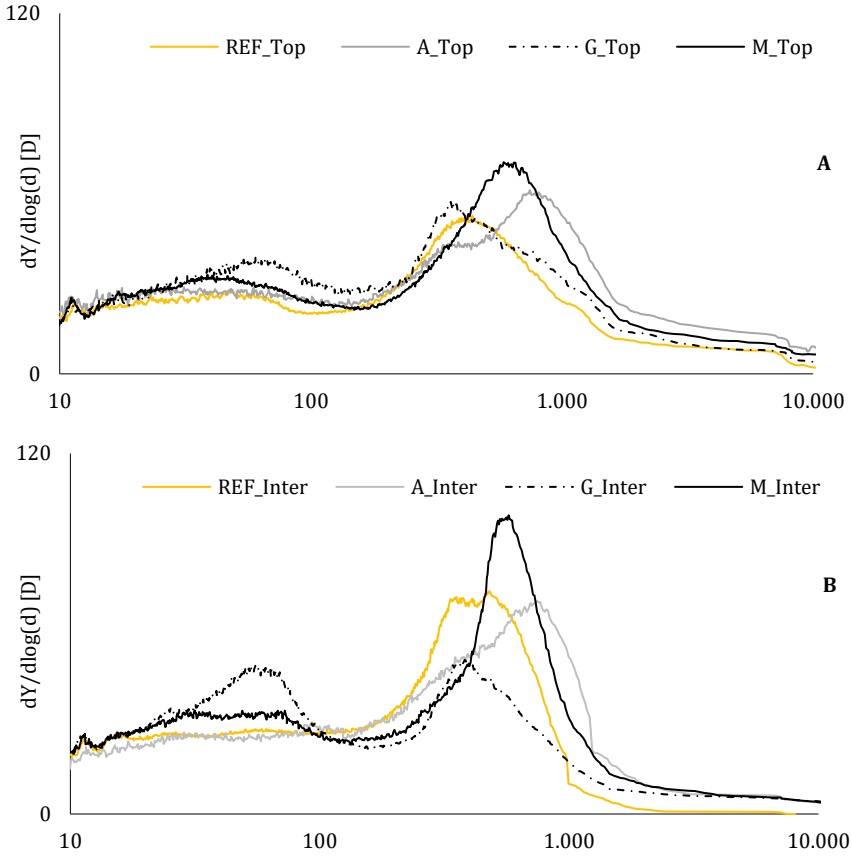

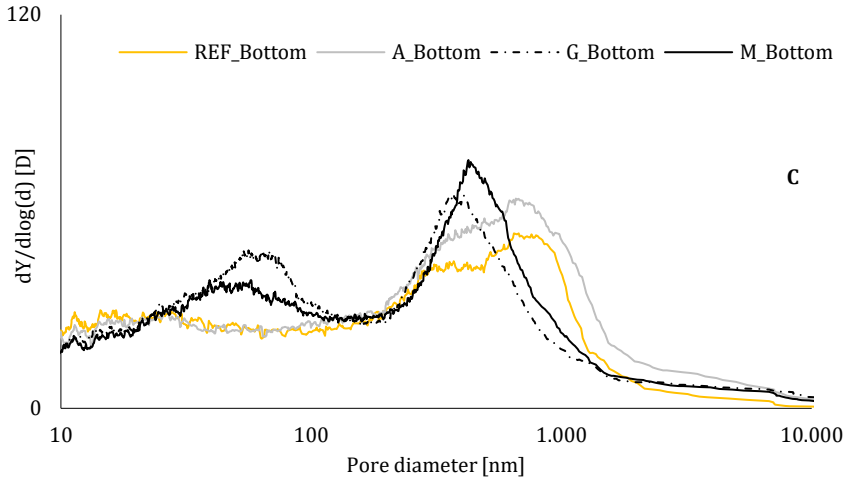

Figure 6.14: Derivative intrusion curves for top (A), inter (B) and bottom (C) zones obtained out of printed specimens with and without the addition of SAPs (n=1)

6.5.2. Macro-porosity

Table 6.5 represents the polymer diameters, obtained by a microscopic analysis of the dry and saturated SAP particles as well as the voids (macropores) they leave behind in 28-day old samples of A017, G025 and M022, respectively. Table 6.5 also includes the expected diameters E(d) [µm] respectively calculated as follows:

- In the mean dry state ($E(d)_{dry}$) as the ones tabulated in Chapter 3;
- In saturated state ($E(d)_{sat}$) as the equivalent spherical diameter obtained after swelling in DW, based on the absorption capacity of mixing water and starting from the initial dry size of the selected SAPs;
- The theoretically expected macropores ($E(d)_{theor}$) due to the absorption of mixing water, starting from the initial mean size and assuming spherical pores.

Table 6.5: SAP diameters obtained by microscopical analysis in dry and hardened form [µm]

		SAP A [µm]	SAP G [µm]	SAP M [µm]
DRY	d	83	137	416
	$E(d)_{dry}$	100 ± 2	157 ± 82	486 ± 141
SAT	d	479	812	2145
	$E(d)_{sat}$	496	842	2431
THEOR	d	308	522	1010
	$E(d)_{theor}$	296 ± 65	391 ± 204	1262 ± 366
d_{sat}/d_{dry}		5.8	5.9	5.2
d_{theor}/d_{dry}		3.7	3.8	2.4

The diameter of a swollen particle in DW is about 6 times that of a dry particle. The diameters obtained from testing are approximately 4% to 12% smaller than the ones theoretically estimated, which can be ascribed to the test solution of DW which can have impurities and due to the assumption of spherical particles which is not the case due to bulk polymerization. On the other hand, the diameter of the void one polymer leaves behind in hardened specimens is about 3 to 4 times that of a dry particle. A considerably lower value (i.e. 2.4) is found for SAP M. This phenomenon is attributed to the macropores the SAPs leaves behind in the hardened concrete, which lies in the same size range as the sand particles.

Consequently, during mixing, they are more resistant to desorption under sand attack, but they seem to be hindered to reach their maximum capacity as well. SAP G on the other hand appear to lose water again during mixing, but once at rest, they are able to reach their full swelling capacity, as theoretically estimated.

6.5.2. Air void analysis

Figure 6.15 depicts the cumulative air content obtained by RapidAir measurements. One can observe that the addition of superabsorbent polymers causes an increase in the total air content. The latter is more or less proportional to the amount of polymers added, or equivalent with the amount of dry volume added. The expected size of the resulting macro pores based on the initial mean size of the SAP particles and the absorption capacity of mixing water while assuming spherical pores is 296 ± 65 µm, 391 ± 204 µm and 1262 ± 366 µm for A017, G025 and M022, respectively. These values

correspond to the sizes of the macropores microscopically obtained on the polished sections which amounted to 308 µm, 522 µm and 1010 µm, respectively (Table 6.5). This is also the range found by RapidAir measurements, where increments in air content are found around these void sizes (Figure 6.15), indicating that the digital manufacturing technique allows the SAPs to behave similar as in conventionally cast concrete.

The total air content is also related to the amount of macropores. The theoretical additional amount of voids in SAP mixtures compared to the REF mixture is linked to the amount of additional water and SAPs. This is 4.2% of the total surface area and corresponds perfectly with the results discussed in the previous section. The slightly higher value for M022 can be ascribed to an increased count of voids around its interlayer, compared to the other test series (Figure 6.16). The reason why M022 is likely to be affected more from entrapped air at the interface between two superposed printed layers is accounted to its relatively dry surface, even at zero-time gap in combination with its relatively worse dimensional stability. The slightly lower value for A017 can be ascribed to the further hydration within the smaller macropore voids due to internal curing.

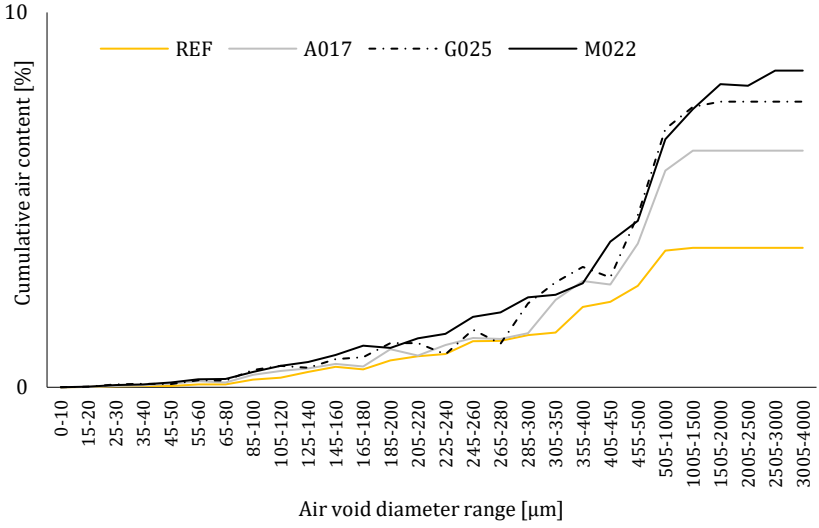

Figure 6.15: Cumulative air content in hardened specimens (n=1)

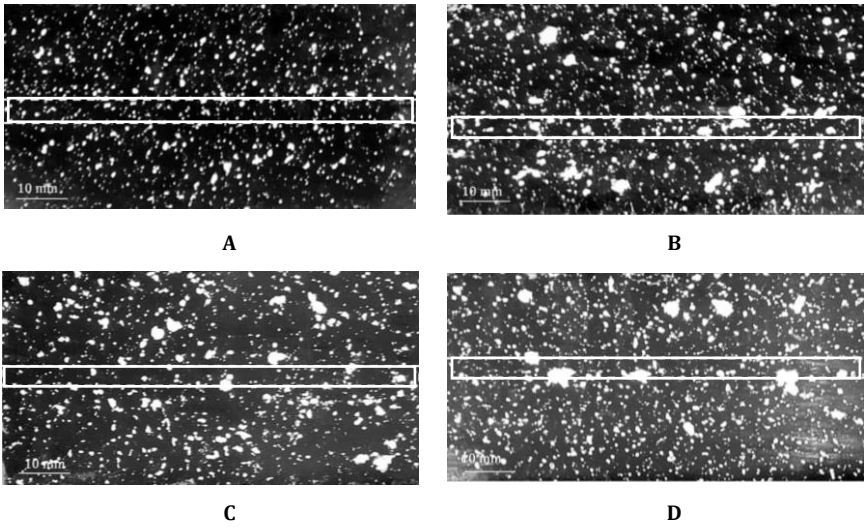

Figure 6.16: Studied specimens in RapidAir test: REF (A), A017 (B), G025 (C) and M022 (D) (n=1). White rectangles indicate the position of the interlayer.

The printing procedure might also lead to entrapped air at the interface of two layers. In addition, larger swollen SAPs (for example SAP M), which might have a lubricating effect when being pumped, could migrate to the outer edges of the mixture under pressurization. As such, the swollen polymers would likely to be found at the outer surface of the printed filament and end up at the interlayer.

6.6 Conclusions

The influence on the microstructure of various print process parameters is investigated thoroughly within this chapter. Conventionally cast elements show in general a lower porosity, irrespective of the particle size the author considered. Considering the capillary pores, three main conclusions can be drawn: *(i)* the capillary porosity decreases with an increasing print velocity, due to the higher pressure exerted during printing, *(ii)* the capillary porosity is lower for the bottom part of the samples as the additional weight of the successive layer increases the compaction degree of the substrate layer, and *(iii)* a higher time gap decreases the critical diameter of the pores in the bottom part, confirming the lower W/C-ratio due to evaporation.

Focusing on the air voids, similar trends can be observed. Although the overall porosity is higher in printed specimens, a uniform porosity can be observed for conventionally cast elements and elements printed with a zero-minute time gap. At a 10- and 30-minutes time interval, the porosity at the IR increases significantly, while no clear trend could be observed for the specimens printed with a 60 minutes time gap due to their increased amount of slightly larger voids throughout the layers.

In printed or conventionally cast elements with SAP additions, similar trends could be observed: SAP's tend to reduce the amount of nanopores in the range of 100 nm to 500 nm and increase the number of voids with a diameter above 700 nm. This can be ascribed to the better hydration rate around the SAPs, closing up all the smaller pores as well as to their autogenous shrinkage reduction.

Chapter 7

Water transport in 3D printed materials

7.1. General aspects of water ingress

Transport processes and permeation properties are highly significant for the ingress and internal redistribution of substances that are harmful to concrete, its constituents or the reinforcement, either individually or when combined with other effects [123]. Important examples are:

- Ingress of chlorides from sea water or deicing salts, initiating corrosion of the reinforcement;
- Ingress of carbon dioxide (CO_2) from the air, penetrating the concrete cover and destroying the passivity of the reinforcing steel;
- Penetration of water that saturates the capillary pores, fills the air voids and freezes to cause frost damage;
- Movement of water and moisture from external and internal sources;
- Diffusion of oxygen participating in the corrosion process;
- Dissolution and diffusion of entrapped air in and from the air void system that makes further water absorption possible.

Water can move in different states and therefore it is usually referred to as moisture. The moisture movement is a combination of the movement of water vapor in the smaller pores, liquid water in the larger pores and adsorbed water at the pore wall. Although water itself is usually not harmful for building materials, it serves as a medium for the transport of aggressive substances [123].

In general, one can distinguish three mechanisms that govern the water movement through a porous medium: permeation, diffusion and absorption. Due to permeation, water will be transported through the cementitious material under a hydraulic pressure, while in case of diffusion or absorption water moves respectively as a result of a concentration gradient or capillary suction forces [124].

As extensively discussed in the doctoral thesis of Bjorn Van Belleghem [125], permeability is frequently used as a water transport indicator for building materials. However, as structural elements are not completely saturated during their service life, this will not always result in relevant conclusions as, according to the saturation degree, the water ingress will be controlled by a combination of sorption and diffusion processes. Especially in terms of printed specimens, where the material is anisotropic and interlayers serve as additional ingress paths, the transport mechanism becomes even more complex and multi-directional. This phenomenon will be explained in more detail in Chapter 8.

To quantify the capillary water absorption during the first 6 hours after water submersion, many researchers still rely on Eq. [7.1], which expresses a linear relationship between the cumulative absorbed volume of water i [kg/m^2], expressed per unit of area of the inflow surface and the square root of time t [$h^{0.5}$] through the sorptivity coefficient S [$kg/m^2/ h^{0.5}$]:

$$i = S \cdot \sqrt{t} \qquad [7.1]$$

After 6 hours, the capillary water absorption mechanism deviates from the latter relationship, which could be attributed to different phenomena, however, none of the explanations are generally accepted in literature. In addition, this theory is also counteracted by a recent study performed by Villagrán Zaccardi et al. [126], who observed a better fitting with $t^{0.25}$ compared to $t^{0.5}$ and this was explained based on the hygroscopicity of the cementitious material and swelling caused by the interaction with water.

The absorption capacity of a cementitious material depends on many parameters among these, the W/C ratio, sample compaction, porosity, saturation degree, moisture distribution, temperature and relative humidity are the most important ones. In terms of 3D printed materials, this list with influencing factors will be extended by process-related parameters such as printing speed and interlayer time interval. The latter factors will affect the quality of the interlayer and might create 'weak links' in the structural component which may allow for high capillary suction from the surface deep into the structure. The latter phenomena were already observed by Schröfl at al. [127], who visualized through neutron radiography a preferential ingress of water via the interlayers of multi-layered specimens.

There are many methods, both destructive and non-destructive, to measure the moisture distribution in cement-based materials [128, 129]. However, the standard experimental method to investigate the entrance of water by capillary action is the gravimetrical method. Water uptake of the material is then obtained by weighing samples at regular time intervals. Although the test is easy to perform and the results can be obtained relatively fast, information about the spatial water distribution nor the water movement can be gained, which is crucial in terms of printed elements due to the non-uniform pore distribution. However, a visualization of the water ingress can be obtained by nuclear magnetic resonance imaging (NMR) [74], radiation attenuation methods (X-ray, ϒ-ray [130]) or neutron radiography [131]. These visualization methods are fast and can be performed with a very high resolution and accuracy.

7.2. Mortar composition and sample preparation

The same nomenclature and mix compositions as explained in Chapter 3 are valid. Capillary water absorption tests and gravimetrical measurements were performed on samples composed of the reference composition, without the addition of fibers or SAPs. Both manufacturing techniques (traditional casting and printing) were hereby considered. In case of 3D printed elements, multiple print velocities (S1 and S2) and interlayer time intervals (T0, T10, T30 and T60) were considered. The sample size and storage conditions are similar as the ones described in Chapter 3.

On the other hand, neutron radiography measurements were performed to visualize the water movement during capillary water uptake on mixtures with and without SAP addition. In this case, only printed samples were considered, fabricated with two printing speeds (S1 and S2) and two different time gaps (T0 and T30). Similar as for the gravimetrical measurements, samples composed of two, three and four layers were considered to study more specifically the water ingress into the different interlayers.

7.3. Capillary water absorption and gravimetrical measurements

The capillary water absorption was measured according to the European standard NBN EN 13057 [132] in a climate room at 20 $\pm$ 2°C and 60 $\pm$ 5% relative humidity. Before starting the absorption test, small cylinders (Ø = 14 mm, h = 20 mm, Figure 6.3A), drilled from original two-layered printed specimens, and small cubes (l = 25 mm), cut from mold-cast elements were stored in an oven at 40°C until the mass difference between two consecutive measurements in 24 hours was less than 0.1%. The latter temperature was selected in order to minimize microstructural damage. Thereafter, sample surfaces, except the exposure surface, were covered with aluminum foil in order to ensure unidirectional water ingress. These sample preparations allow the author to draw conclusions about the capillary absorption capacity of the bulk material. The (detrimental) effect of the outer sides of a printed element, which are directly exposed to drying after extrusion and of which the composition could differ as a result of the print process (S1 vs. S2), is excluded within these experiments and will be considered during neutron radiography measurements.

The initial dry mass of the samples was registered by weighing them on a scale with an accuracy of 0.01 g. Thereafter, the specimens were placed on two line supports in a sealed container to avoid evaporation during the

absorption test. The line supports were positioned parallel to the print direction and the bottom of the substrate layer served as exposure surface, while for mold-cast specimens one of the cast surfaces was exposed to water. The container was filled with water till a level of 3 ± 1 mm above the supports. The water uptake into the cementitious material was determined by weighing the samples at predefined time intervals. Therefore, the samples were taken out of the container, wiped to remove surplus water and weighed. Thereafter, they returned immediately to the container. The mass of the samples was recorded after 1, 3, 7, 15, 30, 60 minutes and every hour up to 6 hours after water contact. After this first test period, the samples were weighed again after 24 and 144 hours. The test was performed in triplicate per test series.

By subtracting the initial mass of a sample from the recorded mass, the cumulative water uptake could be derived as a function of time. Subsequently, the cumulative water uptake was divided by the surface area exposed to water during the absorption test. The cumulative water absorption per unit surface area [g/mm^2] was then plotted for each sample as a function of the square root of time √t [√s]. From this plot, one or multiple capillary sorption coefficients could be derived. When the plot shows a linear curve, one single sorption coefficient can be defined as the gradient of the resulting curve. However, as mentioned in section 7.1, when the immersion lasts longer than 6 hours, the water uptake in a cementitious material is non-linear with the square root of time. According to ASTM C1585-20 [133], two sorption coefficients can then be derived. The initial sorption coefficient S_i is defined as the slope of the line from the first recorded point to the cumulative mass of the water uptake after 6 hours. The secondary sorption coefficient S_s is defined as the slope of the line that is the best fit to the plotted cumulative water uptake against the square root of time using all measuring points from 1 to 7 days.

The results of the capillary water absorption test, performed on conventionally cast specimens and specimens printed with different time gaps and print velocities, are shown in Figure 7.1. All derived sorption coefficients are shown in Table 7.1. As can be observed, conventionally cast concrete specimens are less prone to capillary absorption compared to printed elements, resulting in a lower initial absorption rate for cast samples.

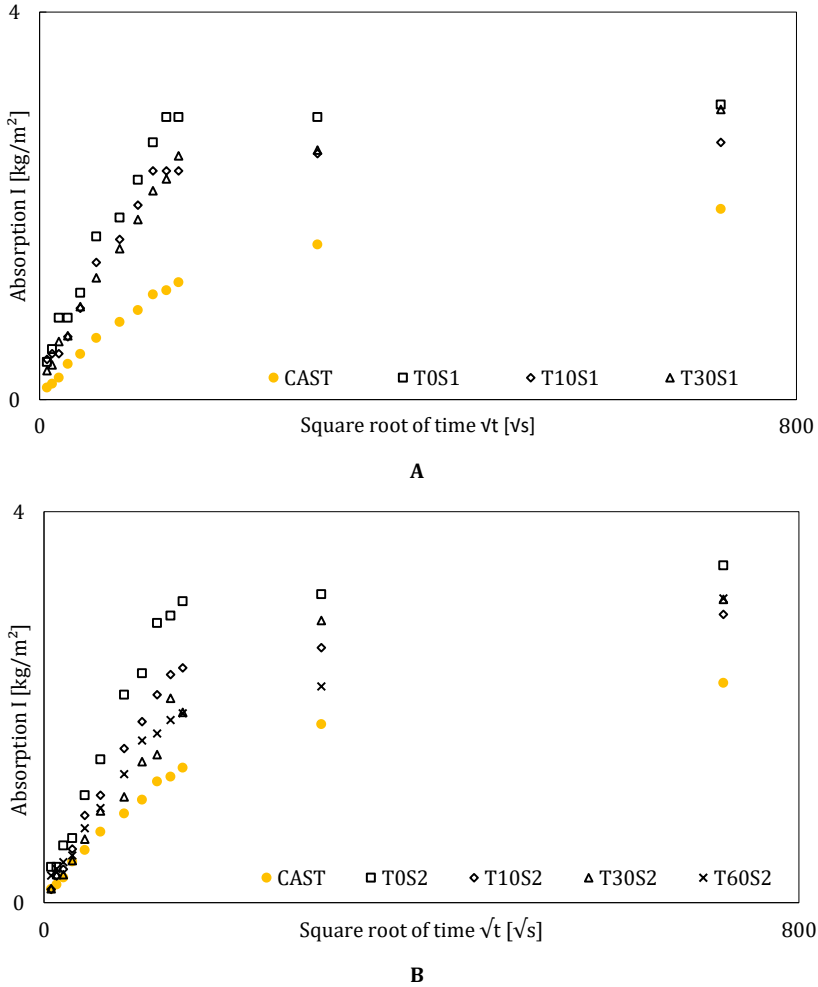

Figure 7.1: Capillary water absorption tests on conventionally cast specimens compared with specimens fabricated with low (A) and high printing speed (B) (n=3, error bars are left out for clarity)

This difference between the fabrication methods is more pronounced for S1 samples. Compared with 3D printed specimens, the secondary absorption rate of mold-cast samples is slightly higher, indicating a slower water uptake in the early stage of water exposure due to the denser cement matrix, but the water uptake will last for a longer period. The only exception to this statement is the second absorption rate of T60 S2, which exceeds the absorption rate of conventional cast elements, indicating that the longer the time gap, the more important diffusion will become. For printed samples it is also noticed that, by increasing the interlayer time interval, the capillary

absorption and the initial rate of water absorption decrease. Specimens with enlarged time gaps contain more larger pores, as visualized by µCT-scanning in Chapter 6. As a consequence, it can be assumed that these larger pores contain less water at the end of the absorption stage (i.e. after 6 hours). This will increase the concentration difference between the entering water and the pore liquid in the specimen and increase the secondary absorption rate (Table 7.2). These general observations are regardless of the printing speed.

Capillary action is inversely related to the pore radius. With a larger pore size, such as macro pores, the capillary action is decreased until gravity is overcome. As could be observed in Chapter 6, µCT-scanning revealed larger pores with an increasing interlayer time gap, resulting in a lower water absorption rate. Although the differences are small, higher printing speeds cause larger voids, with a lower absorption rate as a result.

Table 7.1: Initial and secondary water absorption rate [$kg/m^2.s^{0.5}$]

	Initial rate	Secondary rate		Initial rate	Secondary rate
CAST	0.0079	0.0012			
T0 S1	0.0187	0.0002	T0 S2	0.0185	0.0005
T10 S1	0.0158	0.0003	T10 S2	0.0147	0.0008
T30 S1	0.0157	0.0009	T30 S2	0.0117	0.0011
T60 S1	-	-	T60 S2	0.0112	0.0014

As the water ingress during the first 6 hours of water immersion is mainly driven by capillary absorption, it becomes possible to make a rough estimation of the water front height x [mm] based on Eq. [7.2] and expressed as a function of time. Within this equation, B [$mm/s^{0.5}$] equals the water penetration coefficient and t [s] the exposure time. Coefficient B can be derived based on Eq. [7.3], with S [$mm.s^{0.5}$] the initial sorption coefficient, ρ_w [g/cm^3] the density of water and φ_a [-] the active porosity available for capillary transport, obtained based on MIP experiments (Chapter 6).

$$x(t) = B(t) \cdot \sqrt{t} \qquad [7.2]$$

$$S(t) = \frac{\rho_w \cdot \varphi_a}{\sqrt{\frac{1}{B(t)}}} \qquad [7.3]$$

Table 7.2 represents the calculated height of the water front, obtained after 6 hours of water exposure. The latter confirms the observations stated before. First of all, molded specimens are less prone to capillary absorption.

After 6 hours of water immersion, the water front reached 48% of the total height, compared with 78% and 72% in case of specimens with a zero-minute time interval printed at low and high speeds, respectively. A comparison between molded specimens and specimens printed with enlarged time gaps is less relevant as only in case of a zero-minute time interval between the layers the material can be assumed as being homogenous.

Secondly, the capillary action of printed specimens reduces with increasing time gaps and increasing printing speed. In case of a lower print velocity (S1), the water front reaches (and even exceeds) the interlayer (located at 10 mm) for every time gap. This in contrary to specimens printed at a higher speed, where only in case of smaller time gaps (i.e. T0 and T10) the position of the interlayer (i.e. 10 mm) is reached. The latter can be attributed to the higher number of larger pores in the vicinity of the interlayer.

Table 7.2: Calculated height of the water front [mm] due to capillary absorption obtained after 6 hours of water immersion

	Water front height [mm]		Water front height [mm]
CAST	12.1		
T0 S1	15.8	T0 S2	14.6
T10 S1	12.8	T10 S2	11.4
T30 S1	12.3	T30 S2	9.2
T60 S1	-	T60 S2	9.2

After 6 hours of water immersion, the water absorption curves flatten over time. As stated in literature, there will be a shift in transport mechanism. While capillary absorption causes early fast ingress of water, at a later stage diffusion becomes the more dominant mechanism. Unlike capillary absorption, diffusion is driven by a concentration difference between the pores. As mentioned before, due to the higher porosity of the samples printed with enlarged time gap, it can be assumed that these larger pores contain less water at the end of the absorption stage (i.e. after 6 hours). This will increase the concentration difference between the entering water and the pore liquid in the specimen and increase the secondary absorption rate (Table 7.2).

After conducting the capillary water absorption test, the specimens were vacuum saturated with water for 24 hours. The first 4 hours, the specimens were put in a chamber at 25 mbars at 20 $\pm$ 2°C. Afterwards, water was added until the specimens were completely submerged.

The specimens were then hydrostatically weighed (m_h) and the saturated mass was determined (m_s). The specimens were then stored at 40°C for 7 days until constant mass and weighed to determine the dry mass. The author acknowledges that this temperature is lower than the one prescribed by NBN EN 1936. However, the latter temperature is chosen related to the small cylindrical dimensions and in order to minimize microstructural damage. The apparent volumetric mass (ρ_{app} [g/cm^3]), the porosity accessible to water (ρ_1 [%]) and the amount of absorbed water in fully saturated state (ρ_2 [%]) were determined using the following equations:

$$\rho_{app} = \frac{m_d}{m_s - m_h} \quad [7.4]$$

$$\rho_1 = \frac{m_s - m_d}{m_s - m_h} \quad [7.5]$$

$$\rho_2 = \frac{m_s - m_d}{m_d} \quad [7.6]$$

The results are represented in Table 7.3, with similar trends as observed before. The bulk density of printed specimens is in general lower compared to conventionally cast specimens, due to the macro-pore formation. The porosity accessible for water uptake increases with increasing time gaps, confirming the assumption that a higher volume of larger pores requires more time to be filled with water, causing a higher water-uptake by the samples until complete saturation.

Table 7.3: Bulk density, accessible porosity and water absorption when fully saturated for mold-cast and specimens printed with different printing speeds and time gaps.

	Bulk density [g/cm^3]	Accessible porosity [%]	Water absorption [%]
CAST	2.57 ± 0.21	9.5 ± 0.7	3.7 ± 0.4
T0 S1	2.20 ± 0.20	11.6 ± 0.6	5.3 ± 0.3
T10 S1	2.23 ± 0.12	12.0 ± 0.6	5.4 ± 0.2
T30 S1	2.19 ± 0.02	13.2 ± 0.2	6.1 ± 0.3
T60 S1	-	-	-
T0 S2	2.19 ± 0.04	12.1 ± 0.2	5.6 ± 0.1
T10 S2	2.19 ± 0.06	12.4 ± 0.7	5.7 ± 0.2
T30 S2	2.19 ± 0.08	12.7 ± 0.4	5.8 ± 0.2
T60 S2	2.19 ± 0.09	13.0 ± 0.9	5.9 ± 0.1

7.4. Neutron radiography

Neutron radiography can be applied to study the water ingress into cementitious materials. As for neutron radiography thermal neutrons are used, hydrogen attenuates the neutrons more compared to concrete or to the aluminum containers wherein the samples were positioned. As water consists out of hydrogen, neutron radiography is an ideal technique to visualize the water distribution in the pores with a high resolution. Neutron radiography already proved its efficiency in case of concrete specimens to visualize the effectiveness of water-repellent agents, water migration into cracked and (self-)healed specimens and the water uptake of digitally manufactured specimens [134, 135].

7.4.1. Sample preparation

Neutron radiography was used to visualize and quantify the water penetration into printed specimens. The printed samples were manufactured with two different compositions (REF and A017 as denominated in Chapter 3). Furthermore, both printing speeds (S1 and S2), different interlayer time intervals (T0 and T30) and a different number of layers (two, three and four layers) were considered.

After printing, specimens were stored for 28 days in a climatized environment (20 $\pm$ 2°C; 60 $\pm$ 5% RH). To mimic the conditions of printed elements in service life, specimens were not covered with foil after printing. After a period of 28 days, specimens were saw-cut into length of maximum 20 mm. The irregular shape of the printed samples could not be avoided as they were saw-cut from originally printed elements. Prior to testing, samples were dried in an oven (Termaks, A/S nino lab) for 7 days at 35 °C until constant mass. The latter temperature was selected based on [134, 136] to minimize microstructural damage.

Although commonly applied when visualizing the water uptake by cementitious materials [74, 127, 134-136], in this doctoral thesis printed specimens were not coated with self-adhesive aluminum tape. This in order to limit possible artifacts due to bad adhesion of the tape caused by the irregular shape of the samples and to visualize the difference in water uptake between the bulk material and the sides. Consequently, the author notes that there will be no unidirectional water ingress, as the water can also penetrate from other surfaces, irrespective of the water ingress surface. To visualize and quantify the water uptake of both the bulk material and the interlayers, two different water exposure surfaces were considered (i.e. front and bottom,

schematically represented in Figure 7.2B and Figure 7.2C, respectively). When the front surface of a printed element was exposed to water, the surface was smoothened to ensure a stable set-up; when the bottom surface of the sample was submerged in water, no further sample preparation was executed. An example of both exposure situations is represented in Figure 7.3. The direction of the neutron beam is in both cases parallel to the exposure surface. An overview of the manufactured specimens, mix composition, applied print parameters and water exposure surfaces investigated is presented in Table 7.4. For every test series, at least two samples were tested.

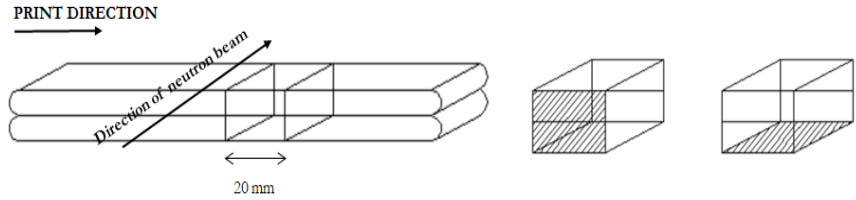

A B C

Figure 7.2: Schematic representation of the studied water exposure surfaces: originally printed samples (A), water exposure surface 'front' (B) and water exposure surface 'bottom' (C). The exposure surfaces are depicted for two-layered specimens but the same principles are applied for three and four layered elements.

A B

Figure 7.3: Representation of samples, cut from original multi-layered specimens, used for water ingress measurements, with the front (A) or bottom (B) surface as exposure surface. When the front surface of a printed element was exposed to water, the surface was smoothened to ensure a stable set-up.

Table 7.4: Specimens denomination, print parameters and number of layers

Mix	Denomination	Velocity	Time gap [min]	# layers [-]	Exposure surface
REF	RS1_F_Lx	S1	0	2, 3 and 4	Front
	RS1_B_Lx	S1	0	2, 3 and 4	Bottom
	RS2_F_Lx	S2	0	2, 3 and 4	Front
	RS2_B_Lx	S2	0	2, 3 and 4	Bottom
SAP	SAP_F_Lx	S1	0	2, 3 and 4	Front
	SAP_B_Lx	S1	0	2, 3 and 4	Bottom
	SAP30_F_Lx	S1	30	2, 3 and 4	Front
	SAP30_B_Lx	S1	30	2, 3 and 4	Bottom

7.4.2. Neutron beam line and test setup

The beam used in this investigation was a neutron beam with a proton current of 1.5 mA at the measuring station NEUTRA, the thermal radiographic facility at the Swiss spallation source SINQ of the Paul Scherrer institute (PSI), in Switzerland [137] (Figure 7.4).

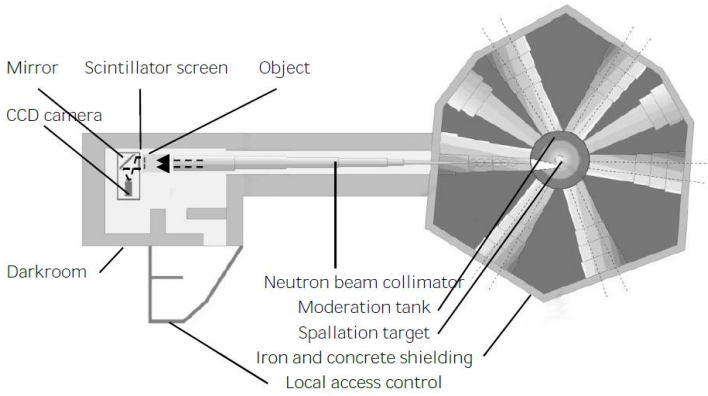

Figure 7.4: NEUTRA beam line with various parts [137]

The NEUTRA beam line consists of a neutron source, in which neutrons are created by means of spallation of lead after being bombarded by protons. The neutrons are moderated and slowed down by heavy water. A collimator parallelizes the neutron beam and leads it towards the object space. The neutron beam travels subsequently through the studied object. After traversing the sample, the incoming neutron beam is detected using a MAXI-camera box fitted with a 100-µm thick LiF/ZnS scintillator screen.

Afterwards, the light emitted from the scintillation screen is collected using a 50 mm AFS NIKKOR lens onto a scientific complementary metal oxide semiconductor (sCMOS) camera detector (Andor Neo) with 2160 (H) x 2560 (V) pixels. This imaging arrangement provides images with a field of view of approximately 308 x 365 mm size with a corresponding pixel size of 142.5 µm. The exposure time of a single raw radiography was equal to 20 s.

The relationship between the intensity values and the composition of the sample is described by the law of exponential attenuation (Beer-Lambert law, which can be expressed in a dry state (Eq. [7.7]) and wet state (Eq. [7.8]).

$$I_{dry} = I_0 \cdot \exp(-\Sigma_{dry} \cdot d) \quad [7.7]$$

$$I_{wet} = I_0 \cdot \exp(-\Sigma_{dry} \cdot d - \Sigma_{water} \cdot d_{water}) \quad [7.8]$$

Where I_{dry} [$mA^{-1}.cm^{-2}.s^{-1}$] is the flux transmitting through the sample in dry state, I_0 [$mA^{-1}.cm^{-2}.s^{-1}$] the intensity of the incident ray, $\sum_{dry}$ [cm^{-1}] the attenuation coefficient of the sample, d [cm] the specimens thickness, $\sum_{water}$ [3.64 cm^{-1}] the attenuation coefficient of water and d_{water} [cm] the water layer thickness. As each pixel had its own intensity value, cracks, material edges, defects, etc. were distinguishable from neighboring pixels due to differences in grey values. Also, water was visible as water attenuates the neutrons more in comparison to the dry cementitious material. Based on the latter, the water content W [g/cm^3] at different time steps can be calculated based on Eq. [7.9].

$$W = -\frac{\rho_w}{\sum_{water} \cdot d} \cdot \ln\left(\frac{I_{wet}}{I_{dry}}\right) \quad [7.9]$$

Before the start of the capillary absorption test, specimens were weighed with a Sartorius BP 3100 S balance (accuracy 0.01 g) and afterwards placed on line supports into a water basin mounted on a support frame (Figure 7.5). Before the water basins were filled with water, reference images of the samples were taken in dry state. Subsequently, water was added manually 3 min before the actual start of the neutron radiography measurements. The samples were approximately 4 mm immersed in the liquid. Subsequently, radiographs were made every 20 s for a total measurement time of 6 hours. In this way, the water penetration through capillary suction could be followed as a function of time. After the measurement, the specimens were weighted again to quantify the amount of absorbed moisture. This value was divided by the bottom area in contact with water to receive the total water uptake per square centimeter. The latter results could thereafter be compared with the values obtained by post-processing the neutron radiographs. After this beamtime, specimens were again approximately 4 mm immersed in water for

another 18 hours. After 24 hours of water suction, specimens were weighed and a last neutron radiograph was made to correlate in a qualitative way with the neutron image obtained after 6 hours of water exposure.

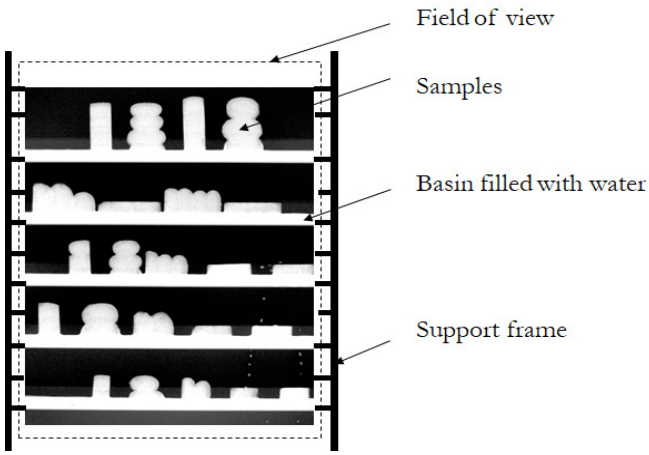

Figure 7.5: Schematization of the test setup used for capillary water absorption tests with neutron radiography

7.4.3. Scatter deviations and image analysis

For a qualitative and quantitative comparison, each radiograph needed to be filtered and corrected with the image correction tool "Quantitative Neutron Imaging" (QNI). The reason for this processing is that the attenuation is influenced by several deviations. The QNI program takes into account the CCD dark current, the background scattering, the sample scattering, the spectral effects, the intensity and the flat field corrections. The QNI program uses Monte-Carlo simulations to describe the scattering distribution of the neutron beam. The main reason for occurring deviations is that the neutrons are not only absorbed by or undisturbed passing through the sample's atoms, they can also be scattered. Many relevant materials (e.g. water) have even higher probability for scattering than for absorption. The scattered neutrons can hit the detector and overestimate the measured value. This pretended high transmission is misunderstood as a too small thickness or density of the measured samples [74].

Another reason for the deviation from the exponential law of attenuation is the poly-energetic spectrum of the neutron beam. Since most of the cross sections increase for lower energies in the thermal region, it is not possible to give them a general value. Also, the cross section of the detector is fixed, but what is measured by the detector will depend on the energy. These spectral effects affect the effective cross section, used for the evaluation of the quantitative mass thickness from the measured neutron flux.

In order to deal with the above-mentioned deviations, the QNI program considers the CCD dark current, the open beam and the black body radiographs. The open beam is the image obtained without any sample in the beam. The dark current images are obtained in the absence of beam illumination, measuring the background noise and camera offset with the shutters closed. For the measurements of the sample and background scattering components, two additional sets of images are required using a reference frame with and without the samples in the beam. In both cases, images are acquired with an interposed frame containing neutron absorbers or black bodies (BB). The BBs are opaque to neutrons; therefore, the measured neutron flux behind them can be interpreted as the scattered neutrons component. Before every new set of measurements, to obtain the black body images, the BB frame is placed close to the sample holder. Then, a set of open beam images with the interposed BB grid are acquired. This measurement aims at recording the scattering component of the background only, i.e. neutrons scattered at the shielding or the instrumentation and the light reflected from the mirror back to the scintillator. Then, the sample is placed onto the holder and a set of images with the interposed BB grid is acquired [138]. All corrections were based on an average of five radiographs per correction factor, to further optimize the obtained results.

After post-processing of these radiographs, further image operations were all performed using ImageJ. This software allows the calculation of the water content at every interlayer of a printed specimen, regardless of the applied print parameters, using a grey-level profile plot. The water content at the interlayer(s) of specimens with their front surface exposed to the water, was calculated after different exposure times (60 and 360 minutes). These calculations were made using a small rectangle grey-level profile plot (0.3 mm x H_{inter}), centered at every interlayer position. Together with the identification of the different interlayers and the representation of the water exposure surface as a blue zone, these rectangular zones are depicted in Figure 7.6A.

Furthermore, based on the same radiograph, a distinct water content profile along a horizontal axis was calculated, making use of another rectangle grey-level profile ($L_{specimen}$ x 0.3 mm, Figure 7.6B), located 0.5 mm above the water level and this at different times after water exposure (i.e. 15, 30, 60, 120 and 360 minutes). This method allows a more in-depth study and visualization of the water movement over time. When the samples were exposed to the water with their bottom surface, a distinct water content profile along a vertical axis was calculated using a rectangular zone (0.3 mm x $H_{specimen}$, Figure 7.6C) located at the middle of the sample. The latter was also calculated at different times after water exposure (i.e. 15, 30, 60, 120 and 360 minutes).

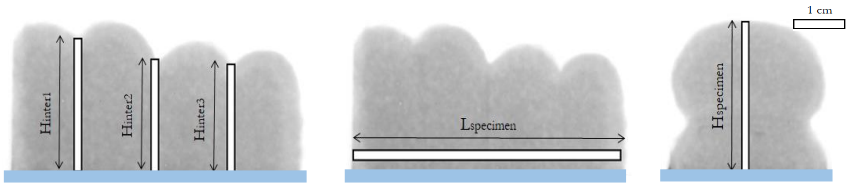

A **B** **C**

Figure 7.6: Visualization of the different zones, used for calculation of the water content: (a) rectangular zone (H_{inter} x 0.3 mm) used for the water content calculation at the interlayers (Water exposure surface: 'Front', (b) rectangular zone ($L_{specimen}$ x 0.3 mm) used for the calculation of the horizontal water profile (Water exposure surface: 'Front) and (c) rectangular zone (0.3 mm x $H_{specimen}$) used for the calculation of the vertical water profile (Water exposure surface: 'Bottom'). Blue zones represent the water exposure surface.

7.4.4. Visualization of water absorption

A qualitative analysis can be made based on the differential radiographic images, where dark grey zones correspond to places where water is available. In general, Figure 7.7 compares the capillary water uptake of the different test series (RS1, RS2, SAP, respectively) in case of two-layered specimens as a function of time, wherein the bottom area acts as ingress area.

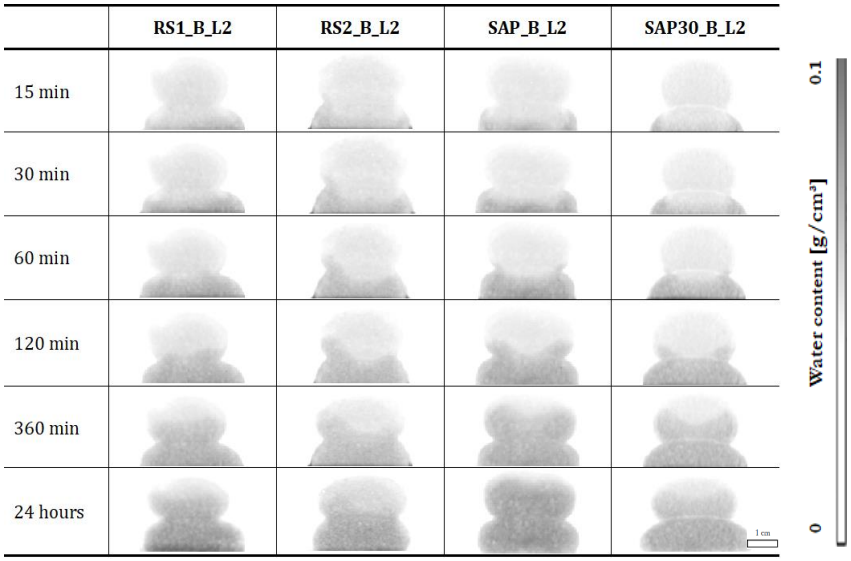

Figure 7.7: Neutron radiographs obtained as a function of water exposure time

Purely based on the visualization of the water font in two different samples per test series, one can conclude that, regardless of the print velocity and the mix composition, the water uptake during the first 15 minutes of water suction is the most pronounced at the sample sides, which can be attributed to possible artifacts and cracks induced by the manufacturing process. With an increased exposure time, the water front rises gradually in case of S1 samples and exceeds the interlayer over the entire width after 120 minutes, whereafter the water uptake proceeds in the same consistent way. After 24 hours, the entire specimen took up a certain amount of water. Whether the sample was completely saturated could not be quantified. An increased printing speed causes microstructural changes, as discussed in Chapter 6, which is translated by an irregular behavior of the water front. Within the first minutes after exposure, the water uptake at the sides is higher compared to the bulk material and this effect becomes more pronounced with enlarged exposure times. After 30 minutes, the water front exceeds the interlayer for the first time at the side surfaces. However, unlike S1 samples, after 120 minutes the water front in the bulk material did not yet completely cross this interlayer. After 24 hours, the shape of the water front is comparable for both printing speeds. Similar phenomena can be observed in case of three and four layered specimens and can be explained based on the results discussed in Chapter 4, wherein a higher printing speed causes a lower surface roughness as there is a higher kinetic energy working on the sand particles, forcing them deeper into the printed layer. As a consequence, the bulk

material of layers printed with a higher velocity contain a higher sand fraction and will be more compacted compared with the interlayer and with the outer sides of the printed layers, limiting the water ingress and creating a non-uniform water front. In case of a low printing speed, the composition of the bulk material, the material of the outer sides and the material of the interlayer zone are more or less comparable, resulting in a uniform water ingress over the whole specimen.

The addition of superabsorbent polymers does not change the cement matrix in between the SAPs, resulting in a water front behavior which is comparable with the reference material. However, the polymers will also swell in their respective macro pores and cause an increase in the measured capillary water absorption. The latter effect is also visualized in Figure 7.7, where the SAP containing elements have a darker grey level. The addition of SAPs enlarges the water uptake rate, which results in a higher level of the water front compared with the reference composition, irrespective of the exposure time. As a similar sample thickness is considered within every series (i.e. 2 cm), the latter phenomenon can also be confirmed in a qualitative way via neutron radiography as these radiographs (Figure 7.7, SAP_B_L2) are colored darker grey compared to the other series. As already discussed before, enlarged time gaps will reduce the interlayer quality. However, this phenomenon could not be observed when the bottom surface was submerged in water (Figure 7.7, SAP30_B_L2), although, based on the grey level, the water uptake tends to be lower compared with the zero-minute test series.

In service life, the front surface of printed structures will be most affected by environmental conditions (i.e. rain, wind, deicing salts, etc.). Inherent to its mix design and indifferent to the applied print parameters (i.e. speed or time gap), a similar ingress of the water front can be observed when the front surface is submerged to water (Figure 7.8). In case of two layered specimens (SAP_F_L2 and SAP_F_L4), the water front rises in a quite consistent way through the printed sample as a function of time. At first instance, these observations seem quite illogical, as a preferential water uptake through the interlayers was expected but these results can be explained based on the observations mentioned in Chapter 4. First of all, due to the short time gap of approximately 15 s, the interlayer of the printed specimens seems not to be deteriorated in a significant way resulting in an approximately homogenous material. Secondly, based on MIP measurements, the pores (amount, size and distribution) are comparable over the entire height of a two-layered specimen when a short time gap ($\pm$ 15 s) is considered between the printed layers. This phenomenon is also confirmed in this case, as from a neutron radiographic point of view it seems that there is no increased porosity at the

interlayer. On the other hand, Figure 7.8 represents the effect on the ingress capacity in case of an increased number of layers. The top layer, which is less compressed by the weight of the successive layers, will have the highest water uptake capacity. This is also visualized in Figure 7.8 where a higher water content results in a darker grey zone at the right of the sample SAP_F_L4 (corresponding with the top layer of the sample). In case of enlarged interlayer time gaps more differentiation in the pore size and pore size distribution between the different zones was observed, which consequently results in a preferential ingress through these interlayers (SAP30_F_L2, Figure 7.8). One can also see that after intrusion at the interlayer, the water ingress perpendicular to this layer is higher compared with the bulk material, although this is in direct contact with water. This confirms the conclusions of a higher porosity and a higher number of microcracks in the interlayer region. In case of an increased number of layers, the latter phenomenon is still observed, however, to a lower extend due to the higher compaction as a result of the additional layers.

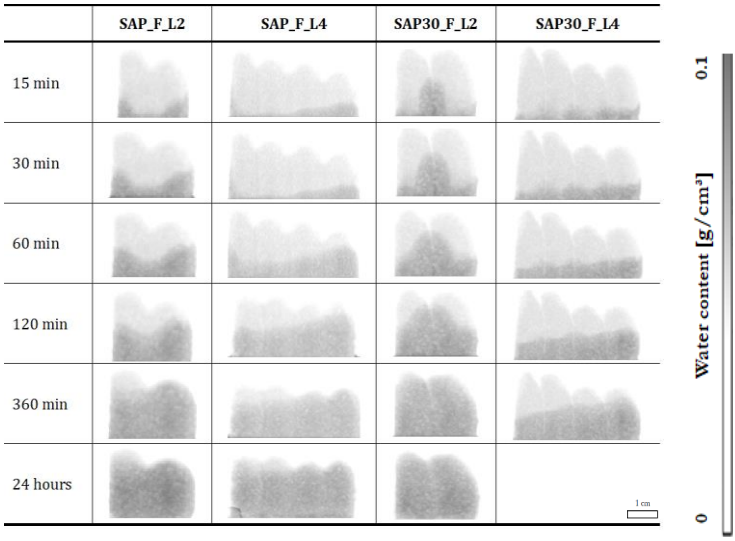

Figure 7.8: Neutron radiography obtained after different times of water exposure, represented for SAP_F and SAP30_F samples with 2 (L2) and 4 layers (L4)

7.4.5. Quantification of water absorption

Based on the obtained radiographs, it becomes possible to calculate the water content in an accurate way. This was also reported by several other researchers [139-141]. De Beer et al. [140] stated that a big advantage of neutron radiography, compared to gravimetric measurements, is that

quantitative distribution information can be obtained non-destructively instead of obtaining bulk measurements.

Capillary water ingress from the bottom surface

The water content as a function of the square root of time with the bottom area as exposure surface is represented in Figure 7.9. The amount of water is calculated over a small rectangular zone in the middle of the printed element as depicted in Figure 7.6C, considering the bulk material of the printed elements. The negative water content values, visualized in Figure 7.9, are impossible from a physical point of view but indicate the fact that a certain margin of error should always be considered with regard to the water content measurements.

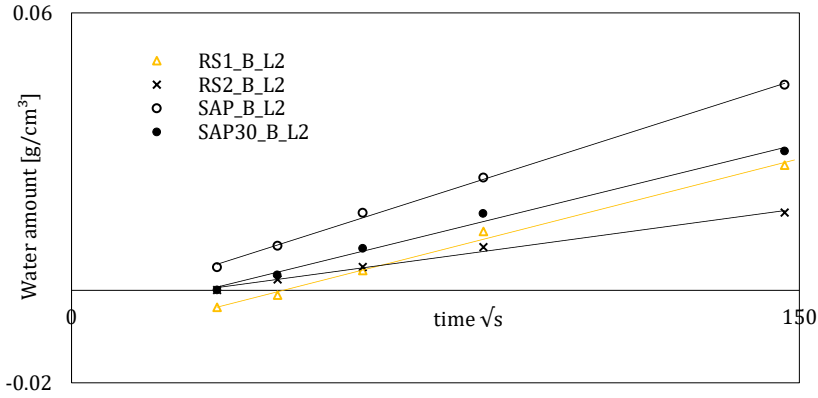

Figure 7.9: Water content [g/cm^3] as a function of water exposure time of elements printed with different print parameters and mix compositions. (Water exposure surface: 'Bottom', n=2), for samples with a different number of layers (L2, L3 and L4).

During the first 6 hours of water exposure, the transport is mainly driven by capillary absorption, resulting in an almost linear relationship between the water content and the square root of time for every test series. The slope of this linear increase gives more information about the water uptake rate. Based on a statistic analysis, one can conclude that only the water uptake rate for RS2_B_L2 differs in a significant way, although the slope of SAP_B_L2 is slightly higher. The water uptake rates of test series RS1_B_L2 and SAP30_B_L2 are similar. The microstructure of the specimens will not only affect the water uptake ability, but will also have an influence on the water content and the height of the water front, measured in the bulk material. First of all, if one compares the water content at predefined time gaps, the results differ in a more significant way. Samples containing superabsorbent

polymers show the highest amount of water (i.e. 0,044 g/cm^3), which is approximately twice the water content of SAP30 specimens. The water content of SAP30 elements does not significantly differ with the water content of the reference material printed with S1, stating that the negative effect of the weak interlayers is counteracted by the positive effect of the superabsorbent polymers. The highest printing speed has the lowest water uptake ability and consequently also the lowest water content after 6 hours of water exposure (i.e. 0.015 g/cm^3). These phenomena could be explained based on the microstructure of the samples. The addition of superabsorbent polymers increases the capillary porosity of the mix composition, as already discussed in Chapter 6. Secondly, SAPs are also able to take up some water by themselves. The combination of both phenomena results in a higher water uptake. Enlarging the time gap in between the extrusion of two successive layers, dries the printed surface, and will counteract the beneficial effect of the SAP addition, causing a similar behavior as RS1_B_L2 samples. An increased printing speed densifies the bulk material due to the higher forces working on the sand particles. As for this representation the amount of water is measured in the middle of a printed specimen, with the bottom area as water exposure surface, this denser bulk material blocks the water uptake, resulting in a lower water content and water uptake speed. This phenomenon was also depicted in Figure 7.7, where the sides of the surface showed a more preferential ingress of water.

Secondly, the above-mentioned phenomena are also confirmed when comparing the height of the water front, reached in the bulk material, obtained as a function of time and represented in Figure 7.10. Considering the same sample height, irrespective of the test series, the water front reached 70% of the sample height, compared with 55% and 48% in case of RS1_B_L2/SAP30_B_L2 and RS2_B_L2, respectively. In absolute values, this results in a height of 13 mm or 9.2 mm for samples printed with a low or high printing speed, respectively. Comparing these values with the ones represented in Table 7.2, one can conclude that, although both calculation methods only consider the bulk material of a printed specimen, gravimetrical water absorption methods result in an overestimation of the water front height. However, it is important to note that the comparison between both calculation methods is not straight forward. First of all, gravimetrical measurements are performed on samples covered with aluminum tape, which ensures unidirectional water ingress from the bottom surface. Secondly, as the samples are drilled from original two-layered specimens, the effect of the side surfaces is excluded which, as depicted in Figure 7.7, will have a significant influence especially in case of higher printing speeds. The latter also explains the higher overestimation in case of test series RS2_B_L2.

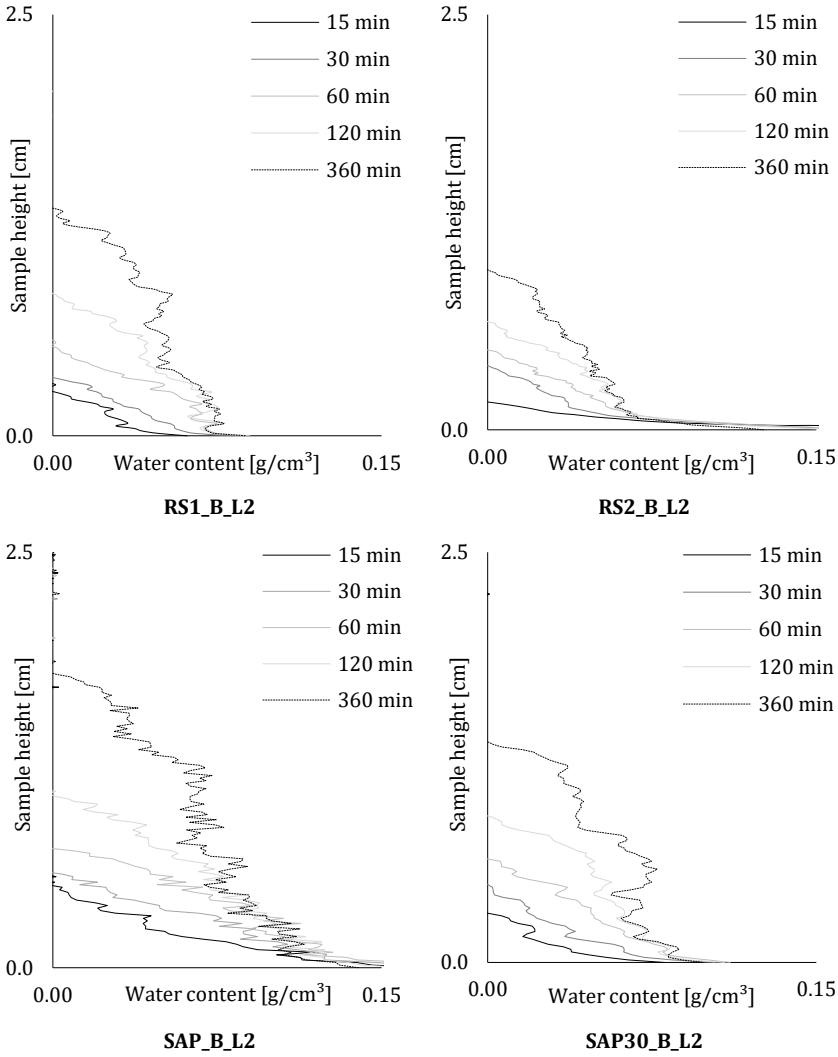

Figure 7.10: Evolution of the vertical water profiles of two-layered specimens as a function of time (n=2, error bars are left out for clarity)

Regardless of the print parameters or the mix composition, similar conclusions can be drawn between the different test series with regard to an increased number of layers. In general, a higher layer amount decreases the water uptake velocity. The deposition of a new layer will increase the loading on the substrate layer by ρ.g.h, depending on the density of the material and the height of a single layer. The height of the layers is kept constant during extrusion (i.e. 1 cm), so one can assume that the load will increase linearly with the number of layers, which would then lead to a linear densification of

the substrate layer and a consequently similar blocking of the water ingress when the samples are submerged with their bottom surface. However, this assumption could not be verified based on Figure 7.11. Although the water uptake velocities are linear regardless of the number of layers, only the speed is significantly higher for two-layered specimens. Specimens containing 3 or 4 layers do not significantly differ, nor in water ingress rate, nor in water content after 6 hours of water immersion. The author assumes that this can explained based by the variation in material density. However, the extend of this variation is not considered in depth within this doctoral thesis.

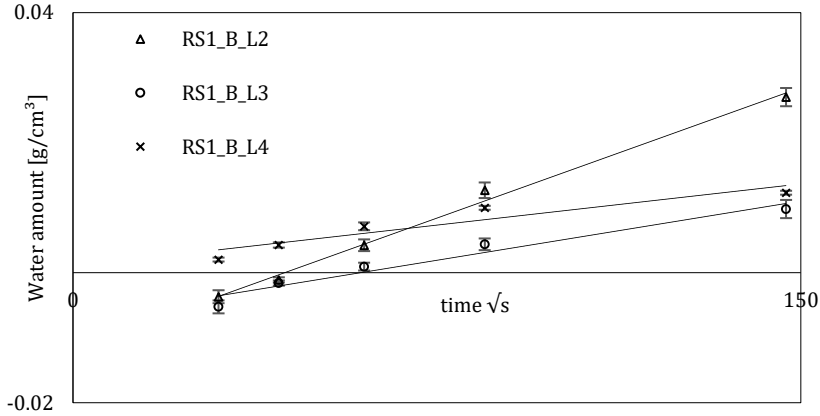

Figure 7.11: Water content [g/cm^3] of RS1_B as a function of water exposure time (Water exposure surface: 'Bottom', n=2, error bars indicate standard deviation), for samples with a different number of layers (L2, L3 and L4).

Capillary water ingress from the front surface

Regardless of the printing speed and the mix composition, the interlayers between the printed layers do not show any preferential water uptake when the front surface is exposed to the water, which can be attributed to the short interlayer time gap, causing an approximately homogenous material. This phenomenon is already depicted in Figure 7.8, but is also confirmed when plotting the water profiles as a function of time (Figure 7.12). The latter shows a higher water content in the bulk material of the layers compared with the interlayer zone, however, this effect is smoothened with larger exposure times. Due to a similar capillary pore diameter of the top and bottom layer, as discussed in Chapter 6, the water amount at different water exposure times is comparable in the bottom and top layer of the printed element. Based on Figure 7.13, the same conclusions are valid in case of an increased amount of layers. The bulk material shows a higher water content

compared to the interlayer zones. In case of a multiple layered specimen, the water content increases with the specimen height, which confirms the fact that the lowest layer is more compacted due to the additional weight of the upper layers. The same conclusions can be made for the different test series.

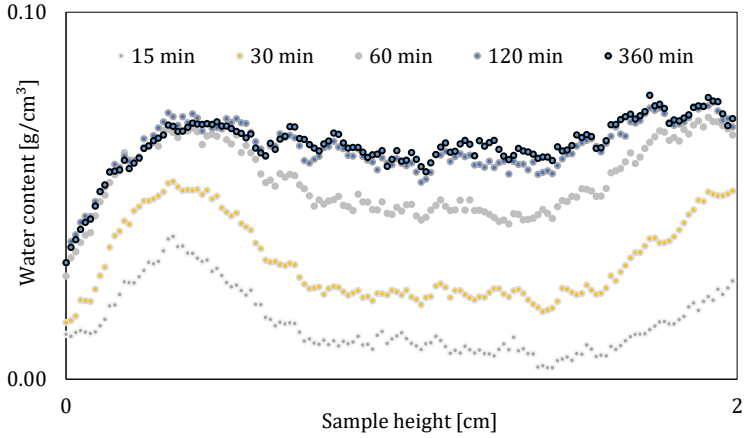

Figure 7.12: Water profiles as a function of time, in case of a two-layered RS1_F_L2 specimens (water exposure surface: 'Front', n=1)

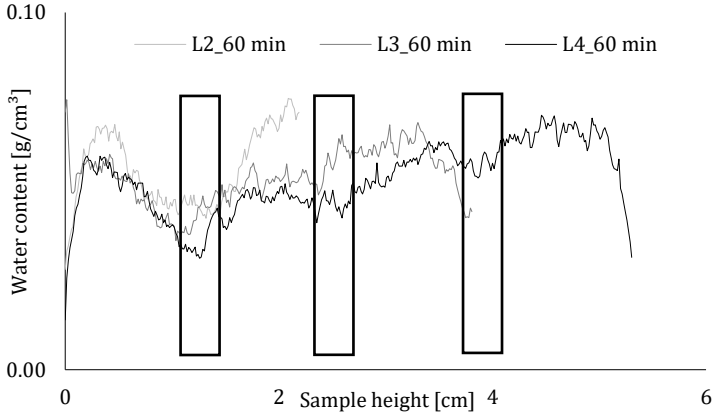

Figure 7.13: Water profiles, plotted after 60 min of water exposure, in case of different layered RS1 specimens (water exposure surface: 'Front', n=1). The interlayers of the specimen are indicated within the black rectangles.

The lowest water content cannot be observed in the lowest layer, which was expected due to the higher densification and the increased load. Possible explanations could be the higher amount of microcracks within the first printed layer, especially for zero-minute time gaps, increasing the water uptake ability or changes in material density.

Figure 7.14 represents the water content at the interlayer in case of multiple layered specimens after 360 min of water exposure where Interlayer1 (Figure 7.6A) represents the lowest interlayer in the specimen and Interlayer3 the highest one. As stated before, comparing the different interlayers, Interlayer1 shows the lowest water content as this zone is the most compacted. Similar conclusions can be made regardless of the printing speed and the mix composition. However, the water content at the interlayers themselves will be lower in case of higher printing speeds and higher when adding superabsorbent polymers to the composition due to microstructural changes.

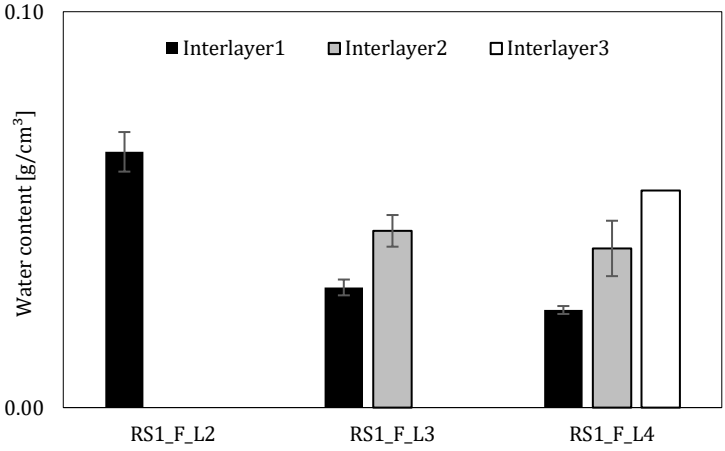

Figure 7.14: Water content at the interlayers in case of different layered RS1 specimens after 360 min of water exposure ('Water exposure surface: 'Front', n=2, error bars represent standard deviation).

The above-mentioned conclusions are obtained based on samples printed with a zero-minute time gap. When the interlayer time interval increases, the quality of the interlayer decreases (Chapter 4), not only as a result of a lower surface moisture, but also as more voids and microcracks are likely to occur. The effect of this weakened interlayer was not pronounced when the bottom layer of the specimens was exposed to water. However, when the interlayers are in direct contact with water (i.e. front surface as exposure surface), this effect becomes more pronounced and the weakened interlayer will take up

more water. One can also observe the preferential ingress through the interlayer, as the water content at the interlayer itself remains more or less constant over the entire exposure time.

More specifically, the water content at the interlayer is almost doubled compared with the bulk material of the layers (i.e. 0.08 g/cm^3 and 1.41 g/cm^3 in the bulk and at the interlayer, respectively). This phenomenon is represented in Figure 7.15.

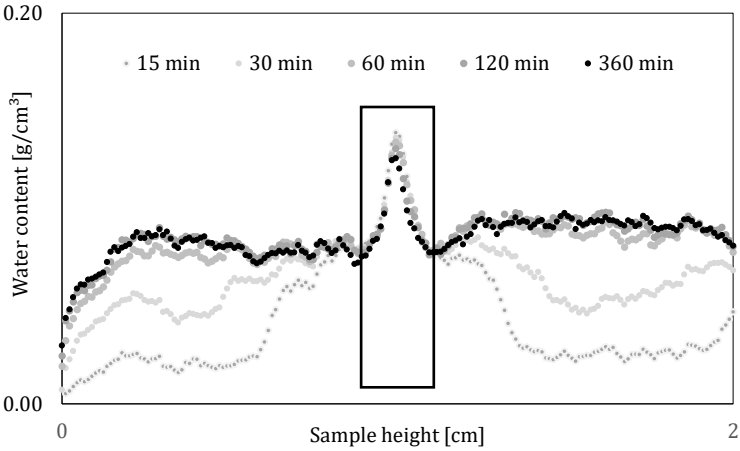

Figure 7.15: Water profiles, as a function of time, in case of a two-layered SAP30 specimen (water exposure surface: 'Front', n=1). The interlayer of the specimen is indicated within the black rectangle.

The latter phenomenon is also observed when the water content at the interlayer itself is calculated and compared for two-layered samples with superabsorbent polymers, printed with a zero-minute (SAP) and 30-minutes time interval (SAP30, Figure 7.16). After an exposure time of 60 minutes, the water content at the interlayer itself is almost a triplicate, showing the preferential water uptake through the interlayer and through the cracks in the vicinity of this interlayer. However, after 6 hours of water immersion, the water content at the interlayer is comparable between the test series. The fast water ingress in first instance will saturate the interlayer faster.

Based on Figure 7.15 one can also conclude that the transport of water is mainly driven by capillary absorption. Although the interlayers are weak spots and more prone to cracks and void formation, the water front increases in a uniform way in the non-saturated parts of the bulk material.

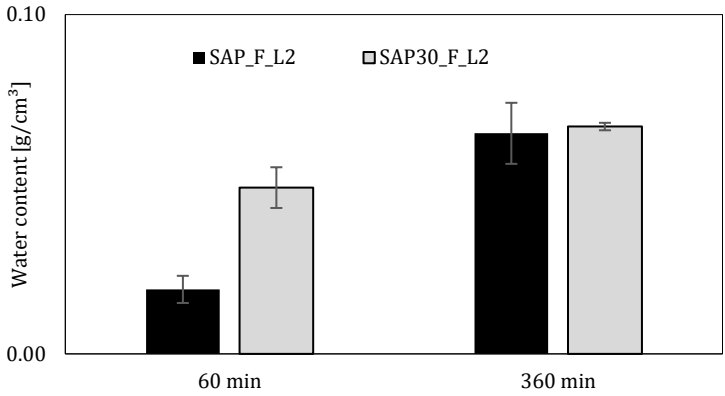

Figure 7.16: Water content at the interlayer of two layered specimens, printed with a zero-minute and 30-minute time gap after 60 and 360 min of water exposure (water exposure surface: 'Bottom', n=2)

An increased number of layers will result in similar findings about the preferential water ingress at the interlayers (Figure 7.17 and Figure 7.18). The effect is more pronounced at Interlayer3 as this interlayer is less loaded compared with the other layers. However, after 30 minutes, the preferential water absorption at the interlayers is slowed down, as depicted in Figure 7.18. After 30 minutes of water exposure, the water front is more or less uniform, considering the fact that the highest layer is less loaded and contains a higher amount of water, which is in contrast with the results of specimens printed with a zero-minute time gap.

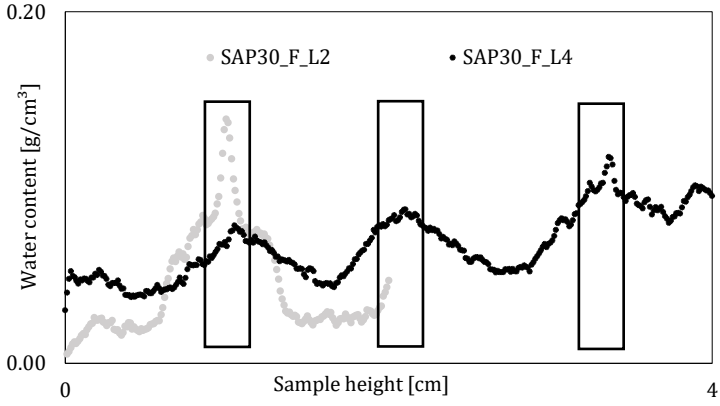

Figure 7.17: Comparison between the water profiles, obtained after 15 minutes of water exposures for two and four layered SAP30_F specimens (water exposure surface: 'Front', n=1). The interlayers of the specimens are indicated within the black rectangles.

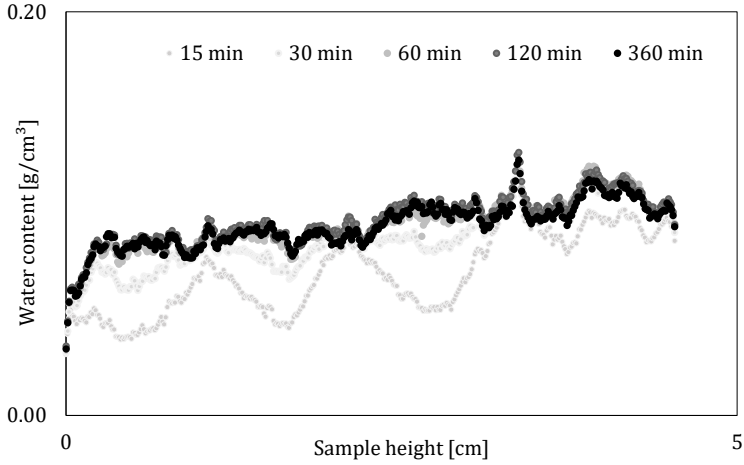

Figure 7.18: Water profiles, as a function of time, in case of SAP30_F_L4 specimen (water exposure surface: 'Front', n=1, error bars are left out).

7.5. Conclusions

Based on the observations represented within this chapter, the following conclusions can be drawn with regard to the water ingress capacity of printed elements, manufactured with different print process parameters and mix compositions with and without the addition of superabsorbent polymers. First of all, based on the gravimetrical measurements, one can conclude that the water absorption capacity of printed elements is higher compared with mold-cast samples due to the higher porosity induced by the manufacturing process. Secondary, the initial absorption rate decreases for an increasing time gap, irrespective of the applied print velocity. This phenomenon can be explained by the absorption capacity of the specimens, which decreases with an increasing time gap due to the formation of larger voids. Finally, the secondary absorption rate tends to increase for enlarged time gaps, which states the assumption that the water transport due to diffusion becomes more important. Based on neutron radiography measurements, the following trends could be observed: *(i)* when the bottom surface of the samples was submerged in water, the addition of SAPs increased the water uptake ability as a result of the changing microstructure. However, regardless of the print process parameters (print speed and interlayer time interval), deterioration as a result of this layered fabrication process could be observed. However, when the front surface was exposed to water, this preferential ingress at the interlayer became more pronounced in the first hour. This effect was smoothened when the interlayer was saturated and the bulk material absorbed more water.

Chapter 8

Transport mechanisms in 3D printed materials

8.1. Chloride ingress

Chloride ions are one of the most harmful substances in terms of durability of reinforced concrete as they can initiate and propagate corrosion of the reinforcement. The integration of reinforcement in printed elements is nowadays still under development. However, as this integration is required to ensure a full incorporation of this technique in the construction industry, this subject will gain increased importance in the near future.

8.1.1. Origin of chloride ions

Chloride ions can originate from two different sources; they are either (unintentionally) incorporated during mix preparations or they are transported into the hardened material from the surrounding environment.

Chlorides which are part of the mix composition can be present in the mixing water or originate from contaminated constituents/admixtures. By paying attention during mix preparation, this chloride source can be easily avoided. Unlike conventional concrete, printable materials can be characterized by a high amount of binder and the replacement of cement by supplementary cementitious materials (SCM's) will become more important in the upcoming years. Although these materials have environmental benefits as they allow

the (partial) replacement of Portland cement, they may also lead to a new source of chlorides [142]. On the other hand, some supplementary cementitious materials like e.g. fly ash [143], are known to have a beneficial influence on the chloride diffusion by reducing the permeability of the matrix and increasing the chloride binding potential.

In most cases, durability problems caused by chlorides are a consequence of an (additional) transport of chloride ions from the environment. NBN EN 206 [144] differentiates between chlorides coming from sea water and chlorides coming from another source as for example deicing salts. Depending on the location, the salinity of seawater equals 3.5%, which corresponds with 35 g dissolved salts per liter, predominantly sodium and chloride ions. Marine structures are therefore more prone to chloride ingress. Even without direct contact with seawater, they might still be exposed to airborne chlorides. The main source of chlorides aside from seawater is chlorides from deicing salts, which are typically based on NaCl, $CaCl_2$ or $MgCl_2$, and frequently used in strong winters to ensure safer roads. The deicing salt melts snow and ice, thereby creating a chloride solution. The chlorides can either directly penetrate the concrete or can be transported into the matrix when the structure is near the splash zone of vehicles. In addition, chlorides can also be present in salty groundwater or waste water from industry. However, these chloride sources are only of miner importance.

8.1.2. Chloride transport in concrete

Chlorides are mostly dissolved in water when they penetrate the cementitious matrix, which mainly occurs through the capillary pores, in addition to transport via cracks and other defects. In general, four main mechanisms will govern the ingress of chloride ions:

- Convection is a moisture-content-driven mechanism. Internal equilibrium is created by water movement towards zones with a lower moisture content. Convection can occur when concrete is not completely saturated and when concrete is drying. In that case, the chloride containing pore liquid will be transported to the evaporation surface, causing a concentration of chlorides (wick action). Savija et al. [145] explicitly include capillary absorption in this category. Water together with chlorides will be sucked in the capillaries due to the surface tension. These capillary absorption forces are also present in cracks. Depending on the crack width, this results in a quick transport of chlorides through the concrete cover layer.

- Diffusion is a concentration-driven mechanism indicating that chlorides will diffuse from a location with a high chloride concentration to a location with a lower concentration. This mechanism will take place through the pore water. As a consequence, the diffusion rate will depend on the saturation degree of the concrete and will occur fastest in fully saturated concrete.

  The diffusion process can be described by Fick's laws. In steady state conditions, meaning that there is no time dependency of the concentration, the diffusion process is described by Fick's first law:

$$J = -D_{SS}\frac{\delta C}{\delta x} \qquad [8.1]$$

  Where J [mol/m^{2}s] is the diffusion flux, D_{SS} [m^2/s] the steady state diffusion coefficient, C [mol/m^3] the ion concentration and x [m] the distance from the exposed surface. In concrete specimens however, the chloride concentration will change over time, resulting in a transient or non-steady state diffusion process. Assuming that there is mass conservation, the latter can be described by Fick's second law (Eq. [8.2]), where D_{NSS} [m^2/s] is the non-steady state diffusion coefficient.

$$\frac{\delta C}{\delta X} = \frac{\delta}{\delta x}\left(D_{NSS}\frac{\delta C}{\delta x}\right) \qquad [8.2]$$

  The solution of Fick's second law (Eq. [7.3]) is usually found by considering the following assumptions:

  - D_{NSS} is independent of x (homogenous material) and time (permanent diffusivity);
  - The chloride surface concentration C_s [mass%] is constant over time;
  - The initial chloride concentration C_0 [mass%] differs from zero.

$$C(x,t) = C_0 + (C_s - C_0)\left(1 - \mathrm{erf}\left(\frac{x}{2\cdot\sqrt{D_{NSS}\cdot t}}\right)\right) \qquad [8.3]$$

  This model, based on Fick's second law, is only a simplification of real-life conditions as in reality the diffusion coefficient also depends on the time, temperature, W/C-ratio, chloride concentration,

chloride binding, etc. However, it can serve as a good approximation for relatively short laboratory experiments [125, 146].

- Permeation is a pressure-driven mechanism and water will be transported through a porous medium under a hydraulic pressure. Permeation can be described by Darcy's law, which allows the calculation of the permeability coefficient. This parameter depends on the pore structure of the porous medium and the viscosity of the liquid or gas [125].

- Migration is a potential-driven mechanism where chloride ions migrate under the influence of an electric field.

The process which mainly governs the chloride transport depends on the boundary conditions as well as on the moisture content and its distribution in the concrete element. For conventional concrete, the penetration of harmful substances occurs initially through capillary absorption (Figure 8.1A). Thereafter, the transport is assumed to be primarily governed by diffusion. However, due to non-uniform distribution of the pores within printed specimens, these aspects have to be relooked, particularly for enlarged time gaps. A possible scenario of the transport mechanism is schematically shown in Figure 8.1. The interconnected pores at the interlayer of digitally manufactured specimens combined with the microcracks created at the surface may lead to a sudden water uptake by absorption or capillary suction (Figure 8.1B). At this stage, movement of the waterfront can depend on various factors such as initial moisture condition of the interface, interlayer time gap, printing speed, etc. Thereafter, the water migrates towards the bulk material from three sides, i.e. the initially exposed surface as well as the saturated bottom and top interface. Like conventional concrete, the ionic transport at this stage will be primarily diffusion controlled (Figure **8.1**C) [2]. Since printed elements are typically made from mixtures with low W/C-ratios, the diffusion into the bulk material can be a slow process. However, at the same time, it must be noted that during the diffusion stage, since the ionic transport progresses through the top and bottom surfaces of the interlayer as well as via the exposed side of the printed element (Figure 8.1C), the effective total exposed surface area is much higher compared with the one-dimensional diffusion that may occur in conventionally cast concrete. This may increase the diffusion rate in the bulk material. Further, if the non-uniform distribution of the pores is considered, the transport mechanisms will become even more complex.

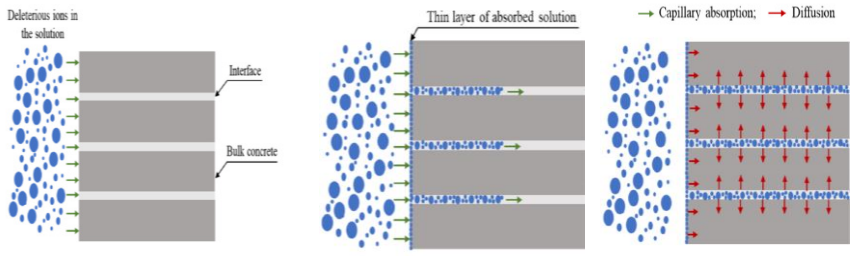

Figure 8.1: Different stages in the transport of harmful ions in printed concrete: Stage I – Printed elements exposed to solution containing harmful substances (A), Stage II – Additional capillary absorption of ions through the interfaces (B), Stage III – Inwards penetration, primarilly diffusion controled from three exposure sides [2]

8.1.3. Test methods for chloride transport

Different test methods are available to evaluate the chloride resistance of concrete. For a complete overview, the reader is referred to the work of Stanish et al. [147]. In the current work, only the main test methods are listed. They can be divided in diffusion or migration tests, performed both in steady and non-steady state conditions.

Steady state diffusion test

In a steady state diffusion test, the concrete sample is connected with two reservoirs on the opposite sides. The reservoirs both contain a NaOH+KOH solution to simulate the bulk (pore) solution of the cementitious material. A concentration gradient is created by adding NaCl to the upstream reservoir. To maintain this concentration gradient, the solutions in the upstream and downstream reservoir have to be checked and renewed on a regular base. Once a constant increase of the cumulated concentration is obtained in the downstream reservoir, the diffusion coefficient can be calculated based on Fick's first law. As this natural diffusion process can take several months, this method is not commonly applied as a standard method due to practical reasons [148, 149].

Non-steady state diffusion test

In current non-steady state diffusion tests according to NT Build 443 [150], also denoted as the bulk diffusion test, chloride penetration is achieved by immersing the specimen in a NaCl-solution for a certain period (Figure 8.2). To ensure unidirectional penetration, all surfaces, except the exposed one, are coated with an epoxy resin. After a certain exposure period (minimum 35

days), samples are taken out of the solution, after which the chloride profile is determined through grinding off layers from the surface downwards and chemical analysis of the obtained powders. By fitting this chloride profile to Fick's second law, the non-steady state diffusion coefficient can be obtained.

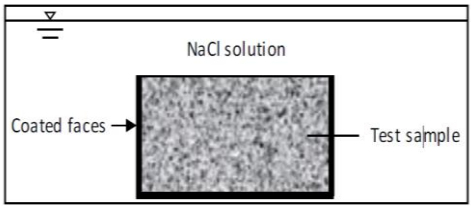

Figure 8.2: Schematic representation of the non-steady state diffusion test [150]

Steady state migration test

In general, migration tests were developed to accelerate the chloride transport. According to NT Build 355 [151], the steady state migration test has a similar test setup as the steady state diffusion test, except for electrodes which are inserted in the upstream (cathode) and downstream (anode) reservoir. Between the electrodes, a potential is applied to create an electric field and to accelerate the chloride transport. The solutions in the up- and downstream reservoir still need to be renewed frequently. A steady state migration coefficient can be calculated using the Nernst-Planck equation [152].

Non-steady state migration test

In non-steady state conditions, Rapid Migration Tests (CTH tests, Figure 8.3) are frequently used in accordance with NT Build 492 [153]. The principle of this test is mainly the same as was explained for the steady state migration test. However, in contrast with the latter, the solutions do not have to be renewed and the testing time will not exceed 24 hours. Once the potential is removed, the specimens are axially split and the chloride ingress is determined by spraying 0.1M of silver nitrate solution on the surfaces. The penetration depth is then used to calculate the non-steady state migration coefficient.

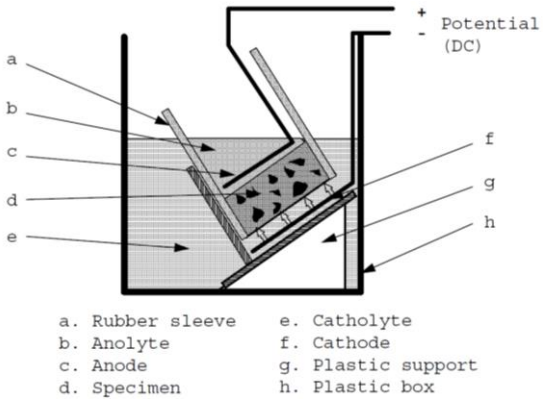

Figure 8.3: Schematic representation of the non-steady state migration test [153]

Comparison and evaluation of different tests methods

Diffusion tests are able to simulate natural conditions but the measuring time can be quite long. To speed up the transport of chloride ions, a potential can be applied, however, this will not generate real-life conditions.

Aside from the different transport mechanisms, varying concentrations of test solutions are often used. In addition, these concentrations are mostly higher than what can be found in marine environments. This can make it difficult to compare test results to one another and to realistic situations.

The rate in which chloride ions penetrate into the concrete also depends on the chloride binding. Chloride binding (chemical and physical) enables to lower the free chloride concentration in the pore solution and slows down the chloride ingress. For faster methods, like the non-steady state migration tests, steady state conditions will not be obtained and chloride binding will not have fully occurred, which influences the results.

The above-mentioned test methods are valid in case of traditional concrete, considering a homogenous material with isotropic properties. Their efficiency and accuracy in case of printed specimens is not proven yet. However, as there are no durability standards available nowadays for printed cementitious materials, they serve as the only evaluation methods for chloride penetration in case of printed specimens.

8.1.4. Chloride penetration quantification methods

The chloride penetration and corresponding concentration can be obtained by several test methods. The colorimetric method by spraying silver nitrate and powder grinding combined with a chemical analysis are the most common ones, although the latter can be time consuming. In case of powder grinding, the collected powder is also a combination of both the aggregate and cement paste. Since the chlorides are primarily contained in the paste, the aggregate dilutes the sample. It would be possible to reduce the amount of material and time needed to complete the test if it were possible to focus the examination of chlorides within the paste [154]. One solution to this problem would be the use of imaging techniques capable of mapping chemistry and discern between the aggregate and the paste with minimal human intervention. Electron Probe Micro Analysis (EPMA), Laser-induced Breakdown Spectroscopy (LIBS), Scanning Electron Microscopy with electron dispersive spectrometer (SEM-EDS) or micro X-ray fluorescence (μXRF) are examples of these non-destructive imaging techniques. However, as the latter require expensive equipment, they are not included in this overview.

Colorimetric method using silver nitrate

A basic visualization of the chloride ingress can be obtained using a colorimetric method. After splitting a specimen perpendicular to its exposure surface, a silver nitrate ($AgNO_3$) solution of 0.1M is sprayed on the split surfaces. In the chloride containing zone, silver and chloride ions will react resulting in the formation of a white precipitate (silver chloride (AgCl)). In the chloride-free zone, silver will react with OH^- ions of the cementitious matrix, forming silver oxide. This zone will have a brownish color.

It is important to note that the chloride-free zone is not completely free of chlorides; the chloride concentration has to be higher than a certain boundary concentration before silver chloride is precipitated. This boundary level equals, as stated by Real et al. [155], 0.01% up to 1.14% by mass of cement and depends on various factors such as cement type, the use of supplementary cementitious materials, W/C-ratio, concrete age, $AgNO_3$ concentration and amount, etc. Nonetheless, it was pointed out that as long as the attack only consists of chlorides, the colorimetric method is a practical, low-cost and efficient qualification technique.

Powder grinding and chemical analysis

One of the most commonly used methods to analyze the chloride ingress in concrete is through chloride profiling. This method is commonly used when a non-steady state diffusion test is performed, as the chloride profile is required to calculate the non-steady state diffusion coefficient. In order to obtain a chloride profile, material is ground off from a concrete sample in layers parallel to the surface which was exposed to the chloride solution. The grinding is usually performed with a diamond coated drilling head. The thickness of the layers can vary, but is commonly in the range of 0.5 – 2 mm. After grinding, powders are dried in an oven at 105 $\pm$ 5°C, followed by a chemical analysis to measure the chloride content. The most common methods to determine the chloride content are the Rapid Chloride test (RCT) [156] and the performance of potentiometric titrations [157]. While being fast, the accuracy of the RCT is generally lower compared with potentiometric titrations, neither does it allow to determine the free chloride content, only the total chloride content.

8.1.5. Factors affecting chloride ingress

Internal factors will affect the transport properties of chloride ions; especially the pore structure and the presence of (micro)cracks will play a major role. On the other hand, various environmental factors such as CO_2 concentration, temperature, relative humidity (RH) and exposure condition cannot be neglected as they will have a great influence on the chloride diffusivity in concrete specimens and the amount of chlorides that can penetrate into the material. Additionally, also the mix composition will have a significant influence on the ingress of chloride ions. The addition of silica fume for example will densify the cement matrix and will lower the ingress of chloride ions. However, as a different mix composition is not the scope of this doctoral thesis, this subject will not be further discussed in the following sections.

Pore structure

The capillary porosity and the interconnectivity of these pores are the most crucial characteristics of the pore structure related to diffusivity. This phenomenon is stated by Yang [158], who observed a linear relationship between the migration coefficients (steady state and non-steady state) and both the capillary pore volume and critical pore diameter which represent the grouping of the largest fraction of interconnected pores. In addition, the migration coefficient also turned out to be linearly related to the thickness and porosity of the interfacial transition zone (i.e. zone between cement paste and aggregates) [159]. As the porosity of the latter increases, the penetration

of destructive agents facilitates. Regarding digital fabrication, the pores are distributed through the sample in a non-uniform way, with an increased porosity at the interface between two printed layers. This creates an additional preferential ingress path for chloride transport, which was also observed in recent research performed by Bran Anleu [160].

Crack formation

Crack formation cannot be avoided for structures in service and has a significant influence on the chloride diffusion. As already stated before, printed elements are more prone to crack formation for two reasons. First, due to the absence of a protective mold and the direct exposure to environmental conditions after extrusion, the plastic and drying shrinkage rate of printed samples increases, causing more micro-cracks at the surfaces of the element. Secondly, due to the differential shrinkage between two superpositioned layers, more cracks are created at the interfaces themselves. Both phenomena will increase of the amount of preferential ingress paths in digital fabricated elements and enlarge the chloride penetration rate compared with uncracked concrete [161].

Environmental factors

Different researchers [162, 163] highlighted the importance of environmental factors such as temperature, relative humidity, exposure time, etc. More specifically, a higher temperature and relative humidity cause faster penetration and larger chloride accumulation as higher chloride concentrations can be dissolved in the pore water.

Another important factor is the intrusion of CO_2. Although the CO_2 concentration in the air is limited, especially in laboratory conditions ($\pm$ 0.03%), the penetration can start immediately after printing. In case of elongated time gaps, the intrusion can also occur through the surface of the interlayer before the deposition of a new layer. Liu et al. [164] observed a reduction in chloride penetration when the chloride ingress is preceded by carbonation. Nevertheless, it was observed that the length of the convection zone was prolonged.

8.2. Carbonation

8.2.1. Origin of carbonation

Carbonation of concrete is a process in which (atmospheric) carbon dioxide reacts with the cementitious matrix. As CO_2 from the surrounding air enters the cement matrix through diffusion, it dissolves in the pore water forming carbonic acid (H_2CO_3).

$$H_2O + CO_2 \rightarrow H_2CO_3 \quad [8.4]$$

The formed carbonic acid reacts with portlandite ($Ca(OH)_2$), present in the cementitious matrix, to form calcium carbonate.

$$H_2CO_3 + Ca(OH)_2 \rightarrow CaCO_3 + 2H_2O \quad [8.5]$$

The consumption of portlandite withdraws hydroxyl ions from the pore solution and reduces the pH from 13 to below 9. When the carbonation front reaches the reinforcement, this pH drop destroys the passivation layer of the steel and initiates corrosion.

Portlandite is not the only constituent that reacts with CO_2. Indeed, as the carbonation process continues, calcium carbonate crystals enclose the portlandite, after which the carbonation of calcium silicate hydrates (CSH) becomes dominant [165]. This reaction causes the formation of silica gel and calcium carbonate. Depending on the tricalcium silicate (C_3S), dicalcium silicate (C_2S) and gypsum content of the cement, other reactions may occur as well. Furthermore, the formed calcium carbonate, which has a very low solubility, will precipitate in the pores, decreasing the amount of smaller pores and lowering the carbonation rate [161]. It is important to note that the phenomena taking place will depend on the used binder, however, as a changing mix composition is not the scope of this doctoral thesis, the effect of the latter on carbonation is not further explored.

The above-mentioned mechanisms indicate that the carbonation resistance of concrete basically depends on two aspects, i.e. the concrete susceptibility to CO_2 diffusion and the amount of available matter that can carbonate. This dependency is clear from the well-known square-root time relationship for carbonation mentioned in Visser [166].

$$x_c = \sqrt{\frac{2 \cdot D_C \cdot C_S \cdot t}{a_c}} = \sqrt{\frac{2 \cdot C_S \cdot t}{R_{carb}}} = A \cdot \sqrt{t} \quad [8.6]$$

With x_c [m] the carbonation depth, D_c [m/s^2] the diffusion coefficient, C_s [kg/m^3] the CO_2 concentration at the surface, a_c [kg/m^3] the amount of carbonatable matter per unit volume, t [s] the exposure time and R_{carb} [$(kg/m^3)/(m/s^2)$] the carbonation resistance. The amount of carbonatable matter is time dependent and will increase as a function of time. An accurate determination of the latter is very difficult and requires extensive thermogravimetric analysis (TGA) for different predefined exposure times.

8.2.2. Test methods for carbonation

As the atmospheric CO_2 content is relatively low ($\pm$ 0.03%), a lot of researchers accelerate the carbonation process in laboratory conditions and subject concrete specimens to elevated CO_2 concentrations ranging from 1% to 10% [115, 167, 168]. However, a concentration higher than 3% is not advised, as this causes important chemical changes, which results in an underestimation of the realistic carbonation depth.

The carbonation depth can be visualized in accordance with RILEM CPC 18 [169] by spraying phenolphthalein on the split surfaces of a concrete specimen. Phenolphthalein has a pink/purple color in alkaline environments. When the pH drops below 9.2 approximately, it becomes colorless. It should be noted that this technique does not allow to determine the total CO_2 ingress as there might be a pH drop below the color change boundary. In addition to this colorimetric test method, carbonation can also be evaluated based on pH measurements of the pore solution by performing thermogravimetric analysis, X-ray diffraction, etc.

8.2.3. Factors affecting carbonation

The deterioration process of concrete carbonation includes physical and chemical processes, which are highly influenced by internal and external factors. The composition and microstructure of the cementitious material largely affects the diffusion of CO_2. These internal factors are related to the mix properties (i.e. W/C-ratio, the addition of SCMs, etc.), the porosity of the material and the presence of (micro-)cracks. However, as a different mix composition is not the scope of this doctoral thesis, this subject will not be further discussed in the following sections. In addition to the internal factors, also the influence of external factors such as relative humidity, CO_2 concentration and the presence of other aggressive ions are significant.

Crack formation

Cracks form preferential ingress paths for the penetration of potential aggressive substances. Cracks in concrete can be subdivided in structural and non-structural cracks. Structural cracks are caused by an insufficient amount of reinforcement, low strength of the concrete, excessive loading, etc. Non-structural cracks on the other hand are mainly initiated by a physical impact (drying shrinkage), a chemical effect (carbonation shrinkage) or a thermal effect (influence of freeze/thaw cycles, temperature gradient). In printed elements, additional cracks will be introduced both on the surfaces and at the interlayers as a result of the applied print process parameters (printing speed, time gap, the additional load executed by printing successive layers, etc.) and the lack of a protective molding.

Alahmad et al. [170] investigated the influence of micro-cracks based on their width and regardless the crack width, the crack path was always carbonated. However, when the crack width became smaller than 9 μm, no carbonation could be observed in the mortar perpendicular to the crack path [170]. Wang et al. [171] on the other hand observed for both flexural and shear cracks a CO_2 penetration perpendicular to the crack. The effect of cracks induced by drying shrinkage was less pronounced. However, in terms of printed concrete, where the surfaces are immediately exposed to environmental conditions, $C0_2$ ingress due to shrinkage related crack formation will become more important.

Relative humidity

Relative humidity is one of the most essential parameters defining whether the carbonation reaction will occur or not. In the first stage of hydration, the pore walls are covered with a thin water film caused by water vapor. The hydration products of cement (mainly CH) and the atmospheric CO_2, which is transmitted into the pores, are dissolved in this water film and react to form calcium carbonate. If the relative humidity is too low (below 50%), the area and thickness of this water film are too small to support the carbonation reaction of the concrete. On the other hand, a high environmental humidity (> 70%) delays the CO_2 diffusion, as the capillary pores are blocked by the presence of water. Under high relative humidity condensation of capillary water, vapor occurs in abundant pores and the generated pore water decreases the pore interconnectivity. Due to the smaller CO_2 transmission coefficient in liquid water, the carbonation rate decreases under high relative humidity. The highest values for carbonation are found when the relative humidity ranges between 50% and 70%.

Temperature and CO_2 concentration

In general, increasing the temperature accelerates carbonation though not in the same way for different cement types due to their change in chemical composition (different amount of portlandite and C/S ratio). In case of CEM I, a linear increase could be observed. Secondly, increasing the CO_2 concentration normally causes a larger carbonation rate. Chen et al. revealed a power function between the carbonation depth and the CO_2 concentration. If the CO_2 concentration increases, a large CO_2 concentration gradient is established over the concrete surface and more carbon dioxide will diffuse into the material.

8.3. Resistance to freeze/thaw deterioration

8.3.1. Origin of freeze/thaw deterioration

Freeze/thaw (F/T) cycles can cause severe damage of structures in cold regions. Over the past century, different researchers attempted to explain how the water-ice phase transition creates freezing-related stresses in the pore space. Hirschwald [172] stated that the 9% volume increase during the solidification of water was the main cause of frost damage. This implies that when a material is 91% water saturated, the volume increase can no longer be accommodated and the material is supposed to suffer frost damage.

Although most researchers agree upon this general definition, there is still a lot of discussion about the underlying deterioration mechanism. Powers [79] stated that the volumetric expansion causes water to be pushed into the smaller capillary pores. This flux could generate a hydraulic pressure that was assumed to exceed the tensile strength of the concrete. This theory enabled Powers to explain the higher frost resistance of air-entrained concrete, assuming that the higher concentration of air voids in air-entrained concrete enables to relief the hydraulic pressure in a more efficient way. If less voids are present in the matrix, the risk of higher pressures in the smaller capillaries would increase.

However, contradictory observations caused Powers to review his theory. Powers and Helmuth [173] reduced the air void spacing to enable an enhanced flux of pore water into the voids. Simultaneous length change measurements revealed a contraction larger than the thermal contraction, while a reduction in expansion by the hydraulic pressure was expected. Moreover, as the cooling was stopped, no relaxation was observed in the concrete containing air voids. According to the hydraulic pressure theory

(Figure 8.4A), a stress relaxation should occur as the water makes its way to the larger air voids. Later, these observations were explained by the introduction of osmotic pressures (osmotic pressure theory). This principle states that a higher alkali concentration is created in larger air voids by the freezing of water, which increases the alkalinity of the remaining water nearby the larger voids. This is supposed to create a chemical potential that causes water to be drawn to the zones with a high alkali content in order to restore the thermodynamic equilibrium. If no adequate air void system is present, the alkali concentration gradient will remain and the osmotic pressure will further increase, resulting in cracking of the concrete [174].

The most plausible explanation for F/T deterioration is however founded on the ability of a crystal to push particles away (crystallization theory, Figure 8.4B). In contrast with the previous mechanism, non-frozen water would rather be attracted to the position where freezing occurs first. The freezing point of water in a pore is known as being inversely proportional to the pore radius, indicating that the freezing of water will start in the larger pores. As soon as the water in the larger pores is frozen, additional water is transported from smaller pores causing further crystal growth in the larger pore. The ice crystals can keep on growing due to the pressure difference between the larger and neighboring smaller pores, which is a consequence of the surface tension between water and ice. When the resulting tensile stresses in the cementitious matrix would become too high, it can induce internal cracking. However, this depends primary on the transport rate of water (vapor) between the pores. In normal circumstances, the excess pressure is not very high in concrete and the ice pressure mechanism only becomes important in case of longer freezing periods [167].

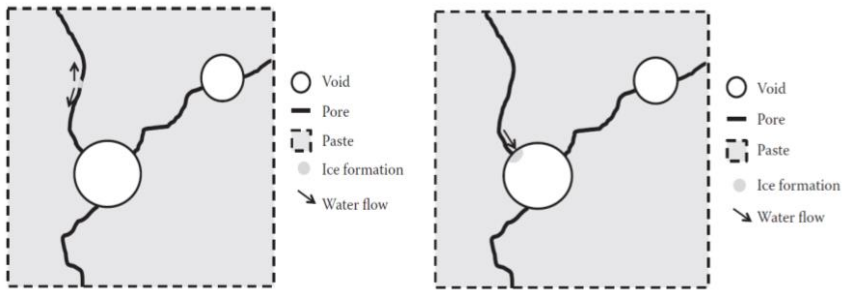

Figure 8.4: Water flow due to ice formation in the capillary pores (hydraulic pressure theory, A) and water flow due to ice formation in the air voids (crystallization theory, B)

8.3.2. Test methods

Various standardized methodologies and specifications exist to measure the frost resistance of conventional concrete, however their applicability to 3D printing is still not assured. In general, current test methods developed for concrete differ in sample form and size, saturation degree, temperature profile, duration and number of F/T-cycles, and whether they use deicing salts or not. For example, NBN B 15 – 231 [175] prescribes specimens which, in fully saturated state, are exposed to 14 F/T cycles of 24 hours each, with temperatures varying from -15°C to 20°C and evaluates the frost resistance based on the mass change before and after freeze/thaw attack. ASTM C666 [176] on the other hand considers two testing methods (A and B) depending on whether freezing is made in air or water. The F/T cycles herein consist of alternately varying the temperature from 5 to -18°C in less than 5 hours. The cylindrical samples are assessed for frost resistance after 300 F/T cycles or when their relative dynamic elasticity modulus, calculated based on ultrasonic measurements, falls below 60%. Test procedures with deicing salts (i.e. NBN EN 1339 [177]) evaluate the frost resistance commonly based on surface degradation. However, within the scope of this doctoral research, only the resistance against frost attack without deicing salts is considered.

8.3.3. Factors affecting freeze/thaw deterioration

Water/cement ratio

The W/C-ratio is a critical parameter in the F/T resistance of concrete elements. A low W/C-ratio lowers the amount of capillary pores and the permeability of the material. It could be reasoned that this will lead to higher hydraulic pressures when ice formation is initiated because the pressurized water cannot easily escape. In practice, however, a lower W/C-ratio will lead to a higher frost resistance. The reduction in pore volume results in a reduced amount of freezable water in the concrete. As a result, the tensile stresses in the concrete matrix, as caused by a limited amount of freezable water, will not cause significant damage in the case of a low W/C-ratio [178]. Additionally, water enclosed in the narrower capillaries will freeze at a temperature lower than the ambient temperature, resulting in less freezable water.

Air void system

In addition to the amount of free expansion volume, which can be deducted from the degree of saturation, the spatial distribution of this expansion volume is also important. The available expansion volume is only effective when it is easily and rapidly accessible for pressurized water or expanding ice. In order to improve frost resistance, air-entraining agents are quite often used in concrete, providing a large amount of small air voids evenly distributed within the cementitious system. A key parameter concerning the successful application of air-entraining agents is the spacing factor, which is related to the maximum distance to the nearest air void. Values below 200 µm are typically considered to provide adequate frost resistance in conventionally cast concrete [178]. However, recent research on 3D printed concrete [179] revealed that the application of these air entrainment agents reduces the interlayer bond strength with 100% and 22% after 56 or 112 F/T cycles, respectively. In addition, it also detrimentally affects the durability, while the layers themselves showed better protection against F/T cycles.

External factors

Some external factors will also influence frost damage to concrete structures:

- Freezing temperature: the lower the temperature, the more damage can be expected;
- Freezing rate: the faster the temperature drops, the more damage can be expected;
- The number of F/T cycles: significant frost damage does not always occur during the first cycles, but rather after a number of repeated cycles. This phenomenon can be attributed to the pump effect where small meso-gel pores are filled with water which were initially not filled during capillary absorption. The additional water absorption can lead to the development of micro-cracks.

The latter was also observed in one study reporting the F/T resistance of 3D printed concrete. Tian and Han [180] noticed a significant increase in porosity after approximately 25 F/T cycles (Figure 8.5). The higher porosity, initially induced by the print process, lowers the distance between the pores. Unlike conventionally cast concrete, this results in a better pressure distribution during the first F/T cycles.

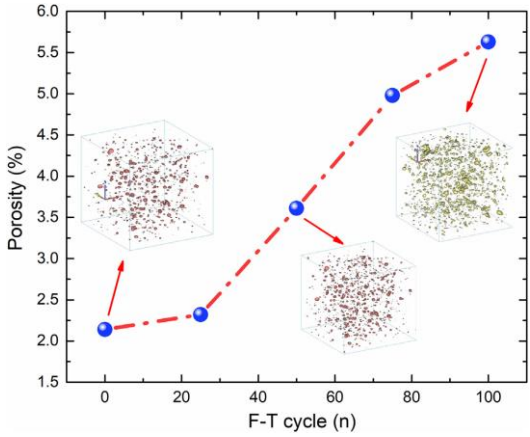

Figure 8.5: Relationship between the porosity (> 0.1 mm) and F/T cycles in 3D printed specimens [180]

8.4. Materials and methods

8.4.1. Chloride diffusion test

The chloride diffusion test is performed according to CEN/TS 12390-11 [181]. A similar test procedure is followed for both conventionally cast and four-layered specimens. The latter were printed with 3 different time gaps (T0, T30 and T60) and both print speeds (S1 and S2), following the procedures as described in Chapter 3. The first and fourth layer of the printed samples were mainly used to avoid side effects, as the ingress of aggressive substances through the interlayer is the primary scope of interest. The chloride diffusion test was only performed for mixtures fabricated with the reference composition, without any additions.

After a hardening period of 21 days in standardized conditions (20 $\pm$ 2°C, 60 $\pm$ 5% RH), samples were dry-cut into specimens with a total length of 40 mm, regardless the fabrication method (Figure 8.6A-Figure 8.6B). Dry-sawing was performed to avoid any disruptions due to changes in the moisture condition. In case of 3D printed samples, As depicted in Figure 8.6D, 3D printed samples were only sawn in the direction orthogonal to the print direction and the side surfaces were not smoothened. To ensure unidirectional diffusion, 5 of the 6 sample sides were coated with epoxy resin (Episol Designtop SF, Resiplast NV), applied in two layers with a waiting time of 24 hours in between (Figure 8.6C-Figure 8.6D).

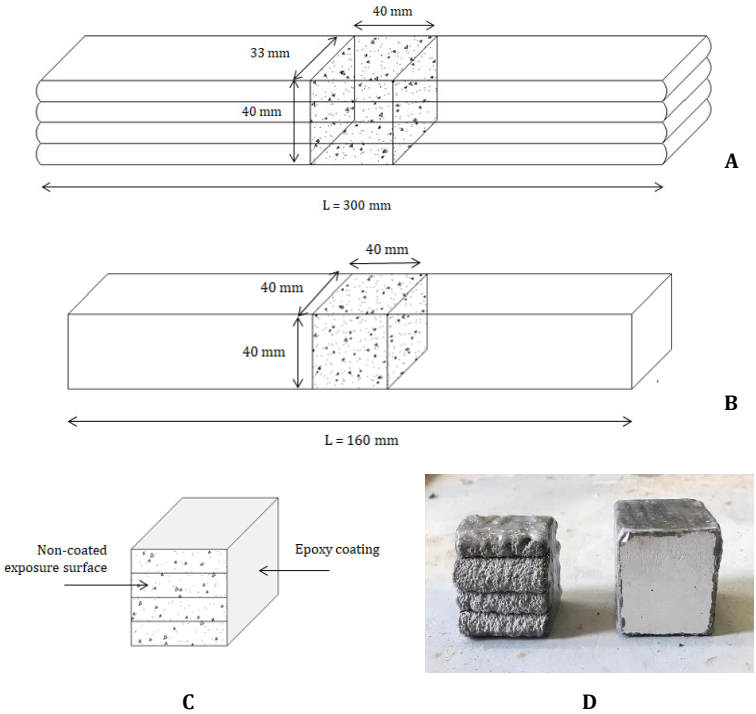

Figure 8.6: Schematic representation of a four-layered printed sample (A) and a traditionally cast specimen (B), schematic representation of the sample preparation, indicating the coated and non-coated surfaces (C) and the original samples (D)

At the age of 28 days, samples were immersed in a 3% by mass aqueous sodium chloride (NaCl) solution for a minimum and maximum of 7 and 70 days, respectively. The used Cl^- concentration corresponds with the normal Cl^- concentration in sea water according to CUR report 100. Evaporation of the Cl^- solution was prevented by storing the samples in sealed boxes and the solution was refreshed on a monthly base. The uncoated sample side was placed upwards in the solution. Contradictory to CEN/TS 12390-11, samples were not saturated prior to testing, this in order to simulate more realistic exposure conditions. Furthermore, as a faster chloride penetration is expected in case of printed elements due to the higher porosity, samples were taken out of the solution starting at one week after exposure instead of 90 days as prescribed by [181]. To ensure an accurate comparison, the same procedure was followed for molded specimens. The ingress of chloride ions was examined in two ways. The chloride penetration front was visualized based on a colorimetric method and a quantification of the chloride content was obtained by performing potentiometric chloride titrations.

Colorimetric method

On a weekly base, three samples of every test series were split perpendicular to their print direction until 10 weeks after chloride exposure. On the freshly broken specimens, an aqueous silver nitrate solution ($AgN0_3$, conc. 0.1 mol/l) was sprayed. Afterwards, two well-defined regions could be easily distinguished. The chloride penetration was evaluated based on both the penetrated area and the penetration depth. These parameters were determined by applying a custom-made plugin in ImageJ, after imaging both halves of the split surfaces and taking into account the following rules of practices:

- The brightness and contrast of every picture was adjusted in ImageJ to ensure similar conditions for all pictures;
- The interfacial transition zone serves as a preferential ingress path for chlorides. However, due to the limited aggregate size, the effect of the latter is rather limited. Therefore, when an aggregate was positioned on the boundary of the chloride penetration front, the author decided to include the aggregate in the chloride containing zone;
- Only the deepest penetration point was considered. Local spots, through which the chlorides did not penetrate, were excluded from the analysis. These spots could be attributed to a local finer pore structure or a higher moisture content which encouraged the formation of hydration products.

The quantification of the penetrated area is visualized in Figure 8.7A and is calculated as the ratio between the chloride containing area (hatched area, Figure 8.7A) and the total area of the split surface, both measured with ImageJ. A similar procedure was followed for cast and printed specimens. The chloride penetration depth in case of a printed sample was measured only at the second and third layer in order to exclude side effects. Therefore, every millimeter, three points were placed on the photograph, indicating the outer boundaries of the sample (Point 1 and 3, Figure 8.7B) and the boundary between chloride-affected and chloride-free zone (Point 2, Figure 8.7B). The penetration depth is quantified as the distance between Point 1 and 2.

As one assumes a homogenous material in case of cast samples, the chloride penetration depth was measured over the entire sample height and the measuring points were placed at a 2 mm interval (Figure 8.7C).

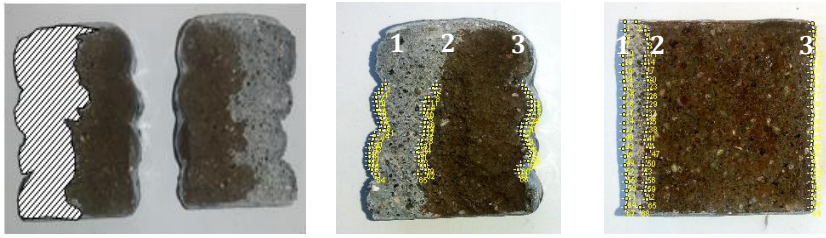

A B C

Figure 8.7: Chloride penetration area (A) and a representation of the measuring points used for ImageJ analysis in case of printed specimens (B) and cast specimens (C)

Potentiometric titrations

The colorimetric method was used to give a qualitative idea about the chloride ingress, rather than delivering quantitative results. Therefore, one specimen per two weeks of exposure (5 specimens in total per test series, until 10 weeks after chloride exposure) was used to perform potentiometric titrations on ground powders obtained from the second interlayer. This method allows to obtain the total amount of chlorides, however, local abnormalities that will alter the results such as cracks or carbonation cannot be identified with this technique [154].

At the second interlayer, nine layers parallel to the exposed surface were grinded. Due to the irregular shape of the printed surface, the first layer had a depth of 5 mm, while the depth of the remaining layers equaled 3 mm. Grinding was performed with a diamond coated drilling head (diameter 8 mm), mounted on a column drill. After grinding, the powders were stored in an oven at 105°C for at least 7 days. The grinding process is visualized in Figure 8.8.

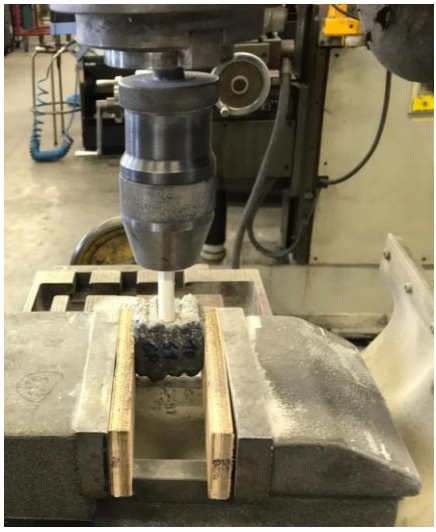

Figure 8.8: Grinding process with an 8 mm drill

The total chloride content of each layer was determined by acid-soluble extraction in a nitric acid (HNO_3) solution, followed by a potentiometric titration [125, 167]. The latter was performed by using a Metrohm 862 Compact Titrosampler automatic titrator with 0.01 mol/l silver nitrate as titration solution. The automatic titration device adds $AgNO_3$ to the test solution until the point of equivalence of the reaction ($Ag^+ + Cl^- \rightarrow AgCl \downarrow$). This point is characterized by a sudden change in the potential of the solution, measured by means of a combined silver ring electrode. Before the automatic titration could be executed, the exact concentration of the $AgNO_3$ solution was determined based on a calibration. The measured $AgNO_3$ volume was implemented in Eq. [8.7] to calculate the exact concentration, assuming that the concentration and volume of the standard NaCl calibration solution equal 0.01 mol/l and 0.005 l, respectively.

$$\text{Conc } AgNO_3 \text{ (mol/l)} = \text{Conc NaCl (mol/l)} \cdot \frac{\text{Vol NaCl (l)}}{\text{Vol } AgNO_3 \text{ (l)}} \qquad [8.7]$$

Based on this calibration, the resulting acid-soluble chloride content of each layer was calculated according to Eq. [8.8].

$$c_t = \frac{35.45 \cdot V_{AgNO_3} \cdot c_{AgNO_3}}{m_{powder}} \qquad [8.8]$$

Within this equation c_t [m% binder] is the acid-soluble chloride content, 35.45 [g/mol] the atomic mass of chloride, V_{AgNO3} [ml] the consumed volume of $AgNO_3$ solution, c_{AgNO3} [mol/l] the exact concentration of $AgNO_3$ after calibration and m_{powder} [g] the mass of concrete powder in the extraction solution.

A complete titration profile was obtained by plotting the measured acid-soluble chloride content against the depth below the exposure surface. The non-steady state diffusion coefficient D_{NSS} [m^2/s] and the surface concentration c_s [m% binder] were estimated by fitting Eq. [8.3] to the measured chloride contents by using non-linear regression analysis. The latter was performed according to the method of least squares fit using SPSS Statistics 27 software. In order to have an appropriate fit and to take into account the fast chloride ingress due to the use of non-saturated samples, the first point of the profile (i.e. 0-5 mm) was omitted from the overall shape of the profile.

8.4.2. Carbonation test

Carbonation tests were performed in accordance with CEN/TS 12390-10 [182], both on four-layered printed specimens and cast samples, with similar dimensions as depicted in Figure 8.6. The carbonation resistance was tested for elements printed with both the 2D- and 3D-print equipment. 2D printed specimens were manufactured with 3 different time gaps (T0, T30 and T60) and both print velocities (S1 and S2), while for 3D printed elements only one printing speed and two time gaps (T0 and T30) were considered. The resistance against carbonation was evaluated for REF and REF_3D mixtures, according to the procedures described in Chapter 3. The first and fourth layer of the printed samples were again used to avoid side effects.

After a hardening period of 7 days, specimens were dry-cut and coated with epoxy (Episol Designtop SF, Resiplast NV), which was carried out in two layers on 5 of the 6 sample sides with a waiting time of 24 hours in between. After a hardening period of 12 days, the coated elements were placed in a carbonation chamber (20 $\pm$ 2°C, 60 $\pm$ 5% RH) containing 1 vol% CO_2. It is important to note that this procedure (i.e. curing time of the samples and time of testing) deviates from the one specified in the standard, but can be justified as follows. It is generally known that the carbonation front proceeds when all the material is carbonated. Due to the high binder content in the reference composition and as Portland cement is the only binder component, the amount of material to carbonate is high. Assuming that the carbonation front

would proceed slowly, the specimens were therefore already placed in the carbonation chamber after a hardening period of 12 days.

After 1, 3, 12 and 24 weeks of exposure, three samples of every test series were split perpendicular to their print direction and a 1% phenolphthalein solution was deposited on the freshly broken surfaces. The carbonated area stayed colorless, while the non-carbonated region turned purple. A quantification of the penetration depth is determined based on ImageJ analysis, with the same plugin and the same assumptions as used for chloride intrusion. The penetrated area was not considered for evaluating the carbonation resistance.

8.4.3. Freeze/thaw resistance

The resistance against freeze/thaw was evaluated according to NBN B 15 – 231 [175]. For this durability evaluation, two-layered specimens and traditionally cast specimens were considered, manufactured according to the procedures as described in Chapter 3. The printed specimens were manufactured with three time gaps (T0, T30 and T60) and both printing speeds (S1 and S2). Two-layered specimens were chosen to ensure similar mechanical test procedures as described in Chapter 4.

Sample preparation for evaluating the resistance against freeze/thaw is depicted in Figure 8.9. After a hardening period of 28 days, the specimens were dry-cut into specimens with a total length of 40 mm (Figure 8.6), following the same procedure as described in section 8.4.1. Submerging the specimens in water for 7 days ensured complete saturation (i.e. mass difference between two successive measurements within 24 hours lower than 0.1%). The temperature within the low-temperature chamber reached a minimum and maximum of –15°C and 20°C, respectively within every cycle of 24 hours.

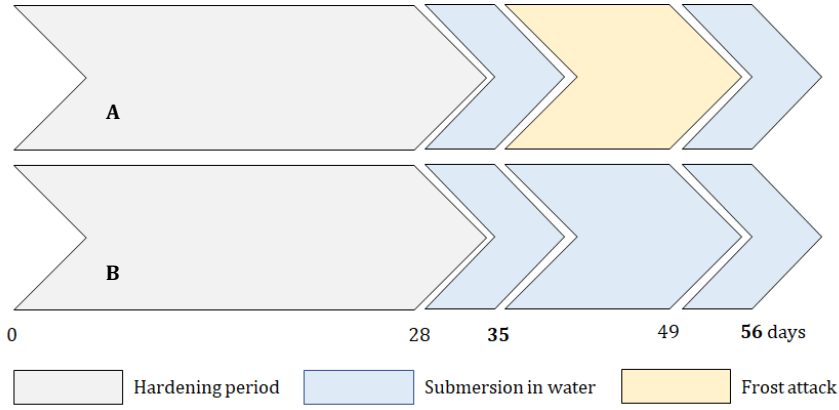

Figure 8.9: Test procedure to evaluate the resistance against freeze/thaw for samples exposed to (A) and not exposed to (B) frost attack. The days indicated in bold represent the days the specimens were weighed

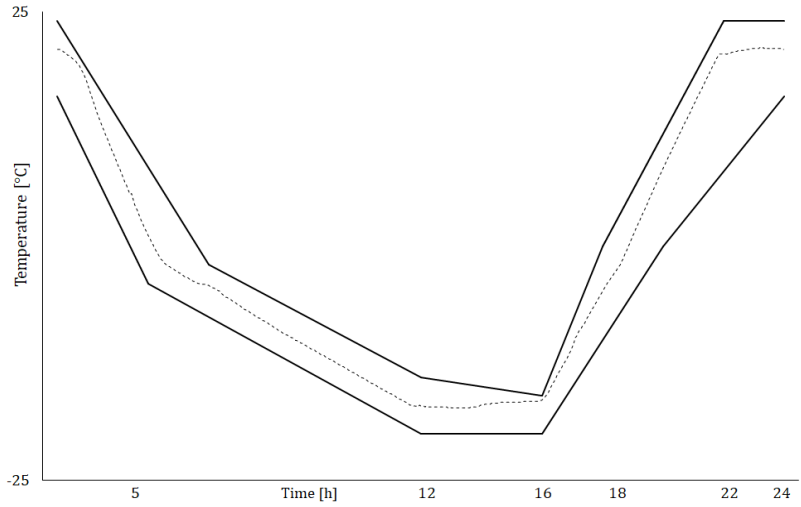

Figure 8.10: Temperature curve of one freeze/thaw cycle

The resistance against freeze/thaw was first evaluated based on the difference in mass (Eq. [8.9]), measured before and after 14 F/T cycles of at least 9 saturated samples per test series. In this formula M [%] is the mass loss and m_x [g] represents the weight of the samples after x days (i.e. 35 and 56 days, respectively, depicted in bold in Figure 8.9).

$$M\ [\%] = \left[\frac{(m_{56} - m_{35})}{m_{35}}\right] \qquad [8.9]$$

After mass determination, cylindrical specimens were drilled from the samples to determine the compressive strength in triplicate per test series, according to the procedure described in Chapter 4. After drilling, samples were stored in climatized conditions (20 ± 2°C, 60 ± 5% RH) for 7 days. The loss in compressive strength was calculated based on Eq. [8.10], where D [%] is the loss percentage and $f_{c,0}$ [N/mm^2] and $f_{c,14}$ [N/mm^2] are the compressive strength of samples without and with F/T deterioration, respectively.

$$D\ [\%] = \left[\frac{(f_{c,0} - f_{c,14})}{f_{c,0}}\right] \qquad [8.10]$$

Ultrasonic measurements served as third evaluation method of the F/T resistance. These measurements were performed in triplicate. Ultrasonic measurements were carried out with a pocket ultrasonic tester (Matest, ± 0.1µs resolution), measuring the transit time of an ultrasonic wave when the ultrasonic impulse amplitude equals 1000V. Transit time measurements were done by placing two contact points on both sides of the test specimen. As the measurements are very sensitive, and could be affected by any unevenness of the surface, both contact points were positioned on the cut surfaces. In addition, also the orientation of the contact points (perfectly perpendicular or slightly oblique) could disturb the measurements. To ensure accurate measurements, measurements were only performed parallel to the printed layers, placing the contact points on the sawn sides of the specimens. The dynamic E-modulus can be derived using Eq. [8.11], where C [m/s] is the ultrasonic transit speed, E_d [MPa] the dynamic Young's modulus, ν [-] the Poisson coefficient (0.2) and ρ [kg/m^3] the density of the sample. The length of the samples was determined before the ultrasonic measurements to calculate the transit speed of each specimen based on the measured transit time.

$$C = \sqrt{\frac{E_{d,x}}{\rho}\frac{(1-\nu)}{(1+\nu)(1-2\nu)}} \qquad [8.11]$$

Based on these measurements, the relative dynamic elastic modulus E could be derived based on Eq. [8.12], where E [-] is the relative dynamic modulus, $E_{d,o}$ and $E_{d,14}$ are the modulus obtained for saturated samples without and with frost deterioration, measured at the age of 56 days.

$$E\ [-] = \left[\frac{E_{d,14}}{E_{d,0}}\right]^2 \cdot 100 \qquad [8.12]$$

8.5. Chloride ingress

8.5.1. Colorimetric measurements

A first visualization allows the classification of the profiles based on the location and depth of the chloride ingress. Class A represents a homogeneous, equidistant penetration front from the exposure surface onwards over the entire height of the sample (Figure 8.11A). Samples of class B show a more local penetration at the interlayer, while characteristic samples for class C show chloride penetration up to the opposite coated side through the interlayer (Figure 8.11B and Figure 8.11C). Class D represents a full penetration through the entire bulk material (Figure 8.11D). Table 8.1 represents the percentages of the different samples, both cast and printed, belonging to the different classes.

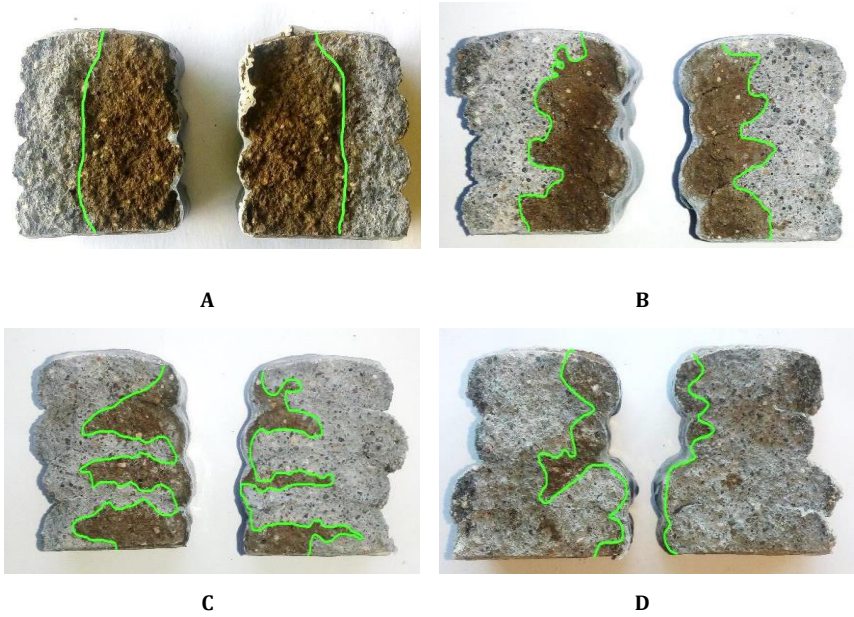

Figure 8.11: Classification of the chloride penetration profiles in four classes: (A) equidistant penetration from the exposure surface, (B) local penetration at the interlayer, (C) chloride penetration up to the opposite coated side through the interlayer and (D) chloride penetration up to the opposite coated side through the bulk material

An equidistant penetration front can be observed in case of mold-casted concrete and samples printed with a zero-minute time gap indicating that for both manufacturing techniques a homogenous material is obtained. On the

other hand, as the time gap increases, the penetration at the interlayer becomes more pronounced. For the highest time gaps (i.e. 30 and 60 minutes), chloride penetration through the entire interlayer and/or bulk material can be observed. In case of higher printing speeds, the samples are more classified in the higher regions as a result of the higher total porosity.

Table 8.1: Classification of the different samples (%), produced by traditional casting (CAST) or by printing with different time gaps (T0, T10, T30 and T60) and printing speeds (S1 and S2) (n=30)

	A	B	C	D
CAST	100 %	/	/	/
T0 S1	100 %	/	/	/
T30 S1	40 %	50 %	7 %	3 %
T60 S1	6 %	50 %	30 %	14 %
T0 S2	87 %	13 %	/	/
T30 S2	27 %	60 %	10 %	3 %
T60 S2	/	60 %	30 %	10 %

Figure 8.12 represents the area penetrated by chlorides, starting from one week till ten weeks after exposure. Regardless of the printing speed, one can conclude that traditionally cast specimens are less prone to chloride ingress compared with printed specimens. The average chloride penetration for cast samples equals 17%, while in case of printed elements approximately 40% is penetrated after only one week. This observation can be explained based on different phenomena. First of all, as stated in Chapter 6, cast elements have a lower porosity as a result of the fabrication process. This in contrast with printed specimens, were more voids are introduced at the interlayer between two successive layers. Secondly, formwork protects mold-casted specimens from drying within the first 24 hours, lowering the formation of shrinkage related cracks. Compared with conventional concrete, the printed surfaces also have more micro-cracks as a result of the print process (i.e. time gap) and the applied nozzle geometry. More specifically, the elliptical nozzle shape will induce a gravity induced flow after extrusion, altering the deformation of the freshly deposited material and the formation of cracks, both at the top and side surfaces. However, as the samples were not saturated, chloride containing water will be sucked into the capillary pores as a result of the surface tension. Thereafter, the chloride rate slows down and the transport of chloride ions will be mainly governed by diffusion instead of capillary absorption. Increased printing speeds enlarge the fast ingress of chloride ions due to capillary absorption in the beginning (56% or 73% for T60 S1 or

T60 S2, respectively). The latter phenomenon confirms also the observations mentioned in Chapter 7, where in case of higher printing speeds, a higher water uptake could be observed at the sides of the printed elements compared to the denser bulk material. For both printing speeds, the chloride penetration area increases with enlarged time gaps and is again more pronounced for higher printing speeds. Increased interlayer time intervals result in a higher total porosity, irrespective of the pore size we consider. In addition, the initial moisture content of the layers lowers with higher time gaps, increasing the water uptake ability of the interlayer itself.

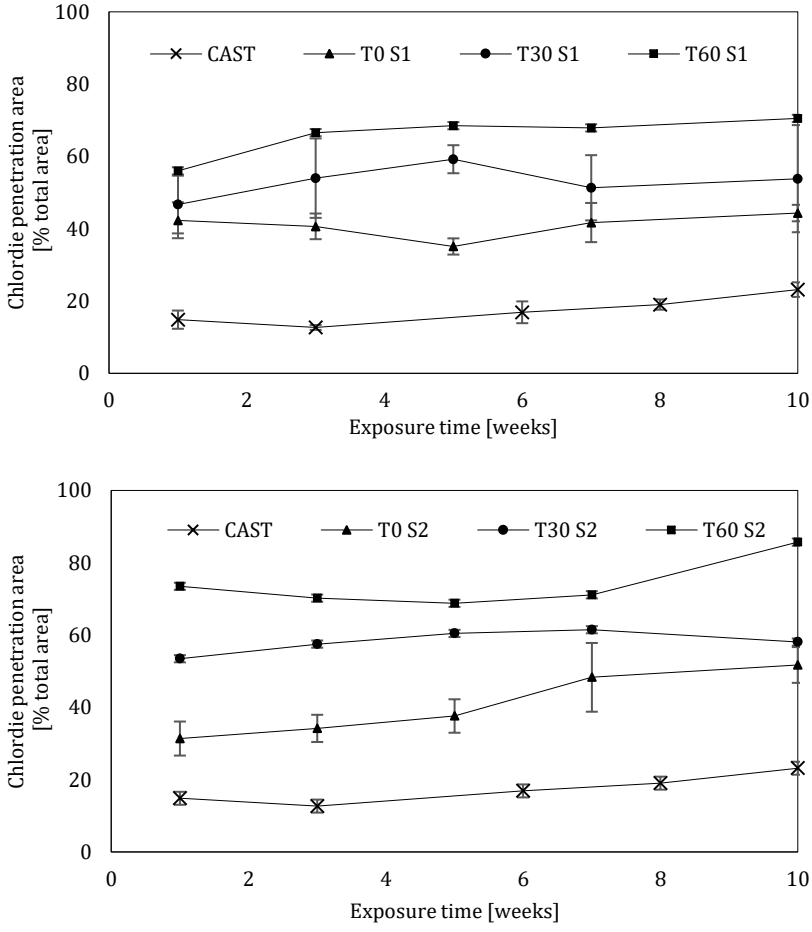

Figure 8.12: Chloride penetration area as a function of the exposure time in case of conventional concrete (CAST) and specimens printed with different time gaps and printing speeds (n=6, error bars represent the standard deviation)

Figure 8.13 and Figure 8.14 represent the chloride penetration depths of conventionally cast and printed samples, expressed as a function of time. A high variability between the different penetration depths and exposure times could be observed, which could be attributed to the fact that the measurements were executed by multiple researchers due to COVID-19 regulations. However, these are only assumptions. Additionally, as these graphs represent the mean value of 3 samples, the preferential ingress at the interlayer, which is clearly visible in Figure 8.11 in case of enlarged time gaps, was therefore sometimes smoothened and less pronounced.

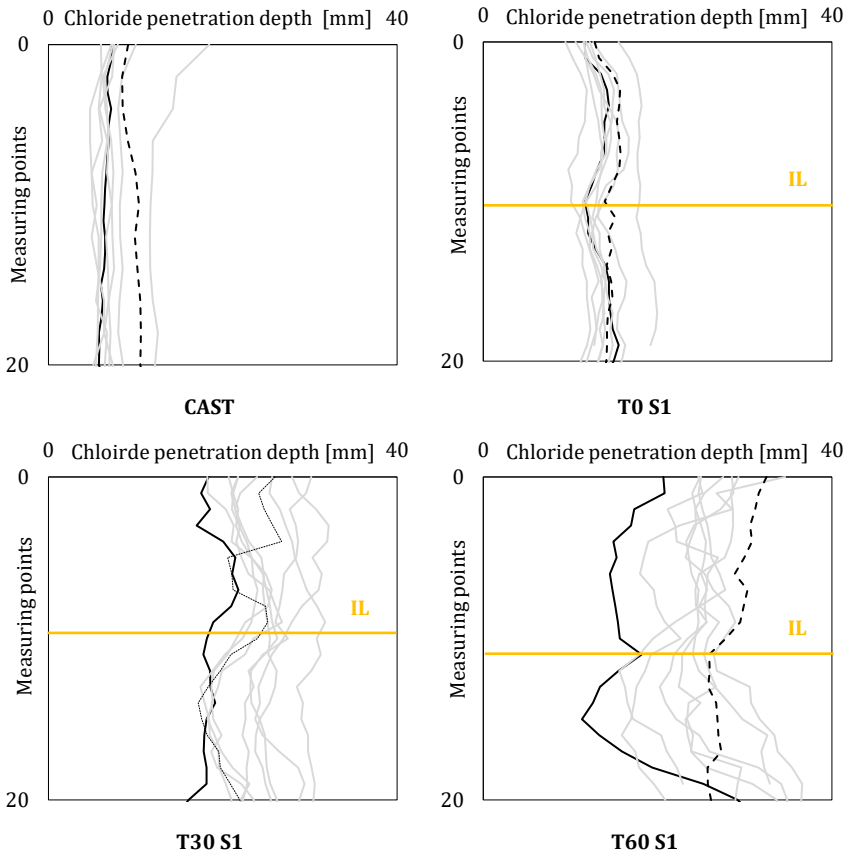

Figure 8.13: Chloride penetration depth [mm] as a function of the exposure time in case of conventionally cast specimens (CAST) and specimens printed with low printing speed (S1) and different time gaps. The full and dotted line represent the chloride penetration after one and ten weeks, respectively. The grey lines indicate the penetration in between. The yellow line represents the position of the interlayer (IL). (n=6, error bars are left out for the sake of clarity)

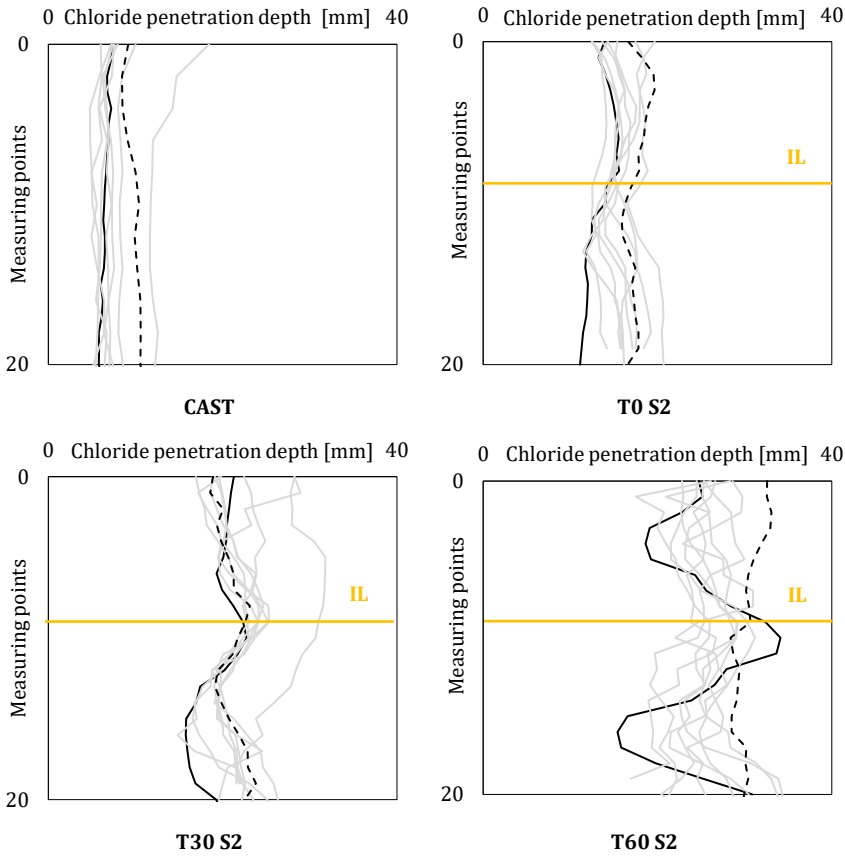

Figure 8.14: Chloride penetration depth [mm] as a function of the exposure time in case of conventional cast specimens (CAST) and specimens printed with high printing speed (S2) and different time gaps. The full and dotted line represent the chloride penetration after one and ten weeks, respectively. The grey lines indicate the penetration in between. The yellow line represents the position of the interlayer (IL). (n=6, error bars are left out for the sake of clarity)

In case of cast concrete and specimens printed with a zero-minute time gap, statistical analysis revealed that the penetration front is uniform, stating the assumption that the material is homogenous. However, as the printing process introduces more voids and micro-cracks, the chlorides penetrate deeper into the material after one week of exposure (i.e. 7 mm for cast specimens compared with 14 mm in case of printed samples). A prolongation of the interlayer time interval causes a lower initial surface moisture content and additional shrinkage cracks at the interlayer itself, whereafter the deeper penetration becomes more pronounced (i.e. 14 mm or 18 mm after one week of exposure for T0 S1 or T60 S1, respectively). Elongated time gaps also show

a more pronounced penetration at the interlayer as well as at the bulk material due to a higher surface area exposed to capillary suction.

Regardless of the printing speed, the ingress rate of chloride penetration stagnates after the first week of exposure. After chloride ingress, some of the chloride ions are captured by the cement hydration products and chloride binding occurs. Chloride binding alters the pore structure due to the formation of Friedel' salt, which may further react with the $Ca(OH)_2$ present and form $CaCl_2$ complexes. As soon as the reaction begins, the binding between the chloride ions and the hydration products can modify the microstructure and can improve the impermeability of the concrete, slowing down the further transport of chloride ions. However, as a lower amount of water is available to form hydration products in case of enlarged time gaps, chloride binding will occur in a lower extent.

8.5.2. Potentiometric titrations

Figure 8.15 represents the chloride penetration profiles of the different samples. Before going deeper into detail, some remarks need to be made. For an optimal comparison between the chloride profiles obtained from colorimetric measurements and potentiometric titrations, the measurements are preferably carried out on the same samples. However, since this was not possible due to practical reasons, the measurements were not carried out on the same samples but on samples of the same batch. Secondly, a direct comparison between both methods is not possible as in case of the colorimetric measurements the free chlorides are visualized, whereas potentiometric titrations quantify the acid-soluble chloride content, which is assumed to correspond to the total (bound + free) chloride concentration. In literature [183], a method was found to compare the water-soluble chloride content with the free chloride content. The relationship between the free chlorides and acid-soluble chlorides is discussed by Yuan et al. [184]. However, all these relationships are valid for conventionally cast concrete, assuming a homogenous material and a unidirectional penetration. Further research is required to confirm their applicability in case of printed materials.

Potentiometric titrations are performed, every two weeks after the start of complete immersion, on one sample of every test series. The total chloride profile is obtained by plotting the measured total chloride concentration (expressed in m% binder) versus the depth below the exposed surface. Subsequently, a mathematical profile, based on the solution of Fick's second law of diffusion, is fitted to the measured profiles. As already mentioned in the description of the test method, the first value was left out of the fitting.

In the following graphs, the measured values are depicted as dots, while the mathematically fitted profile is given as a full line. As the reader can notice, some results are missing or not depicted in the graphs due to the following reasons:

1. Due to COVID-19 regulations, some test series (CAST_W8, T0S2_W10 and T30S2_W10) were not accurately prepared and are therefore excluded from the results;
2. For some test series (CAST_W2 and T0S2_W2), it was not possible to find a fitting line based on SPSS analysis;
3. Outliers with a very high chloride content (e.g. T30S1_W6) were not considered and excluded from the graphs represented below.

The technical specifications in [181] prescribe a minimum of six points to cover the chloride profile. The latter criterion is to prevent that the whole test becomes invalid if the concentration measured for one ground layer is shown to be an outlier. In general, it can be concluded that the chloride content will stagnate to an almost constant value after a certain depth (approximately 15 mm). The total chloride content tends to increase with an enlarged exposure time. This behavior is observed for every test series, regardless of the fabrication process, interlayer time interval and printing speed. In the early stage, the ingress of chlorides is governed by capillary suction as the samples were not saturated. Consequently, the chlorides enter the printed samples mainly through the porous interlayers and cause a high chloride content at larger depths below the exposed surface.

A similar behavior can be noticed for conventionally cast samples, but in a smaller extent. According to literature, capillary absorption can transport chlorides up to a depth of 20 mm below the surface [178], also known as the convection zone. The total chloride content increases when extending the interlayer time interval. The complicated penetration mechanism (absorption + diffusion) leads to a non-Fickian chloride profile, resulting in the formation of a local peak located at the interior of the element rather than at its surface. The latter is referred to as the maximum phenomenon and divides the concrete surface into two different layers with different predominant ionic transport mechanics: the “skin” layer where the chloride content increases with the sample’s depth and the internal or bulk layer where the chloride profile fits the Fickian behavior. The skin effect can be attributed to the different composition of the outer surface of the printed specimens, as already stated in the previous chapters.

Based on the chloride profiles, it is not possible to determine the width of the skin layer and more in-depth investigations of the first 5 mm are required. However, due to the heterogeneity of the surface of the interlayer, this will be a difficult task. Furthermore, carbonation of the exposure surface can occur during hardening and sample preparation. In such case, the carbonated phases in the skin layer have less binding capacity, leading to an apparent maximum in total chloride content just at the boundary of the skin layer and the bulk material. In addition to carbonation, also the physical adsorption of calcium (Ca+) and chloride (Cl-) on the silanon sites (SiOH) from CSH takes place. This behavior is enhanced for hydrated Portland cement paste with a pH above 11.7.

Close to the surface, where the element is in contact with the chloride solution, there is a less favorable condition for chloride absorption due to the lower pH value. At deeper depths, the pH reaches higher values, enhancing the adsorption of calcium and chlorides which leads to the maximum chloride content peak.

As stated before, the fast transport of chloride ions can be attributed to capillary absorption and is largely influenced by both the pore structure (i.e. pore size, pore size distribution, tortuosity and continuity of the pores) and the chloride binding capacity of the cementitious material. The higher total binder content of the 3D printed elements can be attributed to the larger total porosity of these elements and the higher surface area exposed to this transport mechanism.

Chloride binding on the other hand depends on the C_3A and C_4AF content, which can be described as moderate in terms of the used cement type (CEM I 52.5N). Due to the reaction between the chloride ions and C_3A and C_4AF, Friedel's salts and its analogues are formed which retard the chloride penetration as they densify the microstructure.

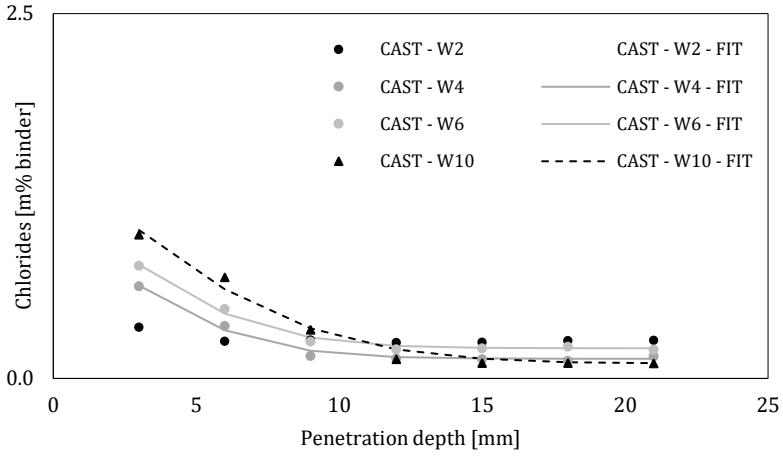
2.5
0.0
Chlorides [m% binder]
0
5
10
15
20
25
Penetration depth [mm]
CAST - W2
CAST - W4
CAST - W6
CAST - W10
CAST - W2 - FIT
CAST - W4 - FIT
CAST - W6 - FIT
CAST - W10 - FIT

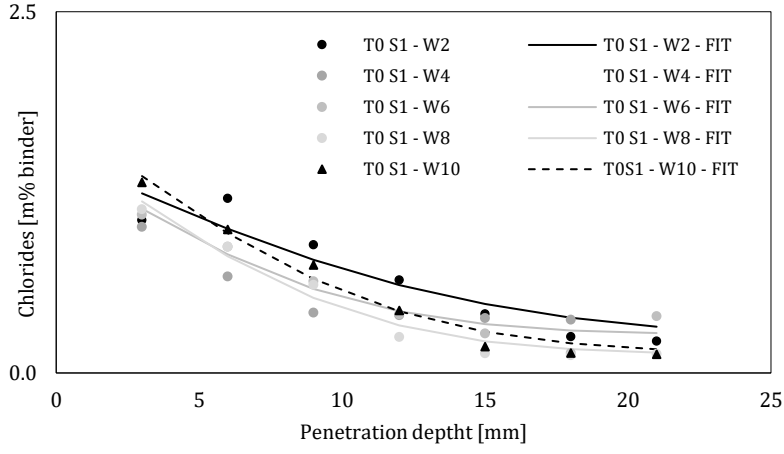
2.5
0.0
Chlorides [m% binder]
0
5
10
15
20
25
Penetration deptht [mm]
T0 S1 - W2
T0 S1 - W4
T0 S1 - W6
T0 S1 - W8
T0 S1 - W10
T0 S1 - W2 - FIT
T0 S1 - W4 - FIT
T0 S1 - W6 - FIT
T0 S1 - W8 - FIT
T0S1 - W10 - FIT

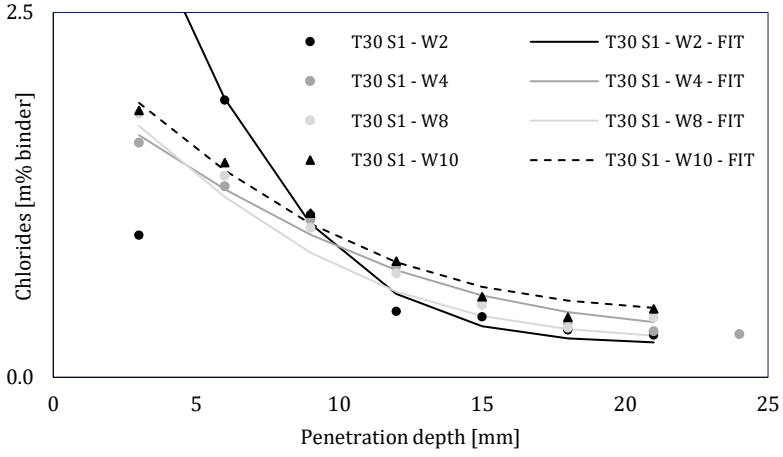
2.5
0.0
Chlorides [m% binder]
0
5
10
15
20
25
Penetration depth [mm]
T30 S1 - W2
T30 S1 - W4
T30 S1 - W8
T30 S1 - W10
T30 S1 - W2 - FIT
T30 S1 - W4 - FIT
T30 S1 - W8 - FIT
T30 S1 - W10 - FIT

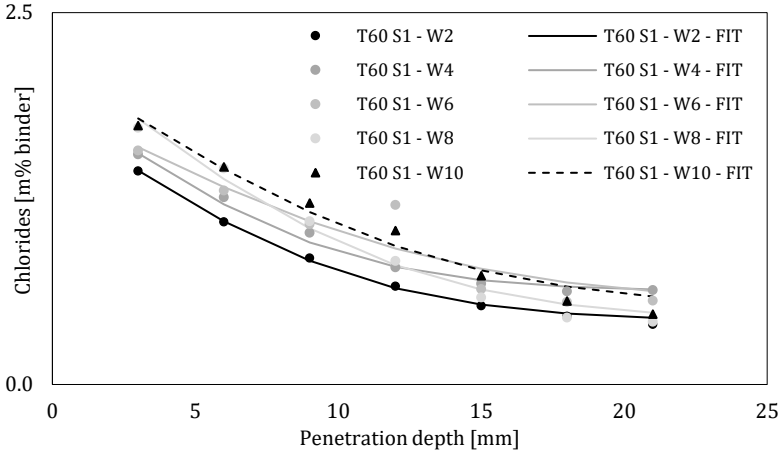
2.5
0.0
Chlorides [m% binder]
0
5
10
15
20
25
Penetration depth [mm]
T60 S1 - W2
T60 S1 - W4
T60 S1 - W6
T60 S1 - W8
T60 S1 - W10
T60 S1 - W2 - FIT
T60 S1 - W4 - FIT
T60 S1 - W6 - FIT
T60 S1 - W8 - FIT
T60 S1 - W10 - FIT

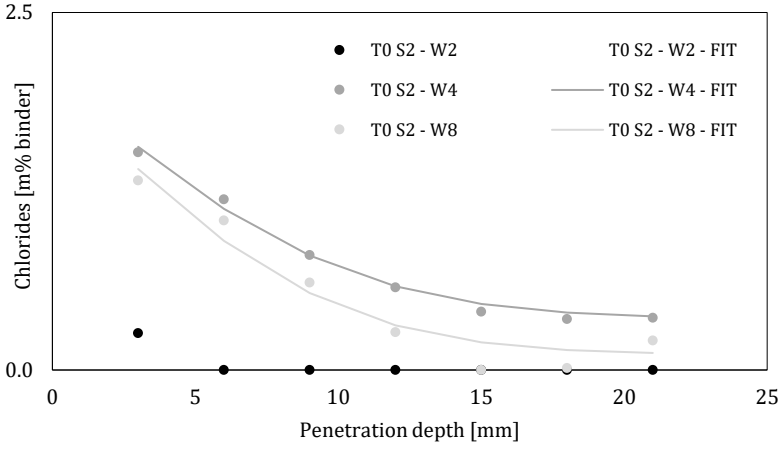
2.5
0.0
Chlorides [m% binder]
0
5
10
15
20
25
Penetration depth [mm]
T0 S2 - W2
T0 S2 - W4
T0 S2 - W8
T0 S2 - W2 - FIT
T0 S2 - W4 - FIT
T0 S2 - W8 - FIT

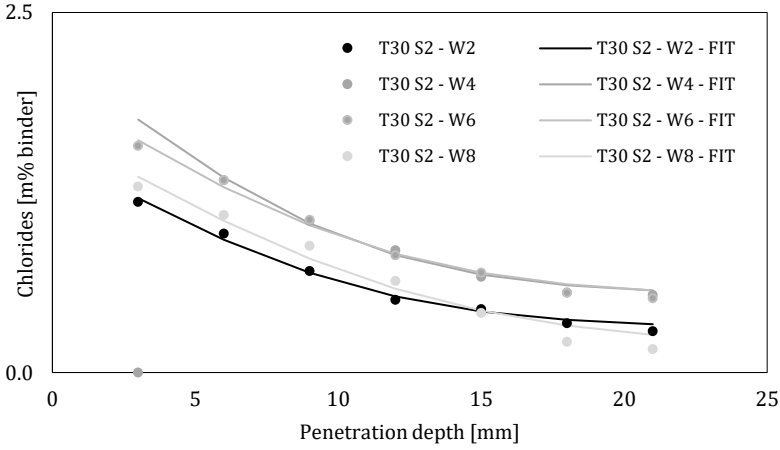
2.5
0.0
Chlorides [m% binder]
0
5
10
15
20
25
Penetration depth [mm]
T30 S2 - W2
T30 S2 - W4
T30 S2 - W6
T30 S2 - W8
T30 S2 - W2 - FIT
T30 S2 - W4 - FIT
T30 S2 - W6 - FIT
T30 S2 - W8 - FIT

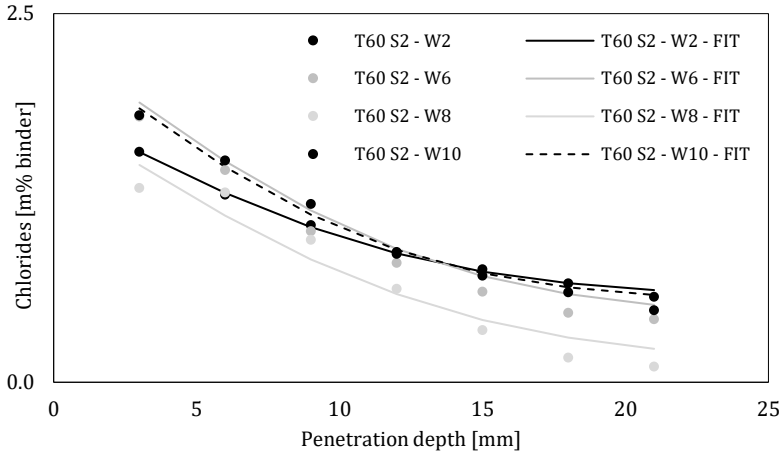

Figure 8.15: Chloride penetration profiles and their corresponding fitting curves in case of conventional cast specimens and specimens printed with different time gaps and different printing speeds. Fitting curves were left out of the graphs when no relevant fitting could be obtained. (n=1)

Figure 8.16 and Figure 8.17 compares the total chloride content for different printing speed after two and ten weeks of chloride exposure. In general, similar conclusions can be drawn. Regardless of the printing speed, the total chloride content increases when extending the interlayer time gap. The latter conclusion is valid both after two and ten weeks of chloride exposure and for every layer depth, confirming that chlorides penetrate further into the printed material compared with molded samples as a result of the higher porosity and enlarged surface area. Although the differences are rather small, the stagnation of the chloride concentration further away from the exposure surface occurs faster in case of S1 compared with S2.

It should be noted that the results of these potentiometric titrations serve as a first estimation as the real chloride content can deviate from the results due to different reasons. First of all, although grinding was performed with the smallest possible drill (diameter 8 mm), the grinded powder remains a combination of bulk and interlayer material. As already stated based on colorimetric observations and as observed by Anleu [160] who quantified the chloride ingress based on μ XRF-mapping, the chloride content in the bulk is lower compared with the one in the interlayer. These results are similar as described in [160, 185].

Secondly, unlike conventional cast concrete, also the curved surface of printed samples should be considered. The latter imposes the need for a test method that allows to obtain a spatial distribution of the aggressive agent.

Without chloride mapping, one could conclude that chloride concentrations are not critical, while the contrary may be true.

Finally, also the variations between the different samples should be considered. These variations can be due to the heterogeneity of the cementitious material, differences initiated by the print process, different environmental conditions, etc. Although these variations were kept as small as possible, it is not possible to exclude them completely.

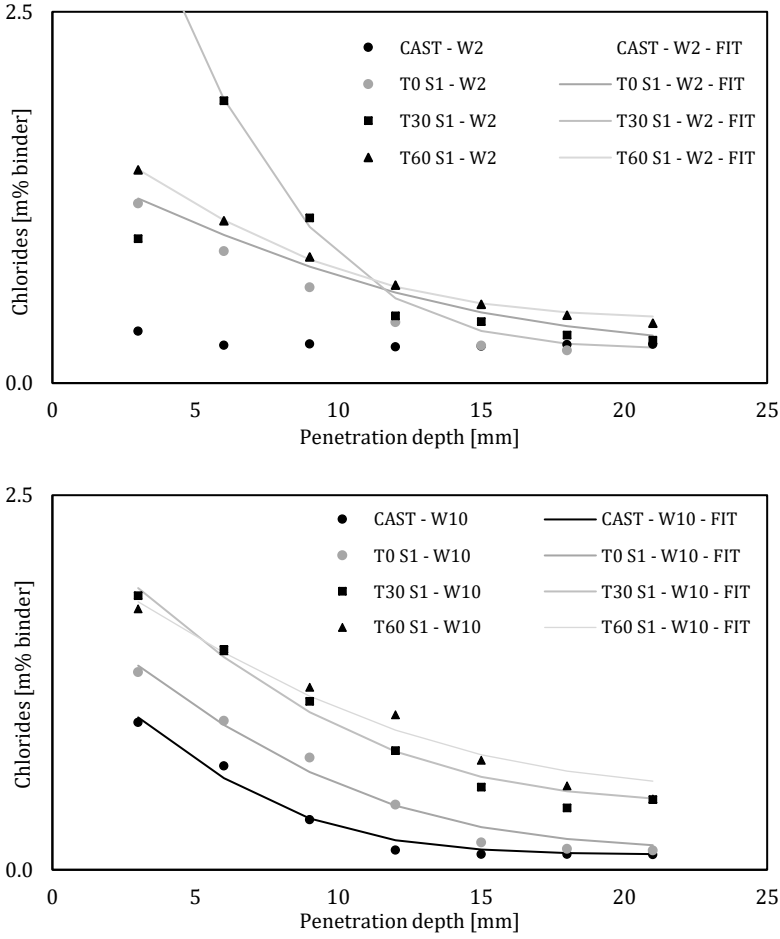

Figure 8.16: Comparison of the total chloride content profiles obtained after two and ten weeks of exposure for conventional cast specimens and specimens printed at low printing speed with different time gaps (n=1)

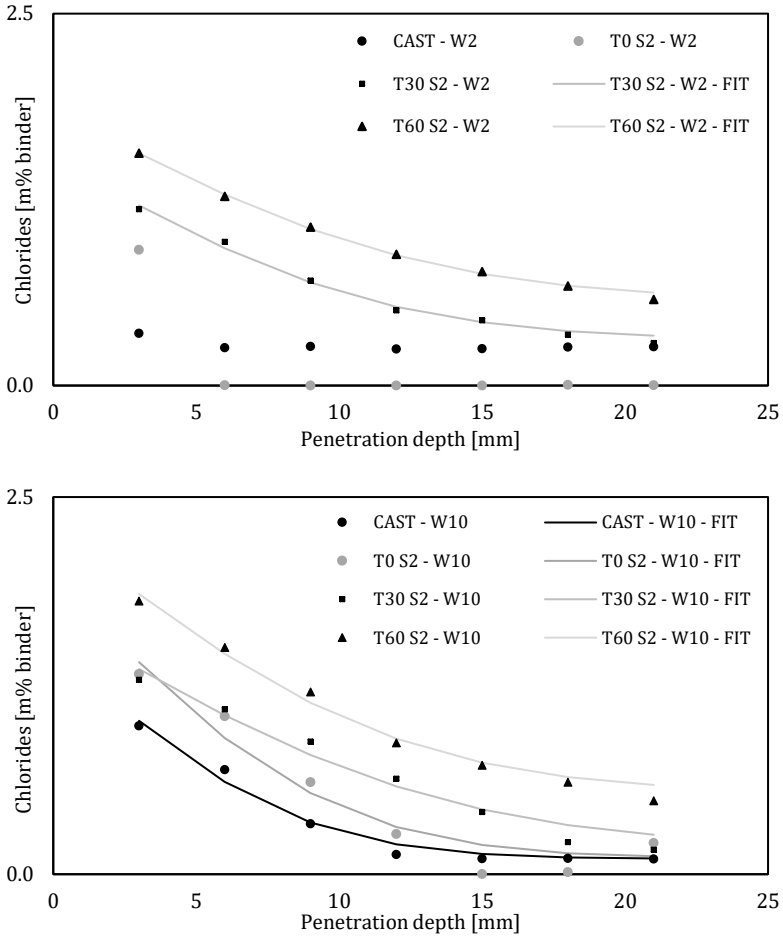

Figure 8.17: Comparison of the total chloride content profiles obtained after two and ten weeks of exposure for conventional cast specimens and specimens printed at low printing speed with different time gaps (n=1)

The non-steady state diffusion coefficients D_{NSS}, calculated according to Eq. [8.3], are summarized in Table 8.2. In general, it can be concluded that the diffusion coefficient decreases with enlarged exposure times. These results are in accordance with the ones obtained in literature [161, 186], confirming the time dependency of the chloride diffusion coefficient. As the chloride ingress proceeds, chloride binding occurs contributing to the deposition of Friedel's salt in the pore structure and reducing the porosity. In addition, the continuation of the cement hydration also lowers the pore volume and as a consequence also the corresponding diffusion coefficient. As stated before, the skin layer of cementitious materials has an influence on the evolution of

the chloride profiles. According to literature, the diffusivity of the skin layer differs from the bulk material. Several researchers [152, 187] suggested a modified version of Eq. [8.3] in order to take this into account. However, as prescribed by [181], the occurrence of this maximum phenomenon is neglected, which might cause an overestimation of the chloride surface concentration.

Table 8.2 summarizes in addition also the chloride surface concentrations, expressed as mass% of the binder. Although the samples were all immersed in a 33 g/l aqueous NaCl solution, some variations in the surface concentration can be noticed. Furthermore, some rather high surface chloride concentrations are observed, especially in case of printed elements, which could be attributed to local irregularities of the individual sample, introduced by the printing process. These results are mentioned, but should be excluded when drawing general conclusions.

This varying behavior requires a more in-depth evaluation. First of all, it must be emphasized that a surface concentration higher than the chloride concentration of the original exposure solution is not an uncommon phenomenon. Van den Heede [167] revealed that this concentration difference could be attributed to condensation phenomena induced by the existence of an electrical double layer (EDL) in the cement paste. This EDL consists out of a diffuse layer and a compact layer, which are close to the surface solids in contact with an electrolyte solution [188]. The compact layer occurs at the interlayer between pore wall and pore solution. Since the hydrated cement surface is negatively charged [167], positively charged particles will be adsorbed to the pore wall. Therefore, the compact layer of a chloride exposed cementitious material, located at the pore wall, mainly consists out of positively charged ions and the EDL causes the formation of a diffuse layer composed out of negatively charged ions. Consequently, a difference in ionic concentration is established between the diffuse layer and the bulk solution. Furthermore, the chloride content in the diffuse layer is much higher compared to the bulk solution which might explain why the chloride concentration at the surface exceeds the concentration of the exposure solution. However, the explanation of the EDL is not conclusive and is still not completely clear nowadays.

Secondly, an overestimation of the chloride surface concentration can be obtained when neglecting the skin layer and fitting the error function equation with the decreasing concentration profile towards the interior. Furthermore, the chloride concentration is also time dependent. A build-up in chloride surface concentration with increasing exposure time is often

observed in literature. Regardless of the printing speed, a general increase of the diffusion coefficient can be observed for enlarged time gaps. Although the higher discrepancy, a similar conclusion can be made in terms of surface concentrations.

Table 8.2: Evolution of D_{NSS} [.10^{-12} m^2/s] and C_s [m% binder] after different weeks of chloride exposure

	D_{NSS} [.10^{-12} m^2/s]					C_s [m% binder]				
	W2	W4	W6	W8	W10	W2	W4	W6	W8	W10
CAST	/	4.6	3.4	/	3.6	/	1.09	1.26	/	1.52
T0 S1	54.0	32.9	7.9	6.6	6.4	1.51	2.23	1.50	1.62	1.81
T30 S1	18.9	21.9	16.7	7.7	7.6	4.71	2.06	5.88	2.39	2.40
T60 S1	29.6	12.4	16.2	9.2	9.1	1.83	1.95	1.89	2.23	2.16
T0 S2	/	13.1	7.6	5.8	/	/	2.06	6.36	5.41	/
T30 S2	32.6	15.1	12.2	11.8	/	1.53	2.21	1.97	1.69	/
T60 S2	41.1	24.6	10.9	12.2	7.2	1.87	5.80	2.33	1.84	2.30

Based on the results, one can conclude that the conventional methods for the determination of chloride penetration could be applied and serve as a first estimation and quantification of both the chloride content and the chloride penetration depth. Therefore, complete mapping of the chloride content on a split surface would seem more interesting in the future. The benefits of the latter procedure are already described by Anleu [160]. However, if we compare the chloride concentrations in case of printed samples with the boundary concentrations available for conventional concrete, literature [161] reveals that regardless of the printing speed or interlayer time gap, the chloride concentration exceeds this limit values. Although the binder content is high, also the print process should be reconsidered in order to increase the durability of the material. For example, side trowels could improve the smoothness of the surface and decrease the micro cracks caused by the manufacturing process. Secondly, a proper curing method can also slow down the chloride ingress in case of printed elements, as noticed by Anleu [160].

8.6. Carbonation

Figure 8.18 and Figure 8.19 represent the carbonation depth, expressed as a function of time for different time gaps and different printing speeds. As mentioned in literature, the ingress of CO_2 into a cementitious material will follow the path with the lowest resistance, i.e. through the capillary pores. The capillary porosity depends on the water and cement content in the mix composition and the composition of the cement. In order to exclude additional effects of the mix composition, a similar mix is used regardless the manufacturing technique. This implies, in ideal circumstances and purely theoretical, that the volume of capillary pores is similar in the different series.

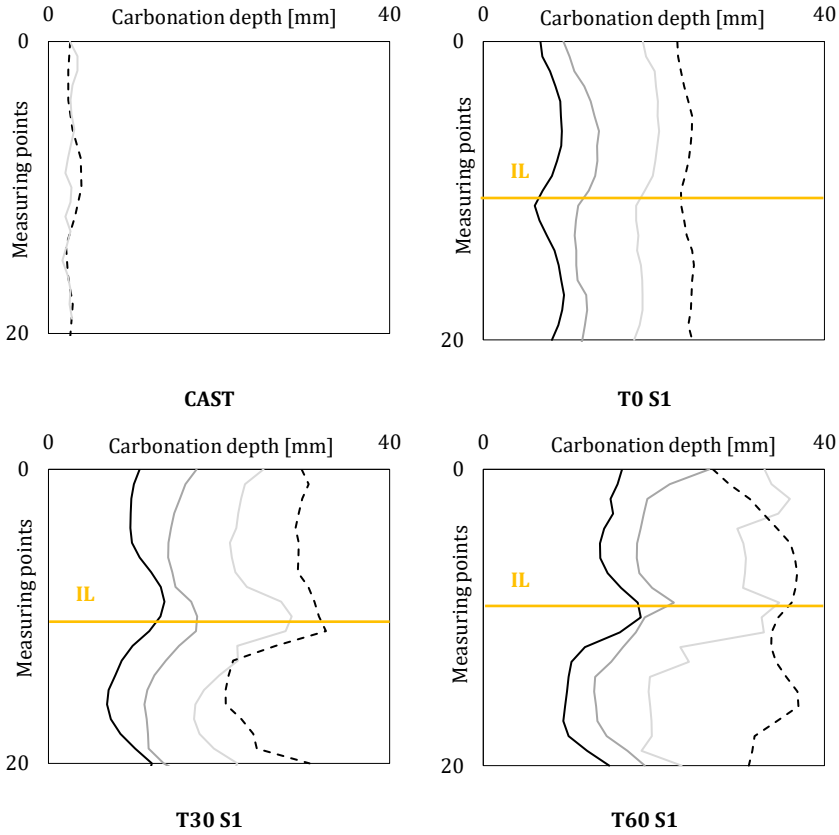

Figure 8.18: Carbonation depth [mm] as a function of the exposure time in case of conventional cast specimens (CAST) and specimens printed with low printing speed (S1) and different time gaps. The full and dotted line represent the carbonation depth after one and twenty-four weeks, respectively. The grey lines indicate the penetration in between. The yellow line represents the position of the interlayer (IL) (n=6, error bars are left out for the sake of clarity)

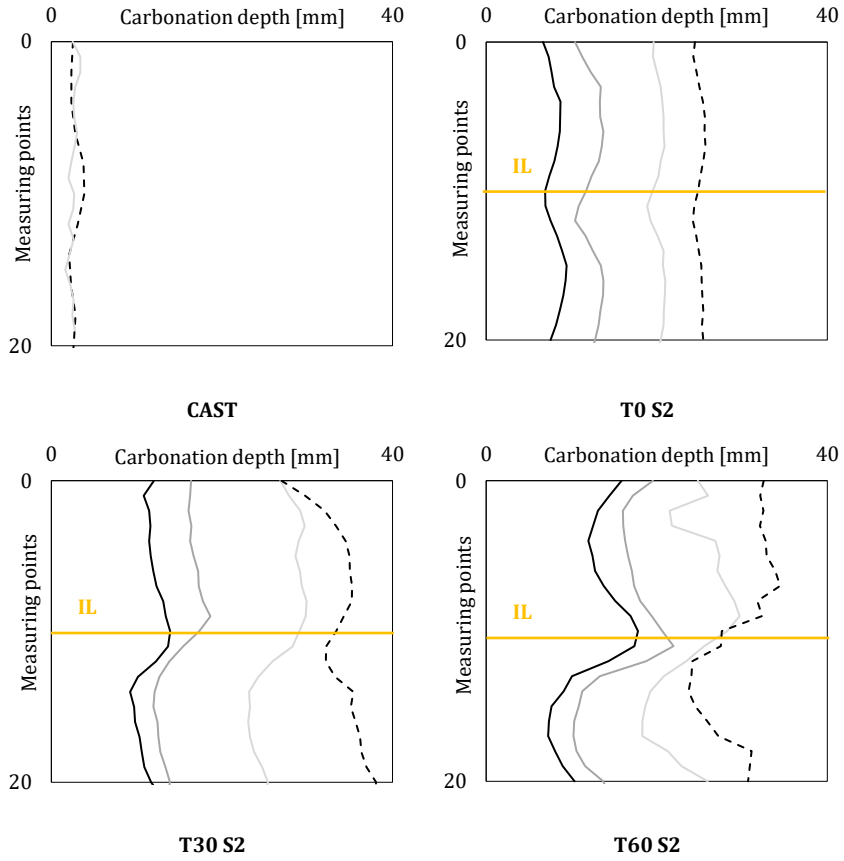

Figure 8.19: Carbonation depth [mm] as a function of the exposure time in case of conventional cast specimens (CAST) and specimens printed with high printing speed (S2) and different time gaps. The full and dotted line represent the carbonation depth after one and twenty-four weeks, respectively. The grey lines indicate the penetration in between (n=6, error bars are left out for the sake of clarity)

However, in case of larger time gaps, the surface of the substrate layers becomes drier as the water evaporates from the surface. This lower amount of water, will decrease the water amount available for the formation of hydration products and a lower hydration rate will be obtained in the vicinity of the interlayers. This phenomenon will be more pronounced with increasing time gaps, extending the number of capillary pores. Furthermore, the intrusion of CO_2 will change the microstructure of the elements. More specifically, larger capillary macropores (100 – 200 nm) will be produced due to carbonation, while smaller capillary mesopores (10 – 100 nm) will be clogged and the total porosity remains more or less the same. These observations were basically founded on literature, as it was very difficult to

found the latter based on own observations; The printed samples were taken from different printed elements and different material batches which could both introduce microstructural changes.

For conventionally cast specimens, the penetration depth is significantly smaller compared to the depth measured for the 3D printed samples. According to the statistical analysis, a vertical carbonation front is observed for the cast samples which confirms again the assumption of a homogenous material. Nevertheless, notion should be taken that no carbonation front could be visualized during the first weeks of exposure. On the one hand, this observation can be attributed to the extensive compaction of traditionally cast elements. On the other hand, the phenolphthalein indicator shows no discoloration when the pH value of the carbonated region does not yet drop below 9. Consequently, the traditionally cast samples could already be partly carbonated during the first week, whereas the pH value did not cross this critical value. Specimens printed with a zero-minute time gap show a deeper penetration of $C0_2$ but, based on statistical analyses, the ingress front can also be assumed as uniform, regardless of the exposure time. The latter has the same origin as already observed in case of chloride ingress and can be attributed to the higher porosity of 3D printed samples and the formation of micro-cracks in a plastic material state.

In case of higher interlayer time intervals, a deeper penetration can be observed at the interlayer as well as in the bulk material of the layers itself and this effect is more pronounced for enlarged time gaps. The more open the pore structure, the easier the ingress of CO_2 into the cementitious material. Furthermore, the pore size distributions of elements printed with a high printing speed have more capillary pores compared with elements fabricated with a lower printing speed, making them more prone to carbonation.

Based on Figure 8.20, one can conclude that a longer time gap in between the deposition of two successive layers, not only increases the ingress at the interlayer but also in the bulk material. This observation confirms the assumption that a more micro-cracks are formed when the time gap is larger. Secondly, increasing the layer number seems beneficial for the resistance against carbonation. As depicted in Figure 8.20, a higher CO_2 intrusion could be observed for the top layer compared with the base layer. The densification of the material due to the additional weight leaves less pores in the lower printed layers and makes them more resistant.

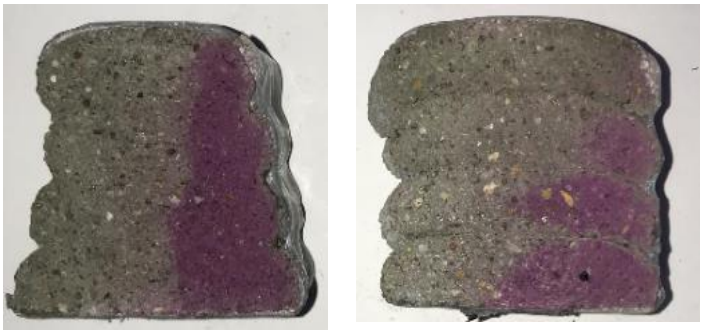

T0 **T60**

Figure 8.20: Penetration front in case of digitally fabricated samples, printed with different interlayer time interval (i.e. 0 and 60 minutes) after 24 weeks of $C0_2$ exposure.

The beneficial effects of a lower S/B-ratio and a different type of sand in combination with a different print technique are depicted in Figure 8.21 and Figure 8.22. The A part of both figures shows the effect of a change in mix composition (i.e. a lower S/B ratio and a change in sand type) after a 30-minute time interval and after different exposure times. Purely based on a visual inspection, one can see that the preferential ingress at the interlayer is less pronounced compared to the other reference material. The finer sand particles create a denser and less porous material. This can also be quantified by ImageJ analysis. After one week of exposure, the ingress at the interlayer equals 9.6 mm and 13.9 mm for REF_3D and REF, respectively, reducing the penetration with 31%; after 10 weeks of CO_2 exposure, the reduction equals 39%. However, the following phenomenon can be observed: the penetration depth of the layers decreases with an increasing number of layers. Part B of both figures represents on the other hand the penetration depth in case of 3D printed samples; the interlayers do not serve as a weak link, despite the enlarged time gap. Based on a statistical analysis of the penetration depth, the ingress front can be considered as uniform, creating a more or less homogenous material. In addition, the penetration depth is relatively low compared with the 2D printed elements; after one week of exposure, the penetration equals only 6 mm (i.e. a reduction of 38% compared with the 2D printed material, fabricated with the same mix composition) and 15 mm after 12 weeks of exposure. This benefit can be attributed to the denser cement matrix, the higher pressure exerted on the material, the application of side trowels, which creates a smoother exposure surface and limits the surface defects, and the rectangular nozzle geometry which counteracts the gravimetrical flow after deposition, limiting the crack formation.

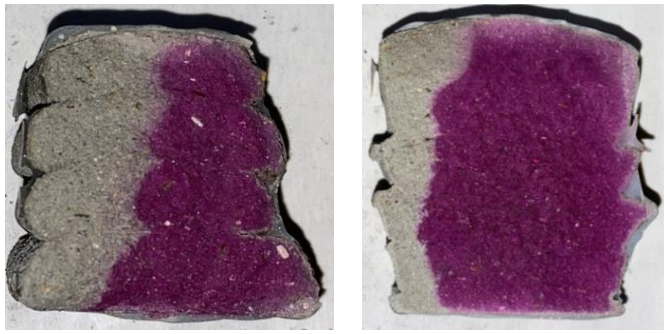

A B

Figure 8.21: Penetration front in case of digitally fabricated samples, printed with the 2D (A) and 3D (B) print equipment after 12 weeks of CO_2 exposure. Both specimens are composed out of REF_3D and are fabricated with a 30-minute time gap.

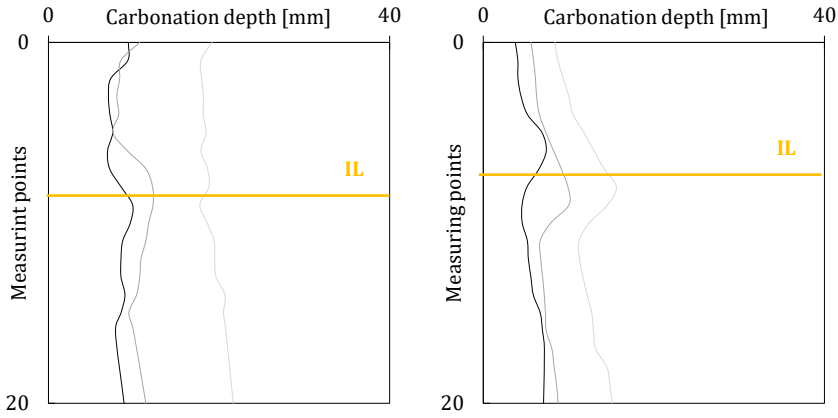

A B

Figure 8.22: Carbonation depth [mm] as a function of the exposure time in case of 2D printed samples and specimens printed with the 3D equipment (B). Both test series were printed with a time gap of 30-minutes and composed out of the REF_3D mixture. The full line represents the carbonation depth after one and week. The grey lines indicate the penetration in between (n=6, error bars are left out for the sake of clarity)

As resumed by Qui et al. [189], the colorimetric test does not indicate the depth of maximum CO_2 ingress and the actual carbonation depth could be underestimated. Furthermore, the accuracy of the ImageJ analysis could be improved as it depends on the quality of the pictures and the interpretation. To evaluate the magnitude of this underestimation, the penetration depth is preferably studied by for example thin sections or thermogravimetric analysis (TGA). However, these investigations require more preparation and are more labor intensive compared with the colorimetric measurements.

The carbonation rate depends on the capillary porosity, the amount of pore water, the amount of carbonatable matter, etc. and can be calculated based on Eq. [8.6]. In case of conventional concrete, the carbonation front is uniform over the entire concrete samples and a general carbonation rate can be calculated and expressed as a function of the square root of time. Due to the heterogeneity of printed samples, a distinction should be made between the interlayer and the bulk material.

Figure 8.23 represents the carbonation rate for the different test series after one week of CO_2 ingress. One can clearly see the preferential ingress through the interlayer and the effect of a larger area exposed to capillary absorption. This phenomenon is more pronounced in case of enlarged time gaps. In case of a zero-minute interlayer time interval, the penetration rate does not differ in a significant way between the bulk material and the interlayer. Higher time gaps result in higher penetration rates and the difference between the second and third layer becomes also more pronounced. The influence of the printing speed on the penetration rate is negligible.

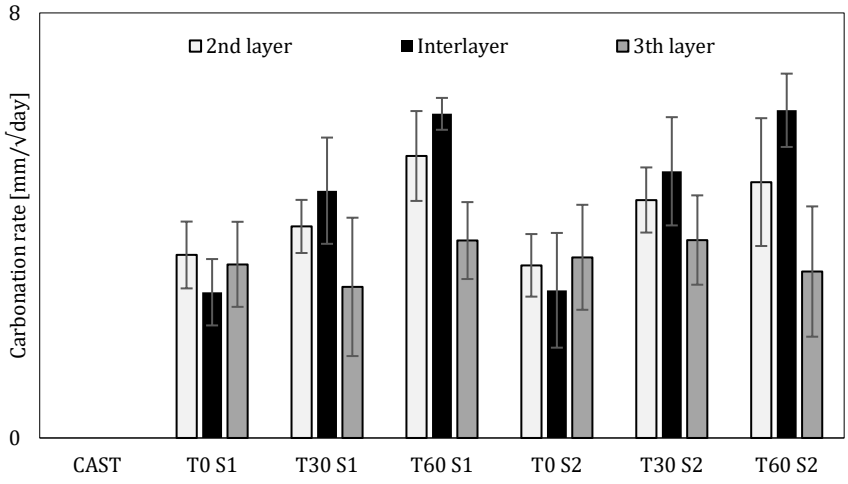

Figure 8.23: Carbonation rate A_{acc} [mm/√day] after one week of CO_2 exposure for conventional cast specimens (CAST) and specimens printed with different printing speeds and different time gaps (n=6, error bars represent standard deviation)

Figure 8.24 represents the carbonation rate at the interlayer as a function of time. One can see that the carbonation rate decreases more rapidly for higher time intervals compared with lower time intervals and a similar penetration rate could be observed after 24 weeks of $C0_2$ intrusion. In case of print speed S2, the results do not significantly differ compared with the results of S1 and similar conclusions can be made.

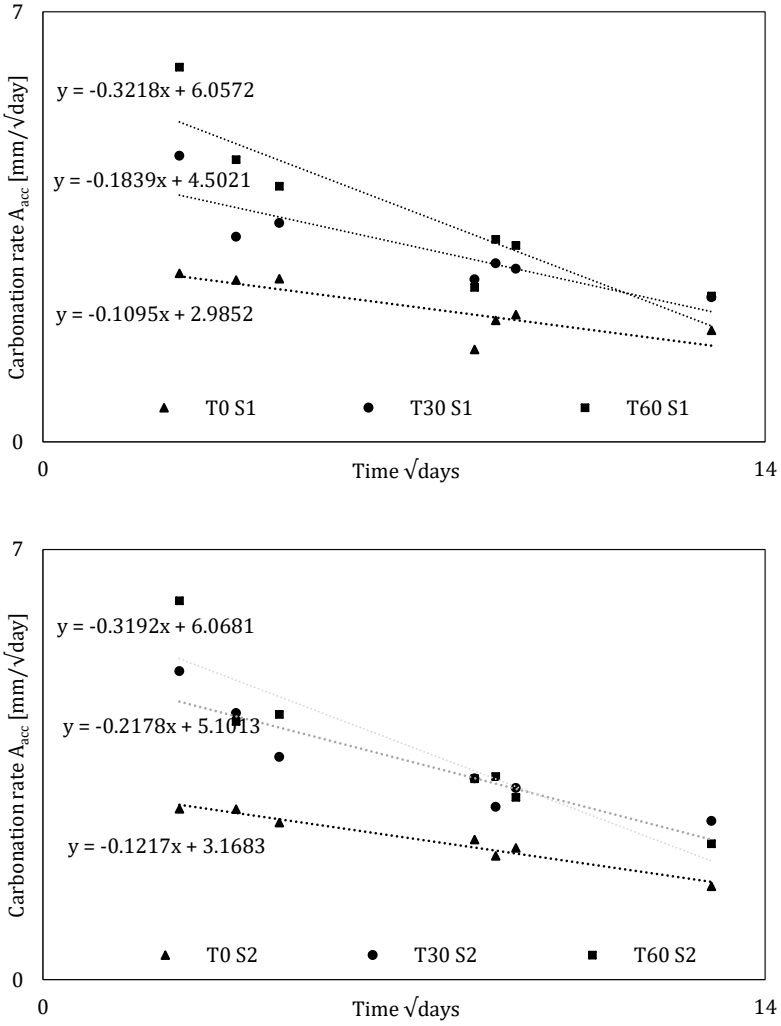

Figure 8.24: Carbonation rate at the interlayer expressed as a function of time for specimens printed with different time gaps (T0, T30 and T60) and different printing speeds (S1 and S2)

It can be concluded that the resistance against carbonation of 3D printed elements is generally inadequate and that the material would result in corrosion of the reinforcement. The durability performance can be increased by an adequate curing method (external or internal). By proper curing, the desiccation of the outer layers will be limited, they will be more hydrated and they will be less porous. This will impede the diffusion of CO_2 and will slow down the carbonation process.

8.7. Freeze/thaw resistance

Table 8.3 represents the mass increase of the samples in fully saturated state and the accompanied standard deviation between brackets. The mass increase is obtained at the age of 35 (m_{35}, n=18) and 56 (m_{56}, n=9) days. Molded specimens have a lower mass increase at the age of 35 days compared with printed samples, due to the lower porosity as stated before. As proven by statistical analysis, the mass increase of printed samples does not depend on the used time gap. When a cementitious material is exposed to freezing temperatures, the pore water can start freezing, which results in the formation of ice and induces possible damage. Ice formation is initiated first in the larger pores within the capillary pore structure, expelling the pore water from the freezing pores due to the aforementioned volume increase, finding its way to air voids where the crystallization process starts. Due to the thermodynamic imbalances, the new ice crystals in the air voids start to grow and the water will attract water from the neighboring smaller pores and the transport is reversed. As the crystals have a lot of space to grow within the air void, there will be no or little crystallization pressure in this situation. Due to the higher porosity, the water uptake in terms of printed specimens will be higher.

Table 8.3: Mass increase after 14 F/T cycles (n=9), measured in fully saturated state [%]. Standard deviation is mentioned between brackets.

	Δm_{35} [%]	$\Delta m_{56,freeze}$ [%]
CAST	1.33 (0.11)	1.58 (0.10)
T0 S1	4.80 (0.21)	5.11 (0.21)
T30 S1	4.91 (0.08)	5.04 (0.09)
T60 S1	4.90 (0.15)	5.07 (0.17)
T0 S2	4.69 (0.18)	5.09 (0.12)
T30 S2	4.01 (0.21)	4.29 (0.15)
T60 S2	4.52 (0.16)	4.69 (0.15)

Based on statistical analysis, the compressive strength seems not to be affected by the F/T cycles. A first explanation of this phenomenon could be the increased amount of air voids at the interface and in the bulk material as a result of the print process. As a consequence, more space is available to accommodate ice crystals without the crystals having to exert pressure on the pore walls. Therefore, the risk of damage seems smaller. Secondly, as already stated in section 8.3.2, the porosity of the samples is only minor affected when the number of F/T cycles does not exceed 25 in total. The latter indicates the need of proper standards in terms of digital concrete [175]. After 14 F/T cycles, the cast specimens show a reduced compressive strength. However, this number of F/T cycles barely influences the printed samples and has to be increased as the porosity is already higher and damage will be induced in a later stage.

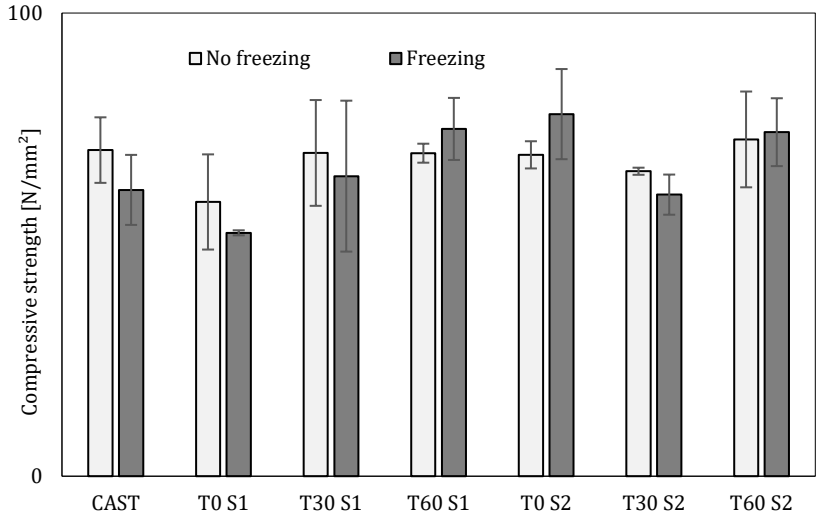

Figure 8.25: Compressive strength [N/mm^2] before and after freeze/thaw attack (n=3, error bars indicate standard deviation)

The latter is also confirmed based on ultrasonic measurements (Table 8.4). Recent research, performed on real scale structural elements, revealed that damage is induced when the relative elastic modulus equals 60% or lower [185]. After 14 F/T cycles, the relative elastic modulus is, irrespective of the test series, still higher than 80%, with no significant differences between the test series, confirming that the current standards are not sufficient to evaluate the freeze/thaw resistance of digital fabricated elements. In addition, the print process introduces more larger pores, which serve as an alternative for air entraining agents, commonly used in mold-casted concrete

to alter the F/T resistance. Based on the compressive strength and the relative elastic modulus, specimens printed with a higher speed show better freeze/thaw resistance, which can be attributed to the lower pressure exerted on the pore walls. In contrast with the resistance against chloride ingress and carbonation, traditionally cast specimens are more affected by the freeze/thaw cycles.

Table 8.4: Relative dynamic elastic modulus E [-]

	$E_{d,0}$ [MPa]	$E_{d,14}$ [MPa]	E [-]
CAST	27319	25002	83.76
T0 S1	32096	30713	91.57
T30 S1	24534	22196	81.84
T60 S1	22268	21848	96.27
T0 S2	33900	33439	97.29
T30 S2	27320	26290	92.60
T60 S2	29413	28776	95.72

8.8. Conclusions

Based on the results obtained after multiple durability tests, the following trends could be observed. Similar as for mold-cast specimens, the ingress of chlorides occurs in a uniform way when the time gap equals zero minutes, confirming the assumption of a homogenous material. Enlarged time gaps and higher printing speeds on the other hand facilitate the ingress of chloride ions, which can be attributed to the higher porosity and the initial dryer surface state of the layers. The results of the potentiometric titrations showed similar trends. However, the high variation in the non-steady state diffusion coefficients and the surface concentrations confirmed the fact that current test procedures should be adapted, considering the multi-directional ingress of the chlorides and the heterogenous character of the material. Similar trends could be observed for the resistance against carbonation. However, it was observed that a change in mix composition (i.e. other sand type and lower S/B-ratio) and a change in print technique could counteract the detrimental effects of an increased time gap. Irrespective of the test procedure, it was not possible to draw relevant conclusions about the freeze/thaw resistance of printed specimens. 14 F/T-cycles do not induce microstructural damage and it seems that the larger pores act as air entraining agents, improving the resistance against frost attack. However, further research is required to confirm these assumptions.

Chapter 9

Shrinkage

9.1. Shrinkage

Like conventionally cast specimens, shrinkage is one of the major challenges for printed concrete elements. It will lead to unwanted deformations that affect the geometry as well as the mechanical properties. Especially when the deformations are restrained, shrinkage may lead to tensile stresses and cracking that degrade the quality of the (printed) element. In general, shrinkage can be categorized according to two characteristics: *(i)* time (and duration) and *(ii)* chemical or physical cause. In the following sections, a brief overview of the most commonly known types of shrinkage is given. Although they are all discussed separately, in practice it is rather hard to distinguish each of them properly.

9.1.1. Plastic shrinkage

Plastic shrinkage occurs during the first hours after mixing, when the mortar is still in its plastic state, and will continue until setting. The paste is still fresh and can be considered as solid particles suspended in water (Figure 9.1A). The environmental conditions (e.g. wind, temperature, low humidity, etc.) might cause rapid loss of water to the surroundings (cf. drying shrinkage but in plastic state) by evaporation. First, shrinkage is caused simply due to the volumetric loss of water. After a while, however, the water loss can no longer be replenished fast enough and not all solid surfaces are surrounded by water anymore. As such, menisci start to form between the inter-solid pores, giving

rise to capillary pressure (Figure 9.1B). This pressure is a result of the adhesive forces between water and solids, as well as the surface tension in the menisci. Both will literally try to pull the solids closer together, ending up in a volume reduction, known as plastic settlement and plastic shrinkage (Figure 9.1C). When evaporation continues, the menisci will break due to a continued loss of water and the capillary pressure build-up will drop (Figure 9.1D). This last state is especially detrimental as it will limit hydration too. When shrinkage deformation is restrained, and the stresses become larger than the tensile strength developed at that time, cracks will occur.

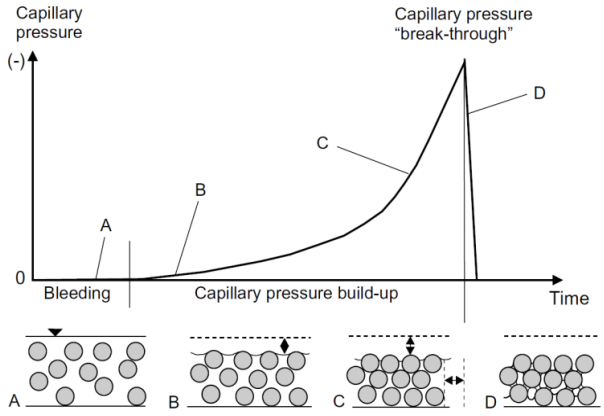

Figure 9.1: Plastic shrinkage caused by the capillary pressure build-up [190]

In ordinary concrete construction, the accumulation of bleeding water on top of the surface prevents the evaporation of pore water and reduces shrinkage. However, it is presumed that 3DCP would generally produce less bleeding water due to the large quantity of fines and low W/C-ratio. The pore water would therefore be exposed to evaporation for a longer time, resulting in more pore water loss and shrinkage [191].

The rate and extent of plastic shrinkage depend on numerous factors, including the size of the area susceptible to drying, the relative humidity and temperature of the surrounding environment, as well as the air flow. On the other hand, it is likely that the interlayer and extrusion-induced shearing will also have an effect on the plastic shrinkage cracking. It is possible for the interlayer to affect the pore water exchange between the layers or the transfer of shrinkage strain from one layer to another. In addition, the pore shape and size distribution are different in 3DCP and can also affect shrinkage.

Recent research on plastic shrinkage in case of 3D printed specimens [192] revealed that, although a higher surface was directly exposed to environmental conditions, neither the length nor the number of layers had a significant influence on the maximum or mean strain results of printed specimens. The rate of shrinkage, as well as the peak strain, were however several times higher compared with ordinary concrete.

9.1.2. Chemical shrinkage

Chemical shrinkage is the loss of volume (approximately 10%) due to the reduced volume taken by the hydration products compared to their reactants It starts immediately after the addition of water and the chemical shrinkage rate is the highest during the first hours and days. Since chemical shrinkage of cement paste is merely based on the volumes of the initial and final hydration products, it becomes possible to calculate the latter based on their molecular weight (Equation [9.1]), wherein CS is the chemical shrinkage, V_{ci} the volume of cement before mixing, V_C the volume of hydrated cement, V_{wi} the water volume before mixing, V_w the volume of reacted water and V_{hy} the volume of hydration products. The complication with this calculation is the difficulty to know the exact volume of various components within the matrix without doing elaborated tests.

$$CS = \frac{(V_c + V_w) - V_{hy}}{V_{ci} + V_{wi}} \cdot 100 \qquad [9.1]$$

Another way to quantify the magnitude of chemical shrinkage is to mathematically examine the product volumes based on the molecular weight and densities of the compounds when they change from basic to final reaction product (Eq. [9.2]). The percentage of each phase can be calculated based on the Bogue equations.

$$V_{CS,total} = 0.0532\,[C_3S] + 0.0400\,[C_2S] + 0.1113\,[C_4AF] + 0.1785\,[C_3A] \qquad [9.2]$$

Based on this mathematical calculation, it becomes clear that the cement chemistry will affect the autogenous shrinkage due to the varying chemical shrinkage in the very early ages. In addition, chemical shrinkage is considered as independent of the W/C-ratio. The W/C-ratio and the fineness of cement will only affect the shrinkage rate. In case of a W/C-ratio lower than 0.3, the initial rate will be up to 20% higher compared to higher ratios. Above 0.3, the (initial) rate of chemical shrinkage is similar for all water-cement factors [193]. Unfortunately, chemical shrinkage cannot be omitted, as it is inherent to the hardening process of the cementitious components [194, 195].

9.1.3. Autogenous shrinkage

Autogenous shrinkage acts by two different modes, depending on the time: before or after structuration. During hydration, but before gaining much rigidity, chemical reactions will consume water, that become chemically bound in CSH. This leads to chemical shrinkage, possibly creating voids in the system. Since a percolation structure is not fully developed yet, the created voids will collapse under self-weight. This means that, before structuration, autogenous and chemical shrinkage cannot be distinguished from each other and are regarded as equal.

As the cement hydration proceeds, particles are gradually interlocked (hydrates percolation) and finally form a solid skeleton that can therefore support and transfer stresses. As a result, the apparent volume, which is considered as the volume of liquid and solid phases including voids filled with gas, remains almost constant afterwards, although the hydration is not finished.

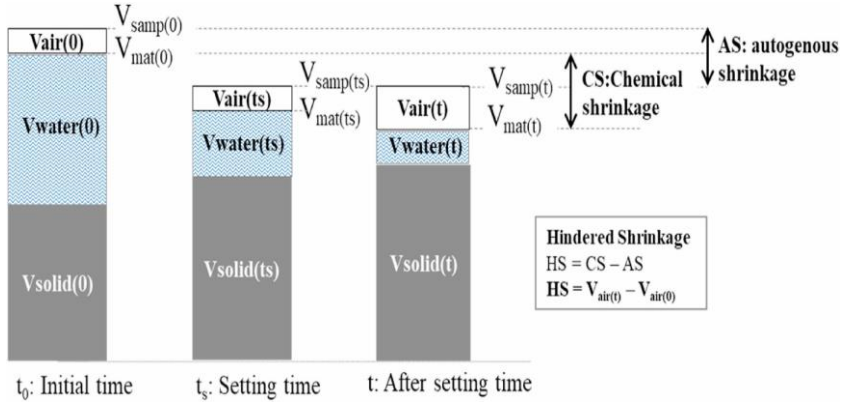

Figure 9.2: Relationship between chemical and autogenous shrinkage [196]

Thereafter, cement still consumes water and creates suction because the total deformation is hindered by the solid network rigidity. The latter is also called self-desiccation and decreases the relative humidity in the pores when no additional water is provided. The resulting decrease of the water menisci radii, formed in the capillary pores, creates tension both at the surface of the cementitious material and in the pore water, pulling the matrix closer together and causing shrinkage. The relationship between the capillary pressure and the relative humidity can be expressed based on Equation [9.3]

$$P_C = -\frac{\rho RT}{M}\ln(RH) \quad [9.3]$$

Wherein P_c [Pa] is the capillary pressure, ρ [kg/m^3] the density of the pore fluid, R [J/mol.K] the ideal gas constant, T [K] the absolute temperature, M [kg/mol] the molar weight of the pore fluid and RH [-] the relative humidity. The ongoing hydration will result in the formation of menisci in the smaller pores after the larger pores are being emptied, resulting in a further decrease of the internal RH and an increase in the capillary pressure and autogenous shrinkage.

For relevant autogenous shrinkage comparisons, the choice of the reference age is primordial. In the study by Baroghel – Bouny et al. [193], the Vicat setting time, as well as the so-called 'knee-point' (i.e. the distinctive bending point which implies the transition between solid and fluid state of a suspension) were used as the onset of deformation comparison. This was also stated by [197], were no relevant difference in autogenous shrinkage could be observed when choosing the final setting time or knee-point as reference time. However, choosing the knee-point seems more suitable since it can easily be determined from the results of the autogenous shrinkage test.

9.1.4. Drying shrinkage

Drying shrinkage refers to the reduction in concrete volume, continued over the whole lifetime, caused by water evaporation from the matrix to the surrounding environment. Initially, free water escapes to the concrete surface as bleeding water, which can evaporate to the environment. Once the bleeding water is completely evaporated, an excess amount of water will be pulled from the interior of the concrete mass. The most common situation resulting from drying shrinkage at early ages is the appearance of surface cracking. It is generally accepted that the drying mechanisms causing shrinkage are dependent on the microstructure; the larger pores will be the first ones to lose their internal water. Digital manufactured specimens are, due to the lack of molding, directly after extrusion exposed to environmental conditions and show in general a higher porosity due to the print process. Therefore, it can be assumed that the effect of drying shrinkage will be more pronounced and detrimental compared to mold-casted specimens.

9.1.5. Carbonation shrinkage

Carbonation is generally known as the chemical transformation of cement hydration products in the presence of CO_2 from the air into calcium carbonate (and water) and the specific details of these reactions are already explained

in Chapter 8. However, the main consequences of the latter are dehydration and decalcification and both are causes of carbonation shrinkage. The dehydration, or loss of bound H_20, triggers the same reaction as drying shrinkage. Water that was once bound (or held under the form of hydroxide) is freed and can now be lost to the environment and thus adds to drying shrinkage. Decalcification on the other hand reduces the Ca/Si ratio in the remaining hydrates, causing a morphology change into a more sheet-like structure. This structural reorganization leads to shrinkage of the overall volume, while paradoxically the transformation of $Ca(OH)_2$ into $CaCO_3$ is volume expanding (3% to 19%, depending on the crystal form taken).

9.1.6. Thermal shrinkage

Cement hydration is an exothermic reaction and thus heat producing. This phenomenon will heat up the setting concrete as well as the unbound water, which might evaporate to the environment. Thermal shrinkage happens at the same time as plastic or autogenous shrinkage. On the other hand, the contraction of hardened concrete due to a decrease in temperature is also a type of thermally induced shrinkage. It is well known and omnipresent for all matter. In conventional cast concrete, the effect of the latter will not be dominant nor considered in the overall discussion. However, in digital fabrication, the binder content is generally higher, causing an elevated temperature during the hydration process. Consequently, the result of the latter will be more pronounced.

9.1.7. Shrinkage in 3DCP

It is important to note that in general, very few studies are available with regard to shrinkage in 3DCP. Le et al. [13] studied the drying shrinkage of printable cementitious materials and investigated the influence of external environmental conditions. However, these measurements were performed on mold-cast samples with the same composition as printable concrete. Later, Zang et al. [198] studied the drying shrinkage of printed elements by attaching clips at the ends; however, this application is not possible in the fresh state due to practical limitations and could create cracks near the interfaces. To ensure accurate shrinkage measurements in 3DCP, non-contact measurements like Digital Image Correlation (DIC) would be a more feasible option and the efficiency of the latter to visualize free and restrained shrinkage in printed samples is already confirmed by Moelich et al. [192]. However, similar as for the mechanical characterization, accurate and standardized test methods which also consider the practical difficulties in

terms of digital fabrication are a current need for this manufacturing technique in terms of durability.

Another aspect is the differential shrinkage deformation between the printed layers. As the 3D printed layers get deposited at different time intervals, the subsequent, non-uniform moisture distributions cause differential length changes as a result of the combination of shrinkage, creep and strain relaxation effects, which could also have a negative effect on the bond strength between the printed layers. However, the latter phenomenon has not been investigated yet.

9.2. Mitigation of shrinkage

There are different strategies to improve the resistance of cementitious materials against shrinkage. These strategies include *(i)* the addition of shrinkage reducing admixtures (SRA), (ii) the application of internal or external curing and *(iii)* the addition of inorganic materials. In the next paragraphs, these different strategies are discussed.

9.2.1. Shrinkage reducing admixtures

Shrinkage reducing admixtures are added to the cementitious material because of their ability to prevent shrinkage cracking; they decrease the surface tension of the pore solution and the capillary tension. The disadvantage of SRA's is that they cause a delay in the hydration reaction and have a negative effect on the mechanical performance [199].

9.2.2. Curing methods

Curing methods can be applied internally or externally and the difference between these methods is depicted in Figure 9.3. Internal curing refers to the introduction of water inclusions to the cementitious material, mainly in order to counteract autogenous shrinkage. When the internal RH drops, the water absorbed by the internal curing agent can gradually be released towards the cement matrix to compensate the water consumption by the hydrating cement paste. Hence, the internal humidity can be maintained at a higher level and the self-desiccation can be suppressed. The most common materials to provide an extra water amount for internal curing are lightweight aggregates (LWA) or superabsorbent polymers (SAPs). However, unlike conventional cast concrete, aggregates sizes in 3D printing applications are still limited; most printable mixtures listed in literate have aggregate sizes limited to 2 mm. As the aggregate size of LWA is mostly larger than 2 mm, the

use of the latter as an internal curing agent in 3DCP is therefore not considered.

SAPs on the other hand act as internal water pockets in the cementitious material due to their swelling capacity in aqueous solutions. They are able to provide the cementitious matrix with the stored water that is released by increasing the capillary pressure due to plastic shrinkage and self-desiccation leading to autogenous shrinkage [78, 200], resulting in an internal curing effect. However, interesting observations have been done with respect to the polymer geometry. First of all, small-sized SAPs release the curing water more gradually, causing a longer controlled internal curing and less evaporation. This results in a better autogenous shrinkage mitigation and less volumetric changes. When the amount of SAPs increases, the difference between small and large particles diminishes [74, 201]. Secondly, a uniform SAP distribution is paramount for a good mitigation of self-desiccation and the mixing procedure is herein an important stakeholder [194]. An inappropriate mixing procedure can lead to breaking up (swollen) SAPs which might be detrimental. In addition, SAP's tend to have an influence on the ultimate rate of hydration and might partly mitigate drying shrinkage and decrease the related crack formation.

On the other hand, in order to prevent evaporation or the loss of water, curing can also be applied externally by for example adding water or other curing compounds on the concrete's surface (Figure 9.3). In case of 3D printed specimens, this would not only mitigate autogenous shrinkage but also reduce drying and plastic shrinkage as it would prevent water evaporation.

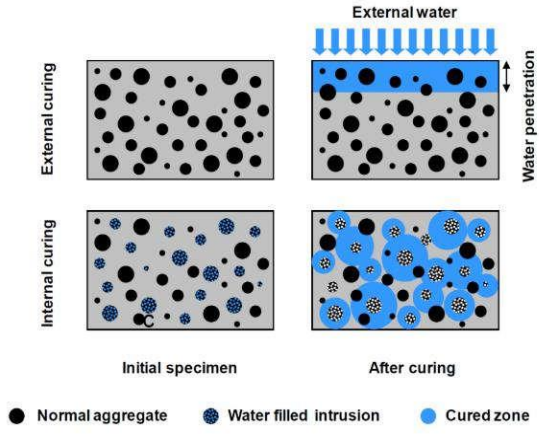

Figure 9.3: Difference between internal and external curing methods [202]

9.2.3. Mix composition

Inorganic additions, e.g. clays or expansive agents based on MgO, can act as shrinkage reducing agents [70]. However, as the addition of nano-clay is not the scope of this research, this will not be further discussed.

The addition of polypropylene fibers cannot be considered as a shrinkage reducing agent, however, it is a widely accepted technique for controlling plastic shrinkage cracking. By improving the strain capacity of the fresh mixture, fibers do not only reduce crack formation, but they are able to disperse cracks in a way that many cracks appear instead of fewer larger ones. In addition, the fibers also mitigate the micro crack propagation from developing into actual plastic shrinkage by providing bridging forces across the cracks to prevent crack propagation [203].

During extrusion in 3DCP, fibers tend to align with the print direction and help the material to remain in place after extrusion, causing lower stresses and less crack formation. In general, an increase in fiber volume fraction was observed to play a major role in controlling plastic shrinkage cracking. Volume fractions >0.1% and >0.5% were found as the upper limit in case of micro and macro fibers, respectively. On the other hand, fibers with finer diameters performed superior to fibers with larger diameters. More specifically, most micro fibers ($d \leq 0.1$ mm) added at volume fractions >0.2% were able to achieve an almost crack free surface [203].

9.3. Materials and methods

In order to counteract shrinkage or shrinkage related cracking in 3D printed elements, mix compositions with superabsorbent polymers (A017, G025, M022, as denominated in Chapter 3) and polypropylene fibers (M3, as denominated in Chapter 3) were fabricated and compared with a reference mixture (REF) without any addition. The mix procedure used to prepare the mixtures is similar as the one explained in Chapter 3.

9.3.1. Drying shrinkage

As shrinkage test methods are not standardized yet for printed concrete samples, drying shrinkage of the printable mixture was measured according to NBN B15-216 [204]. Therefore, two test series of 3 prismatic mold-cast elements (160 x 40 x 40 mm^3) were fabricated per mix composition. Immediately after casting, the molds were covered with foil and demolded after a hardening period of 24 hours. For the first series, water evaporation was prevented by covering the entire specimen with aluminum foil

immediately after demolding, while the second series was left uncovered after demolding. Thereafter, two metallic measuring points were provided on the four 40 x 160 mm^2 prism sides of both test series. The length change of the specimens was measured using a vertical comparator. The initial length (L_0) was measured 1h after demolding. Subsequently, the length (L_t) was measured at 1, 3, 7, 14, 28 and 56 days after the initial measurement and the length change at a certain time t was calculated based on Eq. [9.4]. The length change of the covered prisms ($\varepsilon_{aut,cast}$) serves as an indication of the autogenous shrinkage, while the length change of the uncovered ones ($\varepsilon_{tot,cast}$) represents the total shrinkage. The difference between both is accounted for as drying shrinkage ($\varepsilon_{dry,cast}$ Eq. [9.5]).

$$\varepsilon_{i,cast}\ [\mu m/m] = \frac{L_0 - L_t}{L_0} \cdot 10^6 \mu m/m \qquad [9.4]$$

$$\varepsilon_{dry,cast}[\mu m/m] = \varepsilon_{tot,cast} - \varepsilon_{aut,cast} \qquad [9.5]$$

9.3.2. Autogenous shrinkage

Autogenous shrinkage of the printable mixture was monitored according to ASTM C1698 [205] with corrugated tubes and digital dilatometers (Figure 9.4). The polyethylene tubes were filled in three steps, making use of the in Chapter 3 described mortar gun to minimize the amount of entrapped air. In between the filling steps, samples were vibrated on a vibration table to ensure air floating and complete filling of the tubes. The end-to-end length of the tubes, sealed at both ends with a plug, equaled 420 $\pm$ 5 mm and was recorded manually before the start of the measurement in order to obtain the initial length and to ensure an accurate calculation of the lengths at later ages.

Figure 9.4: Auto-shrink dilatometry (ASTM C1698 [205])

Afterwards, the tubes were placed in an automatic continuous measuring frame with digital dilatometers. Continuous measurements were performed every 10 min for 7 days in a controlled atmosphere of 20 ± 2°C and 60 ± 5% RH. The measurements were performed in triplicate. The linear autogenous strain ε_{auto} [µm/m] was calculated based on Eq. [9.6]:

$$\epsilon_{auto}\,[\mu m/m] = \frac{L(t) - L(t_{ref})}{L(t_{ref})} \cdot 10^6 \mu m/m \qquad [9.6]$$

With L(t) [mm] the length of solely the concrete element inside the mold at time t, t [s] the instant time starting at $t = t_0$ (i.e. the moment of water addition) and t_{ref} [s] the reference time at which ϵ_{auto} [µm/m] is zeroed out. According to ASTM C1698, t_{ref} should be taken equal to t_{fs}, the final setting time as obtained by Vicat measurements.

Eq. [9.6] results in a representation of ϵ_{auto} as a function of time, which is visually inspected to determine the knee-point. The latter is a distinctive bending point which implies the transition between the fluid and solid state of a suspension. From that moment onwards, a more constant behavior of the autogenous shrinkage can be observed. In some research, the latter is used as a reference point. Based on [197], no relevant difference in autogenous shrinkage could be observed when choosing the final setting time or the knee-point as time zero. However, choosing the knee-point seems more suitable since it can easily be determined from the results from the autogenous shrinkage test.

9.3.3. Unprotected shrinkage

Auto-shrink dilatometry allows the assessment of (chemically driven) autogenous and self-desiccative shrinkage in time, as it seals the mortar from the environment. Consequently, plastic shrinkage is therefore not taken into account in the previous technique. But since it has a considerable share in the overall unprotected shrinkage [192], it was deemed paramount for this research to be quantified.

Standardized test methods measure on test samples which are kept for 24 hours in molds, which makes them unsuitable for relevant and accurate measurements in case of 3D printed samples. Because of this, the author proposed a new test method where a Logitech C920 Full HD 1080P webcam takes photographs of single-layered filaments (30 x 150 mm^2), printed on a glass plate. To allow free movement of the printed specimens, a layer of talcum powder was applied on the entire plate surface, covered with a cling film to avoid interaction between the printed material and the talcum

powder. Both ends of the cling film were taped to the bottom of the plate. After extrusion of the layer, the film was cut just before and after the printed layer, providing free movement of the specimen in time.

Immediately afterwards, five fluorescent measuring points were randomly placed on the substrate surface (Figure 9.5). These points were made of iron wire (Ø = 0.5 mm, l = 5 mm), covered in fluorescent paint, and are used together with the digital image analysis software GOM Correlate to register the linear movements in time. The software measures 285 x 622 pixels at a focal length of approximately 6 cm. As such, one pixel accounts for ca. 0.12 mm or a possible strain error of about 1.6 ‰ longitudinally and 3.5 ‰ transversally. According to NBN B15-002 [206], an estimated unprotected shrinkage of about 4‰ is expected at the age of 7 days and measured in laboratory conditions. It is important to note that these expectations are made based on mixtures with a traditional composition. As already discussed before, in 3D printable materials the binder content is higher and these printed materials will subsequently show more shrinkage. This suggests that the proposed testing procedure might over- or underestimate the amount of shrinkage, and that a higher precision camera would be more reliable. However, prior testing has proven the procedure to be accurate for the overall measured two-dimensional shrinkage laying in the range of one percentage point.

Starting from 10 minutes after water addition, photos were taken of the printed layers at a 5-minute time interval. For the first 24 hours, pictures were analyzed with a digital mesh of 15 pixels x 15 pixels applied to the surface of interest, which was determined in accordance with the position of the measuring points. The subsequent 6 days of recorded material was thereafter analyzed at 30-minute intervals, with the same mesh size implemented. The first photograph served as a reference for all others, to which the mean technical strain ϵ_{cam} [µm/m] was calculated both in the printing direction (x) and in transverse direction (y) by Eq. [9.7].

$$\epsilon_{cam,i}\,[\mu m/m] = \left(\frac{\Delta l}{l_0}\right)_i \qquad [9.7]$$

in which i [-] denotes the strain direction (i.e. x or y), Δl [mm] equals the difference in directional length of the complete surface of interest and l_0 [mm] is the initial directional length of the surface of interest. The test was executed in triplicate for each mix design in a controlled atmosphere, which guaranteed a constant temperature (20 ± 2°C) and relative humidity (60 ± 5%).

Figure 9.5: Camera setup for photographic image digital analysis

9.4. Results

9.4.1. Drying shrinkage

Both, the addition of superabsorbent polymers and fibers are beneficial in counteracting drying shrinkage, as depicted in Figure 9.6 and represented in Table 9.1. During the first day of exposure, the addition of fibers (mix composition M3) shows the greatest perspectives and causes a shrinkage reduction of 40% after one day compared with the reference composition. A possible explanation for this behavior could be the higher tensile strength of the fresh concrete where the denser matrix would keep the water inside the cementitious material and reduces the water evaporation rate and the related crack formation. However, this latter explanation is only an assumption of the author as this is not directly measured.

On a longer term (i.e. after 56 days), superabsorbent polymers (mix compositions A017, G025 and M022) are more beneficial and reduce drying shrinkage with approximately 40% (compared with a reduction of 32% in case of fibers). Although the deviation between the results is rather small, and based on a statistical analysis not significant, one can observe a more prolonged effect in case of A017. This can be attributed to the smaller size of the SAPS and the more gradual release of their absorbed water.

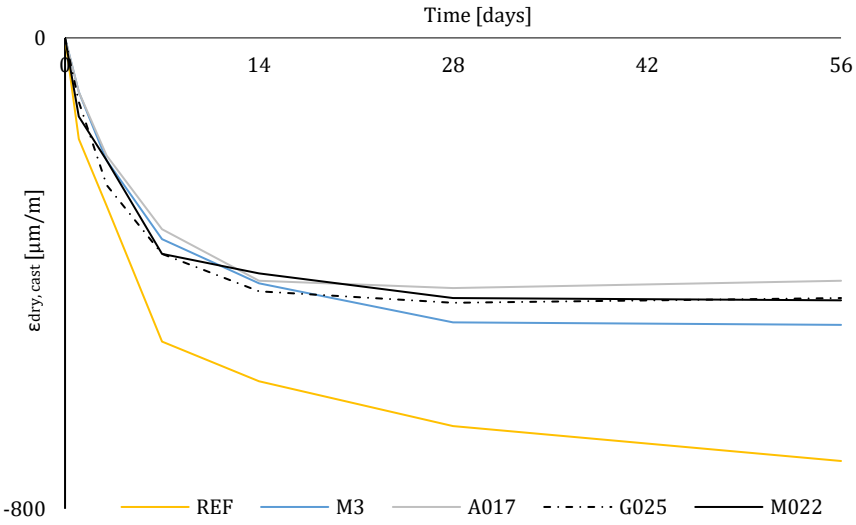

Figure 9.6: Drying shrinkage of the different mix compositions as a function of time (n=3, graphs represent the mean value of the different measurements. The error bars are left out of the figure).

Table 9.1: Drying shrinkage of different mix compositions as a function of time, represented as the mean value (n =3, standard error is included)

	1	3	7	14	28	56
REF [µm/m]	-150 ± 90	-275 ± 65	-450 ± 80	-583 ± 10	-633 ± 96	-758 ± 53
M3 [µm/m]	-92 ± 53	-208 ±23	-342 ± 65	-417 ± 30	-483 ± 50	-488 ± 99
A017 [µm/m]	-92 ± 21	-200 ± 12	-325 ± 99	-413 ± 53	-425 ± 80	-413 ± 76
G025 [µm/m]	-108 ± 30	-250 ± 65	-367 ± 43	-431 ± 52	-450 ± 29	-442 ± 43
M022 [µm/m]	-133 ± 45	-208 ± 53	-367 ± 12	-400 ± 80	-442 ± 22	-446 ± 64

It is important to note that these results only represent the drying shrinkage behavior of the mixture. Nor the influence of the print process, nor the direct exposure to environmental conditions are considered when using the standardized test as described in NBN B15-216 [204]. In addition, the author noticed that the standard error is relatively high. To ensure more accurate and relevant measurements, especially in the very early stage after deposition, the applied standard NBN B15-216 should be adapted and/or more accurate measuring devices should be considered (e.g. DIC, as discussed in section 9.1.7).

9.4.2. Autogenous shrinkage

Figure 9.7 shows a longitudinal autogenous strain plot in time. The first bending point marks the first real change in chemical structure: i.e. the initial setting time or the moment the specimen goes from a pure suspension state to a percolated structure. This denotes the end of vast plastic shrinkage, be it chemically induced by a loss of water to hydration rather than by evaporation, bleeding, and by the elasticity of the corrugated tubes that might slightly deform in the first minutes after filling. The second bending point indicates the final setting time and as such a completely percolated structure of irreversible chemical bonds. From this point onwards, the overall shrinkage is mostly due to the apparent volume change rather than the absolute, as the latter stagnates when the hydration rate diminishes. Consequently, from that moment on the autogenous shrinkage is self-desiccative. By definition, the knee-point coincides with the second bending point.

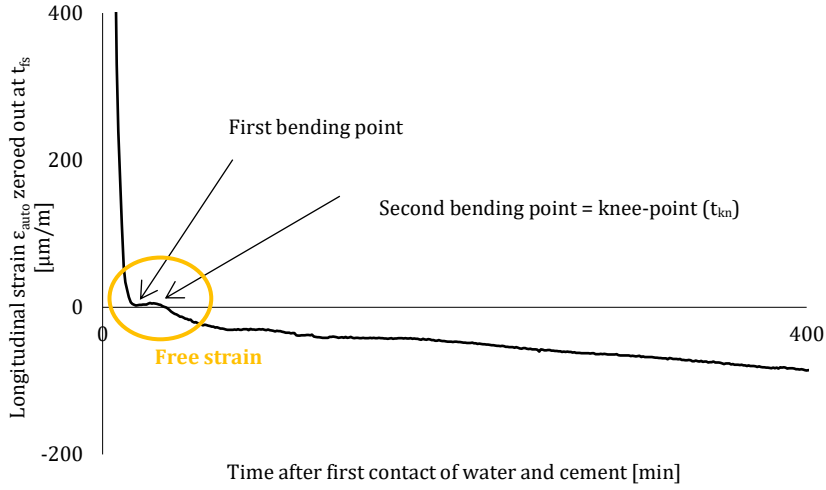

Figure 9.7: Observation of knee-point in ε_{aut} (1 of 3 measurements of REF)

After final setting, self-desiccation of the material starts and a reliable comparison between the different materials in sealed conditions can be made in terms of autogenous shrinkage. The longitudinal autogenous strain, measured by means of corrugated tubes, is plotted in time (zeroed out at $t_{kn,}$ Figure 9.8). The autogenous shrinkage of REF equals -120 µm/m, which is in accordance with the research of Justs et al. [207] and Dudziak et al. [208]. They observed autogenous shrinkage values of - 250 µm/m to -100 µm/m,

respectively. However, these results are in contrast with the material described by Snoeck [74]. The autogenous shrinkage of his reference mixture R0.35, with a W/C-ratio of 0.35, equaled -700 µm/m 6 days after the addition of water. This amounts to a difference of roughly 600 µm/m. However, it is unclear why this difference is so substantial (i.e. a shrinkage reduction of 80%) as the knee-points were derived around the same time. A different chemical composition of the applied cement could serve as a possible explanation; However, this statement cannot be confirmed.

Compared with the reference mixture, a swelling behavior immediately after final setting up to about one day after is present in all mixtures containing SAPs. This is ascribed to their capacity to recapture possible bleeding water that has risen to the interface between tube and mortar and the formation of hydration products in the macropores [209]. After swelling, A017 and M022 show an identical shrinkage rate, which is also comparable with the reference material (-13,9 µm/m/day on average). These conclusions do however not hold for G025, which differs from all other mixtures with an effective significance of less than 0.176.

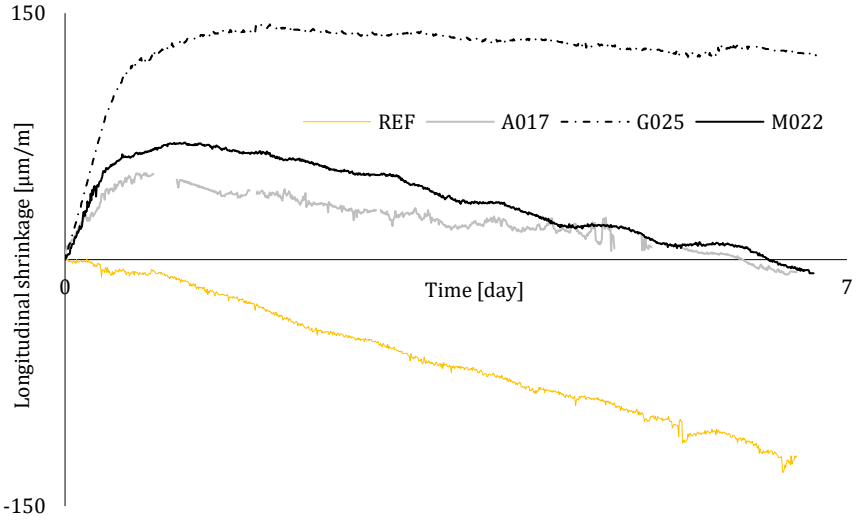

Figure 9.8: Autogenous shrinkage zeroed at the knee-point of mixtures containing superabsorbent polymers (n=3, graphs represent the mean values).

Unlike mix compositions with SAP type A or M, G025 has a shrinkage rate after swelling of –4.9 µm/m/day on average. The autogenous shrinkage mitigation of G025 is explained by the former conclusions for the mixture, described in Chapter 3; during mixing, G025 is slower to reach full swelling capacity, during printing it is the most viscous one and after printing it seems driest, though most dimensionally stable. In addition, SAP G has one of the best swelling capacities in cement filtrate and the shortest setting duration (i.e. period of free strain). As a consequence of the latter, G025 is able to take up more of the mixing water than it was designed for due to its good swelling capacity. It seems to retain the water the longest as well, as the onset of free strain is delayed the longest (as discussed more in depth in section 9.4.5). Therefore, less bleeding water will be lost to the interface of the tube and specimen compared to other mixtures and the effective W/C-ratio will be relatively lower.

When the period of free strain starts, SAP G is more efficient in providing the surrounding cement particles with water for the following reasons: *(i)* internal curing water is only provided within a 2 mm range around the SAP reservoir; *(ii)* the particles are relatively small, abundant and therefore well spread over the specimen; *(iii)* type G particles still hold most of their initially absorbed water. All of this led to an efficient supply of water to the cement particles by SAP G and as such a reduction in setting duration. Since autogenous shrinkage is self-desiccative from final setting onwards, induced by capillary tension, it is countered more in G025 for the same reasons as latterly mentioned – or in short: for its efficiency in providing water to compensate capillary tension. This notion of efficiency can be used to describe the behavior of SAPs as well. Although no significant differences are noted when comparing the mean values, the reasons for a lower swelling tendency right after t_{kn} are believed to be: for SAP A, the loss of water due to bleeding, and for SAP M, the loss of water due to bleeding and a lack of swelling capacity and reabsorption in mortar. In addition, it is marked that G025 has the largest macro- and micropore content (7.6%), but the smallest mesopore content as well (17.1%), in comparison to other mixtures with SAPs. In addition, the better shrinkage mitigation will also reduce the micro cracking related to the autogenous shrinkage.

Although the accuracy of the measurements is not comparable, similar trends can be observed when measuring autogenous shrinkage according to NBN B15-216 (Table 9.2); immediately after demolding, the reference material starts to shrink, while mixtures containing superabsorbent polymers cause in first instance material expansion. In addition, A017 and M022 tend to have a similar shrinkage behavior, while G025 mitigates

autogenous shrinkage the best when comparing the results 7 days after casting.

Table 9.2: Autogenous shrinkage measurements according to NBN B15-216, with and without the addition of superabsorbent polymers measured at 1, 3 and 7 days. (n=3, standard error is included)

	1	3	7
REF [µm/m]	-58 ± 15	-125 ± 22	-155 ± 14
A017 [µm/m]	8 ± 14	18 ± 9	-75 ± 8
G025 [µm/m]	58 ± 20	75 ± 24	-8 ± 18
M022 [µm/m]	17 ± 17	-8 ± 15	-58 ± 5

9.4.3. Chemical shrinkage

Within the scope of this research, chemical shrinkage is not measured in an experimental way. However, as mentioned before, it can be quantified based on the mineralogical composition of the cement and will be the same regardless of the mix composition as a similar cement type is applied. Based on Eq. [9.2], the volume reduction due to chemical shrinkage equals 6.36%.

9.4.4. Unprotected shrinkage

Plastic and drying shrinkage, which are the highest within the first 4 hours after printing, are crucial in case of 3D printed mortars [192, 210] and can be estimated based on the unprotected shrinkage measurements. More specifically, the representation of the measured shrinkage before knee-point allows the author to drawn conclusions about the plastic and drying shrinkage, although not separately, assuming that these are the governing shrinkage mechanism before knee-point, not considering chemical or thermal shrinkage within this time frame of 0 – 4 hours after material deposition. The volumetric changes, occurring before the knee-point are depicted in Figure 9.9 and reveal not much difference between the reference material and the mixtures containing SAPs. The order of magnitude of the measured shrinkage values is comparable with the results obtained by Slowik [190] (i.e. $-2.8.10^3$ µm/m versus $-2.3.10^3$ µm/m in this research). Although the experimental setup in the latter research is much more elaborated than the photographic analysis technique used here, one can conclude based on the results that the technique is deemed valuable and suitable for conclusive discussion.

Additionally, Figure 9.9 also depicts that the highest strain occurs in the first 60 minutes after printing, regardless of the direction. This can be related to the higher evaporation rate and the larger surface area exposed to environmental conditions. Within this first 60 minutes, micro-cracks will be formed on the top surface and at the sides of the fabricated specimens. However, this also implies that, when multilayered specimens are printed with a certain time gap in between the layers, the shrinkage rate and behavior of super positioned layers will differ and this effect will become even more pronounced with larger time gaps with more shrinkage cracks as a result. In addition, the longer the time after printing, the more structure is build-up within the element. The substrate layer will become less deformable over time, and will restrain the shrinkage behavior of the superpositioned layer to a higher extend compared with lower time gaps. The latter will enlarge the stresses and the formation of cracks. Both phenomena will endanger the mechanical behavior (especially the bonding between the layers) and the durability of printed elements, as already proven in Chapter 4 till Chapter 8.

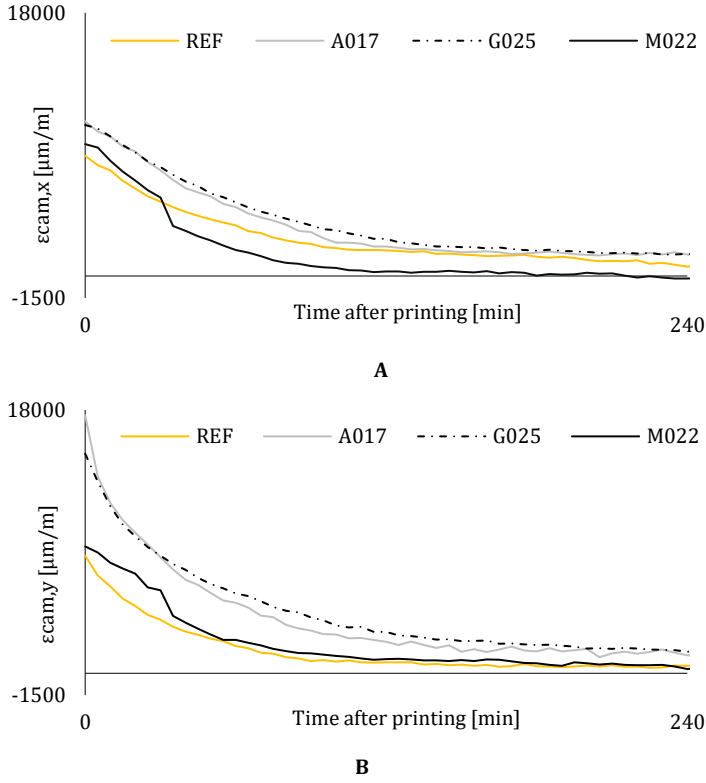

Figure 9.9: Shrinkage measurements immediately after printing in longitudinal (A) and transversal (B) direction (n=3, graphs represent the mean value)

Figure 9.10 and Figure 9.11 represent the unprotected shrinkage, measured in two different directions, starting from t_{kn}. With respect to shrinkage along the printing direction (Figure 9.10), the following observations are made. All mix compositions shrink, however mixtures with SAPs show a minor expansion of about +300 μm/m during the first 12 to 24 hours after the knee-point serving as time zero. During this period, the reference specimens show a relatively large shrinkage of about -1500 μm/m. The expansive effect of SAP addition is ascribed to a combination of their water mitigation capacity and a chemical swelling due to the further hydration by internal curing present in all mixtures. However, in case of REF, the chemical swelling is not strong enough to overcome the omnipresent capillary tension.

After final setting, chemical-structural swelling can occur due to the relatively late formation and growth of calcium hydroxide and to a lesser extend of alumina ferric oxide sulphates (which will be present since their reactants are present in the cement mixture) [193]. This will create a crystallization pressure that counteracts the capillary pore water tension that induces self-desiccation. In the case of samples with SAPs, the solid matrix is believed to be more elastic as there is still water supplied to unhydrated cement particles and as such the structuration continues more actively than in case of REF, which is quite dry in comparison. Also, the fresh CSH rims that are formed around these unhydrated particles surrounded by water, are larger in volume than their unhydrated counterparts [193]. But as the specimens are not protected from continued evaporation, only the ones with a water mitigation capacity can benefit from this swelling tendency. It seems that the reference mixture is not able to counteract the self-desiccation as it cannot produce enough continued chemical-structural swelling.

Once hydration slows down as it reaches its optimum, i.e. about one day after knee-point, all mixtures can only shrink under endured evaporation. The shrinkage rates then align for all mixtures to about -200 μm/m/day. On average, this rate is about -40 μm/m/day lower for the reference mixture. The reason why G025 does not show a noticeable better shrinkage behavior is attributed to the difference in test conditions of this shrinkage measurements: protected from loss of water to the surroundings, in which case the polymer particles can hold on to their absorbed water; or not, in which case they will lose some to the environment under capillary tension.

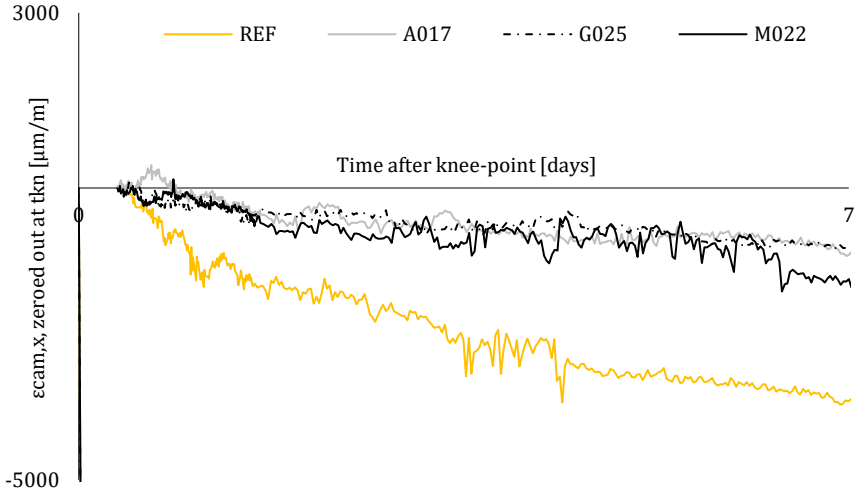

Figure 9.10: Unprotected shrinkage along the printing direction with t_{kn} as time zero (n=3, graphs represent the mean values)

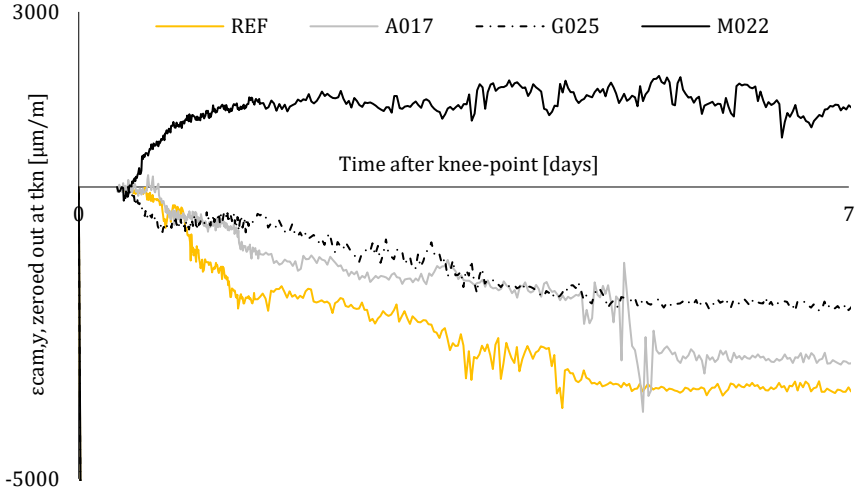

Figure 9.11: Unprotected shrinkage in transversal direction with t_{kn} as time zero (n=3, graphs represent the mean values)

With respect to the unprotected shrinkage transverse to the printing direction (Figure 9.11), the same general trend can be observed: SAPs tend to mitigate the shrinkage. Comparing the shrinkage behavior of the mixtures in both directions, the following trends could be observed. First, the reference

mixture has both in longitudinal and transverse direction the same outcome. Secondly, when the length of the printed samples is sufficient (i.e. 15 cm), the shrinkage in transversal direction seems a magnification of one in longitudinal direction. More specifically, when $\varepsilon_{cam,x}$ shows swelling in the first hours, $\varepsilon_{cam,y}$ will do too; when $\varepsilon_{cam,x}$ continues to shrink after knee-point, $\varepsilon_{cam,y}$ will do as well. The only exception of this rule is M022. This mixture expands the most in transverse direction, while it shrinks considerably in longitudinal direction. In this case, it was later remarked that the sample length was only 11 cm, explaining the opposing phenomenon: a shorter sample means less material to restrict $\varepsilon_{cam,x}$, creating a higher expansion transversally (i.e. Poisson deformation.

Of course, in the field of 3DCP, longitudinal shrinkage will be of greater importance than the transversal shrinkage as the length of a printed element is considerably larger than the width. As the perimeter increases, the volume will do too and as such, the specimen will restrain itself more from shrinkage. In addition, the testing executed in this research was carried out on printed filaments of small sizes allowed to shrink relatively free.

Based on Table 9.3, one can conclude that the measuring method, as described in NBN B15-216, underestimates the real shrinkage behavior of printed samples. The latter effect becomes even more pronounced when no internal curing methods are applied. Unlike conventional cast elements, the total shrinkage 7 days after manufacturing is approximately 7 and 3 times higher when mix compositions without or with SAPs, respectively, are printed. This can be attributed to the direct exposure to environmental conditions and the correlated higher plastic and drying shrinkage.

Table 9.3: Comparison between the total shrinkage, measured on printed or cast samples (n=3, mean values are represented) after 1, 3 and 7 days of manufacturing

	$\varepsilon_{tot,cast}$ [µm/m]			$\varepsilon_{cam,x}$ [µm/m]		
	1	3	7	1	3	7
REF	-208 ± 43	-275 ± 54	-605 ± 23	-1097 ± 54	-2103 ± 67	-3618 ± 42
A017	-83 ± 15	-192 ± 14	-400 ± 15	-240 ± 21	-664 ± 32	-1148 ± 24
M022	-117± 22	-217 ± 17	-425 ± 14	-134 ± 15	-786 ± 22	-1557 ± 72
G025	-50 ± 12	-175 ± 12	-375 ± 16	-372 ± 32	-657 ± 46	-1007 ± 11

In addition, superabsorbent polymers tend to be more beneficial to reduce shrinkage when manufacturing with the 3D printing technology. After 7 days, the total shrinkage is approximately one third compared with the reference composition. Based on this one can conclude that SAPs not only mitigate autogenous shrinkage but also contribute in a beneficial way to the mitigation of drying and plastic shrinkage in the early stage after printing.

9.4.5. Comparison of free strain periods

As represented in Table 9.4, the free strain rates in protected conditions are not significantly different except for the reference mixture REF. All other mix designs have moderate shrinkage rates and show sometimes even expansion. This is solely described to the difference in W/C-ratio; a lower one is leading to more capillary tension. No significant differences in free strain rates are noted in unprotected condition. Though it is remarked that in both conditions, G025 shows the best shrinkage mitigation, undoubtedly due to a combination of the above-mentioned reasons. The vast difference in order of magnitude (10^3) of shrinkages (and rates) monitored in both conditions is ascribed to: (1) evaporation of water to the surroundings; (2) the photographic measurement technique which leaves room for improvement (e.g. a higher precision camera), and (3) the calculation of unprotected shrinkage as technical strain that is translated into an equivalent linear shrinkage in µm/m. A similar factor was mentioned in the research executed by Dudziak et al. [208].

Table 9.4: Strain rates in protected and unprotected shrinkage measured during the free strain period (n=3)

Mixture	Mean free strain rate [µm/m/day]		
	Protected	Unprotected,x	Unprotected,y
REF	-167.6 ± 15	-6.7 10^3 ± 124	-8.9 10^3 ± 65
A017	-3.3 ± 1	-8.0 10^3 ± 42	-12.0 10^3 ± 124
G025	-20.1 ± 4	-7.9 10^3 ± 190	-10.1 10^3 ± 146
M022	+36.5 ± 5	-4.1 10^3 ± 124	-2.8 10^3 ± 198

Figure 9.12 on the other hand depicts the starting time as well as the duration of this free strain period. The onset of setting according to Vicat (n=1) is postponed with the addition of SAPs. It takes about 30 min longer to reach final setting, compared to REF. This is due to the SAPs mitigating the additional water to compensate the loss due to evaporation at the top surface,

which is exposed to the environment. Since the VICAT test will conclude final setting as the moment the needle can no longer penetrate the top surface beyond a certain depth, its state of freshness (i.e. moist) is crucial for the results. The REF mixture will be drier sooner and as such the needle will not be able to penetrate it sooner than for mix designs with SAPs. The same analogy explains the difference in initial setting time for the different techniques. All unprotected shrinkage tests (less distinct for REF) conclude an initial setting time before the one from the Vicat testing. This is explained by the fact that relatively more outer surface is subjected to evaporation in the unprotected shrinkage test setup, creating a drier outer surface with a lower elasticity than the underlying part. On photographs especially, they will appear set, though it might not be completely so. It seems that specimens shielded from the environment in corrugated tubes harden later, as no mixing water is lost and the mortar is kepth fresh. Depending on the retention capacity of the SAPs the effective W/C-ratio is different, leading to small differences observed in Figure 9.12. The larger the effective W/C-ratio, the later the initial setting is marked. The duration of free strain in unprotected specimens is longer than in protected specimens as the latter have a higher effective W/C-ratio, expediting the hydration reaction and as such the hardening process. For all mix designs with superabsorbent polymers, the onsets and durations in unprotected condition differ significantly from the series with REF but not from each other. The onsets in protected conditions show no significant differences.

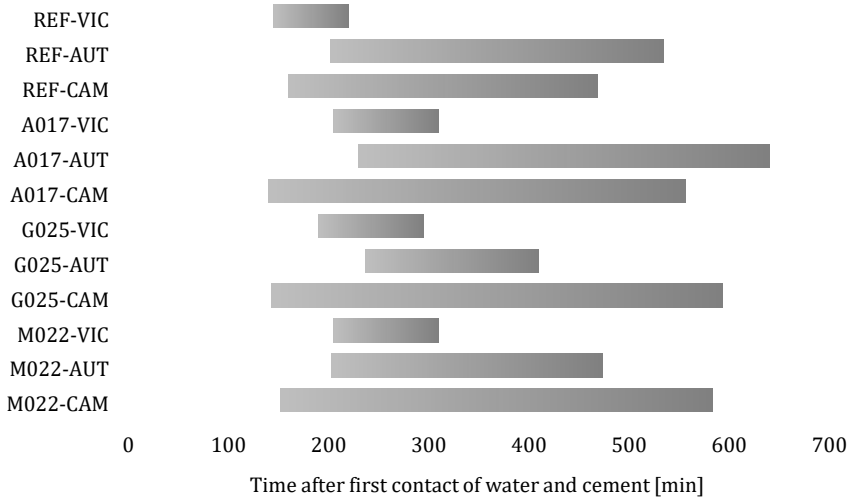

Figure 9.12: Time instant and duration of free strain periods (VIC = Vicat, n=1; AUT = autogenous shrinkage, n=3; CAM = Camera testing, n=3).

9.4.6. Shrinkage modelling

The results represented in the previous sections are measured on traditional cast or one-layered specimens. As already mentioned before, these measurements do not completely correspond with reality, as nor the effect of multiple layers, nor the effect of different time gaps is considered.

fib ModelCode90 and Eurocode2 both provide methods for the quantification of shrinkage as a function of time. Both calculation methods consider the total shrinkage as a combination of autogenous and drying shrinkage. They only differ in the calculation of the coefficient of basic drying shrinkage (Eq. [9.12] and Eq. [9.13]). Autogenous shrinkage is predicted mainly based on the compressive strength of cylindrical specimens at 28 days and the applied cement type. Due to the limited dimensions of printed specimens, compressive strength is determined on small cylindrical samples (Ø = 25 mm, h = 20 mm). This in contrary to the higher dimensions of standard cylinders applied for conventionally cast concrete (Ø = 113 mm, h = 100 mm). However, as the ratio between the diameter and the height equals approximately one in both cases, a similar failure state will be induced in both cases. Drying shrinkage on the other hand is quantified based on the surface exposed to drying. The relative humidity plays a role in both shrinkage predictions.

Autogenous shrinkage

Autogenous shrinkage is calculated as a function of time based on Eq [9.8] till Eq. [9.10], where $\varepsilon_{cbs0}(f_{cm})$ is the basic autogenous shrinkage, f_{cm} [N/mm^2] the compressive strength at 28 day. α_{bs} [-] is a coefficient depending on the cement type and equals 600 for CEM I 52.5 N, the cement type used in all investigated mixtures.

$$\varepsilon_{cbs}(t) = \varepsilon_{cbs0}(f_{cm}) \cdot \beta_{bs}(t) \quad [9.8]$$

$$\varepsilon_{cbs0}(f_{cm}) = -\alpha_{bs}\left(\frac{0.1 \cdot f_{cm}}{6 + 0.1 \cdot f_{cm}}\right)^{2.5} \cdot 10^{-6} \quad [9.9]$$

$$\beta_{bs}(t) = 1 - \exp(-0.2 \cdot \sqrt{t}) \quad [9.10]$$

Figure 9.13 depicts the autogenous shrinkage, calculated according to the standard. Purely based on the compressive strength at 28 days, it is not possible to simulate the real behavior of mixtures containing SAPs (i.e. swelling in the early stage after water addition, as observed in Figure 9.8). Although underestimated, the behavior of the reference material is similar.

On the other hand, based on the compressive strength, it is possible to visualize similar trends. More specifically, the series SAP G tends to mitigate shrinkage the most, while series with SAP A and M show a similar behavior. However, the difference between the different compositions is that small that the conclusions cannot be considered as concise.

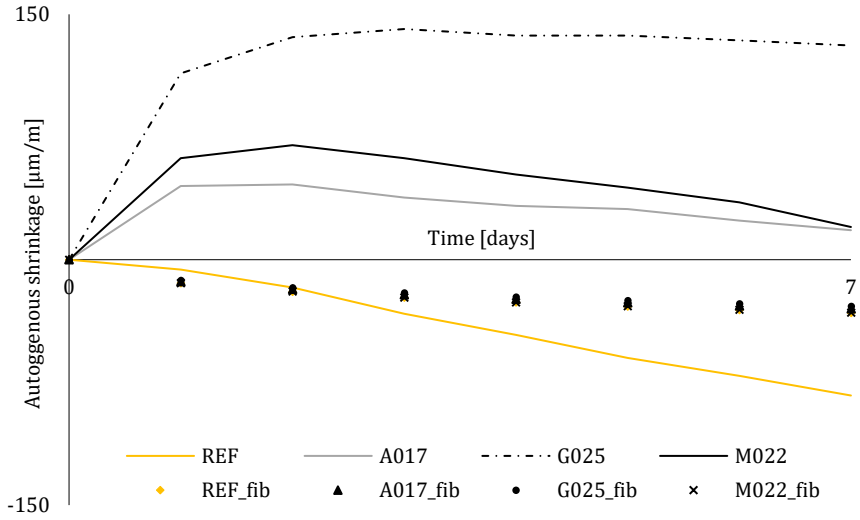

Figure 9.13: Autogenous shrinkage in case of mixtures containing superabsorbent polymers

Drying shrinkage

Drying shrinkage is calculated based on Eq [9.11] till Eq. [9.15], where $\varepsilon_{cds0}(f_{cm})$ is the basic drying shrinkage, f_{cm} [N/mm^2] the compressive strength measured at 28 day.

$$\varepsilon_{cds}(t, t_s) = \varepsilon_{cds0}(f_{cm}) \cdot \beta_{RH}(RH) \cdot \beta_{ds}(t - t_s) \quad [9.11]$$

α_{ds1} [-] and α_{ds2} [-] depend on the cement type and equal 6 and 0.012, respectively (fib ModelCode90. Eq. [9.12]) or 4 and 0.12, respectively (Eurocode2. Eq. [9.13]) for CEMI 52.5 N. f_{cmo} [N/mm^2], used in Eurocode applications, equals 10 N/mm^2 and serves as a standard value for traditional cast concrete. However, as no standard values are available yet in terms of digital fabrication, the effect of the latter will be excluded and further calculations will be purely made based on ModelCode90.

$$\varepsilon_{cds0}(f_{cm}) = [(220 + 110 \cdot \alpha_{ds1}) \cdot \exp(-\alpha_{ds2} \cdot f_{cm})] \cdot 10^{-6} \quad [9.12]$$

$$\varepsilon_{cd,0} = 0.85\left[(220 + 110\alpha_{ds1}) \cdot \exp\left(-\alpha_{ds2} \cdot \frac{f_{cm}}{f_{cmo}}\right)\right] \cdot 10^{-6} \cdot \beta_{RH} \quad [9.13]$$

$$\beta_{RH}(RH) = -1.55 \cdot \left[1 - \left(\frac{RH}{100}\right)^3\right] \quad [9.14]$$

$$\beta_{s1} = \left(\frac{35}{f_{cm}}\right)^{0.1} \leq 1.0 \quad [9.15]$$

$$\beta_{ds}(t - t_s) = \left(\frac{(t - t_s)}{0.035 \cdot h^2 + (t - t_s)}\right)^{0.5} \quad [9.16]$$

Parameter h (Eq. [9.16]) takes into account the surface exposed to environmental conditions and is calculated as the ratio between the cross section and the outline of the section exposed to environmental conditions. Within the calculations, a printed specimen of 150 x 30 x 10 mm^3 (l x b x h) was considered. On could already assume that this calculation method would underestimate the drying shrinkage, as this standard is not designed for elements with their complete surface exposed to drying.

Table 9.5 represents the drying shrinkage of mixtures with and without the addition of SAPs. One can conclude that this calculation method does not represent the real shrinkage behavior: *(i)* based on the calculations, the reference composition tends to shrink less compared with elements including SAP G or SAP M, which is in contrast to the measurements discussed previously, and *(ii)* the calculations overestimate the measured values as represented in Section 9.4.1, especially in the first days after manufacturing. On the other hand, on a longer time period, the results are in the same range. However, they are still an underestimation of the drying shrinkage that occurs in real printed elements

Table 9.5: Drying shrinkage calculated as a function of time according to fib ModelCode90

	1	3	7	14	28	56
REF [µm/m]	-460	-465	-465	-465	-465	-465
A017 [µm/m]	-479	-481	-481	-481	-481	-481
M022 [µm/m]	-600	-601	-602	-602	-602	-602
G025 [µm/m]	-631	-633	-634	-634	-634	-634

9.5. Conclusions

Based on the results presented above, one can conclude that standard methods (both experimental and analytical) do not represent the real shrinkage behavior of printed elements as they do not consider the direct exposure to environmental conditions. More accurate standards and measuring techniques are required and have to be developed. However, the addition of SAPs tends to have more benefits for printed concrete, as they allow not only the mitigation of autogenous shrinkage, but also mitigate drying and plastic shrinkage. However, this is purely based on the latter observations and more in-depth investigations are required to proof this statement further in detail.

Chapter 10

Conclusions and future perspectives

This thesis aimed at investigating the influence of the print process on the mechanical performance and durability of printed elements. In addition, different modification techniques and technologies were investigated to improve these properties and minimize the effect of the print process compared with conventional cast concrete.

General conclusions

3D printing

To focus mainly on the influence of different print process parameters, a basic reference material with a W/C-ratio equal to 0.37 was applied throughout the entire doctoral thesis. In general, printed samples were manufactured with two different print techniques. In case of the first technique, the 2D-print technique, an in-house developed print system was used, made of a mortar gun mounted vertically on a steel frame and fixed on a rigid print table provided with a sliding steel carrier. The mortar gun was equipped with an elliptical nozzle (28 mm x 18 mm). With regard to this equipment, two print velocities (1.7 cm/s and 3.0 cm/s, denoted as S1 and S2, respectively) and four different time intervals (i.e. 0, 10, 30 and 60 minutes denoted as T0, T10, T30 and T60) in between the deposition of two subsequent layers were considered. In order to meet the printability requirements, a higher flow rate was induced appropriate to compensate for the increase of the printing

speed. In case of a zero-minute time gap, the same batch of material was used. In case of enlarged time gaps, the second layer was printed from a new batch of material to ensure similar rheological parameters. The printability of each composition was evaluated based on the extrudability and buildability. The second technique (i.e. the 3D-print technique) was equipped with a Rudolf pump and robotic arm with 6 degrees of freedom (DOF). The selected reference material for 2D-print applications fulfilled all printability requirements, however, the pumpability of that composition was insufficient. The sand-to-binder (S/B) ratio was too high, producing a relatively stiff material with a high yield stress and plastic viscosity. Therefore, to meet in addition also the pumpability requirement, the S/B ratio was lowered (1.5 instead of 2) and the normsand was replaced by sea sand. The flowability of the mixture was optimized by changing the SP content, whereas the W/C-ratio was kept equal compared to that of the 2D reference mix composition. To enable adequate comparisons with regard to the influence of the digital manufacturing technique, a comparison with mold cast specimens was made, using the same composition.

Mechanical performance

In literature is reported that the interlayers can be weak links of a structure and the better the quality of the interlayers, the better the overall structural performance. The quality of the interlayer is mainly affected by the surface roughness, moisture content and the air entrapped in between the layers. As no standard test methods are available for printed specimens, mechanical testing was performed according to the standards for conventional cast concrete. The compressive strength was measured by uniaxial compression testing and the tensile strength with pull-off tests. Therefore, cylindrical specimens, drilled out of original two-layered specimens, were used. The flexural strength was measured with three-point bending tests, executed on prismatic specimens cut from original two-layered printed samples.

Based on the characterization of the printed surface, the author concludes that the surface roughness in the print direction for specimens fabricated with a higher printing speed was 60% lower. Perpendicular to the print direction, a difference of 35% was observed when comparing both printing speeds. The lower surface roughness in case of S2 could be attributed to the higher kinetic energy, acting on the larger sized sand particles and forcing them to penetrate deeper into the bulk material, causing a lower surface roughness. The latter phenomenon was confirmed by microscopic analysis of thin sections.

Regardless of the printing speed, a similar trend in moisture content of the substrate layer could be observed: the longer the time gap, the lower the moisture content and the biggest decrease was noticed after a time gap of 10 minutes. The difference in moisture content for time gaps of 30 and 60 minutes was not significant compared to a time gap of 10 minutes.

Nor the printing speed, nor the time gap had a significant influence on the compressive strength and only a reduction of approximately 10% and 19% for S1 and S2, respectively, could be observed compared with mold cast specimens. However, irrespective of the manufacturing technique, and regardless of the variation in print process parameter, the same fracture mechanism could be observed. The interlayer bonding strength followed the same trend as the surface moisture content; the highest reduction (i.e. 48%) could be observed after an interlayer time interval of 10 minutes. The combined effect of a decreasing surface moisture content and a lower surface roughness in case of printing speed S2 reduced the tensile strength even more. The flexural strength, measured in the print direction, was lower compared with conventional cast specimens, with similar trends as observed in pull-off measurements: the higher the printing speed, the lower the flexural strength. On the other hand, when testing parallel with the printed layers, higher strengths were observed and an opposite trend could be observed: higher speeds cause higher strengths. However, the impact of the interlayer quality could not be observed in the failure mode of the specimen.

Bond improvement

The structural performance is mainly affected by the quality of the interlayer. Different surface modification techniques were applied. The first modification techniques aimed at improving the surface roughness of the interlayer by the addition of different sized sand grains and by changing the nozzle geometry with grooves. The second modification tried to increase the moisture content of the substrate layer and the last technique was aimed at improving the chemical bonding between two layers by the addition of cement. The effectiveness of the different techniques was proved by moisture content measurements, surface roughness measurements and assessment of bond behavior. Based on the mechanical performance, only a different nozzle geometry (rectangle or nozzle with grooves) and the addition of water improved the compressive strength after a prolonged time gap in a significant way. In most cases, the surface modification techniques resulted in a lower interlayer bond strength. The addition of water resulted in similar tensile strengths and an increase in interlayer bonding could only be observed when the nozzle geometry was changed from an elliptical one to a rectangular

nozzle with smaller grooves and side trowels. For some modification techniques, the bonding between the layers after a 30-minute time gap was that bad that complete debonding occurred during sample preparation.

Microstructure

In order to investigate the durability of the printed specimens, the second part of the doctoral thesis started with a fundamental investigation of the microstructural changes induced by the digital manufacturing process, considering different pore sizes and pore types. In first instance, one could observe that the addition of superabsorbent polymers (SAPs) increased the macroporosity compared with the reference material. The pore diameters measured on hardened surfaces of printed elements corresponded with the pore diameters found through microscopic analysis of the SAPs themselves, which was in accordance with the results previously listed in literature for conventionally cast elements. For the larger sized SAPs (i.e. SAP M), a higher amount of entrained air could be observed at the interlayer of the printed material. Mix compositions without SAPs showed a higher void fraction at the interface compared with the bulk material, regardless of the printing speed. Compared with conventional cast elements, also a changing pore morphology was observed. While traditional cast elements contain mostly circular voids, the printing process introduces more elongated pores in the element, oriented mainly in the print direction.

The microporosity (i.e. the capillary porosity) of printed elements with and without the addition of SAPs was evaluated based on Mercury Intrusion Porosimetry (MIP) measurements. In general, the porosity increased as a result of the printing process and a higher print velocity causes a shift towards smaller sized pores due to the higher pressure. However, similar trends could be observed for enlarged time gaps; in the bottom part of a two-layered specimen, the capillary pores become smaller, due to the higher amount of evaporated water. This was also observed at the interlayer, however, as it was not possible to purely measure the porosity at the interlayer itself, the results cannot be considered exclusively. As the second layer of all printed specimens is exposed to the same environmental conditions, the difference in pore diameter was not significant. In printed or conventional cast elements with SAP additions, similar trends could be observed: SAP's tend to reduce the amount of nanopores in the range of 100 nm to 500 nm and the increase of the number of voids with a diameter above 700 nm. This can be attributed to the higher hydration degree around the SAPs, closing up all the smaller pores as well as to their contribution to the reduction of autogenous shrinkage.

Water transport

The durability can be evaluated based on the ingress of water. Similar to conventional cast elements, the capillary water absorption of printed specimens was in first instance based on gravimetrical measurements. The specimens were covered with aluminum foil to ensure unidirectional water ingress. Preliminary results showed that conventionally cast elements were less prone to capillary absorption, which could be observed by a lower initial absorption rate. However, compared with printed specimens, the secondary absorption rate was higher, indicating a lower but longer lasting water uptake. A prolonged time gap between layers resulted in a lower initial absorption rate, regardless of the printing speed.

The water absorption was in addition also quantified based on neutron radiography. Therefore, different printing speeds (S1 and S2), time gaps (T0 and T30), number of layers (2, 3 and 4) were considered for mixtures with and without SAP's. Within the 6 hours of water exposure, the specimens were not covered with aluminum foil to simulate real life conditions as much as possible. When the bottom part of the printed specimens was exposed to water, a low printing speed resulted in a more uniform movement of the water front, while for higher printing speeds, the water uptake was more pronounced at the sides within the first 30 minutes of water exposure. The latter could be attributed to the densification of the bulk material due to the higher pressure applied during printing. The addition of SAPs densifies the cement matrix in between the SAPs. However, as the SAPs are homogenously distributed through the printed element, this densification is not a local effect, which was observed by the uniform water ingress.

When the front surface is exposed to water, a uniform increase of the water front could be observed, irrespective of the printing speed. In case of a zero-minute time gap, the material can be assumed as homogenous and there is no preferential water ingress at the interlayer. A prolonged interlayer time interval weakens the interlayer and the effect of the preferential ingress at the interlayer becomes more pronounced. In case of multilayered specimens, the water ingress was the highest at the top layers, as those were less compacted or loaded by the weight of the successive layers. These observations were made in a qualitative way and confirmed in a quantitative way.

Durability

Besides the ingress of water, also the ingress of harmful substances (chlorides and CO_2) was investigated in order to assess durability indicators. An evaluation of the chloride ingress was performed with the chloride diffusion test. Therefore, molded specimens and four-layered printed elements were manufactured with different time gaps (T0, T30 and T60) and different printing speed. To ensure unidirectional chloride ingress, five out of six sample sides were covered with aluminum foil provided on the samples after a hardening period of 28 days. The chloride ingress was evaluated based on colorimetric measurements by spraying silver nitrate and by a quantification of the chloride content based on potentiometric titrations.

Purely based on the visualization of the ingress front by spraying silver nitrate, one could observe two general trends: the chloride ingress is higher in printed specimens compared with cast specimens (40% and 17% ingress after one week of exposure, respectively) and a uniform ingress front could be observed for elements printed with a zero-minute time gap. Regardless of the printing speed and time gap, the fast penetration of chlorides could be attributed to the higher capillary suction and to the fact that the fabricated samples were not saturated in advance. However, the ingress rate stagnates after the first week of exposure. After the first chloride ingress, the ingress phenomenon is dominated by diffusion and in addition, more chlorides are captured by hydration products causing chloride binding, which alters the pore structure due to the formation of Friedel's salt.

Based on potentiometric titrations, performed to quantify the acid-soluble chloride content, the same trends could be observed. Irrespective of the printing speed, the total chloride content increases when extending the interlayer time gap. The latter conclusion is valid both after two and ten weeks and for every layer depth, confirming that chlorides penetrate deeper into the printed material due to the higher porosity and the higher surface area. Although the differences are rather small, the stagnation deeper into the printed specimen is slightly more pronounced for S1 than for S2. However, it should be noted that these potentiometric titrations serve as a first estimation and the real chloride content could deviate from reality for several reasons: *(i)* grinding is performed with the smallest possible drill (8 mm diameter), but the grinded powder remains a combination of the bulk and interlayer material, *(ii)* the curved surface of printed specimens will affect the unidirectional chloride ingress and *(iii)* the heterogeneity of the material could also affect the results. Fitting the chloride ingress profiles by Fick's second law, the non-steady state diffusion coefficient and the chloride surface

concentration were obtained. In general, the diffusion coefficient decreases and the surface concentration increases with enlarged time gaps.

The carbonation front was visualized by spraying phenolphthalein on split surfaces, considering similar test series as for chloride ingress testing. Although the CO_2 penetrated deeper into the printed material, for both mold cast specimens and specimens printed with a zero-minute time gap, the ingress front could be assumed uniform. The deeper penetration in the latter case had the same origin as in case of chloride ingress: a higher porosity and a higher number of micro-cracks. A prolongation of the interlayer time gap increased the penetration depth, both in the bulk and the interlayer. As the pore structure of elements fabricated with printing speed S2 is more open, the effect of the latter is slightly more pronounced for this test series. In addition, the carbonation rate at the interlayer decreased more rapidly for higher time intervals compared with lower time intervals and a similar penetration rate could be observed after 24 weeks of CO_2 exposure, irrespective of the printing speed. Although the ingress of CO_2 is detrimental and in general inadequate for reinforced concrete, the durability could be increased by an adequate curing method (external or internal), limiting the desiccation of the outer layer and decreasing the porosity.

A third durability indicator studied is the resistance against freeze/thaw. The cementitious material (printed or molded) was exposed to 14 freeze/thaw cycles according to NBN B15-231. The resistance was evaluated based on the difference in weight, compressive strength and ultrasonic pulse velocity before and after exposure to freeze/thaw cycles. Regardless, of the measuring technique the same conclusion could be drawn; after 14 freezing cycles, there was almost no microstructural damage created in the printed specimens, regardless of the printing speed and the interlayer time interval. The latter could be attributed to the presence of larger sized pores and a lower pressure exerted on the pore walls.

Shrinkage

Due to the lack of molding, printed elements are directly exposed to environmental conditions and are consequently more prone to shrinkage (drying and plastic shrinkage). In order to counteract the detrimental effect of shrinkage, SAPs and fibers were added to the reference composition. In this series of tests, three different SAPs (SAP A, SAP G and SAP M) with different diameters (100 µm, 157 µm and 486 µm, respectively) and different swelling times (10 s, 22 s and 65 s, respectively) and one type of polypropylene fibers (Crackstop M195-03, Adfil) with a diameter of 22 µm and a length of 3 mm

were used. The mix composition for both additions was optimized based on flow table tests and a deviation of ± 5 mm on the flow table diameter of the REF material was allowed.

Based on different measuring techniques, a differentiation between the various shrinkage types was made. Drying shrinkage was measured according to NBN B15-216, autogenous shrinkage was measured by corrugated tubes and the overall shrinkage was evaluated based on camera measurement and subsequent image analysis. Based on the results, the author could conclude that both types of addition (SAPs or fibers) have a beneficial effect on the shrinkage. however, the addition of SAPs in a higher extend (i.e. a shrinkage reduction of approximately 80% after one day and 60% after 7 days). In addition, based on the experiments and the correlated shrinkage modelling according to ModelCode90 and Eurocode2, the author concluded that standard design codes do not consider the heterogenous behavior of printed elements accurately.

Future perspectives

The results obtained in this PhD research show that, although 3DCP aimed to have a lot of advantages, it has not yet reached the level needed to fulfil its potential and compete with traditional manufacturing techniques. Although various process parameters have been included in this experimental research, it is recommended to extend them with some additional parameters which could have a significant influence on the mechanical and structural behavior, for instance nozzle standoff distance, number of layers, temperature and relative humidity.

The work presented in this manuscript was mainly based on one single type of material composition, containing OPC as the only binder in the system. Although the environmental impact of the manufacturing technique itself is lower than with conventional casting methods, its benefits are counteracted by the high amount of binder used in most printable materials. Therefore, it is recommended to improve the printable material itself. To create an eco-friendly material, there are different strategies which should be explored: *(i)* the integration of supplementary cementitious materials, *(ii)* using alternative binders (for example CSA cements) and *(iii)* printing with geopolymers. In addition, these improvements could also be beneficial in terms of durability as a lower cement content will consequently result in less shrinkage.

Material characterization, both on a structural and durable level, was mainly performed on two-layered printed elements. Although this low number of layers allowed to focus in a fundamental way on the properties and transport phenomena, the author acknowledges the fact that this is not fully representative for real-life structural components. Therefore, an extension should be made and the influence of multi-layered components on the microstructure and correlated hardened properties should be investigated. In addition, also the process-related dependency of the components should be further explored, considering the 3D print equipment, in combination with different nozzle standoff distances and geometries, printing speeds, etc. Further on, only unreinforced 3D printed elements were incorporated in the experimental investigations. However, with the aim to realize real-life structural applications, the absence of significant tensile capacity and ductility will have to be addressed. As the incorporation of traditional reinforcement will be difficult in a layered manufacturing technique, other techniques must be explored. The addition of fibers or the application of a reinforcement strategy which could be performed simultaneously with concrete extrusion have to be explored. However, regardless of the manufacturing technique, the consequences on both the fresh and hardened properties should be investigated, with special attention to the interlayer between the printed filaments as these are most detrimental for the overall behavior.

Due to the lack of formwork, early-age cracking phenomena should be mitigated. A first step herein is an accurate and complete visualization and quantification of the evaporation rate of the printed layers and the visualization of the correlated crack formations. The evaporation rate and the moisture exchange phenomena can be studied based on neutron radiography. A visualization of the crack formation requires more specialized visualization techniques, as for example X-Ray Tomography or Digital Image Correlation (DIC).

Based on the results, the author states that there is a need for standardized test methods before the integration of digital manufacturing in construction industry can become reality. This standardization is necessary for test methods to characterize both the fresh state and the hardened state taking into account the pitfalls introduced by the manufacturing method (i.e. the anisotropic behavior, the irregular shape of the material, the higher amount of cracks and voids, etc.). In addition, also the design codes should be reconsidered to improve the correlation between expectations and reality.

References

1. Wangler, T., et al., *Digital Concrete: A Review.* Cement and Concrete Research, 2019. **123**: p. 105780.
2. Mohan, M., et al., *Extrusion-based concrete 3D printing from a material perspective: A state-of-the-art review.* Cement and Concrete Composites, 2021. **115C**: p. 103855.
3. Sanjayan, J., A. Nazari, and B. Nematollah, *3D Concrete Printing Technology: Construction and Building Applications*. 2019. 448.
4. De Schutter, G., et al., *Vision of 3D printing with concrete — Technical, economic and environmental potentials.* Cement and Concrete Research, 2018. **112**: p. 25-36.
5. Lim, S., et al., *Developments in construction-scale additive manufacturing processes.* Automation in Construction, 2012. **21**: p. 262-268.
6. Pegna, J., *Exploratory investigation of solid freeform construction.* Automation in Construction, 1997. **5**(5): p. 427-437.
7. Khoshnevis, B., *Automated construction by contour crafting—related robotics and information technologies.* Automation in Construction, 2004. **13**(1): p. 5-19.
8. Labonnote, N., et al., *Additive construction: State-of-the-art, challenges and opportunities.* Automation in Construction, 2016. **72**: p. 347-366.
9. Khoshnevis, B., et al., *Mega-scale fabrication by Contour Crafting.* Int. J. Industrial and Systems Engineering, 2006. **1**.
10. Zhang, J. and B. Khoshnevis, *Optimal machine operation planning for construction by Contour Crafting.* Automation in Construction, 2013. **29**: p. 50–67.
11. Buswell, R.A., et al., *3D printing using concrete extrusion: A roadmap for research.* Cement and Concrete Research, 2018. **112**: p. 37-49.
12. Le, T.T., et al., *Mix design and fresh properties for high-performance printing concrete.* Materials and Structures, 2012. **45**(8): p. 1221-1232.
13. Le, T.T., et al., *Hardened properties of high-performance printing concrete.* Cement and Concrete Research, 2012. **42**(3): p. 558-566.
14. Lowke, D., et al., *Particle-bed 3D printing in concrete construction – Possibilities and challenges.* Cement and Concrete Research, 2018. **112**: p. 50-65.
15. Lloret, E., et al., *Smart Dynamic Casting Slipforming with flexible formwork: Inline measurements and control*. 2017.
16. Wangler, T., et al., *Digital Concrete: Opportunities and Challenges* RILEM Technical Letters, 2016. **1**: p. 67-75.
17. Nematollahi, B., M. Xia, and J. Sanjayan, *Current Progress of 3D Concrete Printing Technologies*. 2017.
18. Bos, F., et al., *Additive manufacturing of concrete in construction: potentials and challenges of 3D concrete printing.* Virtual and Physical Prototyping, 2016. **11**(3): p. 209-225.
19. Van Der Putten, J., et al., *Microstructural Characterization of 3D Printed Cementitious Materials.* Materials, 2019. **12**(18).
20. Venkatesh, N., S. Hempel, and V. Mechtcherine, *Micro- and macroscopic investigations on the interface between layers of 3D printed cementitious elements*, in *International Conference on Advances in Construction Materials and Systems*. 2017: Chennai.

21. Kruger, J., A. du Plessis, and G. van Zijl, *An investigation into the porosity of extrusion-based 3D printed concrete.* Additive Manufacturing, 2021. **37**: p. 101740.
22. Feng, P., et al., *Mechanical properties of structures 3D printed with cementitious powders.* Construction and Building Materials, 2015. **93**: p. 486-497.
23. Rahul, A.V., et al., *Mechanical characterization of 3D printable concrete.* Construction and Building Materials, 2019. **227**: p. 116710.
24. Wolfs, R.J.M., F.P. Bos, and T.A.M. Salet, *Hardened properties of 3D printed concrete: The influence of process parameters on interlayer adhesion.* Cement and Concrete Research, 2019. **119**: p. 132-140.
25. Emmons, P.H. and B.H. Emmons, *Concrete Repair and Maintenance Illustrated: Problem Analysis; Repair Strategy; Techniques*, in *Concrete Repair and Maintenance Illustrated: Problem Analysis; Repair Strategy; Techniques*. 1993. p. 314.
26. Momayez, A., et al., *Comparison of methods for evaluating bond strength between concrete substrate and repair materials.* Cement and Concrete Research, 2005. **35**(4): p. 748-757.
27. Sánchez, M., et al., *External treatments for the preventive repair of existing constructions: A review.* Construction and Building Materials, 2018. **193**: p. 435-452.
28. Asprone, D., et al., *Rethinking reinforcement for digital fabrication with concrete.* Cement and Concrete Research, 2018. **112**: p. 111-121.
29. Hack, N. and w.v. Lauer, *Mesh-Mould: Robotically Fabricated Spatial Meshes as Reinforced Concrete Formwork.* Architectural Design, 2014. **84**.
30. Hack, N., et al., *Mesh Mould: An on site, robotically fabricated, functional formwork*. 2017.
31. Bos, F.P., et al., *Experimental Exploration of Metal Cable as Reinforcement in 3D Printed Concrete.* Materials (Basel, Switzerland), 2017. **10**(11): p. 1314.
32. Bos, F.P., et al. *3D Printing Concrete with Reinforcement*. 2018. Cham: Springer International Publishing.
33. Christ, S., et al., *Fiber reinforcement during 3D printing.* Materials Letters, 2015. **139**: p. 165-168.
34. Hambach, M. and D. Volkmer, *Properties of 3D-printed fiber reinforced Portland cement paste.* Cement and Concrete Composites, 2017. **79**: p. 62-70.
35. Vantyghem, G., et al. *Compliance, Stress-Based and Multi-physics Topology Optimization for 3D-Printed Concrete Structures*. 2019. Cham: Springer International Publishing.
36. Liew, A., et al., *Design, fabrication and testing of a prototype, thin-vaulted, unreinforced concrete floor*. Engineering Structures, 2017. **137**: p. 323-335.
37. Mechtcherine, V., et al., *3D-printed steel reinforcement for digital concrete construction – Manufacture, mechanical properties and bond behaviour.* Construction and Building Materials, 2018. **179**: p. 125-137.
38. Wang, Z., W. L., and X. Zhao, *Apparatus and method for preparing a building structure with 3d printing*, C.C.N.I.P. Administration., Editor. 2018.
39. Kumarji, S. and O. Geneidy. *http://www.iaacblog.com/tag/concrete-3d-printing/*. 2019.
40. Geneidy, O., et al. *Simultaneous Reinforcement of Concrete While 3D Printing*. 2020. Cham: Springer International Publishing.
41. Nerella, V.N., S. Hempel, and V. Mechtcherine, *Effects of layer-interface properties on mechanical performance of concrete elements produced by extrusion-based 3D-printing.* Construction and Building Materials, 2019. **205**: p. 586-601.

42. Beushausen, H. and M.G. Alexander, *Localised strain and stress in bonded concrete overlays subjected to differential shrinkage.* Materials and Structures, 2007. **40**(2): p. 189-199.
43. Agustí-Juan, I., et al., *Potential benefits of digital fabrication for complex structures: Environmental assessment of a robotically fabricated concrete wall.* Journal of Cleaner Production, 2017. **154**: p. 330-340.
44. Weng, Y., et al., *Comparative economic, environmental and productivity assessment of a concrete bathroom unit fabricated through 3D printing and a precast approach.* Journal of Cleaner Production, 2020. **261**: p. 121245.
45. Panda, B. and M.J. Tan, *Experimental study on mix proportion and fresh properties of fly ash based geopolymer for 3D concrete printing.* Ceramics International, 2018. **44**(9): p. 10258-10265.
46. Panda, B., et al., *Synthesis and characterization of one-part geopolymers for extrusion based 3D concrete printing.* Journal of cleaner production, 2019. **220**: p. 610-619.
47. Panda, B., J.H. Lim, and M.J. Tan, *Mechanical properties and deformation behaviour of early age concrete in the context of digital construction.* Composites Part B: Engineering, 2019. **165**: p. 563-571.
48. Nematollahi, B., et al., *Effect of Type of Fiber on Inter-Layer Bond and Flexural Strengths of Extrusion-Based 3D Printed Geopolymer.* Materials Science Forum, 2018. **939**: p. 155-162.
49. Chen, M., et al., *Rheological and mechanical properties of admixtures modified 3D printing sulphoaluminate cementitious materials.* Construction and Building Materials, 2018. **189**: p. 601-611.
50. Chen, Y., et al., *Limestone and calcined clay-based sustainable cementitious materials for 3D concrete printing: a fundamental study of extrudability and early-age strength development.* Applied Sciences, 2019. **9**(9): p. 1809.
51. Weng, Y., et al., *Feasibility study on sustainable magnesium potassium phosphate cement paste for 3D printing.* Construction and Building Materials, 2019. **221**: p. 595-603.
52. Jolin, M., et al., *Understanding the pumpability of concrete.* 2009.
53. Feys, D., *Interactions between rheological properties and pumping of self-compacting concrete*. 2009, University of Ghent.
54. Feys, D., et al., *Interactions between rheological properties and pumping of concrete*, in *15th International Conference on TRANSPORT AND SEDIMENTATION OF SOLID PARTICLES*. 2011: Wroclaw, Poland.
55. Choi, M., et al., *Lubrication layer properties during concrete pumping.* Cement and Concrete Research, 2013. **45**(0): p. 69-78.
56. Choi, M.S., Y.J. Kim, and S.H. Kwon, *Prediction on pipe flow of pumped concrete based on shear-induced particle migration.* Cement and Concrete Research, 2013. **52**(0): p. 216-224.
57. Kaplan, D., F. de Larrard, and T. Sedran, *Design of Concrete Pumping Circuit.* Materials Journal, 2005. **102**(2).
58. Mohan, M., et al., *Rheological and pumping behaviour of 3D printable cementitious materials with varying aggregate content.* Cement and Concrete Research, 2021. **139**.

59. Nerella, V.N., et al., *Inline quantification of extrudability of cementitious materials for digital construction.* Cement and Concrete Composites, 2019. **95**: p. 260-270.
60. Mechtcherine, V., et al., *Extrusion-based additive manufacturing with cement-based materials – Production steps, processes, and their underlying physics: A review.* Cement and Concrete Research, 2020. **132**: p. 106037.
61. Ma, G., L. Wang, and Y. Ju, *State-of-the-art of 3D printing technology of cementitious material—An emerging technique for construction.* Science China Technological Sciences, 2018. **61**(4): p. 475-495.
62. Zhang, Y., et al., *Fresh properties of a novel 3D printing concrete ink.* Construction and Building Materials, 2018. **174**: p. 263-271.
63. Kazemian, A., et al., *Cementitious materials for construction scale 3D printing: Laboratory testing of fresh printing mixture.* Construction and Building Materials, 2017. **145**: p. 639-647.
64. Wolfs, R.J.M., F.P. Bos, and T.A.M. Salet, *Early age mechanical behaviour of 3D printed concrete: Numerical modelling and experimental testing.* Cement and Concrete Research, 2018. **106**: p. 103-116.
65. Casagrande, L., et al., *Effect of testing procedures on buildability properties of 3D-printable concrete.* Construction and Building Materials, 2020. **245**: p. 118286.
66. Wolfs, R.J.M., F.P. Bos, and T.A.M. Salet, *Correlation between destructive compression tests and non-destructive ultrasonic measurements on early age 3D printed concrete.* Construction and Building Materials, 2018. **181**: p. 447-454.
67. Wolfs, R.J.M., *Experimental characterization and numerical modelling of 3D printed concrete: controlling structural behaviour in the fresh and hardened state.* 2019, Technische Universiteit Eindhoven: Eindhoven.
68. Roussel, N., *Rheological requirements for printable concretes.* Cement and Concrete Research, 2018. **112**: p. 76-85.
69. Perrot, A., D. Rangeard, and A. Pierre, *Structural built-up of cement-based materials used for 3D-printing extrusion techniques.* Materials and Structures, 2016. **49**(4): p. 1213-1220.
70. Marchon, D., et al., *Hydration and rheology control of concrete for digital fabrication: Potential admixtures and cement chemistry.* Cement and Concrete Research, 2018. **112**: p. 96-110.
71. De Schutter, G., *Smart Casting of concrete structures by active control of rheology*. 2016 - 2021, ERC.
72. Roussel, N. and F. Cussigh, *Distinct-layer casting of SCC: The mechanical consequences of thixotropy.* Cement ad Concrete Research 2008. **38**: p. 624-632.
73. Khalil, N., et al., *Use of calcium sulfoaluminate cements for setting control of 3D-printing mortars.* Construction and Building Materials, 2017. **157**: p. 382-391.
74. Snoeck, D., *Self-healing and microstructure of cementitious materials with microfibres and superabsorbent polymers*, in *Faculty of Engingeering and Architecture* 2015, Ghent University.
75. Zohuriaan, J. and K. Kabiri, *Superabsorbent Polymer Materials: A Review.* Iranian Polymer Journal (English Edition), 2008. **17**.

76. Snoeck, D., C. Schröfl, and V. Mechtcherine, *Recommendation of RILEM TC 260-RSC: testing sorption by superabsorbent polymers (SAP) prior to implementation in cement-based materials.* Materials and Structures, 2018. **51**(5): p. 116.
77. 12350-5:2019, N.E., *Beproeving van betonspecie - Deel 5: Schudmaat*. 2019: Bureau voor Normalisatie, Brussel.
78. Mejlhede Jensen, O. and P. Freiesleben Hansen, *Water-entrained cement-based materials: I. Principles and theoretical background*. Vol. 31. 2001. 647-654.
79. Powers, T.C. and T.L. Brownyard, *Studies of the Physical Properties of Hardened Portland Cement Paste.* Journal Proceedings, 1946. **43**(9).
80. Ma, G. and L. Wang, *A critical review of preparation design and workability measurement of concrete material for largescale 3D printing.* Frontiers of Structural and Civil Engineering, 2018. **12**(3): p. 382-400.
81. 196-3, N.E., *Methods of testing cement - Part 3: Determination of setting times and soundness*. 2016: Bureau voor Normalisatie, Brussel.
82. Kruger, J. and G. van Zijl, *A compendious review on lack-of-fusion in digital concrete fabrication.* Additive Manufacturing, 2021. **37**: p. 101654.
83. Panda, B., et al., *Measurement of tensile bond strength of 3D printed geopolymer mortar.* Measurement, 2018. **113**: p. 108-116.
84. Sanjayan, J.G., et al., *Effect of surface moisture on inter-layer strength of 3D printed concrete.* Construction and Building Materials, 2018. **172**: p. 468-475.
85. Lee, H., et al., *Correlation between pore characteristics and tensile bond strength of additive manufactured mortar using X-ray computed tomography.* Construction and Building Materials, 2019. **226**: p. 712-720.
86. Liu, Z., et al., *Interlayer Bond Strength of 3D Printing Cement Paste by Cross-Bonded Method.* Journal of the Chinese Ceramic Society 2019. **47**(5): p. 648-652.
87. Santos, P.M.D. and J. Eduardo Nuno Brito Santos, *Factors Affecting Bond between New and Old Concrete.* Materials Journal, 2011. **108**(4).
88. Keita, E., et al., *Weak bond strength between successive layers in extrusion-based additive manufacturing: measurement and physical origin.* Cement and Concrete Research, 2019. **123**: p. 105787.
89. Tay, Y.W.D., et al., *Time gap effect on bond strength of 3D-printed concrete.* Virtual and Physical Prototyping, 2018. **14**: p. 104-113.
90. He, Y., et al., *Effects of interface roughness and interface adhesion on new-to-old concrete bonding.* Construction and Building Materials, 2017. **151**: p. 582-590.
91. Zareiyan, B. and B. Khoshnevis, *Effects of interlocking on interlayer adhesion and strength of structures in 3D printing of concrete.* Automation in Construction, 2017. **83**: p. 212-221.
92. Kruger, J., S. Zeranka, and G. van Zijl, *An ab initio approach for thixotropy characterisation of (nanoparticle-infused) 3D printable concrete.* Construction and Building Materials, 2019. **224**: p. 372-386.
93. Kruger, J., S. Zeranka, and G. van Zijl, *3D concrete printing: A lower bound analytical model for buildability performance quantification.* Automation in Construction, 2019. **106**: p. 102904.

94. Kruger, J., S. Zeranka, and G. van Zijl. *Quantifying Constructability Performance of 3D Concrete Printing via Rheology-Based Analytical Models*. 2020. Cham: Springer International Publishing.
95. Luković, M. and G. Ye, *Effect of Moisture Exchange on Interface Formation in the Repair System Studied by X-ray Absorption.* Materials, 2016. **9**.
96. Panda, B., et al., *The effect of material fresh properties and process parameters on buildability and interlayer adhesion of 3D printed concrete.* Materials, 2019. **12**(13): p. 2149.
97. Paul, S.C., et al., *Fresh and hardened properties of 3D printable cementitious materials for building and construction.* Archives of Civil and Mechanical Engineering, 2018. **18**(1): p. 311-319.
98. Franck, A. and N. De Belie, *Concrete Floor–Bovine Claw Contact Pressures Related to Floor Roughness and Deformation of the Claw.* Journal of Dairy Science, 2006. **89**(8): p. 2952-2964.
99. 12390-3, N.E., *Testing hardened concrete - Part 3: Compressive strength of test specimens*. 2019: Bureau voor Normalisatie, Brussel
100. 196-1, N.E., *Methods of testing cement - Part 1: Determination of strength*. 2016: Bureau voor Normalisatie, Brussel.
101. 1542, N.E., *Producten en systemen voor de bescherming en reparatie van betonconstructies - Beproevingsmethoden - Bepaling van de hechtsterkte door middel van de afbreekproef*. 1999: Bureau voor Normalisatie, Brussel.
102. B15-220, N., *Proeven op beton: bepalen van de druksterkte*. 1990: Belgisch Instituut voor normalisatie, Brussel.
103. Van Zijl, G.P.A.G., S.C. Paul, and M.J. Tan, *Properties of 3D Printable Concrete*, in *2nd International Conference on Progress in Additive Manufacturing* 2016: Singapore.
104. Hamad, A.J., *Size and shape effect of specimen on the compressive strength of HPLWFC reinforced with glass fibres.* Journal of King Saud University - Engineering Sciences, 2017. **29**(4): p. 373-380.
105. Panda, B., S. Chandra Paul, and M. Jen Tan, *Anisotropic mechanical performance of 3D printed fiber reinforced sustainable construction material.* Materials Letters, 2017. **209**: p. 146-149.
106. Kim, K., et al., *Evaluation of Shear Strength of RC Beams with Multiple Interfaces Formed before Initial Setting Using 3D Printing Technology.* Materials, 2017. **10**: p. 1349.
107. Beushausen, H. and M.G. Alexander, *Bond strength development between concretes of different ages.* Magazine of Concrete Research, 2008. **60**(1): p. 65-74.
108. Neville, A.M., *Properties of concrete*. Vol. 4. 1995: Longman London.
109. Marchment, T., J. Sanjayan, and M. Xia, *Method of enhancing interlayer bond strength in construction scale 3D printing with mortar by effective bond area amplification.* Materials & Design, 2019. **169**: p. 107684.
110. Peled, A. and S.P. Shah, *Processing Effects in Cementitious Composites: Extrusion and Casting.* Journal of Materials in Civil Engineering, 2003. **15**(2): p. 192-199.
111. Bissonnette, B., L. Courard, and A. Garbacz, *Concrete surface engineering*. Modern Concrete Technology Series, ed. A. Bentur and S. Mindess. 2016.

112. Zareiyan, B. and B. Khoshnevis, *Interlayer adhesion and strength of structures in Contour Crafting - Effects of aggregate size, extrusion rate, and layer thickness.* Automation in Construction, 2017. **81**: p. 112-121.
113. Sonebi, M., M. Amziane, and A. Perrot, *Mechanical Behavior of 3D Printed Cement Materials*, in *3D Printing of Concrete: State of the Art and Challenges of the Digital Construction Revolution* 2019. p. 101-124.
114. Mehta, P.K. and P.J.M. Monteiro, *Concrete : microstructure, properties, and materials*. 3rd ed. ed. 2006: New York (N.Y.) : McGraw-Hill.
115. Boel, V., *Microstructuur van zelfverdichtend beton in relatie met gaspermeabiliteit en duurzaamheidsaspecten*. 2007, PhD-dissertation, University of Ghent p. 320.
116. Mönnig, S., *Superabsorbing additions in concrete: applications, modelling and comparison of different internal water sources.* 2009.
117. Snoeck, D., et al., *Effect of high amounts of superabsorbent polymers and additional water on the workability, microstructure and strength of mortars with a water-to-cement ratio of 0.50.* Construction and Building Materials, 2014. **72**: p. 148-157.
118. Boel, V.T.W., K.T.W. Audenaert, and G. De Schutter, *Gas permeability and capillary porosity of self-compacting concrete.* Materials and Structures, 2008. **41**: p. 1283-1290.
119. Snellings, R., et al., *Clinkering Reactions During Firing of Recyclable Concrete.* Journal of the American Ceramic Society, 2012. **95**(5): p. 1741-1749.
120. Guang, Y., *Experimental Study and numerical simulation of the development of the microstructure and permeability in cementitious materials*. 2003, Technical University of Delft: Delft, The Netherlands. p. 207.
121. Masschaele, B., et al., *HECTOR: A 240kV micro-CT setup optimized for research.* Journal of Physics: Conference Series, 2013. **463**: p. 012012.
122. Kloft, H., et al., *Influence of process parameters on the interlayer bond strength of concrete elements additive manufactured by Shotcrete 3D Printing (SC3DP).* Cement and Concrete Research, 2020. **134**: p. 106078.
123. Nilsson, L.-O., *Durability concept; pore structure and transport processes.* Advanced Concrete Technology, 2003. **2**.
124. Castro, J., D. Bentz, and J. Weiss, *Effect of sample conditioning on the water absorption of concrete.* Cement and Concrete Composites, 2011. **33**(8): p. 805-813.
125. Van Belleghem, B., *Effect of capsule-based self-healing on chloride induced corrosion of reinforced concrete*, in *PhD-thesis*. 2018, Ghent.
126. Zaccardi, Y.A.V., N.M. Alderete, and N. De Belie, *Improved model for capillary absorption in cementitious materials: Progress over the fourth root of time.* Cement and Concrete Research, 2017. **100**: p. 153-165.
127. Schröfl, C., V.N. Nerella, and V. Mechtcherine. *Capillary Water Intake by 3D-Printed Concrete Visualised and Quantified by Neutron Radiography*. 2019. Cham: Springer International Publishing.
128. Phillipson, M., et al., *Moisture measurement in building materials: an overview of current methods and new approaches.* Building Services Engineering Research and Technology, 2007. **28**(4): p. 303-316.

129. Roels, S., et al., *A comparison of different techniques to quantify moisture content profiles in porous building materials.* Journal of Thermal Envelope and Building Science, 2004. **27**(4): p. 261-276.
130. Nizovtsev, M., et al., *Determination of moisture diffusivity in porous materials using gamma-method.* International Journal of Heat and Mass Transfer, 2008. **51**(17-18): p. 4161-4167.
131. Vontobel, P., et al., *Neutron tomography: Method and applications.* Physica B: Condensed Matter, 2006. **385**: p. 475-480.
132. 13057:2002, N.E., *Products and systems for the protection and repair of concrete structures - Test methods - Determination of resistance of capillary absorption*. 1999: Bureau voor Normalisatie, Brussel.
133. -20, A.C., *Standard Test Method for Measurement of Rate of Absorption of Water by Hydraulic-cement Concretes*. 2020: ASTM International, West Conshohocken.
134. Van Tittelboom, K., et al., *Use of neutron radiography and tomography to visualize the autonomous crack sealing efficiency in cementitious materials.* Materials and Structures, 2013. **46**(1): p. 105-121.
135. Snoeck, D., et al., *Visualization of water penetration in cementitious materials with superabsorbent polymers by means of neutron radiography.* Cement and Concrete Research, 2012. **42**(8): p. 1113-1121.
136. Van den Heede, P., et al., *Neutron Radiography Based Visualization and Profiling of Water Uptake in (Un)cracked and Autonomously Healed Cementitious Materials.* Materials, 2016. **9**(5): p. 311.
137. Lehmann, E.H., P. Vontobel, and L. Wiezel, *Properties of the radiography facility neutra at sinq and its potential for use as a European reference facility.* Nondestructive Testing and Evaluation, 2001. **16**(2-6): p. 191-202.
138. Carminati, C., et al., *Implementation and assessment of the black body bias correction in quantitative neutron imaging.* Plos One, 2019. **14**(1).
139. de Beer, F.C., J.J. le Roux, and E.P. Kearsley, *Testing the durability of concrete with neutron radiography.* Nuclear Instruments and Methods in Physics Research Section A: Accelerators, Spectrometers, Detectors and Associated Equipment, 2005. **542**(1): p. 226-231.
140. de Beer, F.C., W.J. Strydom, and E.J. Griesel, *The drying process of concrete: a neutron radiography study.* Applied Radiation and Isotopes, 2004. **61**(4): p. 617-623.
141. Brew, D.R.M., et al., *Water transport through cement-based barriers—A preliminary study using neutron radiography and tomography.* Nuclear Instruments and Methods in Physics Research Section A: Accelerators, Spectrometers, Detectors and Associated Equipment, 2009. **605**(1): p. 163-166.
142. Joseph, A.M., et al., *The use of municipal solid waste incineration ash in various building materials: a Belgian point of view.* Materials, 2018. **11**(1): p. 141.
143. Cheewaket, T., C. Jaturapitakkul, and W. Chalee, *Long term performance of chloride binding capacity in fly ash concrete in a marine environment.* Construction and Building Materials, 2010. **24**(8): p. 1352-1357.
144. 206-1, N.E., *Beton - Deel 1: Specificatie, eigenschappen, vervaardiging en conformiteit*. 2001: Bureau voor Normalisatie, Brussel.

145. Šavija, B., J. Pacheco, and E. Schlangen, *Lattice modeling of chloride diffusion in sound and cracked concrete.* Cement and Concrete Composites, 2013. **42**: p. 30-40.
146. Savija, B., *Experimental and numerical investigation of chloride ingress in cracked concrete.* 2014.
147. Stanish, K., R.D. Hooton, and M. Thomas, *Testing the chloride penetration resistance of concrete: a literature review.* 1997.
148. Arsenault, J., J. Bigas, and J. Ollivier, *Determination of chloride diffuison coefficient using two different steady-state methods: influence of concentration gradient.* 1995.
149. Truc, O., J. Ollivier, and M. Carcassès, *A new way for determining the chloride diffusion coefficient in concrete from steady state migration test.* Cement and Concrete Research, 2000. **30**(2): p. 217-226.
150. NT Build 443, *Concrete, hardened: Accelerated chloride penetration*. 1995: Nordic cooperation.
151. NT Build 355, *Concrete, mortar and cement based repair materials: chloride diffusion coefficient from migration cell experiments*. 1997-11: Nordic cooperation.
152. Andrade, C., *Calculation of chloride diffusion coefficients in concrete from ionic migration measurements.* Cement and Concrete Research, 1993. **23**(3): p. 724-742.
153. NT Build 492, *Concrete, mortar and cement-based repair materials: chloride migration coefficient from non-steady state migration experiments*. 1999-11: Nordic cooperation.
154. Khanzadeh Moradllo, M., et al., *Using micro X-ray fluorescence to image chloride profiles in concrete.* Cement and Concrete Research, 2017. **92**: p. 128-141.
155. Real, L., et al., *AgNO3 spray method for measurement of chloride penetration: the state of art.* Revista ALCONPAT, 2015. **5**: p. 142.
156. Petersen, C.G., *Rapid Chloride Test, the RCT-method: Measurements of the chloirde content in-situ*, I. Germann Instruments, Editor. 1991.
157. Song, M., *Chloride penetration and Service-life prediction of Cracked Self-Compacting Concrete*, in *Faculty of Engingeering and Architecture* 2012, Ghent University.
158. Yang, C.C., *On the relationship between pore structure and chloride diffusivity from accelerated chloride migration test in cement-based materials.* Cement and Concrete Research, 2006. **36**(7): p. 1304-1311.
159. Mohammed, M.K., A.R. Dawson, and N.H. Thom, *Macro/micro-pore structure characteristics and the chloride penetration of self-compacting concrete incorporating different types of filler and mineral admixture.* Construction and Building Materials, 2014. **72**: p. 83-93.
160. Bran Anleu, P.C., *Quantitative Micro XRF Mapping of Chlorides: Possibilities, Limitations, and Applications, from Cement to Digital Concrete*. 2018, ETH Zurich.
161. Audenaert, K., *Transportmechanismen in zelfverdichtend beton in relatie met carbonatatie en chloridepenetratie*. 2006, PhD-dissertation, Univeristy of Ghent p. 369.
162. Oh, B.H. and S.Y. Jang, *Effects of material and environmental parameters on chloride penetration profiles in concrete structures.* Cement and Concrete Research, 2007. **37**(1): p. 47-53.
163. Hu, S., et al., *Influences of time, temperature, and humidity on chloride diffusivity: Mesoscopic numerical research.* Journal of Materials in Civil Engineering, 2017. **29**(11): p. 04017223.

164. Liu, J., et al., *Understanding the interacted mechanism between carbonation and chloride aerosol attack in ordinary Portland cement concrete.* Cement and Concrete Research, 2017. **95**: p. 217-225.
165. Thiery, M., et al., *Investigation of the carbonation front shape on cementitious materials: Effects of the chemical kinetics.* Cement and concrete research, 2007. **37**(7): p. 1047-1058.
166. Visser, J.H., *Accelerated carbonation testing of mortar with supplementary cementing materials-Limitation of the acceleration due to drying.* Heron, 2012. **57**(3): p. 231-247.
167. Van den Heede, P., *Durability and sustainability of concrete with high volumes of fly ash*. 2014, Gent : Universiteit Gent.
168. Gruyaert, E., *Effect van hoogovenslak als cementvervanging op de hydratatie, microstructuur, sterkte en duurzaamheid van beton*. 2011, PhD dissertation, Univerisity of Ghent.
169. *CPC-18 Measurement of hardened concrete carbonation depth.* Materials and Structures, 1988. **21**(6): p. 453-455.
170. Alahmad, S., et al., *Effect of crack opening on carbon dioxide penetration in cracked mortar samples.* Materials and Structures, 2009. **42**(5): p. 559-566.
171. Wang, X.-H., et al., *Influence of loading and cracks on carbonation of RC elements made of different concrete types.* Construction and Building Materials, 2018. **164**: p. 12-28.
172. Hirschwald, J., *Die Prüfung der natürlichen Bausteine auf ihre Wetterfeständigkeit*, ed. W.E. Sohn. 1908: . 320.
173. Powers, T.C. and R. Helmuth. *Theory of volume changes in hardened portland-cement paste during freezing*. in *Highway research board proceedings*. 1953.
174. Deprez, M.W.E., V.p.W.E. Cnudde, and G.c.T.W. De Schutter, *A multiscale experimental identification of freeze-thaw induced pore-scale processes in porous mineral building materials*. 2020, Universiteit Gent. Faculteit Wetenschappen 2020.
175. B15-231, N., *Proeven op beton: vorstbestandheid*. 1987: Belgisch Instituut voor normalisatie, Brussel.
176. C666/C666-15, A., *Standard Test Method for Resistance of Concrete to Rapid Freezing and Thawing*. 2015: ASTM International, West Conshohocken.
177. 1339, N.E., *Proeven op betontegels - Eisen en beproevingsmethoden*. 2003: Bureau voor Normalisatie, Brussel.
178. De Schutter, G., *Damage to Concrete Structures*. 2012, Belgium: CRC Press. 202.
179. Assaad, J.J., F. Hamzeh, and B. Hamad, *Qualitative assessment of interfacial bonding in 3D printing concrete exposed to frost attack.* Case Studies in Construction Materials, 2020. **13**: p. e00357.
180. Tian, W. and N. Han, *Pore characteristics (>0.1 mm) of non-air entrained concrete destroyed by freeze-thaw cycles based on CT scanning and 3D printing.* Cold Regions Science and Technology, 2018. **151**: p. 314-322.
181. 12390-11, C.T., *Testing hardened concrete - Part 11: Tersting hardened concrete - Part 11: Determination of the chloride resistance of concrete: unidirectional diffusion*. 2007: European Committee for Standardization, Brussels.

182. 12390-10, C.T., *Testing hardened concrete - Part 10: Deteramination of the relative carbonation resistance of concrete*. 2007: European Committee for Standardization, Brussels.
183. Shafikhani, M. and S. Chidiac, *RELATIONSHIPS BETWEEN FREE AND WATER-SOLUBLE CHLORIDE CONCENTRATIONS IN CONCRETE.* 2019.
184. Yuan, Q., et al., *Chloride binding of cement-based materials subjected to external chloride environment – A review*. Construction and Building Materials, 2009. **23**(1): p. 1-13.
185. Zhang, Y., et al., *Hardened properties and durability of large-scale 3D printed cement-based materials.* Materials and Structures, 2021. **54**(1): p. 1-14.
186. Nosratzehi, N. and M. Miri, *Experimental Investigation on Chloride Diffusion Coefficient of Self-compacting Concrete in the Oman Sea.* Periodica Polytechnica Civil Engineering, 2020.
187. Khanzadeh Moradllo, M., S. Sadati, and M. Shekarchi, *Quantifying maximum phenomenon in chloride ion profiles and its influence on service-life prediction of concrete structures exposed to seawater tidal zone – A field oriented study.* Construction and Building Materials, 2018. **108**.
188. Friedmann, H., O. Amiri, and A. Aït-Mokhtar, *Physical modeling of the electrical double layer effects on multispecies ions transport in cement-based materials.* Cement and Concrete Research, 2008. **38**: p. 1394-1400.
189. Qiu, Q., *A state-of-the-art review on the carbonation process in cementitious materials: Fundamentals and characterization techniques.* Construction and Building Materials, 2020. **247**: p. 118503.
190. Slowik, V., M. Schmidt, and R. Fritzsch, *Capillary pressure in fresh cement-based materials and identification of the air entry value.* Cement and Concrete Composites, 2008. **30**(7): p. 557-565.
191. Boshoff, W.P. and R. Combrinck, *Modelling the severity of plastic shrinkage cracking in concrete.* Cement and Concrete Research, 2013. **48**: p. 34-39.
192. Moelich, G., J. Kruger, and R. Combrinck, *Plastic shrinkage cracking in 3D printed concrete.* Composites Part B: Engineering, 2020: p. 108313.
193. Baroghel-Bouny, V., et al., *Autogenous deformations of cement pastes: Part II. W/C effects, micro–macro correlations, and threshold values.* Cement and Concrete Research, 2006. **36**(1): p. 123-136.
194. Mechtcherine, V. and L. Dudziak, *Effects of Superabsorbent Polymers on Shrinkage of Concrete: Plastic, Autogenous, Drying*, in *Application of Super Absorbent Polymers (SAP) in Concrete Construction: State-of-the-Art Report Prepared by Technical Committee 225-SAP*, V. Mechtcherine and H.-W. Reinhardt, Editors. 2012, Springer Netherlands: Dordrecht. p. 63-98.
195. Holt, E., *Early Age Autogenouts Shrinkage of Concrete.* Tech Res Centre Finland: VTT Publicat, 2001. **446**.
196. Craipeau, T., et al., *Mortar pore pressure prediction during the first hours of cement hydration.* Cement and Concrete Composites, 2021. **119**: p. 103998.
197. Tenório Filho, J.R., et al., *Discussing Different Approaches for the Time-Zero as Start for Autogenous Shrinkage in Cement Pastes Containing Superabsorbent Polymers.* Materials (Basel, Switzerland), 2019. **12**(18): p. 2962.

198. Zhang, Y., et al., *Rheological and harden properties of the high-thixotropy 3D printing concrete.* Construction and Building Materials, 2019. **201**: p. 278-285.
199. Saliba, J., et al., *Influence of shrinkage-reducing admixtures on plastic and long-term shrinkage.* Cement and Concrete Composites, 2011. **33**(2): p. 209-217.
200. al., B.e., *The effect of Superabsorbent polymers on the Mitigation of Plastic Shrinkage Cracking of Conventional Concrete, Results of a RILEM inter-laboratory test by TC 260-RC.* Under submition, Materials and Structures, 2019.
201. Mechtcherine, V. and H.W. Reinhardt, *Application of superabsorbent polymers (SAP) in concrete construction: State of the art report prepared by technical committee 225-SAP*. 2012. 1-164.
202. Castro, J., et al. *Extending internal curing concepts (using fine LWA) to mixtures containing high volumes of fly ash*. in *2010 Concrete Bridge Conference: Achieving Safe, Smart & Sustainable BridgesNational Concrete Bridge CouncilFederal Highway AdministrationPortland Cement Association*. 2010.
203. Bertelsen, I.M.G., L.M. Ottosen, and G. Fischer, *Influence of fibre characteristics on plastic shrinkage cracking in cement-based materials: A review.* Construction and Building Materials, 2020. **230**: p. 116769.
204. B15-216, N., *Proeven op beton: krimpen en zwellen*. 1974: Belgisch Instituut voor normalisatie, Brussel.
205. C1698-19, A., *Standard Test Method for Autogenous Strain of Cement Paste and Mortar*. 2019: ASTM International, West Conshohocken, PA.
206. 2, NBN B.-E., *Berekening van betonconstructies - Deel 1-1: Algemene regels en regels voor gebouwen*. 1999: Belgisch Instituut voor normalisatie, Brussel.
207. Justs, J., et al., *Internal curing by superabsorbent polymers in ultra-high performance concrete.* Cement and Concrete Research, 2015. **76**: p. 82-90.
208. Dudziak, L. and V. Mechtcherine, *Enhancing early-age resistance to cracking in high strength cement-based materials by means of internal curing using Super Absorbent Polymers.* International Rilem Conference On Material Science, 2010. **3**: p. 129-139.
209. Snoeck, D., O.M. Jensen, and N. De Belie, *The influence of superabsorbent polymers on the autogenous shrinkage properties of cement pastes with supplementary cementitious materials.* Cement and Concrete Research, 2015. **74**: p. 59-67.
210. Federowicz, K., et al., *Effect of Curing Methods on Shrinkage Development in 3D-Printed Concrete.* Materials, 2020. **13**: p. 2590.

Curriculum Vitae

Personal information

Name:	Jolien Van Der Putten
Date of Birth:	December 4th 1990
Place of Birth:	Zottegem – Belgium
Nationality:	Belgian
Address:	Monseigneur Meulemanstraat 2, 9520 Sint-Lievens-Houtem
Email:	Jolien.VanDerPutten@UGent.be

Education

2014 – 2021	Doctorate (PhD) in Civil Engineering
	Faculty of Engineering and Architecture at Ghent University
	Specialist courses
	Concrete Microscopy course (Delft University of Technology)
	Introduction to Computational Fluid Dynamics (Ghent University)
	SCIA Engineer – Fundamentals 1 & 2
	International Short Course on Advanced High-resolution 3D imaging (Ghent University)
	SCIA Engineer – Fundamentals 1 & 2
	Seminars in transferable skills:
	Advanced Academic English: Writing skills ((Bioscience) Engineering)
	Basic assistant training
	Effective Graphical Displays
	Writing abstracts

2012 – 2014	Master of Science in Civil Engineering
	Major: Construction Design
	Faculty of Engineering and Architecture, Ghent University
	Graduated *'cum laude'*
	Master thesis: 'Opstellen van interactiekrommen ter verificatie van het *compressible packing model*'
2008 – 2012	Bachelor and Master of Science in de Industriële wetenschappen: bouwkunde
	Faculty of Engineering and Architecture, Ghent University
	Graduated *'cum laude'*
	Master thesis: 'Bevestiging van zonnepanelen op een steel-deck plat dak met pvc-dakafdichting'
2002 – 2008	General Secondary Education: Latin-science
	Onze-Lieve-Vrouwcollege campus Bevegem, Zottegem

Employment

2014 – 2021	PhD Student
	Magnel – Vandepitte Laboratory for Concrete Research
	Department of Structural Engineering and Building Materials
	Faculty of Engineering and Architecture
	Ghent University, Belgium
	PhD Research
	Mechanical Properties and Durability of 3D Printed Cementitious Materials
	Teaching activities
	Exercises: Concrete Technology
	Exercises: Geotechnical Engineering
	Exercises: Structural Engineering II
	Counsellor of 17 master students

A1 Publications

Van Der Putten, J., Dils, J., Minne, P., Boel, V., De Schutter, G. (2017) Determination of packing profiles for the verification of the compressible packing model in case of UHPC pastes, Materials and Structures, Volume 50:118.

Van Der Putten, J., Deprez, M., Cnudde, V., De Schutter, G., Van Tittelboom, K. (2019) Microstructural characterization of 3D printed cementitious materials, Materials Special Issue "Concrete 3D Printing and Digitally-Aided Fabrication", Volume 12 (18): 2993, available online.

Van Der Putten, J., Azima, M., Van den Heede, P., Van Mullem, T., Snoeck, D., Carminati, C., Hovind, J., Trtik, P., De Schutter, G., Van Tittelboom, K. (2020) Neutron radiography to study the water ingress via the interlayer of 3D printed cementitious materials for continuous layering, Construction and Building Materials, Volume 258, 119587.

Van Der Putten, J., Snoeck, D., De Coensel, R., De Schutter, G., Van Tittelboom, K. (2021) Early age shrinkage phenomena of 3D printed cementitious materials with superabsorbent polymers, Journal of Building Engineering, special issue “Advances in 3D Concrete Printing and Digital Construction Technologies for Buildings”, Volume 35, 102059.

Van Der Putten, J., Van den Heede, P., De Volder, M., Deprez, M., Cnudde, V., De Schutter, G., Van Tittelboom, K (2021). Transport properties of 3D printed cementitious materials with prolonged time gap between successive layers. Cement and Concrete Research, in preparation

A2 Publications

Van Der Putten, J., De Schutter, G., Van Tittelboom, K., (2019) Surface modification as a technique to improve inter-layer bonding strength in 3D printed cementitious materials, RILEM Technical Letters, Volume 4, 40, pp. 33-38. doi: 10.21809/rilemtechlett.2019.84.

Van Der Putten, J., Van den Heede, P., De Volder, M., Deprez, M., Cnudde, V., De Schutter, G., Van Tittelboom (2020) Chloride-indringing 3D-geprint beton, Cement.

Book chapters

Van Der Putten, J., Nerella, V.N., Mechterine, V., Sonebi, M., D'Hondt, M., Weger, Wang, Z., Van Tittelboom, K., De Schutter, G., Roussel, N., Lowke, D., Chapter 5 – Properties and testing of printed materials in hardened state, RILEM State-of-the-art Report.

C1/P1 Publications

Van Der Putten, J., Lesage, K., & De Schutter, G. (2016). Influence of the particle shape on the packing density and pumpability of UHPC. In E. Fehling, B. Middendorf, & J. Thiemicke (Eds.), Ultra-High-Performance Concrete and High-Performance Construction Materials (Vol. 27, pp. 1–8). Presented at the Ultra-High-Performance Concrete and High-Performance Construction Materials (HIPERMAT).

Van Der Putten, J., De Schutter, G., Van Tittelboom, K., (2018), The effect of print parameters on the (micro)structure of 3D printed cementitious materials, 1st RILEM International Conference on Concrete and Digital Fabrication, DC 2018, T. Wangler and R. J. Flatt (Eds.), RILEM Bookseries 19, pp. 234–244, 10-12 September 2018, Zurich, Switzerland.

Van Der Putten, J., De Schutter, G., Van Tittelboom, K., (2019), Surface modification as a technique to improve inter-layer bonding strength in 3D printed cementitious materials, RILEM Spring convention and international conference on Sustainable Materials, Systems and Structures, SMSS 2019, M. Serdar, N. Stirmer and J. Provis (Eds.), pp. 532, 18-22 March 2019, Rovinj, Croatia.

Van Der Putten, J., Azima, M., Van den Heede, P., Van Mullem, T., De Schutter, G., Van Tittelboom, K. (2019), Neutron radiography to study water ingress via the interlayer of 3D printed cementitious materials, 2nd International conference on Sustainable building materials, ICSBM, V. Caprai and H.J.H. Brouwers (Eds.), pp. 130-137, 12-15 August 2019, Eindhoven, the Netherlands. ISBN: 978-90-386-4898-9.

Van Der Putten, J., Snoeck, D., Van Tittelboom, K. (2019), 3D printing of cementitious materials with superabsorbent polymers, LORCENIS final conference, Durable concrete for infrastructure under severe conditions, M. Araújo, N. De Belie, K. Van Tittelboom (Eds.), pp. 86-89, 10-11 September 2019, Ghent, Belgium.

Van Der Putten, J., Azima, M., Lesage, K., De Schutter, G., Van Tittelboom, K. (2019), Combination of Portland cement and Calcium-SulfoAluminate cement: the highroad for durable 3D printing? 2nd International RILEM Conference on Rheology and processing of Construction materials (RheoCon2) and 9th International RILEM Symposium on Self-compacting concrete (SCC9), 08-11 September 2019, Dresden, Germany.

Van Der Putten, J., Van den Heede, P., De Volder, M., De Schutter, G., Van Tittelboom, K (2020), 3D printing of concrete: the influence on chloride penetration, 2nd RILEM International Conference on Concrete and Digital Fabrication, Eindhoven, the Netherlands, full online conference.

Van Der Putten, J., Van Olmen, A., Aerts, M., Ascione, E., Beneens, J., Blaakmeer, J., De Schutter, G., Van Tittelboom, K. (2020), 3D concrete printing on site: A novel way of building houses? 2nd RILEM International Conference on Concrete and Digital Fabrication, Eindhoven, the Netherlands, full online conference.

C3 Publications

El Cheikh, K., Lesage, K., **Van Der Putten, J.,** Van Tittelboom, K., & De Schutter, G. (2017). 3D printing of cementitious materials. In G. De Schutter, N. De Belie, A. Janssens, & N. Van den Bossche (Eds.), 14th International Conference on Durability of Building Materials and Components (XIV DBMC) (pp. 263–264). Paris: RILEM Publications.

Van Der Putten, J., De Schutter, G., Van Tittelboom, K., (2019), Surface modification as a technique to improve inter-layer bonding strength in 3D printed cementitious materials, RILEM Spring convention and international conference on Sustainable Materials, Systems and Structures, SMSS 2019, M. Serdar, N. Stirmer and J. Provis (Eds.), pp. 532, 18-22 March 2019, Rovinj, Croatia.

3D printing of cementitious materials as an innovative construction technique.
© BESIX